

In-situ Condition Monitoring of Components in Small Modular Reactors Using Process and Electrical Signature Analysis

Reactor Concepts

Dr. Belle R. Upadhyaya

University of Tennessee-Knoxville

In collaboration with:

Oak Ridge National Laboratory

Timothy Beville, Federal POC

Richard Wood, Technical POC

In-situ Condition Monitoring of Components in Small Modular Reactors Using Process and Electrical Signature Analysis

Final Report – Volume 1 Development of Experimental Flow Control Loop, Data Analysis and Plant Monitoring

**Report No. NEUP-11-3212-Y3Q4-2014-1
NEUP Contract Number: 00120767
DE-AC07-05IDPS07-07ID14517**

**Belle R. Upadhyaya
(Principal Investigator)
J. Wesley Hines
(Co-Principal Investigator)
Brian Damiano
(Collaborator, Oak Ridge National Laboratory)**

**Chaitanya Mehta, Price Collins, Matthew Lish, Brian Cady
(Graduate Research Assistants)
Victor Lollar, Dane de Wet
(Undergraduate Research Assistants)
Duygu Bayram
(Visiting Scholar)**

**The University of Tennessee
Department Nuclear Engineering
Knoxville, TN 37996-2300
E-mail: bupadhya@utk.edu**

**TPOC: Richard Wood
Federal Manager: Tim Beville**

December 2014



EXECUTIVE SUMMARY

In-situ Condition Monitoring of Components in Small Modular Reactors Using Process and Electrical Signature Analysis

1. Background and R&D Objectives

For reliable and economic long-term operation of Small Modular Reactors (SMRs), it is imperative that continuous in-situ monitoring of critical equipment must be developed and incorporated in the reactor design phase. This capability is attractive for remote deployment of SMRs with longer fuel cycle duration and for minimizing forced outages, thus enhancing the utilization of these power generating systems in small electric grid environments. These technologies contribute to smart condition-based maintenance, reduced human resources, remote monitoring of reactor components, and autonomous operation. In integral pressurized water reactors (iPWR) and other designs of SMRs, the pressure vessel incorporates most of the critical equipment used for power generation. Examples of such plant components include: steam generators, motors, coolant circulation pumps, motor-operated valves, control rod drive mechanisms (CRDM), in-core instrumentation, and reactor internal structures.

The development of these techniques is also important in monitoring critical parameters during severe accidents and for post-accident recovery. Small integral light water reactors have in-vessel space constraints and many of the traditional instrumentation are not practical in actual implementation. In order to resolve this issue, research is being performed to develop techniques for indirect measurement of process parameters. Examples of some of the process measurements of interest are primary coolant flow rate in the reactor vessel, characteristics of motor-driven coolant pumps, water levels in steam generators where the secondary water flows through the steam generator tubing, in a once-through steam generator configuration, and others.

The purpose of this NEUP funded research and development project was to develop and demonstrate in-situ equipment monitoring methods for small modular reactors (SMRs) with applications to reactor internals such as coolant pumps, valve-actuators, and control rod drive mechanisms. The overall objective was to integrate electric signature analysis (ESA) and process measurements to perform remote monitoring of SMR components. The primary reactor vessel in a typical SMR has limited space for the installation of control, safety, and system monitoring instrumentation. The focus of this research is to develop monitoring and diagnostics methods

using easily accessible measurements. Both experimental and physics-based modeling approaches were developed to establish the feasibility of implementing such techniques and incorporate them during the SMR design phase.

Recent activities by light water reactor SMR vendors and developers (NuScale Power, Generation mPower, Westinghouse, CAREM, KAERI, and others) have indicated an increased interest in the development of integral pressurized water reactors for deployment by 2025. SMRs in the 25-200 MWe range are useful for power supply in remote areas, especially in locations with limited infrastructure. SMRs can also be used for co-generation, combining electricity production and process heat for industrial applications, including water desalination. Because of the modular nature of SMRs and limited vessel penetrations, safety and security of such installations are greatly enhanced.

The research and development under this project was focused on the following three major objectives:

Objective 1: Identification of critical in-vessel SMR components for remote monitoring and development of their low-order dynamic models, along with a simulation model of an integral pressurized water reactor (iPWR).

Objective 2: Development of an experimental flow control loop with motor-driven valves and pumps, incorporating data acquisition and on-line monitoring interface.

Objective 3: Development of stationary and transient signal processing methods for electrical signatures, machinery vibration, and for characterizing process variables for equipment monitoring. This objective includes the development of a data analysis toolbox.

The project tasks were performed in collaboration with the Measurement Sciences and Systems Engineering Division of ORNL. All the tasks and deliverables were completed by the end of the project execution period.

2. Project Technical Summary

The following is a summary of the technical accomplishments under this project:

- A detailed literature review of various SMR types and electrical signature analysis of motor-driven systems was completed. A bibliography of literature is provided at the end of this report. Assistance was provided by ORNL in identifying some key references.
- A review of literature on pump-motor modeling and digital signal processing methods

was performed.

- An existing flow control loop was upgraded with new instrumentation, data acquisition hardware and software. The upgrading of the experimental loop included the installation of a new submersible pump driven by a three-phase induction motor. All the sensors were calibrated before full-scale experimental runs were performed.
- MATLAB-Simulink model of a three-phase induction motor and pump system was completed. The model was used to simulate normal operation and fault conditions in the motor-pump system, and to identify changes in the electrical signatures.
- A simulation model of an integral PWR (iPWR) was updated and the MATLAB-Simulink model was validated for known transients. The pump-motor model was interfaced with the iPWR model for testing the impact of primary flow perturbations (upsets) on plant parameters and the pump electrical signatures. Additionally, the reactor simulation is being used to generate normal operation data and data with instrumentation faults and process anomalies.
- A frequency controller was interfaced with the motor power supply in order to vary the electrical supply frequency. The experimental flow control loop was used to generate operational data under varying motor performance characteristics. Coolant leakage events were simulated by varying the bypass loop flow rate. The accuracy of motor power calculation was improved by incorporating the power factor, computed from motor current and voltage in each phase of the induction motor.
- A variety of experimental runs were made for steady-state and transient pump operating conditions. Process, vibration, and electrical signatures were measured using a submersible pump with variable supply frequency. High correlation was seen between motor current and pump discharge pressure signal; similar high correlation was exhibited between pump motor power and flow rate. Wide-band analysis indicated high coherence (in the frequency domain) between motor current and vibration signals.
- Wide-band operational data from a PWR were acquired from AMS Corporation and used to develop time-series models, and to estimate signal spectrum and sensor time constant. All the data were from different pressure transmitters in the system, including primary and secondary loops. These signals were pre-processed using the wavelet transform for filtering both low-frequency and high-frequency bands. This technique of signal pre-processing provides minimum distortion of the data, and results in a more optimal estimation of time constants of plant sensors using time-series modeling techniques.

- The experimental loop data indicate a clear relationship between motor power and pump discharge (flow rate). This relationship can be used to infer pump flow rate using the computed motor power.
- The iPWR physics model was used to simulate normal operation data and operation with faulty sensors, primary coolant flow rate anomaly, and variations in process parameters such as heat transfer coefficients and reactivity feedback coefficients. The iPWR dynamic model was interfaced with the pump-motor model, and this feature was used to introduce variations in the electrical supply frequency and other anomalies in the equipment to simulate their degradation.
- The iPWR model was extended to include the dynamics of fission product poisoning and its long-term effect on reactor operation.
- A laboratory scale wireless data acquisition and transmission network was developed and demonstrated successfully.
- A micro-controller based data acquisition and analysis module was developed and tested for monitoring machinery vibration. Such low-investment devices are attractive for monitoring a large number of similar plant equipment.
- A data analysis toolbox was developed for processing both loop operational data and wide-band sensor data. It includes all the computational functions that were developed and used in the project; these are classical data analysis and modern digital signal processing (DSP) techniques.

3. Student Participation and External Collaboration

The NEUP grant was beneficial in training both graduate and undergraduate students, and in providing opportunities for parallel collaboration with other related projects.

The project PI and the Co-PI are engaged in three synergistic research projects. One of these is a DOE STTR Phase-1 and Phase-2 projects with the industrial partner, Analysis and Measurement Services (AMS) Corporation, with an emphasis on SMR on-line monitoring. The second is collaboration with Korea Atomic Energy Research Institute (KAERI) on a DOE I-NERI project, and is related to monitoring safety critical functions during beyond design basis accidents in light water reactors. The latter also addresses station blackout, remote sensing, self-powered detectors, energy harvesting, and wireless communication. The third collaborative

project is an IRP titled *Integral Inherently Safe Light Water Reactor (I²S-LWR)*, with Georgia Institute of Technology as the lead for this NEUP-IRP. These illustrate the value of this NEUP project in enhancing the safety and operational reliability of both existing and future nuclear power plants.

The following students and visiting scholars were engaged in making research and development contributions during the project period. These included 1 Ph.D. student, 3 MS students, 2 undergraduate research assistants, and two visiting scholars – from Istanbul Technical University (ITU) and from Korea Atomic Energy Research Institute (KAERI).

Graduate and Undergraduate Students:

- Matthew Lish (Ph.D., Dynamic modeling an iPWR with helical coil steam generators; currently engaged in I²S-LWR research funded by IRP)
- Chaitanya Mehta (M.S., Condition Monitoring of Equipment in Small Modular Reactors Using Electrical and Process Signature Analysis, 2013)
- Price Collins (M.S., Dynamic Analysis and Fault Simulation for Small Modular Reactors, 2014)
- Brian Cady (M.S., Modeling a three-phase induction motor and pump system; currently working for an engineering services company)
- Victor Lollar (B.S., Nuclear Engineering, 2014; currently M.S. student)
- Dane de Wet (B.S., Nuclear Engineering, junior)

Visiting Scholars:

- Seop Hur, Instrumentation, Controls, and Human Factors Division, KAERI, ROK.
- Duygu Bayram, Department of Electrical Engineering, Istanbul Technical University, Turkey.

Publications:

The following are journal and conference publications resulting from the NEUP project.

Journal Publications

1. B.R. Upadhyaya, C. Mehta, and D. Bayram, “Integration of Time Series Modeling and Wavelet Transform for Monitoring Nuclear Plant Sensors,” *IEEE Transactions on Nuclear Science*, Vol. 61, No. 5, pp. 2628-2635, October 2014.
2. B.R. Upadhyaya, C. Mehta, V.B. Lollar, and J.W. Hines, “Remote Monitoring of

Equipment in Small Modular Reactors,” Chemical Engineering Transactions, AIDIC, Italy, Vol. 33, pp. 841-846, August 2013.

3. *Monitoring Pump Parameters in Small Modular Reactors Using Electric Motor Signatures*, manuscript prepared for submission to ASME Journal on Nuclear Engineering and Radiation Science.
4. *Process Fault Simulation and Monitoring for an Integral Pressurized Water Reactor*, manuscript prepared for submission to IEEE Transactions on Nuclear Science.

Conference Publications

5. P.A. Collins and B.R. Upadhyaya, “Small Modular Reactor Response to Errors in Process Variables and Sensors,” Transactions of the American Nuclear Society, Vol. 111, ANS Winter Meeting, Anaheim, CA, November 2014.
6. B.R. Upadhyaya, C. Mehta, V.B. Lollar, J.W. Hines, and D. de Wet, “Approaches to Process Monitoring in Small Modular Reactors,” Proceedings of the ASME 2014 Small Modular Reactors Symposium, Washington, D.C., April 2014.
7. C. Mehta, V.B. Lollar, B.R. Upadhyaya, J.W. Hines, and D. Bayram, “Development of a Method for Monitoring Pump Parameters in Small Modular Reactors Using Motor Signatures,” Transactions of the American Nuclear Society, Vol. 109, pp. 278-279, Washington, D.C., November 2013.
8. B.R. Upadhyaya, P. Collins, M.R. Lish, J.W. Hines, and C. Mitra, “Modeling and Dynamic Simulation of an Integral Pressurized Water Reactor,” Transactions of the American Nuclear Society, Vol. 108, pp. 173-175, Atlanta, Georgia, June 2013.
9. B.R. Upadhyaya, C. Mehta, V.B. Lollar, J.W. Hines, and B. Damiano, “In-situ Condition Monitoring of Components in Small Modular Reactors,” Transactions of the American Nuclear Society, Vol. 107, pp. 843-844, San Diego, California, November 2012.
10. V.B. Lollar, B.R. Upadhyaya, J.W. Hines, J.B. Coble, and D. de Wet, “Data-based Modeling for Monitoring and Fault Detection in Small Modular Reactors,” accepted for conference presentation, NPIC&HMIT 2015, Charlotte, NC, February 2015.
11. R. Wetherington, B. Van Hoy, L. Phillips, B. Damiano, and B.R. Upadhyaya, “Evaluation of A Consumer Electronics-Based Data Acquisition System for Equipment

Monitoring,” accepted for conference presentation, NPIC&HMIT 2015, Charlotte, NC, February 2015.

12. B.R. Upadhyaya, J.-T. Kim, and J.W. Hines, *Development of Diagnostics and Prognostics Methods for Sustainability of Nuclear Power Plant Safety Critical Functions*, Final Report prepared for the DOE I-NERI Project-ROK, 2011-004-K, November 2014; presented at the I-NERI Review Meeting, Washington, D.C., November 2014.

4. Final Report and Future Directions

The Final Report of the three-year project is presented in two volumes:

- Volume 1: Development of an experimental flow control loop with instrumentation, data acquisition, and analysis for demonstrating in-situ condition monitoring of SMRs.
- Volume 2: Development of dynamic models and simulation of anomalies for a small modular pressurized water reactor.

The report presents all the information related to the project, including technical work, computer codes, and the discussion of results.

It is anticipated that the results and deliverables of this R&D project would be useful in further developing and implementing remote monitoring and intelligence maintenance technologies in future light water SMRs and other integral reactors. During the course of the project and discussion with various collaborators, suggestions were made and ideas were developed for future research activities in extending instrumentation and controls strategies for advanced reactors.

DISCLAIMER

Any opinions, findings, and conclusions or recommendations expressed in this report are those of the authors, and do not necessarily reflect the views of the U.S. Department of Energy or the Oak Ridge National Laboratory.

CONTENTS

SECTION	PAGE
EXECUTIVE SUMMARY	1
1. INTRODUCTION	10
1.1. Background and Project Objectives	10
1.2. Summary of R&D Contributions Presented in Volume 2	12
1.3. Organization of the Report	14
2. REVIEW OF LITERATURE	16
2.1. Introduction	16
2.2. Frequency Domain Analysis of Motor Current Signature	18
(Motor as a Transducer)	
2.3. MCSA for Centrifugal Pumps	21
2.4. Critical SMR Components for On-line Monitoring	26
2.5. Small Modular Reactors of the IPWR Type	26
2.6. Monitoring Control Rod Drive Mechanisms	32
3. EXPERIMENTAL FLOW CONTROL LOOP, SYSTEM CALIBRATION AND DATA ACQUISITION	41
3.1. Introduction	41
3.2. Experimental Facility Upgrade	42
3.3. Loop Instrumentation System and Devices	47
4. CHARACTERIZING PUMP POWER, FLOW RATE, AND PRESSURE MEASUREMENTS IN THE EXPERIMENTAL FLOW LOOP	58
4.1. Introduction	58
4.2. Pump Characteristics	58
4.3. Motor Power Calculation	59
4.4. Characterizing Pump Power, Flow Rate, and Pump Discharge Pressure	60
4.5. Remarks on Experimental Results	66
4.6. Repeatability of Experimental Data	66
5. TIME-FREQUENCY ANALYSIS OF TRANSIENT DATA	70
5.1. Non-Stationary Data and Short-Time Fourier Transform	70
5.2. Description of Transient Data	71
5.3. Short-Time Fourier Transform	74
5.4. Transient Data Analysis Using Hilbert-Huang Transform	76

6. CONDITION MONITORING BY USING STOCHASTIC TIME SERIES MODELS	81
6.1. Discrete-Time Stochastic Modeling of Wide-Band Data	81
6.2. Data Pre-processing Using Wavelet Transform	84
6.3. Analysis of Operational Data from a PWR	86
6.4. Estimation of Response Time of Process Transmitters	91
7. DATA-BASED MODELING OF PROCESS AND ELECTRICAL MEASUREMENTS IN THE FLOW CONTROL LOOP	96
7.1. Introduction	96
7.2. Tools for Empirical Model Development	96
7.3. AAKR Modeling without Water Level Control	99
7.4. AAKR Modeling with Water Level Control	111
7.5. Remarks on Data-based Modeling	130
8. DEVELOPMENT OF A LABORATORY WIRELESS DATA ACQUISITION AND COMMUNICATION SYSTEM	132
8.1. Introduction	132
8.2. Overview of Wireless Communication	133
8.3. Literature Review and Summary of System Development	136
8.4. Testing the Wireless Data Acquisition and Transmission System	139
8.5. Remarks on the Implementation of Wireless Data Acquisition	143
9. DEVELOPMENT OF A LOW-COST MICROCONTROLLER-BASED ... EQUIPMENT MONITORING SYSTEM	145
9.1. Introduction to Microcontrollers	145
9.2. Setting up and Testing the BeagleBoard XM Device	145
9.3. Evaluation of a Consumer Electronic-Based Data Acquisition System for Equipment Monitoring (ORNL)	149
10. CONCLUDING REMARKS, SUMMARY AND RECOMMENDATIONS FOR FUTURE R&D	162
8.1. Concluding Remarks	162
8.2. Summary of Significant Contributions Reported in Volume 1	163
8.3. Recommendations for Future Research and Development	164
REFERENCES AND BIBLIOGRAPHY	166
APPENDIX A. MATLAB-based Data Analysis Toolbox	176
A.1. Introduction	176
A.2. Toolbox Module One	176
A.3. Toolbox Module Two	184

1. INTRODUCTION

1.1. Background and Project Objectives

The development of small modular reactors (SMRs) such as the NuScale Power, Westinghouse-SMR and the mPower reactor in the U.S., the start-up of the OPAL reactor in Australia, and the construction of the CARAM-25 reactor designed and developed by CNEA, Argentina, signify the importance of SMRs for power generation, process heat utilization, water desalination, and medical isotope production. Safe and economic long-term operation of these small reactors requires improved design of instrumentation and control systems, remote monitoring, and fault tolerant control for load-following scenarios. This is generally true of all integral reactor designs.

One of the advantages of small modular reactors (SMRs) is their possible deployment in remote locations and continued long-term operation with minimum downtime. In order to achieve this operational goal, the SMRs may require remote and continuous monitoring of process parameters. This feature is also important in monitoring critical parameters during severe accidents and for post-accident recovery. Small integral light water reactors have in-vessel space constraints and many of the traditional instrumentation are not practical in actual implementation. In order to resolve this issue, experiments were carried out on a flow test loop to characterize the relationship among process variables (flow rate, pressure, water level) and pump motor signatures. This volume of the Final Report presents the findings of this research with implications in relating electrical signatures to pump parameters. Additionally, the project scope was extended to include the demonstration of wireless data acquisition in the test loop. In collaboration with Oak Ridge National Laboratory a microcontroller-based data acquisition and analysis technique was demonstrated. ORNL demonstrated the use of the deployment of sensor arrays for data acquisition in chiller systems using inexpensive micro-controllers. This approach to distributed equipment monitoring (primarily vibration monitoring of rotating machinery) was implemented as a low-cost consumer electronic-based hardware deployment in an industrial plant.

These technologies contribute to smart condition-based maintenance, reduced human resources, remote monitoring of reactor components, and autonomous operation [1], especially in areas with limited infrastructure. In integral pressurized water reactors (iPWR) and other designs of SMRs, the pressure vessel incorporates most of the critical equipment used for power

generation. Examples of such plant components include: steam generators, motors, coolant circulation pumps, motor-operated valves, control rod drive mechanisms (CRDM), in-core instrumentation, and reactor internal structures. In order to resolve this issue, research is underway to develop techniques for indirect measurement of process parameters. Examples of some of the process measurements of interest are primary coolant flow rate in the reactor vessel, electrical signatures of motor-driven coolant pumps, water levels in steam generators and steam flashing drums, vessel lower plenum and upper plenum coolant temperatures, and others.

The overall objective of the project was to develop and demonstrate in-situ equipment monitoring methods with applications to reactor components such as coolant pumps and control rod drive mechanisms. The goal is to integrate electric signature analysis (ESA) and process measurements to perform remote monitoring of reactor components. Both steady-state and transient signal processing techniques are being incorporated into an on-line monitoring toolbox. This research, specific to the SMRs, is necessary because of their special features. SMRs have components that are somewhat different from conventional PWRs. For example, the coolant pumps may be internal to the vessel or mounted on the vessel without any additional piping, and therefore component instrumentations are limited, making ESA one of the viable methods for ascertaining component condition. Furthermore, the control rod drive mechanism is internal to the vessel. This R&D project focused on the following three major objectives. The R&D tasks were carried out in collaboration with the Measurement Sciences and Systems Engineering Division of ORNL.

Objective 1: Identification of critical in-vessel SMR components for remote monitoring and develop their low-order dynamic models, along with a simulation model of an integral pressurized water reactor (iPWR).

Objective 2: Development of an experimental flow facility with motor-driven valves and pumps, incorporating data acquisition and on-line monitoring interface. This objective includes the task of demonstrating wireless data acquisition and the implementation of microcontroller-based data acquisition and analysis for machinery monitoring.

Objective 3: Development of stationary and transient signal processing methods for electrical signatures, machinery vibration, and for characterizing process variables for equipment monitoring.

Volume 1 of the report describes the identification of critical in-vessel SMR components for remote monitoring, development of the experimental flow control loop and associated sub-tasks, data analysis and the discussion of results.

Figure 1.1 shows the organizational diagram indicating the interaction among the project personnel. Table 1.1 shows the task schedule and milestones.

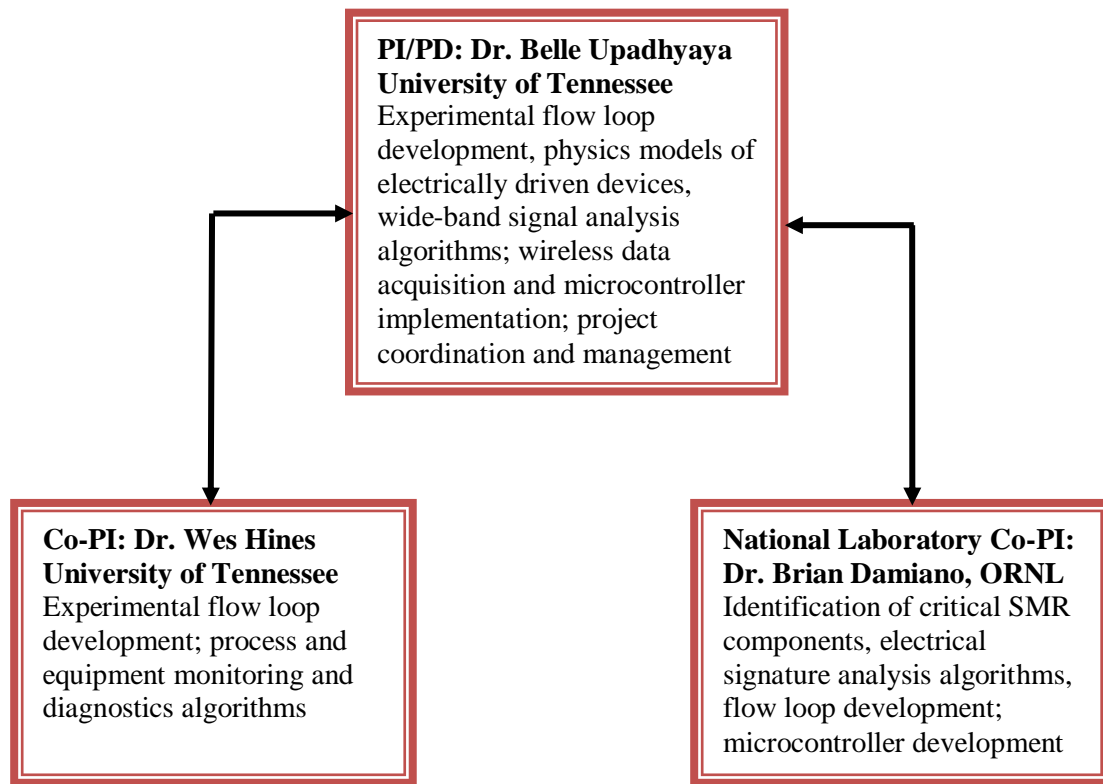


Figure 1.1: Project organizational chart and project coordination. Quality assurance is the responsibility of each of the partnering organizations.

1.2. Summary of R&D Contributions Presented in Volume 1

The following are the significant accomplishments of the project described in Volume 1 of the report.

- A detailed literature review of various SMR types and electrical signature analysis of motor-driven systems was completed. A bibliography of literature is provided at the end of this.
- A review of literature on digital signal processing methods was performed.

- An existing flow control loop was upgraded with new instrumentation, data acquisition hardware and software. The upgrading of the experimental loop included the installation of a new submersible pump driven by a three-phase induction motor. All the sensors were calibrated before full-scale experimental runs were performed.
- A frequency controller was interfaced with the motor power supply in order to vary the electrical supply frequency. The experimental flow control loop was used to generate operational data under varying motor performance characteristics. Coolant leakage events were simulated by varying the bypass loop flow rate. The accuracy of motor power calculation was improved by incorporating the power factor, computed from motor current and voltage in each phase of the induction motor.
- A variety of experimental runs were made for steady-state and transient pump operating conditions. Process, vibration, and electrical signatures were measured using a submersible pump with variable supply frequency. High correlation was seen between motor current and pump discharge pressure signal; similar high correlation was exhibited between pump motor power and flow rate. Wide-band analysis indicated high coherence (in the frequency domain) between motor current and vibration signals.
- Wide-band operational data from a PWR were acquired from AMS Corporation and used to develop time-series models, and to estimate signal spectrum and sensor time constant. All the data were from different pressure transmitters in the system, including primary and secondary loops. These signals were pre-processed using the wavelet transform for filtering both low-frequency and high-frequency bands. This technique of signal pre-processing provides minimum distortion of the data, and results in a more optimal estimation of time constants of plant sensors using time-series modeling techniques.
- The experimental loop data indicate a clear relationship between motor power and pump discharge (flow rate). This relationship can be used to infer pump flow rate using the computed motor power.
- A laboratory scale wireless data acquisition and transmission network was developed and demonstrated successfully.
- A micro-controller based data acquisition and analysis module was developed and tested for monitoring machinery vibration. Such low-investment devices are attractive for monitoring a large number of similar plant equipment.
- A data analysis toolbox was developed for processing both loop operational data and

wide-band sensor data. It includes all the computational functions that were developed and used in the project; these are classical data analysis and modern digital signal processing (DSP) techniques.

- The publications during the reporting period included two journal articles, five conference papers, and a DOE I-NERI review meeting presentation and a project report.

The project PI and the Co-PI are engaged in three synergistic research projects. One of these is a DOE STTR Phase-1 and Phase-2 project with the industrial partner, Analysis and Measurement Services (AMS) Corporation, with an emphasis on SMR on-line monitoring. The second is collaboration with Korea Atomic Energy Research Institute (KAERI) on a DOE I-NERI project, and is related to monitoring safety critical functions during beyond design basis accidents in light water reactors. The latter also addresses station blackout, remote sensing, self-powered detectors, energy harvesting, and wireless communication. The third collaborative project is an IRP titled *Integral Inherently Safe Light Water Reactor (I²S-LWR)*, with Georgia Institute of Technology as the lead for this NEUP-IRP. These illustrate the value of this NEUP project in enhancing the safety and operational reliability of both existing and future nuclear power plants.

1.3. Organization of the Report

Volume 1 of the Final Report provides a description of the tasks performed under objectives 2 and 3 during the project period 11/2011 – 10/2014. The following topics are described in Sections 2-10.

Section 2: Literature review of SMRs and electrical signature analysis.

Section 3: Experimental flow control loop, data acquisition, and system calibration.

Section 4: Control loop experiments and discussion of results.

Section 5: Time-frequency analysis of transient data.

Section 6: Analysis of wide-band data for sensor monitoring.

Section 7: Fault monitoring and diagnostics by using data-based modeling of measurements.

Section 8: Wireless data acquisition and transmission.

Section 9: Development of low-cost microcontroller-based equipment monitoring system.

Section 10: Concluding remarks and future work.

Appendix A: MATLAB-based data analysis toolbox.

A complete list of references and related bibliography is given at the end of the report.

Table 1.1: Schedule of tasks/milestones

→	T	I	M	E	---	---	M	O	N	T	H	S
Tasks/Milestones	1-3	4-6	7-9	10-12	13-15	16-18	19-21	22-24	25-27	28-30	31-33	34-36
Task 1: Identification of critical in-vessel SMR components; functional models	X	X	X	X	X	X	X	X				
Task 2: Development of Electrical Signature Analysis (ESA); relationship to process dynamics	X	X	X	X	X	X	X	X				
Task 3: Development of stationary and transient signal processing methods. Time-series modeling technique for sensor response monitoring		X	X	X	X	X	X	X				
Task 4: Development of an experimental flow loop with SMR-type devices and demonstration of relationship among process variables and electrical signatures	X	X	X	X	X	X	X	X				
Task 5: Development of a MATLAB toolbox for analysis of measurements; data-based modeling for condition monitoring			X	X	X	X	X	X	X	X		
Task 6: System integration and demonstration. Wireless data acquisition; low-cost microcontrollers for equipment monitoring					X	X	X	X	X	X	X	
Deliverables: Progress reports →	X	X	X	X	X	X	X	X	X	X	X	X
System demonstration →									X	X	X	X

2. REVIEW OF LITERATURE

2.1. Introduction

This section provides a summary of techniques available for on line monitoring, with focus on electrical signature analysis. A brief description of small modular reactors is included.

Electrical signature analysis (ESA) is a versatile, powerful, and a non-intrusive technology that has been developed by ORNL and others for monitoring the health of electro-mechanical equipment. As shown in Figure 2.1, the diagnostic and prognostic information is acquired by installing voltage and current sensors on electrical lines carrying input or output power, rather than requiring the placement of sensors on the equipment itself. In many industrial applications, these electrical lines are consolidated at the motor control center (MCC), which can be far removed from the equipment. Thus, an ESA-based monitoring system is intrinsically nonintrusive to equipment operations and provides remote monitoring capabilities that are especially beneficial when the monitored equipment is located in hazardous environments.

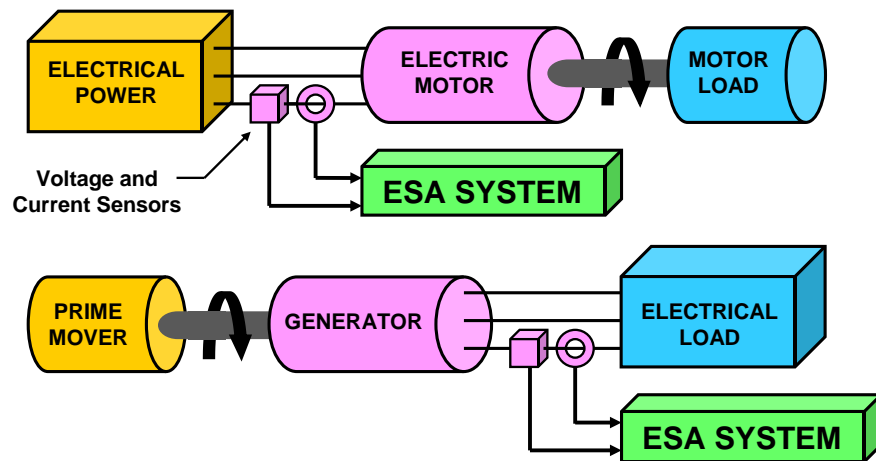


Figure 2.1: Electrical Signature Analysis (ESA) basic principle [80].

The ESA takes advantage of the capability of electric motors and generators to sense variations in equipment performance and condition, and then to act as transducers by providing corresponding variations in their electrical signals. ORNL has developed techniques for monitoring and analyzing electrical signatures for the purpose of detecting and diagnosing degraded conditions before any loss in performance is observed. By detecting component wear and degradation at this early stage, maintenance can be scheduled and performed before

unexpected (and often catastrophic) failures occur. ESA was initially developed and applied by ORNL in the mid-1980s as part of the Nuclear Plant Aging Research (NPAR) program, funded by the U.S. Nuclear Regulatory Commission [2]. The NPAR program was established to assess the effects of aging and service wear of selected nuclear power plant components and systems, and to identify condition monitoring methods that could be applied to maintenance, testing, and inspection activities to detect and mitigate the effects of aging prior to equipment failures.

In support of the NPAR program, ORNL first demonstrated the benefits of ESA as a remote and sensitive method of monitoring the condition and performance of motor-operated valves (MOVs) used in many plant safety systems. Tests performed by ORNL demonstrated that ESA could be used to detect a large number of MOV abnormalities, including gear and stem nut wear, insufficient stem nut and gearbox lubrication, degraded voltage, incorrect torque and limit switch settings, bent valve stem, and others. In addition to motor-operated valves, ORNL has pioneered the development of ESA as a condition monitoring tool for a wide variety of electro-mechanical equipment including compressors, pumps, fans, electrically-operated valves and actuators, electric generators, and aircraft components. ESA has been shown to be sensitive to a variety of disorders such as degraded and misaligned motors and generators, worn bearings, gears and belts, unstable process conditions, and power system degradation. The bibliography provides a complete list of references.

In the late 1990s, ORNL discovered that ESA methods could be useful in detecting and characterizing pump hydraulic instability, suction conditions, and other running load fluctuations [23]. An example of the strong correlation between pump motor power fluctuations and fluid pressure perturbations is shown in Figure 2.2. The time-dependent spectral features in the fluid pressure spectrogram are replicated in the pump motor power spectrogram. Other studies have shown that abnormalities and flow restriction changes in a pump loop can be detected and diagnosed by using ESA signatures [15]. This is an excellent demonstration of the relationship between electrical signatures and process parameters. In the current project, this correspondence between the two forms of measurements was further verified in an experimental flow loop that was used as a generic test bed for this project. The following sections describe some specific SMR components and approaches for their monitoring.

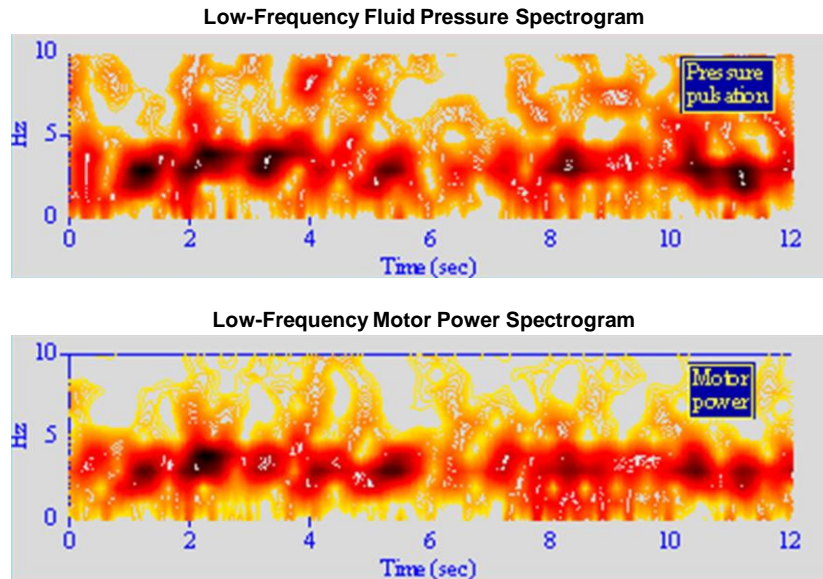


Figure 2.2: Pump pressure (top) and motor power (bottom) spectrograms provide similar features. In these displays, the dark areas are indicative of larger magnitude events [80].

2.2. Frequency Domain Analysis of Motor Current Signature (Motor as a Transducer)

Whenever the load on an induction motor changes, the current drawn by the motor changes. Changes in both frequency and magnitude characteristics are seen in the motor current and motor power signatures. Thus the motor in this case acts as a transducer. Therefore, the broad-band measurement of line current with a simple current transducer (along with voltage) may be used to perform diagnostics of motor faults and driven equipment. In most cases, mechanical and some electrical-related problems can be detected and isolated using vibration analysis, combined with thermography, lubrication oil analysis, and process analysis (using pressure and temperature measurements). Electrical signature analysis provides an alternative approach to machinery monitoring and often can be used to confirm results from traditional condition monitoring techniques. Electrical measurements are non-evasive and can be performed at the motor control center. It is not necessary to be near large equipment to make the measurements. This is especially advantageous in monitoring large horsepower motors, and motor-driven equipment located in radioactive or chemically toxic environments.

The motor current signal during the steady motion of the valve stem contains information about the frequency features of the MOV system. Most of these frequencies are defined as a

function of the motor shaft speed. Another important frequency in the operation of induction motors is the slip frequency:

Slip frequency = Synchronous frequency of the stator current - actual motor shaft frequency.

The slip frequency increases with the motor load and is a maximum at full load. The ratio of the slip frequency and the synchronous frequency is of the order of 3-5 %. Figures 2.3 and 2.4 are typical power spectral density functions of running current during open-to-close and close-to-open strokes of an MOV, respectively.

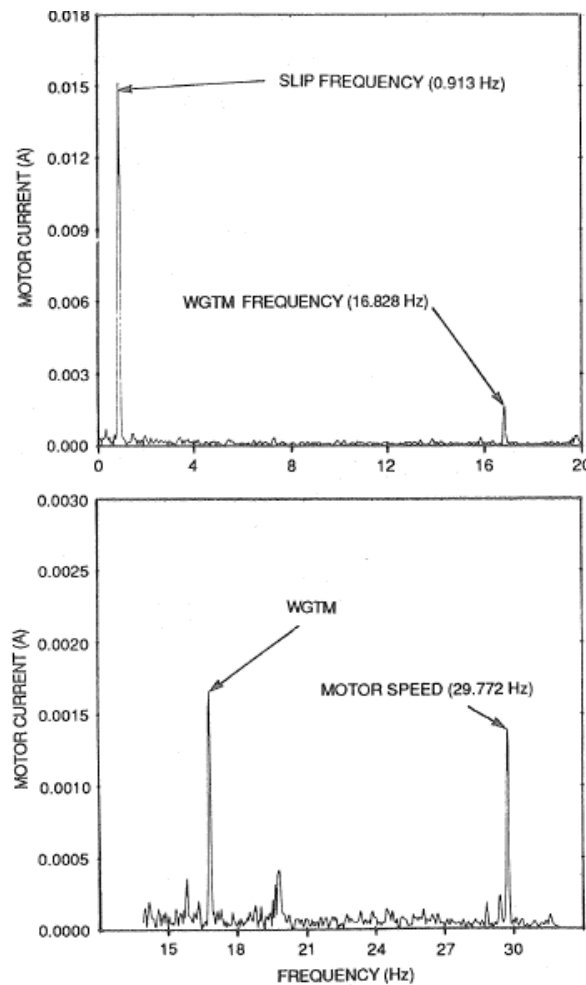


Figure 2.3: Motor current spectral analysis (open-to-close stroke) [26].

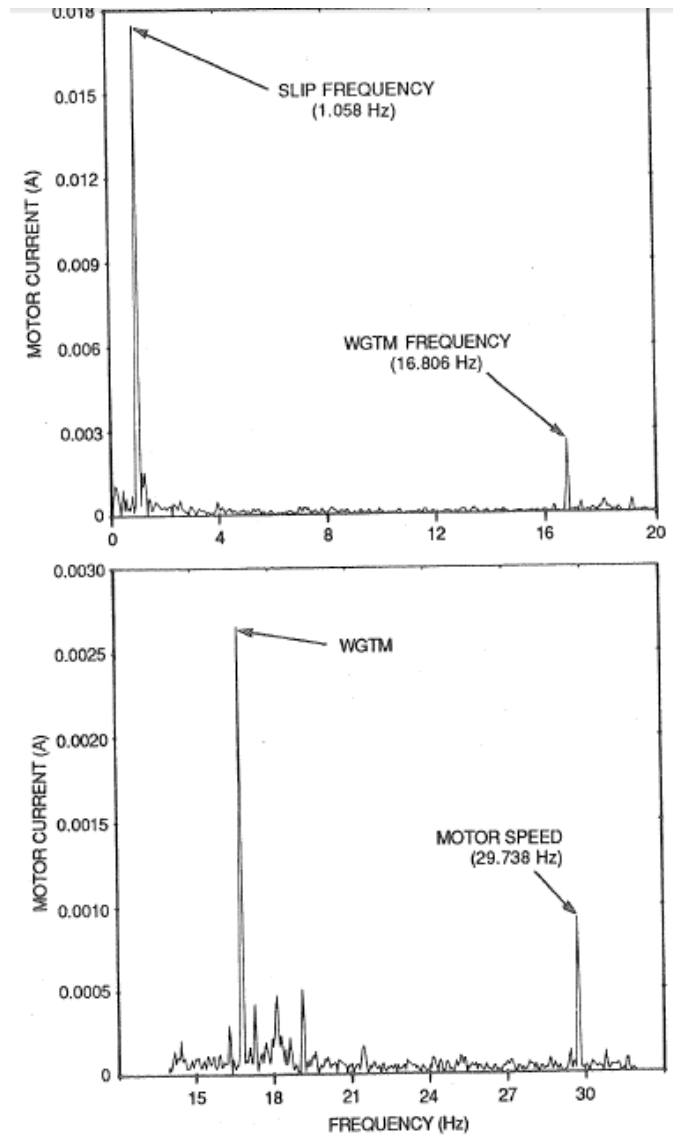


Figure 2.4: Motor current spectral analysis (close-to-open stroke) [26].

The following observations are made from the frequency-domain plots in Figures 2.3 and 2.4.

- If properly preconditioned, motor current signals could be effectively examined for frequency content with standard spectrum analysis equipment.
- Slip Frequency is the predominant peak in the frequency spectrum.
- $SF \text{ (in Hz)} = (\text{synchronous speed} - \text{actual speed}) \times (\# \text{ of motor poles})$.
- Variations in motor speed are observed as variations in the slip frequency.
- $AMS \text{ (actual motor speed in RPM)} = 60 \times [30 - (SF/4)]$ for a 4 pole ac 60 Hz induction motor.

- f. WGTM (worm gear tooth meshing) frequency and the sidebands that were spaced from the WGTM peak at multiples of the worm-gear rotation frequency
- g. These tests demonstrate that performance indicators from frequency analyses like WGTM, stem nut (worm-gear) rotation, motor shaft speed, motor slip, and unidentified peaks may be related to loads resulting from bearings, limit-switch gearing, etc. Fundamental frequencies accompanied by harmonics and sidebands may indicate eccentricity and/or wear [26].

2.3. MCSA for Centrifugal Pumps

As mentioned above, motor current analysis methods have been developed to aid in condition monitoring of various equipment. This sub-section describes the application to centrifugal pump monitoring.

2.3.1 Experimental Setup

The experiment of Casada and Bunch [14] consisted of a 50 HP motor connected to an eddy current brake dynamometer; changing balance using a dynamic balancer was used to check whether change in mechanical balance had any effect on motor accuracy. It was found [14] that a correlation exists between motor vibration and the motor input. According to the authors, motor data were not very sensitive to mechanical imbalance [14]. The authors observed that the motor was a good transducer for detecting shaft misalignment.

Motor signatures also provide good information about the hydraulic condition of the pump. The spectral analysis of motor current data provided several interesting features of operation [14]. See Figure 2.5.

- As the flow rate was reduced there was an increase in the level of low frequency noise. The level of noise increased as a function of the suction power of the pump. A single suction pump would have a higher spectral noise at low frequencies.
- Relative amplitude of the running speed peak increased as the flow was reduced. The authors site the reasons to be normalization to the average power and that the power at low flow rates was less than at BEP (Best Efficiency Point) [14].

The motor inherently acts as a low pass filter, thus reducing the higher frequency energy levels in the motor power.

The authors also compared the vibration data for the pumps and observed that the vane pass energy peak decreased as the flow was decreased. The suction and discharge pressure spectra were examined at different net positive suction head available (NPSHA) conditions. The most dramatic change that they observed was the change in the suction pressure pulsation spectrum with the absence of vane-pass frequency energy for the reduced NPSHA case [14].

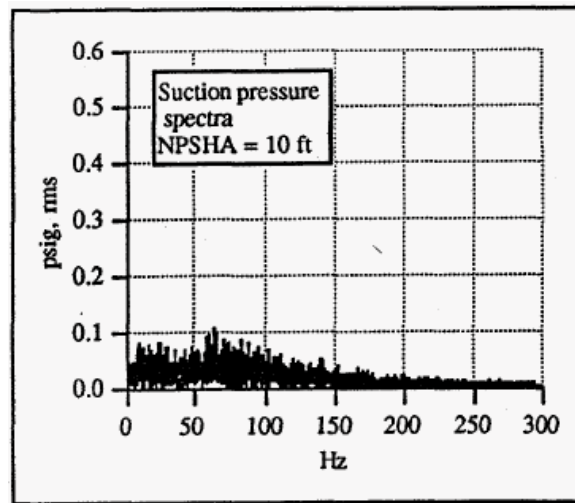


Figure 2.5: Suction pressure spectrum [14].

The authors also compared motor power and pressure pulsation data. It was observed that the power and pressure pulsations were more closely related at higher flow rates (Figure 2.6).

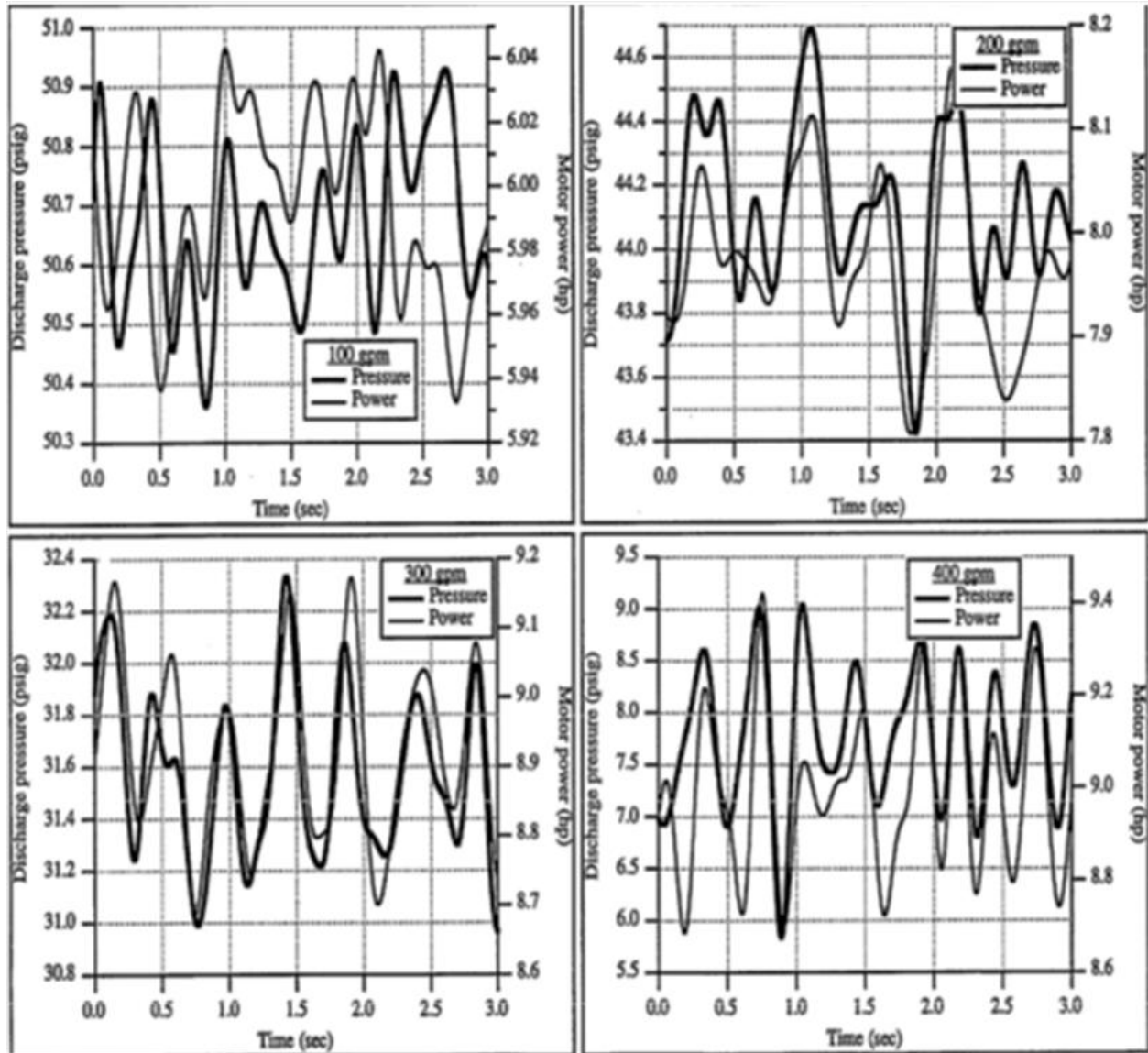


Figure 2.6: Pressure pulsations and motor power time waveform at four flow rates [40].

The cross correlation functions between motor power and fluid pressure at different flow rates are shown in Figure 2.7. It was stated in reference [40] that at higher flow rates there was a positive coincident relationship. This indicates that at low flow rates, the motor power and fluid pressure are in phase with each other. This relationship changes at higher flow rates.

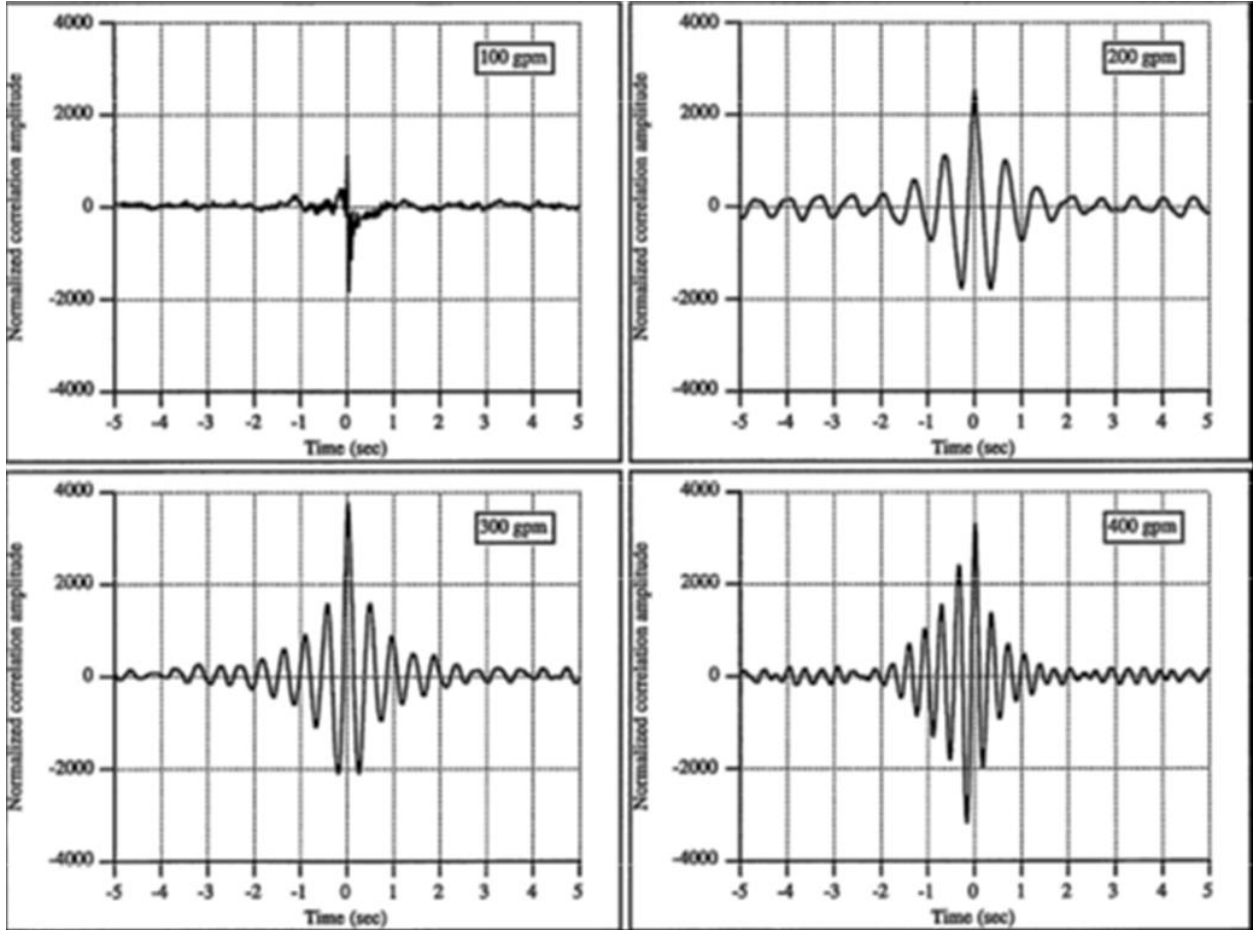


Figure 2.7: Normalized cross-correlations between fluid pressure and motor power at different flow rates [40].

The authors also mention the simplified single figure of merit for the stability of load. An instability ratio, defined as the ratio of the standard deviation of the power to the average power, was developed for this purpose.

Motor current monitoring was proven to be useful in detecting degraded component conditions. In order to create condition of clogged suction strainer, the authors used a valve located upstream. The motor current characteristics were used to check for clogged suction strainer. The vibration data observed for the cases with the clogged and clear strainer did not show significant differences (Figure 2.8). Pressure pulsations were found to not be highly sensitive for this form of anomaly [14].

The motor current was found to not be useful in monitoring motor bearing. Vibration spectral data were more sensitive to bearing fault conditions than motor signatures [14]. The

plots in Figure 2.9 show that the vibration spectrum is more useful in determining degradation in machinery bearings.

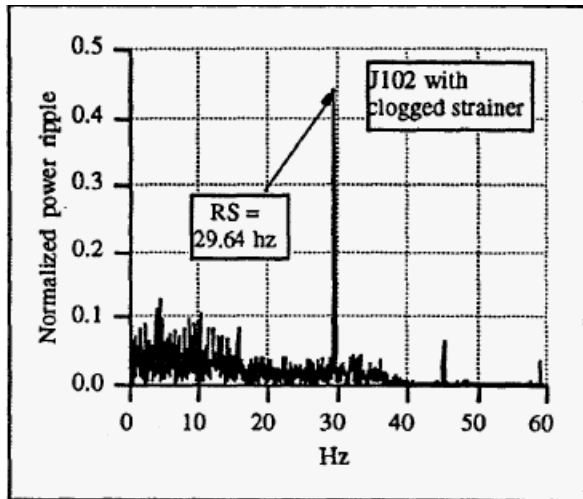


Figure 41. Motor Power Spectrum for Pump with Clogged Suction Strainer

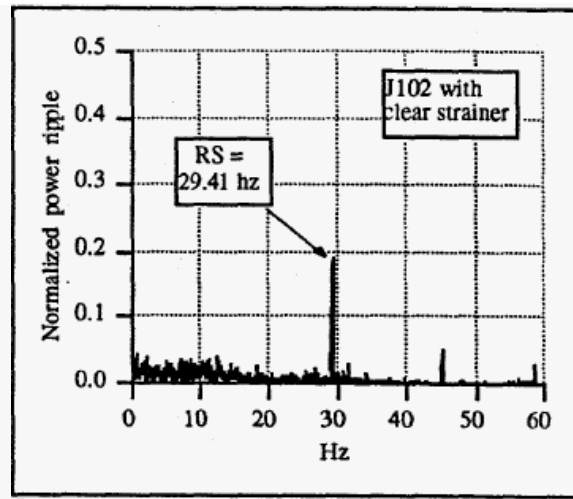


Figure 42. Motor Power Spectrum for Pump with Clean Suction Strainer

Figure 2.8: Motor pump spectrum for checking clogged suction strainer [14].

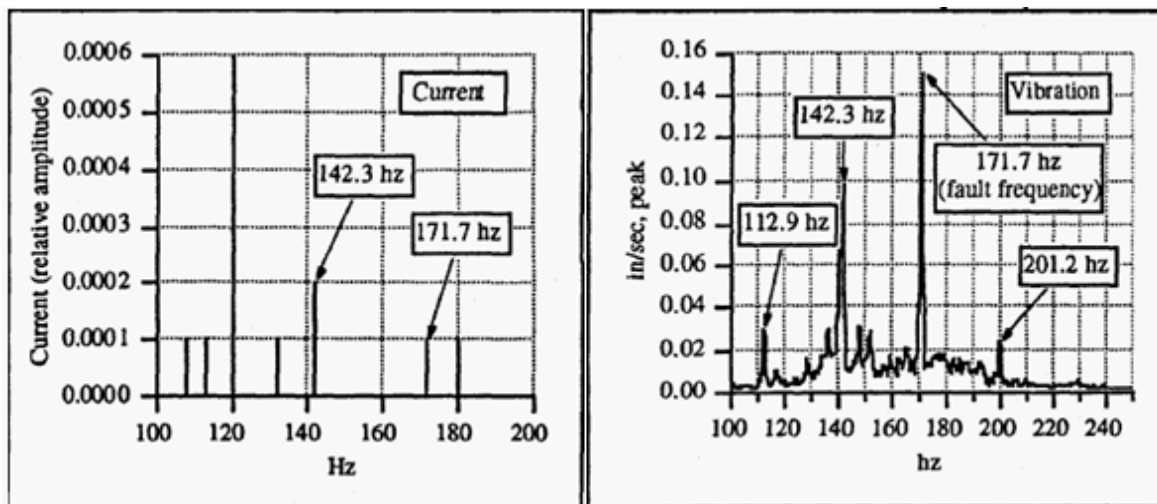


Figure 2.9: Current spectrum (L) and vibration spectrum (R) with damaged bearing [14].

2.4. Critical SMR Components for On-line Monitoring

Based on the review of SMR design and the need for continuous operation for an extended fuel cycle (4-5 years), the following in-vessel and other components are indentified as candidates for continuous on-line monitoring.

- Control rod drive mechanisms (CRDM).
- Motor-operated valves used for feed flow regulation and turbine control valves for steam flow regulation.
- Canned or submersible pumps used as reactor coolant pumps (RCP), located at the core upper plenum.
- Pressurizer heater banks.
- Steam generator tubing integrity. This is important since the steam generators are integral to the vessel.
- Steam generator water level monitoring.
- Validation of feed flow rate, hot leg and cold leg temperatures, steam flow rate, pressurizer pressure, and pressurizer level instrumentation.

2.5. Small Modular Reactors of the IPWR Type

This section outlines different proposed designs of small modular reactors.

2.5.1 International Reactor Innovative and Secure (IRIS)

IRIS is an integral medium size reactor with an electric output of 335 MW. An early Westinghouse design, this is a pressurized water reactor that utilizes an integral reactor coolant system layout. The reactor vessel houses nuclear fuel, control rods, pumps, steam generators, pressurizer, control rod drive mechanisms, and nuclear reflector. This is the reason for the IRIS vessel to be larger than the traditional PWR design. There are no primary pipings, thus significantly reducing the overall size of the containment. Figure 2.10 shows a layout of the integral primary system, consisting of eight helical coil steam generators (HCSG). The secondary water flows through the HCSG tubing and the steam generator produces super-heated steam. The primary water is pumped from the upper plenum down through the annular space between the reactor vessel and the shielding.

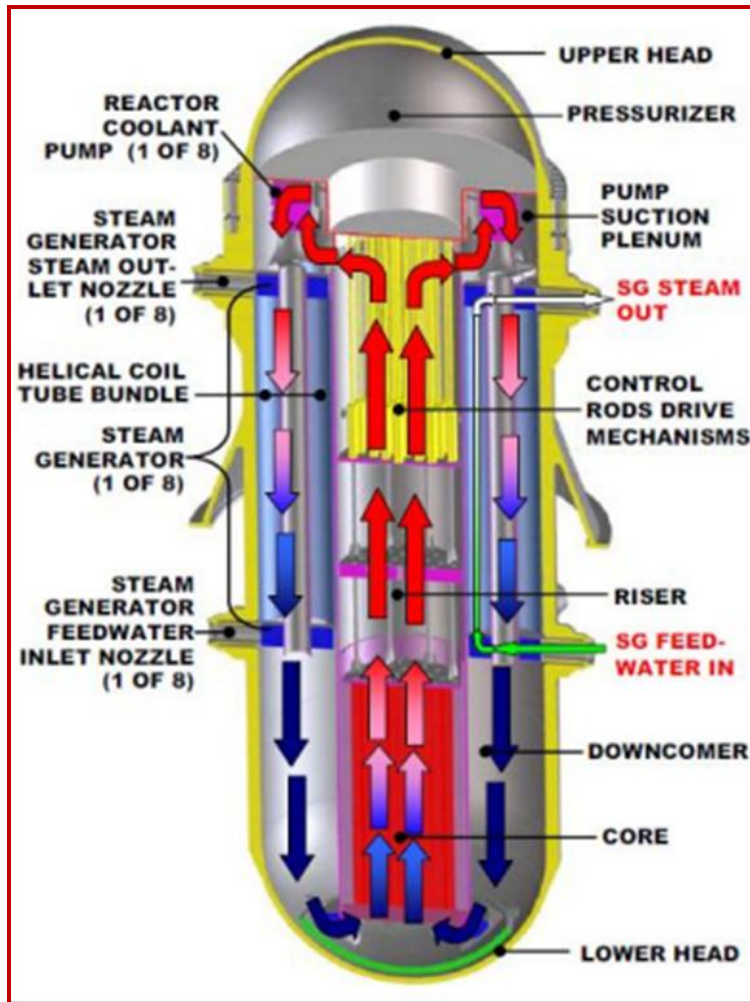


Figure 2.10: IRIS reactor vessel layout [31].

2.5.2 System-integrated Modular Advanced Reactor (SMART)

SMART is an iPWR designed by the Korean Atomic Energy Research Institute and has a design electrical rating of 100 MW. Figure 2.11 shows a schematic of the SMART system. As the diagram shows all the critical components are inside the reactor vessel. Another feature is that there are no pipe connections between the different components of the nuclear reactor. There are four sections in SMART; each section comprises of three steam and feed water pipes from the adjacent steam generator [55].

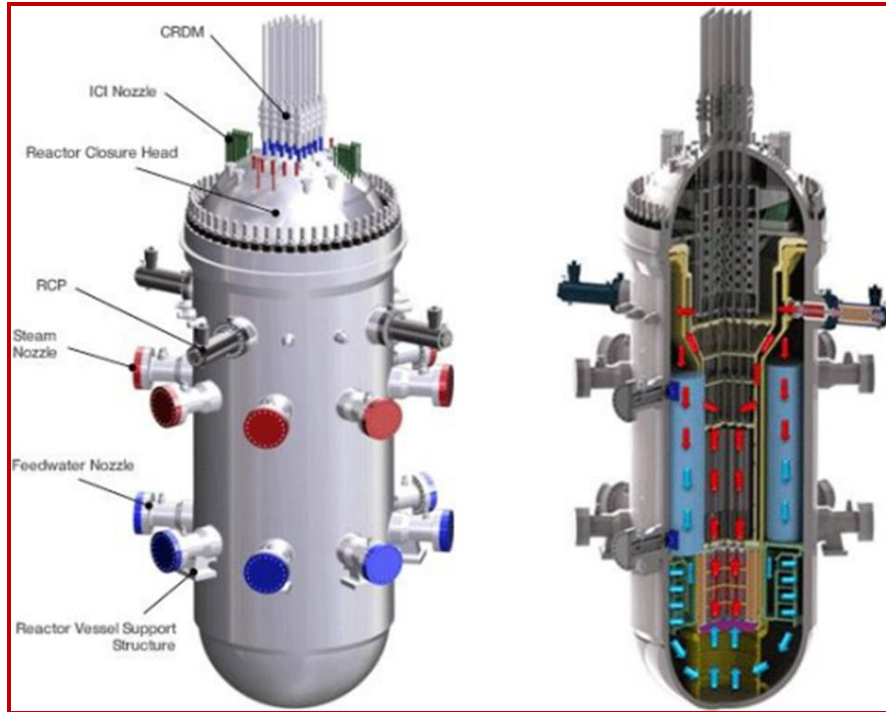


Figure 2.11: Schematic of SMART [55]

2.5.3 B&W mPower Reactor

The Babcock and Wilcox mPower reactor is a simplified, light water cooled, pressurized water reactor, with the reactor core, steam generator, control rod drive mechanisms, coolant pumps, and pressurizer all located in one pressure vessel. The once-through steam generators produce superheated steam. The mPower design, like all SMRs, eliminates the need for large reactor coolant piping, thus eliminating large loss of coolant accidents. The reactor is designed to have an electric output of 180 MW, and has a refueling cycle of four years, with a design life of 60 years. The mPower reactor is designed for deployment of multiple modules at one site. For example, four modules at a site would provide a total of 720 MWe of generation capacity. The scalable modular design has a 4-5 year operating cycle between refueling. A schematic of a single unit is shown in Figure 2.12. Babcock & Wilcox is planning to apply for design certification by the end of 2013, and plans to build the first unit at TVA's Clinch River site.

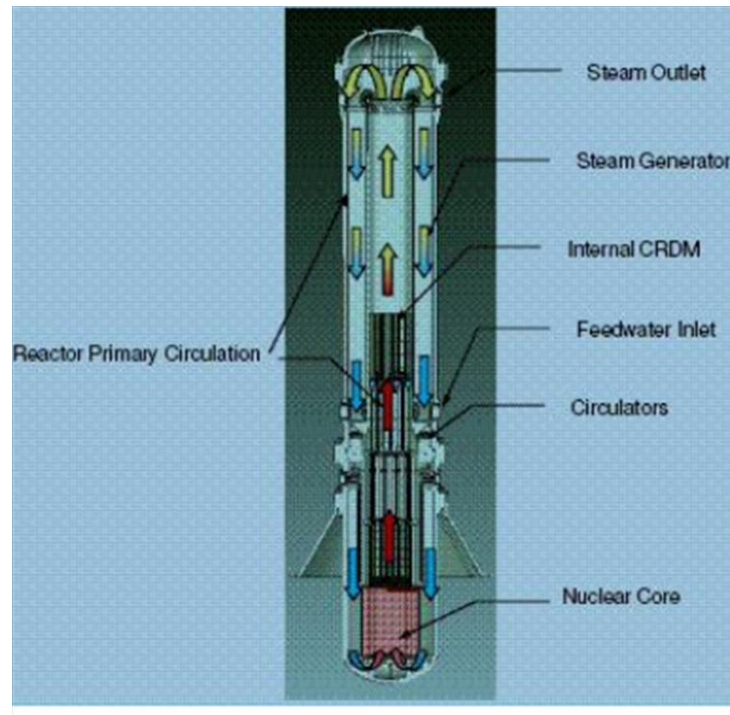


Figure 2.12: B&W mPower reactor vessel diagram [31].

2.5.4 Westinghouse Small Modular Reactor (WSMR)

The Westinghouse SMR design [42] is a 800 MWth integral PWR with straight-tube steam generators that produce saturated steam. The reactor vessel has a diameter of 32-ft and an overall height of 89-ft. The reactor incorporates some of the features of AP-1000 such as passive safety (natural circulation cooling) and high-temperature and pressure version of the AP-1000 CRDM. On the steam generator side, the primary coolant flows through the tubing with the secondary fluid on the shell side of the steam generator. There are eight steam generators with eight reactor coolant pumps, similar to the canned pumps in the AP-1000 system. The steam separator drum is located outside the vessel and results in pure steam (quality ~ 1) that is supplied to the turbine. Figure 2.13 is a representation of this SMR [43]. It is anticipated that this SMR design might be the first to be approved for design certification by the US NRC.

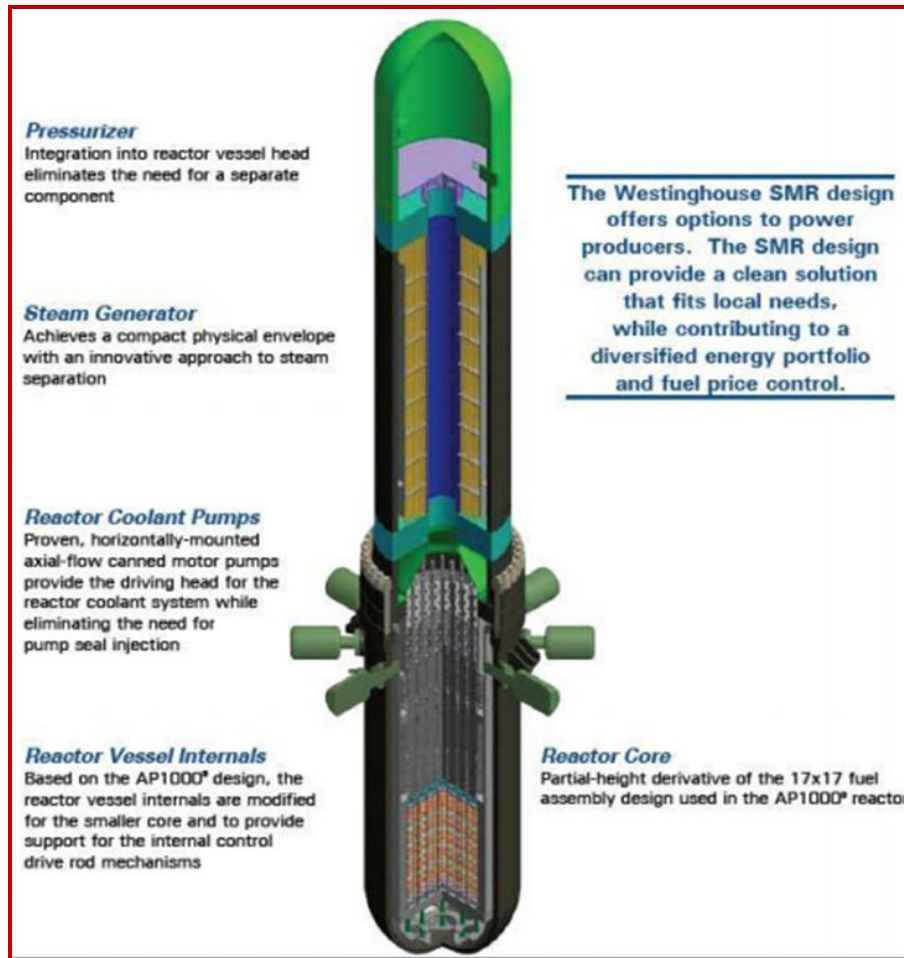


Figure 2.13 : Schematic of the Westinghouse SMR [43].

2.5.5 NuScale SMR

NuScale SMR is a 45 MWe unit designed and developed by NuScale Power Incorporated. It has a natural circulation primary system with passive safety features. Figure 2.14 [56] shows the schematic of a NuScale SMR module with the containment submerged in a pool of water. The reactor pressure vessel is inside the containment. The pressure vessel is 45-ft tall and 9-ft in diameter. The plan is to house 12 reactor modules in a single large water tank below the ground level, with the 12 containments separating the reactor units. The final design consists of an in-line refueling system with remote handling, with fuel loading occurring once every two years. The 12 modules will be built and installed as desired, providing a total power of 540 MWe. The NuScale design consists of two helical coil steam generators (HCSG) that surround the hot leg riser (see Figure 2.14). A feed water header and a steam header are fabricated into the HCSG and provide interface with the balance-of-plant system which is situated above ground.

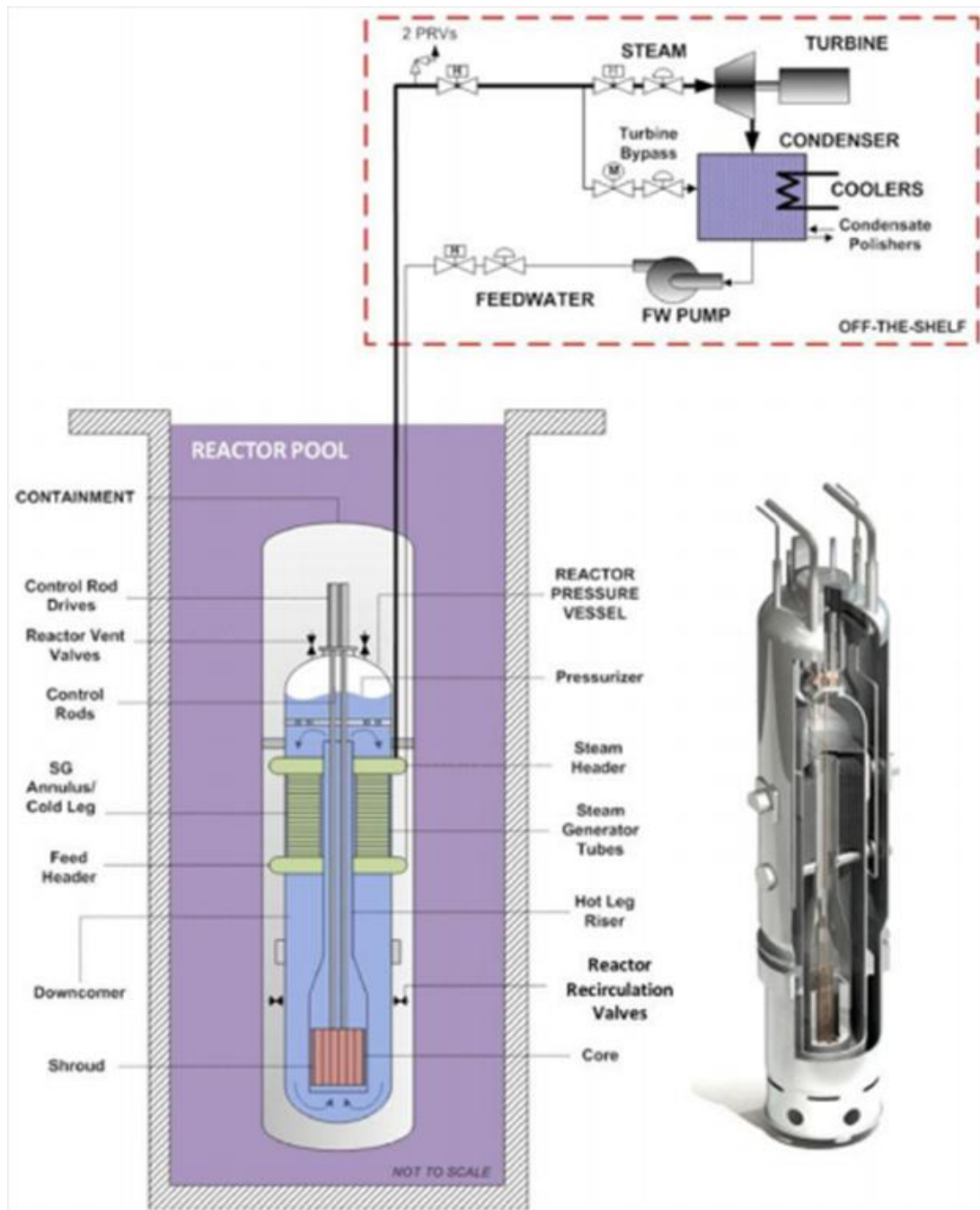


Figure 2.14: Schematic of NuScale Power SMR system [56]

2.6. Monitoring Control Rod Drive Mechanisms

The control rod drive mechanism (CRDM) is responsible for moving the control rods in and out of the reactor core. Currently, CRDMs are monitored by current and voltage signatures collected at test points in the logic and power cabinets. In current SMR designs, the monitoring of the CRDM could be accomplished by using existing methods. The following sections provide a short overview of the CRDM, as well as current monitoring and diagnostic techniques used in PWRs..

2.6.1 Description of a Control Rod Drive Mechanism (CRDM)

The primary purpose of the control rod drive mechanism (CRDM) is to physically position the control rods within the core in response to electrical current command pulses. Figure 2.15 is a block diagram of a typical CRDM system. The following are the different subcomponents of a CRDM.

- a. Coil stack assembly: It is comprised of three electromagnetic coils: the stationary gripper coil, the movable gripper coil and the lift coil. During normal plant operation only the stationary gripper coil is energized. When a rod is moved, current is supplied to the other coils in a precise manner so the grippers can raise or lower the rod.
- b. Power cabinets: 2 separate power cabinets convert 260V three-phase AC power to dc power that is supplied to the coil stack assembly.
- c. Logic Cabinets: Communicates between the control room and the power cabinets to move control rods. They also provide information for rod drive step counting.
- d. Rod Position Indication Subsystem: The nuclear industry currently has a large variety of systems for rod position indication used today. This project will focus on two widely used systems, the analog and digital rod position indication system (ARPI and DRPI) [11].

2.6.2 Control Rod Drive Movement

Moving a control rod one step, or $5/8''$, is a complex process and requires multiple steps by the CRDM. These steps are listed below:

1. The movable coil is energized and latches into the control rod complementing the already latched stationary coil.
2. The stationary coil is turned off and unlatches from the rod, leaving only the movable coil to hold the rod.
3. The lift coil is energized and the entire assembly and rod are lifted one step
4. The stationary coil is energized and latches into the rod
5. The lift coil current is reduced and the stationary gripper latches
6. The movable coil is de-energized and disengages from the rod
7. The lift coil is de-energized and the CRDM is back to its normal hold mode

2.6.3 Control Rod Drive Mechanism Timing and Sequencing

To verify proper timing and sequencing of CRDMs, the current to the stationary, movable, and lift coils is monitored. Proper timing and sequencing is essential to ensure correct movement of the rods. Improper rod movement can result in degradation of the mechanism or its eventual failure. A normal CRDM timing trace can be seen in Figures 2.17 and 2.18, while an example of improper CRDM timing can be seen in Figure 2.19.

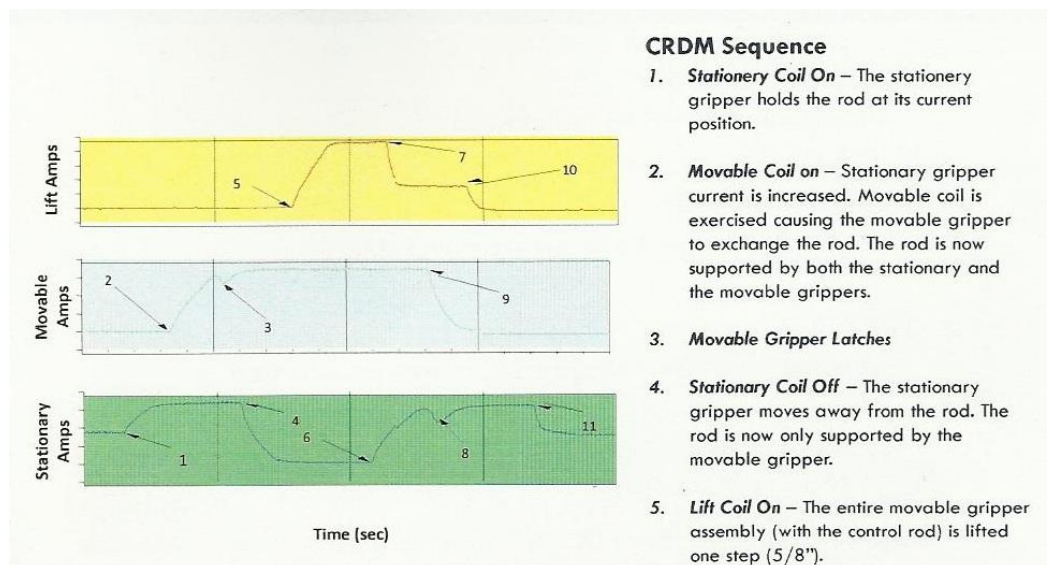


Figure 2.17: Normal CRDM Timing (Courtesy of AMS)

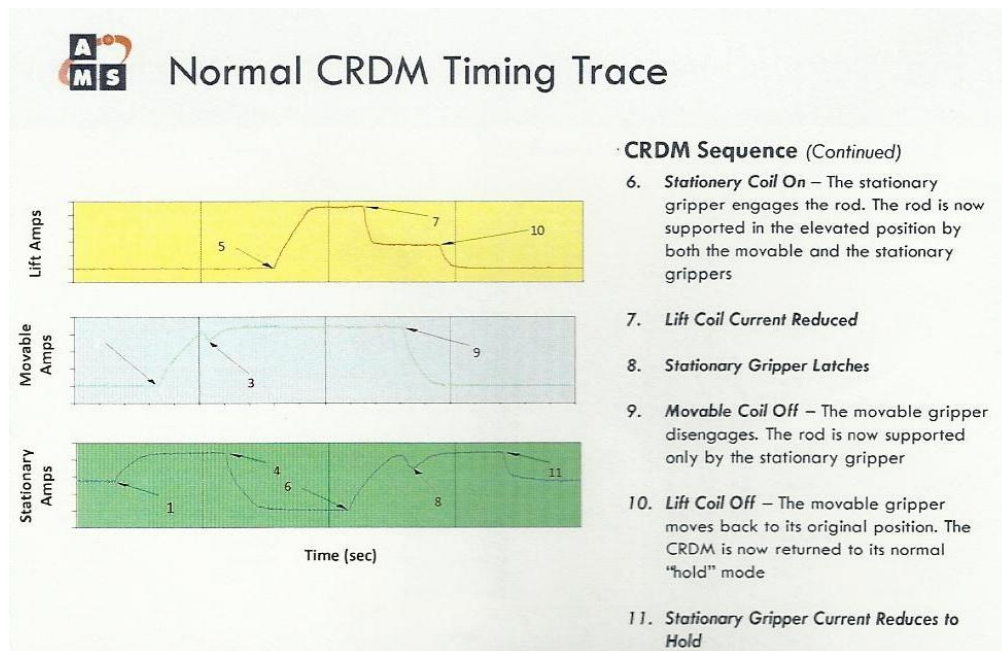


Figure 2.18: Normal CRDM Timing (Courtesy of AMS)

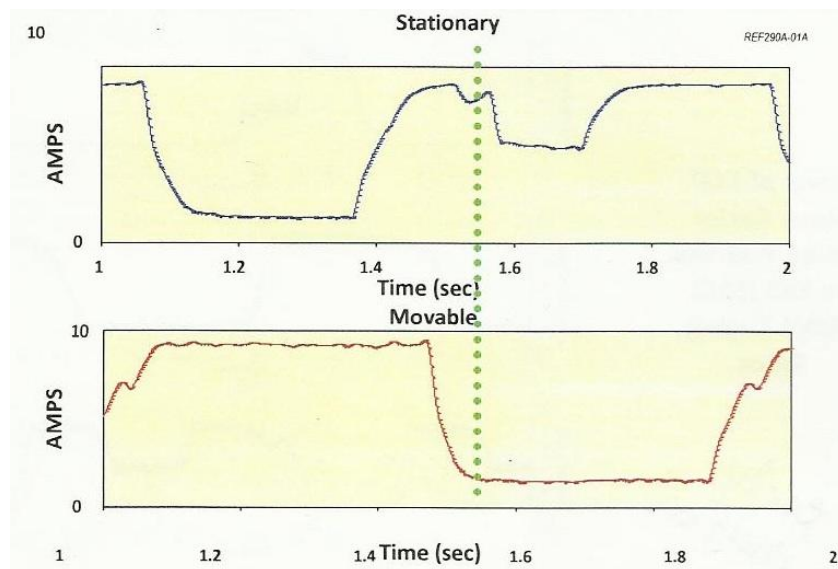


Figure 2.19: Improper CRDM Timing (Courtesy of AMS)

For the improper timing example, it can be seen that the movable gripper disengages (seen by drop in current drawn) before the stationary gripper is fully engaged with the rod.

2.6.4 Rod Position Indication

Rod position indication, or RPI, is crucial to the proper operation of the CRDM. The RPI system allows the operator to know the insertion length of each control rod into the core.

Analog Rod Position Indicator (ARPI)

One of the most widely used rod position indication systems is the ARPI system. The ARPI system, shown in Figure 2.20 consists of a 12 foot long detector on top of the CRDM. The detector consists of alternately stacked primary and secondary coils. The coils act as a variable transformer while the rod itself acts as the armature of the transformer. The primary side of the coils is energized with 120 Vac, 60 Hz power. All of the detectors are connected in parallel and energized by the same source. The magnetic coupling between the primary and secondary coils produces an AC voltage which is proportional to the position of the rod. A fully inserted rod (0 steps) produces ~8 V while a fully withdrawn rod (230 steps) produces ~12.5 V [12]. A signal conditioning module is then used to convert the AC voltage signal into a DC voltage that is sent to the control room to display the rod position.

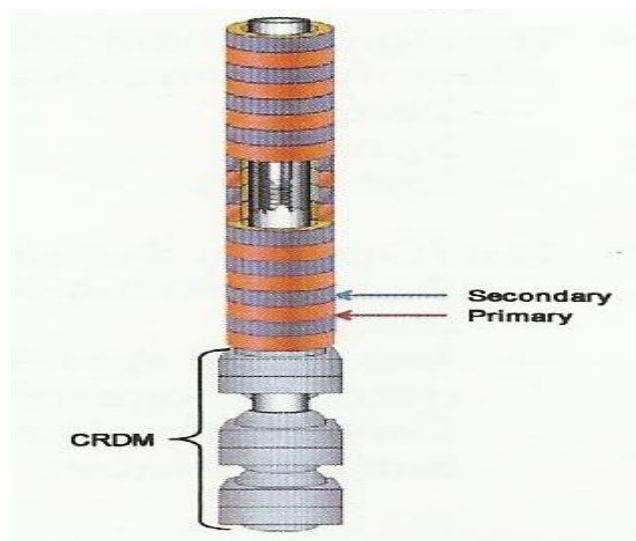


Figure 2.20: The primary and secondary detector coils of the ARPI system (Courtesy of AMS)

Digital Rod Position Indicator (DRPI)

Another popular rod position indication system is the DRPI system. The DRPI system also uses sets of coils placed over the length of the rod travel housing. There are 42 coils per detector that are spaced in 3.75-inch intervals. A 6 VAC 60 Hz transformer energizes the coils.

The 60 Hz frequency allows the electromagnetic flux generated by the coils to penetrate the rod travel housing. The rod's presence changes the impedance in the circuit and increases the flux, thus decreasing the current. The current without a rod is ~ 0.32 A while the current is ~ 0.23 A with a rod present. The changing impedance also changes the voltage in the coil. Twenty one resistors are placed in-between each coil to sample the voltage from the detector coil. A coil with a rod will have a RMS voltage of ~ 1.15 V while a coil without a rod will output ~ 1.60 V-rms. Differential amplifiers placed between coils then determine the position of the rod by outputting a ~ 0.45 V signal (difference between the 1.6 V and 1.15 V signals) at the coil with the top of the rod while all other amplifiers output 0 volts. The position of the rod is then known by which amplifier sends the signal [81]. Figure 2.21 depicts the coil locations with the differential amplifiers.

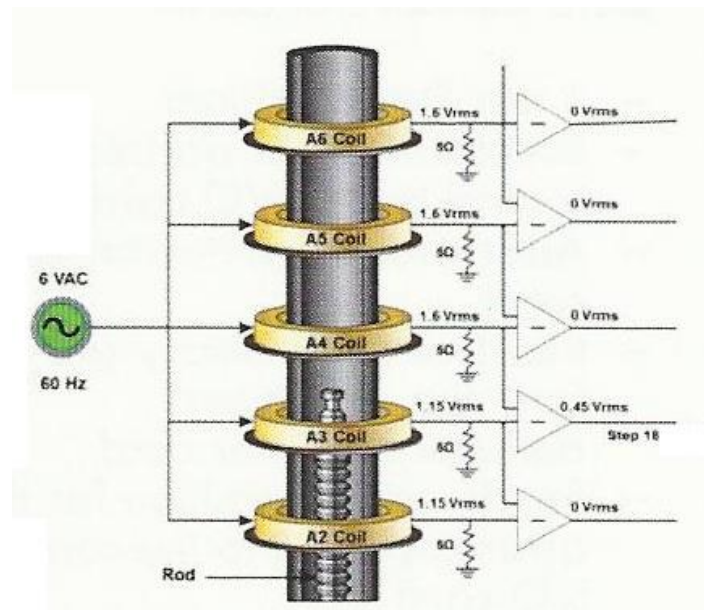


Figure 2.21: DRPI detector coils shown with differential amplifiers (Courtesy of AMS)

2.6.5 Rod Drop Testing

Rod drop testing has been around for many years as a way to confirm the correct operation of a control rod during a reactor trip. It is a measure of time it takes for a rod to go from fully withdrawn to dashpot entry. A rod drop test is performed by withdrawing the control rod to the full out position. The DRPI system is then de-energized and power to the CRDM is removed, similar to a reactor trip. In normal operation, the detector coils are energized, however, during a rod drop test; the rod sequentially penetrates each of the detector coils and induces

voltage. The sum of all the induced voltages from the coils then makes up the rod drop trace profile [80]. Sample rod drop traces can be seen in Figures 2.22 and 2.23.

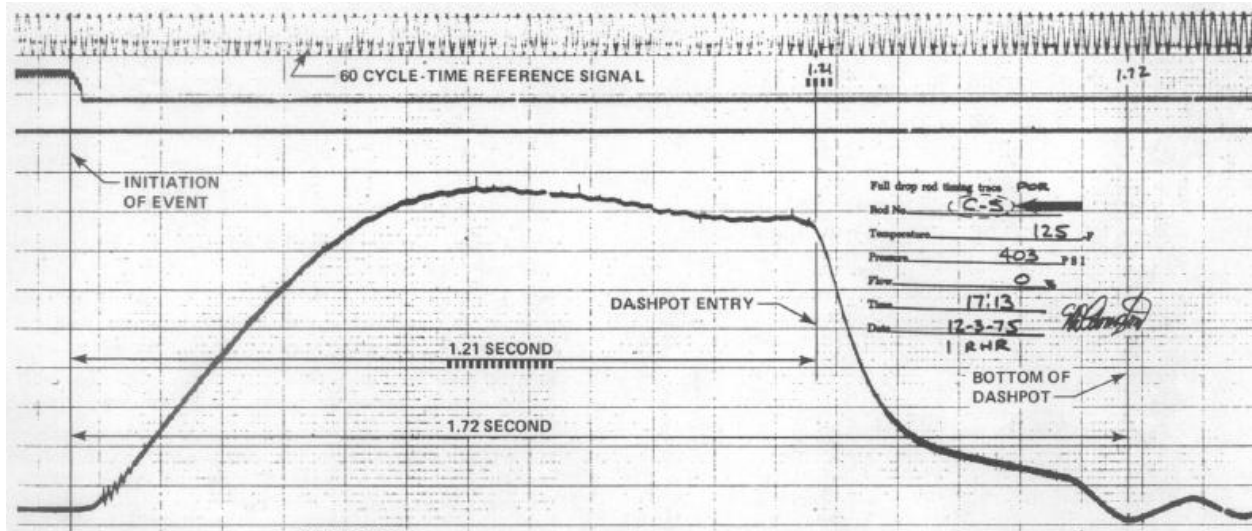


Figure 2.22: Typical rod drop test signal with A and B coil voltage summed [80]

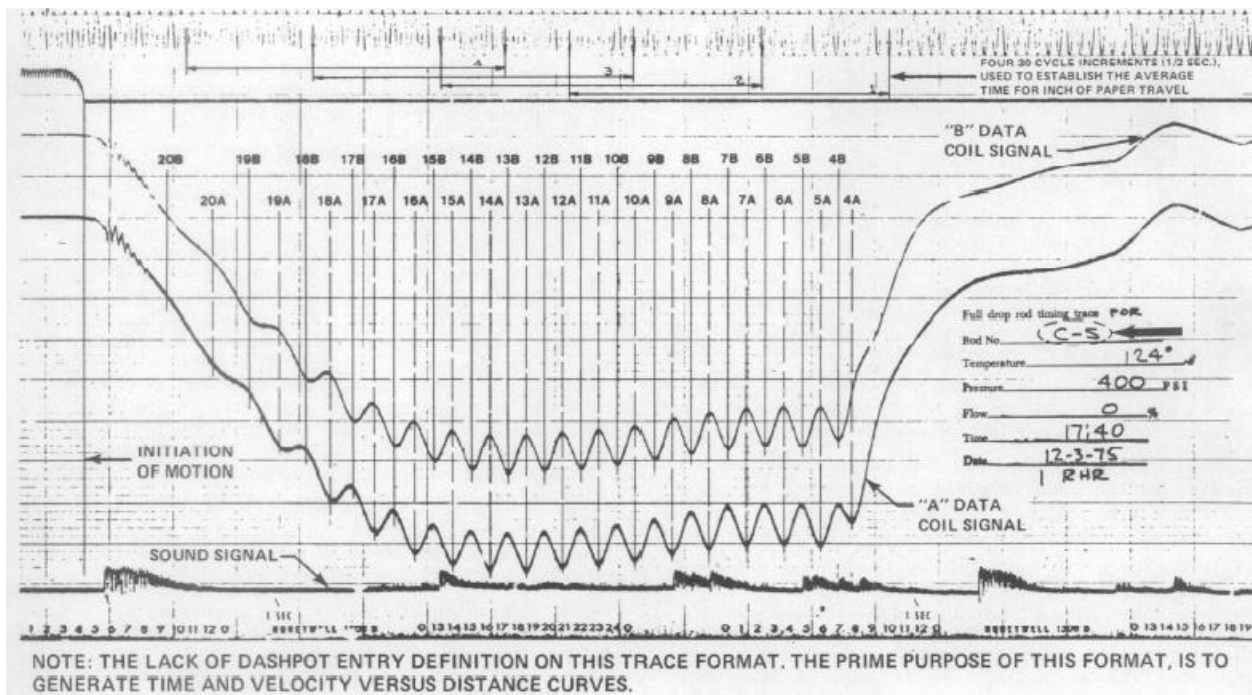


Figure 2.23: Typical rod drop test signal with A and B coil voltages separately [80].

The first figure is used when rod drop time is the parameter of interest. The second figure is used to generate time and velocity versus distance curves. Since the time between coil peaks are calculated for each of the DRPI coils, and the distance between each coil is 3.75-inch, the rod velocity can be calculated by $V = \frac{\Delta d}{\Delta t}$. An example of a time and velocity versus distance curve is shown in Figure 2.24.

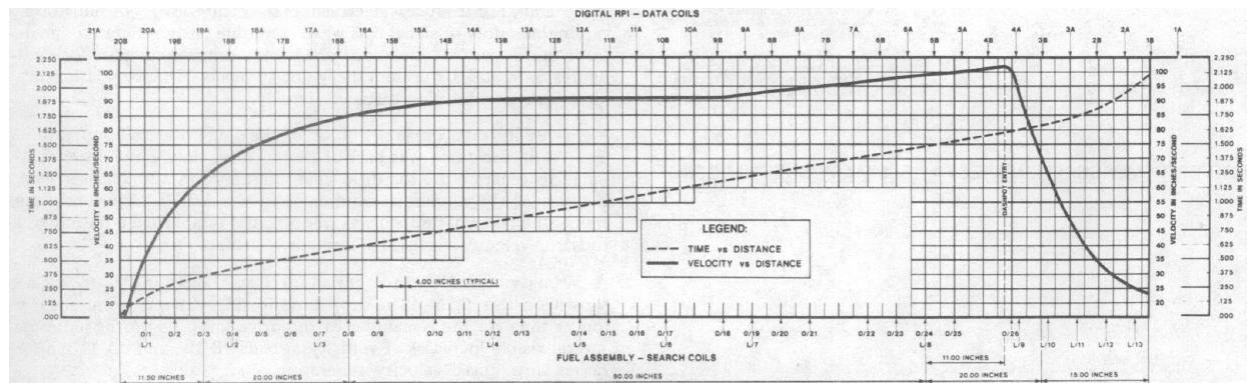


Figure 2.24: Time and Velocity versus Distance in Rod Drop Test [80]

Rod drop testing data can be used for baseline generation, archiving, and trending. Several parameters in the rod drop testing signature can be observed to diagnose issues with a rod drop.

One example of such parameters is bad recoil when the rod bounces off of the bottom of the dashpot. Figure 2.25 demonstrates the difference in the rod drop signal for rods with good and bad recoil.

ARPI Rod Drop Testing at Shutdown

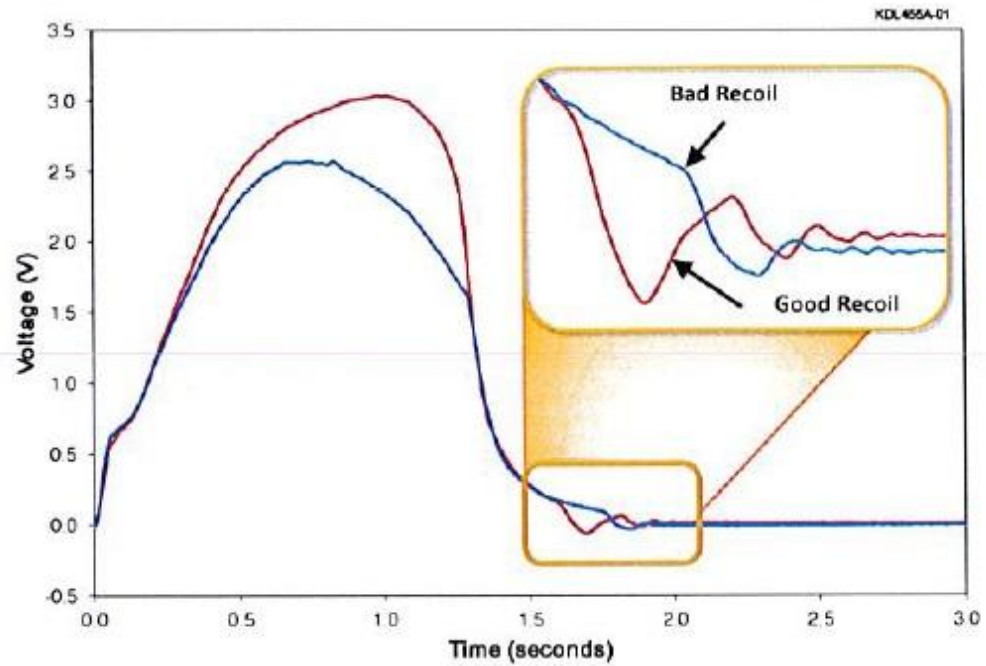


Figure 2.25: Rod Drop Test showing the difference between good and bad recoil
(Courtesy of AMS)

3. EXPERIMENTAL FLOW CONTROL LOOP, SYSTEM CALIBRATION AND DATA ACQUISITION

3.1. Introduction

This section provides a complete description of an existing flow control loop at the University of Tennessee following an equipment upgrade. A submersible pump was added to the loop to approximate a pump that might be installed in a SMR along with several new process instruments which were installed and interfaced with a data acquisition (DAQ) system. The full data acquisition system consists of process measurements, vibration signatures, and pump motor electrical signatures.

One of the main tasks of this project was to upgrade an existing experimental flow control facility to incorporate new equipment and instrumentation (Fig. 3.1).

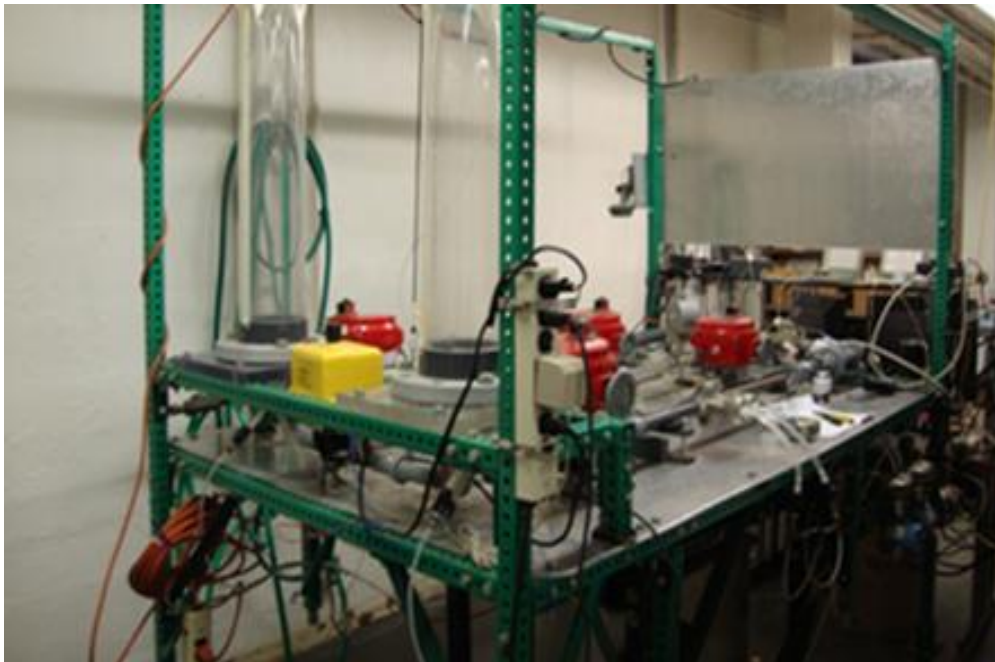


Figure 3.1: Experimental flow control loop before upgrade

The loop consists of two coupled water tanks, control valves (Motor-Operated Valves (MOV)), a half horsepower pump, orifice flow meters, turbine flow meters, water level measurement using differential pressure transmitters, a data acquisition system, a monitoring computer, and digital control for valve actuation using PI control algorithms. A schematic of the loop is also provided to observe the water flow path (Figure 3.2).

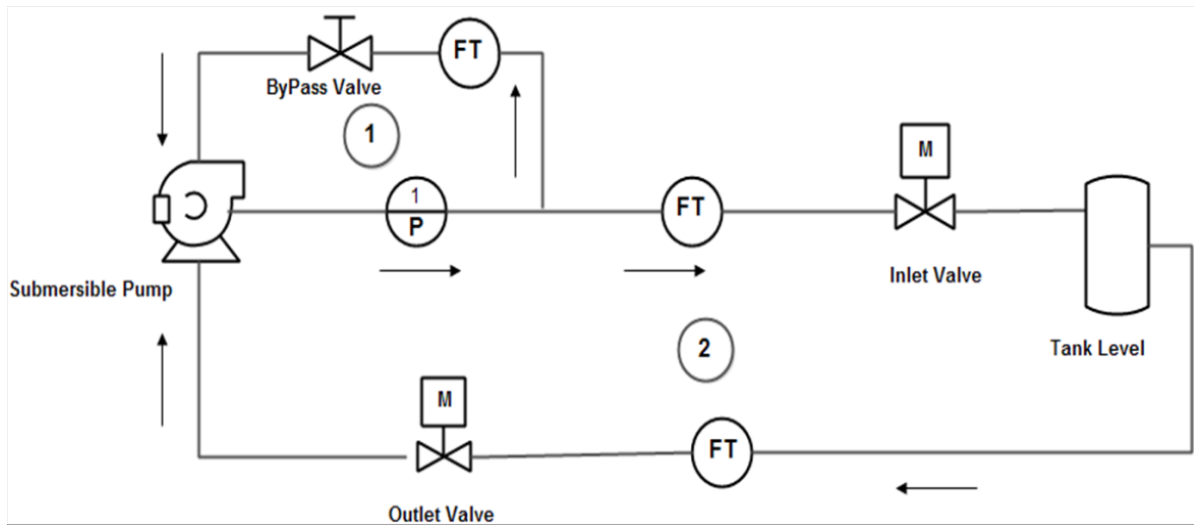


Figure 3.2: Schematic of flow loop

3.2. Experimental Facility Upgrade

The objective of upgrading and using the test facility was to simulate anomalies in certain system devices and acquire data from instrumentation that includes both process measurements and electrical signatures. The following equipment and instrumentation were added to the flow loop as part of the upgrade:

- 0.5 HP submersible (canned) Gould pump.
- Turbine flow meters.
- Orifice flow meters.
- Motor current (current clamps) and supply voltage measurements.
- Accelerometers for pump/motor vibration monitoring.
- National Instruments (NI) data acquisition hardware and software.
- Fluid pressure measurements
- Frequency Drive

3.2.1 Submersible Pump

A submersible pump was selected to replace the existing pump in order to approximate the canned pumps expected to be used in SMRs. The pump chosen was a Gould's Submersible Dewatering pump, model # 1DW51C1EA. The pump is driven by a .5 HP motor that operates

with a 230 V three-phase power supply, has a no load speed of 3,600 RPM, and draws a maximum load of 2.3 Amperes (Fig. 3.3).



Figure 3.3: Submersible three phase pump installed in the loop

The pump was placed vertically in the water supply tank with inlet suction ports at its base. It operates by drawing water through the rectangular holes at its base and one small hole on its underside. The water is propelled upwards by the impeller and is discharged at the top through the discharge outlet [52].

In order to interface the new pump with the existing loop, a new structure was built to accommodate the water supply tank and pump. The structure is supported on wheels and is mobile for easy alignment of the pump outlet with the existing loop piping. The structure uses *Telestrut* telescopic tubing and has four legs for support. An aluminum sheet for supporting the water tank was then bracketed at the bottom and fastened to all the four legs. The pump rests in the tank on a vulcanized rubber pad to reduce vibration. Adjustable brakes are attached to the structure to ensure stability when experiments are in progress (Fig. 3.4).



Figure 3.4: Water tank support structure with wheels and adjustable brakes

The pump outlet is connected to the loop with the aid of flexible tubing which is connected to the pump with connectors (Figure 3.5).

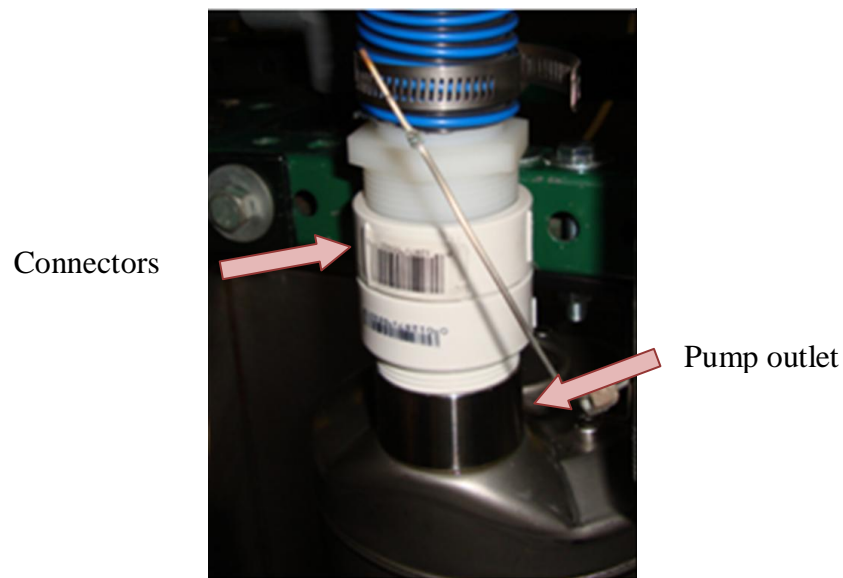


Figure 3.5: Connection of pump to the loop piping with flexible tubing.

3.2.2 Motor Frequency Drive

A motor frequency drive from Anacon Systems, model # ODE-2-12010-3H012 was added to the loop to vary rotational speed of the three phase pump (Fig. 3.6).



Figure 3.6: Motor frequency drive for adjusting pump rotational frequency

The frequency drive allows the rotational speed of the pump to be varied between 5 and 60 Hz via a 10 kilo-ohm potentiometer. However, the pump is not operated below 50 Hz as any lower could damage the pump. The frequency drive is connected between the three phase power supply from the wall and the pump motor. It is used in experiments with varying pump speeds to determine the relationship between process variables and electrical signatures.

3.2.3 Water Filtration System

The turbine flow meter and possibly other components can become clogged due to impurities in the water. This deposition of impurities hinders the proper operation of the flow meters and can degrade the pump components. Therefore, the water flowing through the loop must be purified to ensure efficient operation. A reverse osmosis (RO) filtration unit from *Bulk Reef Supply* was installed to filter out the impurities and provide clean water for the experimental loop (Figure 3.7). The system uses a five-stage system to effectively remove all impurities.



Figure 3.7: Five stage reverse osmosis water filtration system

3.2.3 Data Acquisition System

A National Instruments (NI) compact digital acquisition system was installed as the new DAQ system. A chassis from NI is used to hold the different modules, which receive signals from the sensors and interfaces with the computer (Figure 3.8).

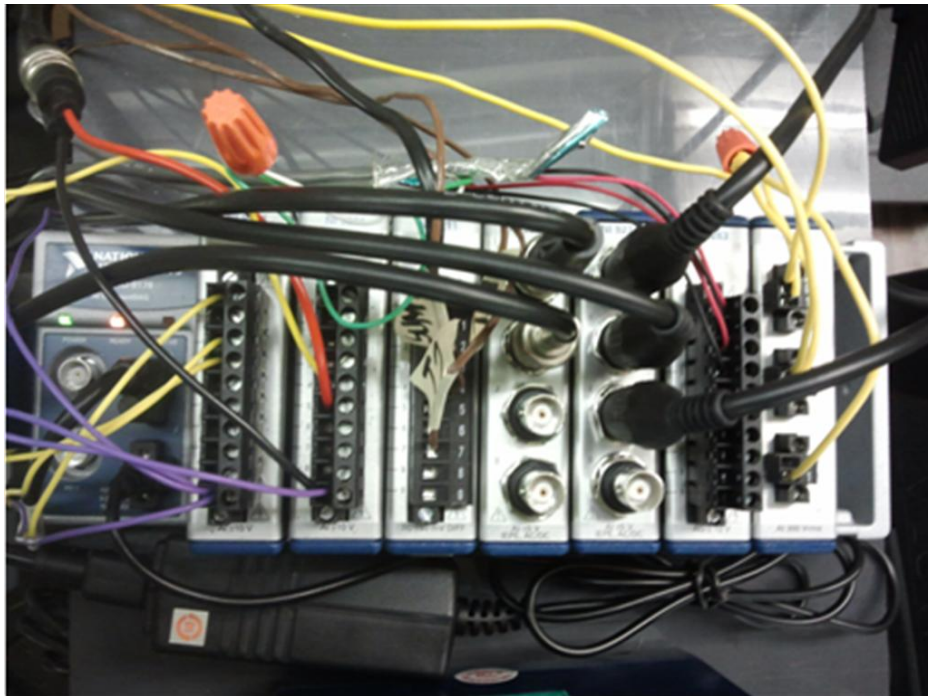


Figure 3.8: National Instruments chassis with individual modules installed

The following is a summary of the data acquisition modules installed:

1. NI 9201: This is an 8-channel voltage input module with a common terminal which is internally connected to an isolated ground. Pressure transmitters, flow meters, and motor-operated valves use this module [47].
2. NI 9234: This analog input module deliver 102 dB of dynamic range and incorporates IEPE (2-mA constant current) signal conditioning for accelerometers. The module also has built-in DC filtering, allowing only fluctuations from the DC level to be recorded. Accelerometers and current clamps use this module for its specialty in vibrational analysis and its inherent DC filtering capability [51].
3. NI 9263: This voltage output module is capable of outputting a DC voltage signal. It is used with a control program on the computer to adjust the opening position of the MOV.
4. NI 9225: This voltage input module is capable of receiving high voltage signals up to ± 300 Vrms and is used to record the 3 phase voltage from the pump.

3.3. Loop Instrumentation System and Devices

This section details the various types of sensors installed for measuring process and electrical signature in the loop, as well as the operation of the motor operated valves.

3.3.1 Accelerometers

A typical accelerometer consists of a piezoelectric component made of quartz or ceramic crystals to generate an electrical signal that is proportional to the applied force (or acceleration). The piezoelectric effect produces charged particles on the crystal, the total charge being proportional to the applied force or stress. The electronics inside the accelerometer convert the high impedance charge signal into a low impedance voltage signal that can be readily transmitted (Fig. 3.9).

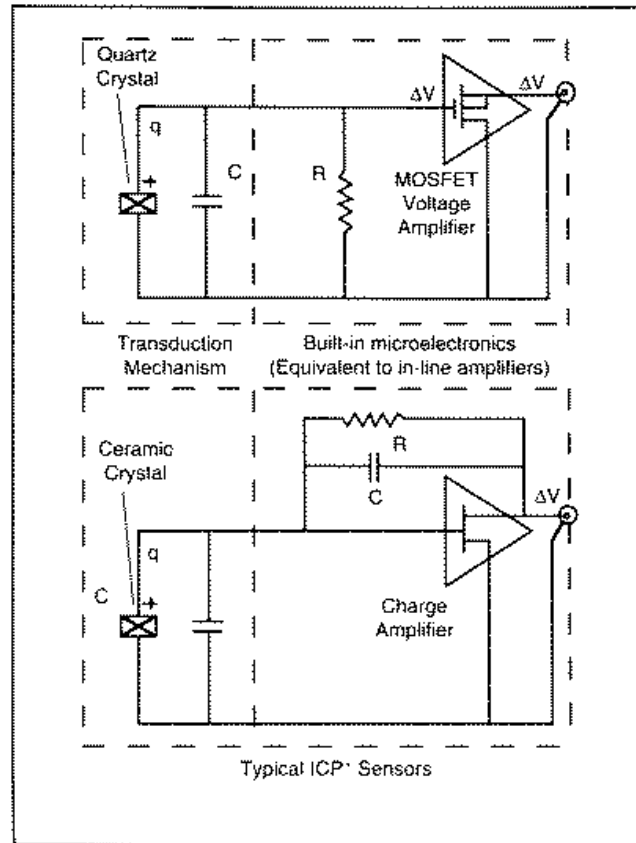


Figure 3.9: Accelerometer internal circuitry [57].

A signal conditioner is used to supply the electronics inside the ICP accelerometers with the required excitation current from a DC voltage source (Figure 3.10).

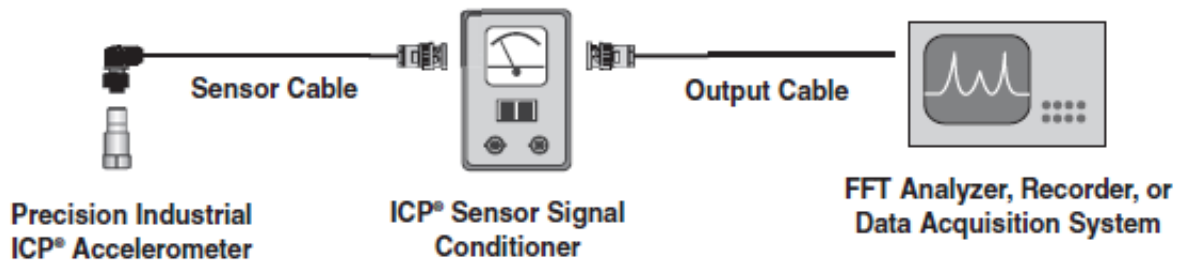


Figure 3.10: Set up for accelerometer analysis [58]

The NI module 9234 is capable of delivering an excitation current of 2 mA to accelerometers connected to it; however, the accelerometers used in this experiment require an excitation current of 4-20 mA. In addition to providing the required excitation, signal conditioners may also incorporate additional signal conditioning, such as gain, filtering, buffering, and overload

indication. The PCB 482C54 signal conditioner is used in order to provide the required excitation current to the accelerometers and to amplify the signals (Figure 3.11).



Figure 3.11: Signal conditioner used with PCB accelerometers.

Hermetically sealed accelerometers were attached to the submersed pump to ensure that water does not damage the connection between the accelerometer and the output cable. An IMI model 608A1 accelerometer was selected for its submersible measurement capabilities. A circular mounting pad which allows the accelerometer to be screwed in (model # 080A93 from IMI) was attached to the pump on both the vertical and radial positions with high-bonding glue. The vertical accelerometer was placed near the discharge outlet and the radial accelerometer was placed as close to the motor pump coupling as possible on the side of the stainless steel shell (Figure 3.12). The mounting position for the horizontal accelerometer was determined by tapping along the pump casing and identifying the position at which the vibration peaks were the largest.



Figure 3.12: Positioning of the two accelerometers on the pump casing

3.3.2 Pressure Transmitter

A pressure transmitter was installed on the piping near the pump outlet to measure the pressure in the loop (Figure 3.13).



Figure 3.13: Pressure Transmitter installed near pump discharge

The pressure transmitter works by converting pressure into a direct signal using a strain-gauge transducer. The conversion of pressure into an electrical signal is achieved by the physical deformation of strain gauges which are bonded into the diaphragm of the pressure transducer and wired into a Wheatstone bridge configuration. Pressure applied to the pressure transducers produces a deflection of the diaphragm which introduces strain the gauges which produces a change in the electrical resistance proportional to the pressure [64]. The pressure transmitter is manufactured by *Dwyer Instruments* and has a measurement range of 0-30 psig. The output of the pressure transmitter is 4-20mA but must be converted to a voltage signal in order to be accepted by the NI modules. This is accomplished by placing a 200 ohm resistor across the terminals and measuring the voltage across the resistor. The resulting voltage signal is wired into the NI voltage module for easy measurement.

3.3.3 Orifice Flow Meter

An orifice flow meter was installed on the inlet piping leading to a MOV and the vertical water tank. The orifice meter uses Bernoulli's principle to measure the volumetric flow rate through the pipe. Bernoulli's principle states that for a fixed datum, the sum of the fluid velocity and pressure heads remains constant. The orifice meter uses a thin plate with an opening in the center and pressure taps to measure the differential pressure across the plate (Figure 3.14).

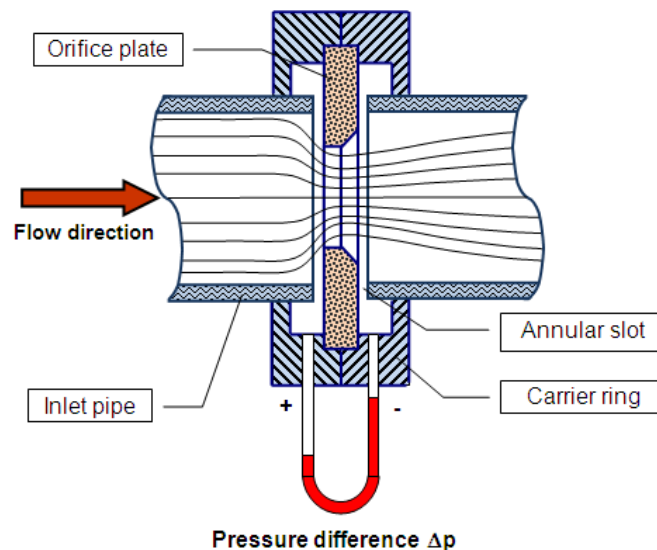


Figure 3.14: Cutout view of orifice meter internals

When the fluid passes through the orifice plate the pressure and velocity at the inlet and outlet of the orifice plate change. The differential pressure is then measured by two pressure taps connected to the orifice plate by short tubes. The differential pressure is then output as a current signal by its electronics. A 330 Ohm resistor was installed across the two terminals so that a voltage signal can be recorded with the NI module and LabVIEW. The voltage output is then matched with a known flow rate and a calibration curve can be generated, relating the voltage to the flow rate. If Δp is the pressure difference between the inlet and the outlet, as measured by a differential pressure transmitter, A_1 and A_2 are the respective inlet and outlet areas of cross section, ρ is the mass density of the fluid, the mass flow rate is given by W (Kg/m^3).

$$W = A_1 \rho \sqrt{\frac{2 \Delta p}{\rho \left[1 - \frac{A_1^2}{A_2^2} \right]}} = K \sqrt{\Delta p} \quad (3.1)$$

The orifice constant, K , may also include a factor to account for friction loss across the orifice.

In order to calibrate the orifice meter, the following steps were performed:

1. Tank #1 was isolated.
2. The outlet control valve was closed so that the water could only flow into the tank.
3. The inlet valve was then opened in 0.5 V increments (from 0 to 5 V, 0 V representing completely closed and 5 V completely open).
4. For each valve position, the flow rate was recorded by recording the time it took for the water level to reach a whole number of liters by using the liter marks on the tank
5. The voltage output from the orifice meter was also recorded and a plot of flow rate versus voltage was made to provide a calibration curve.
6. Two trials were run at the same valve positions and the averages were recorded for a final calibration. The final averaged datasheet and graph are given in Table 3.1 and Figure 3.15.

Table 3.1: Orifice Meter (OM) Calibration

Valve Position	OM Voltage	Liters Filled	Flow Rate L/s	Flow Rate (GPM)
0	1.31	0	0	0
1	1.31	0	0	0
1.5	1.31	0	0	0
2	1.39	8	0.052805856	0.836972813
2.5	1.92	8	0.14160401	2.244423559
3	3.385	8	0.262365591	4.158494624
3.5	5.26	8	0.355731225	5.638339921
4	6.455	8	0.421052632	6.673684211
4.5	6.48	8	0.470588235	7.458823529
5	6.48	8	0.470588235	7.458823529

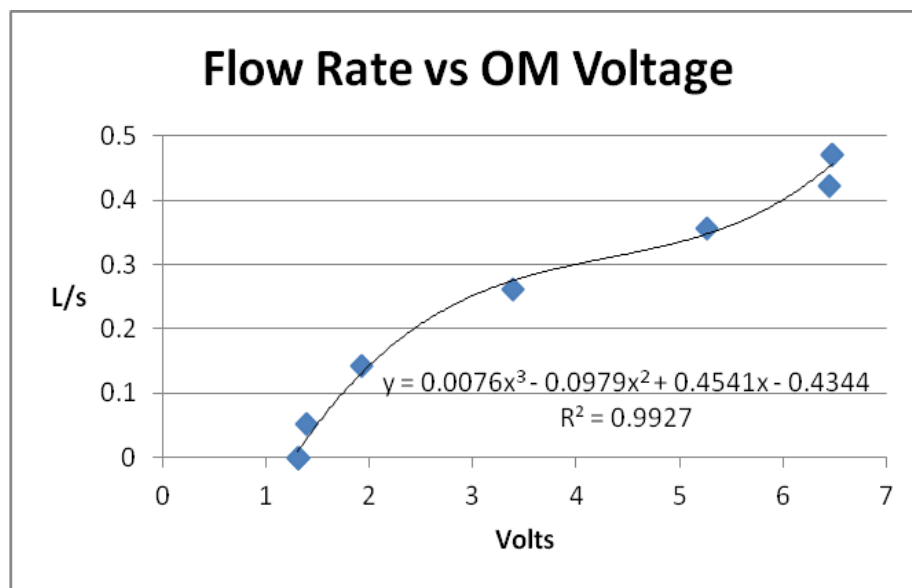


Figure 3.15: Calibration curve for the Orifice meter as a function of voltage

3.3.4 Turbine Flow Meter

Two turbine flow meters (TFMs) are installed on the loop to measure the volumetric flow rate by measuring the rotational speed of a small turbine as the water passes through it. A magnetic field is produced at the base of the transducer and as each turbine blade passes through the field, an AC voltage pulse is generated that is proportional to the flow rate of the fluid traveling through the meter. A frequency-to-voltage converter is used with each turbine to convert the AC voltage frequency to a DC voltage that can be easily measured. A *Blancett* flow meter is installed on the tank outlet piping to measure the flow rate of water exiting the tank while an *Omega* turbine flow meter is installed on the bypass tubing. The tank exit TFM outputs a voltage of 0-5V and the bypass TFM outputs at 0-10 V. The associated range of each meter is used to produce a formula for the flow rate based on the incoming voltage signal.

To calibrate the turbine flow meter installed on the exit pipe of the tank, the voltage output signal was wired into LabVIEW through an NI module. The TFM was calibrated against the already calculated flow rate read through the orifice meter. To do this, the control valve input and output flows were varied by opening and closing the valves until a steady state was reached in the tank. Once a steady state was reached and the level constant, the flow going into the tank is equal to the flow leaving the tank. Therefore, we were able to record the OM's flow rate reading and the voltage reading from the TFM to plot a calibration curve. The recorded data and the calibration curve are shown Table 3.2 and Figure 3.16.

Table 3.2: Turbine flow meter calibration

Tank Level	CV 1 positon	CV 4 positon	OM Flow Rate	TFM Voltage
81	2	4	0.149	2.52
103	2	3.4	0.147	2.39
16	2	2.75	0.11	1.38
62	2	4.5	0.148	2.35
104	2.1	5	0.166	2.82
18	1.9	5	0.133	1.87
			0	0

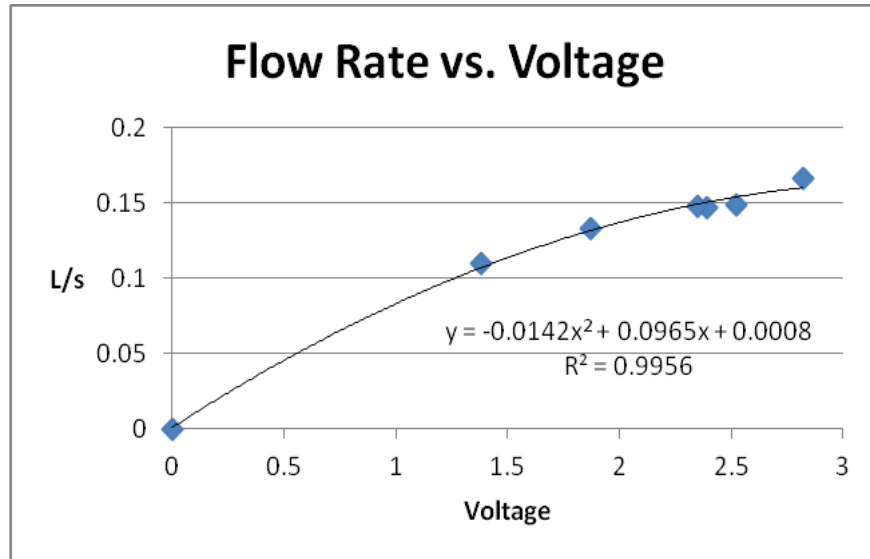


Figure 3.16: Calibration curve for the turbine flow meter

A bypass valve was also installed in the loop to decrease the pressure and flow to manageable levels. It is also used in the experiments to test for leakage and blockage in a system. A turbine flow meter was installed before the bypass valve so that the bypass flow rate could be measured. The flow meter installed here is manufactured by Omega and can read up to 29 GPM or 1.83 L/s with a voltage output of 0-10 V. To calibrate this meter, a linear relationship was used where every 1 V represented 0.183 L/s of flow.

3.3.5 Tank Level Measurement using a Differential Pressure Transmitter

A pressure transmitter is used to measure the pressure exerted by the column of water in the tank. The sensor output is 4-20 mA current. A 250 ohm resistor is used to change the output to voltage. Since we are not interested in the pressure inside the tank, the output voltage of the sensor was correlated to indicate the tank water level. To calibrate the sensor, the tank was first labeled in one liter increments up to 10 liters. The pressure sensor's output voltage was then recorded for various amounts of water in the tank. Several trials were then performed to ensure accuracy and repeatability. A sample of the raw data and its calibration curve used are given (Table 3.3 and Figure 3.17).

Table 3.3: Tank water level calibration

Trial 1	
Tank level (% full)	Pressure transmitter (Volt)
100	3.8665
90	3.589
70	3.06
50	2.52
30	1.99
10	1.46
0	1.22

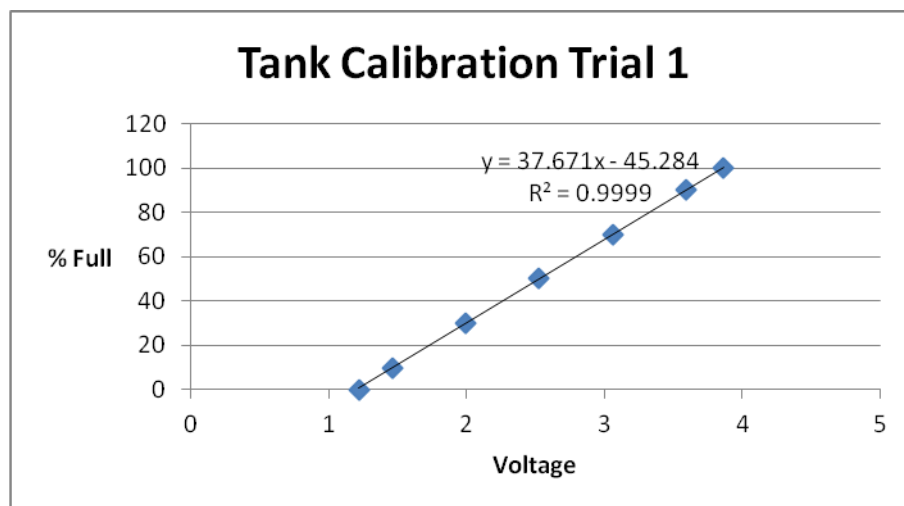


Figure 3.17: Calibration curve of differential pressure sensor.

3.3.6 Motor Operated Valves

Motor operated valves (MOVs) are used to control the flow rate throughout the loop. There is one MOV located on the inlet and outlet piping connected to the tank. The MOV circuitry includes DIP switches and inlet and outlet wire terminals (Figure 3.18).

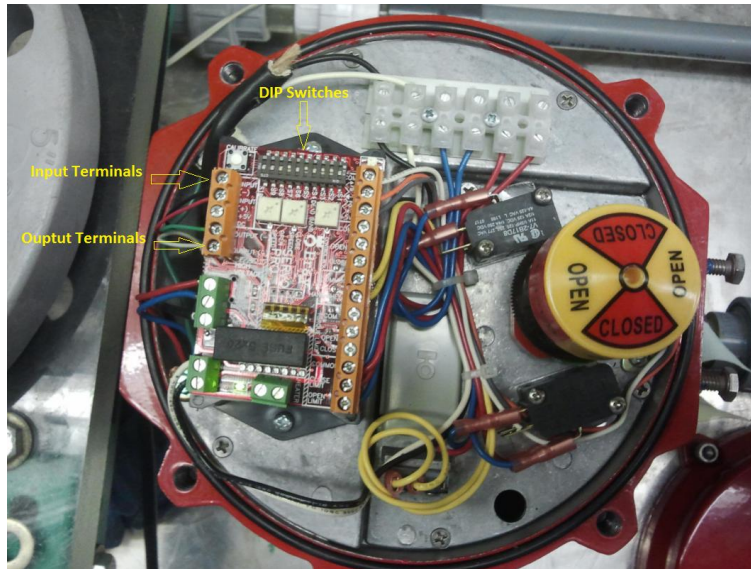


Figure 3.18: MOV circuitry with terminals and switches highlighted

The DIP switches are used to set the stroke of the MOV. These switches were set to allow for a 0-5 V stroke. A 0-Volt signal means that the MOV is completely closed while a 5-V signal means that the MOV is completely open. A signal is sent to the desired MOV using the NI 9263 voltage output module via a LabVIEW program.

3.3.7 Pump Motor Electrical Signatures

The electrical signatures recorded from the pump motor included three phase current and voltage measurements. The motor current is measured using current measuring clamps that attach around the three wires. A central ferromagnetic core in the clamp experiences a change in the magnetic flux. A coil is wound around this central core and a voltage is induced due to the magnetic flux in the core. This voltage is proportional to the original current in the main conductor and it can be calibrated to measure the current flowing through the conductor. A Fluke I200s current clamp is used to measure the motor current. The output of the current clamp is a voltage signal that is divided by a scaling factor of 10mV/A to determine the current drawn by the motor [53]. In order to calculate the power drawn by the motor, the voltage from each of the three phases had to be recorded. This was done by connecting wires from the frequency drive voltage inputs to the NI high voltage module.

4. CHARACTERIZING PUMP POWER, FLOW RATE, AND PRESSURE MEASUREMENTS IN THE EXPERIMENTAL FLOW LOOP

4.1. Introduction

This section deals with the study of the relationship among the flow rate, pump discharge pressure, and pump motor power. The goal is to relate them experimentally, and use this relationship to detect indirectly any changes in the pump flow rate by calculating the motor power. Some preliminaries of pump power and motor power calculations are given [87].

4.2. Pump Characteristics

The term ‘head’ is used instead of the differential pressure in defining the performance of a centrifugal pump. The head generated is a measure of the increase in specific energy (energy/unit mass) of the fluid between the pump suction and discharge. The pump head is an energy term represented by equation 4.1 where Q is the flow rate (m^3/hour), H is the pump head (meters) at the given flow rate Q , and SG is the specific gravity of the fluid at the pumped temperature.

$$\text{Pump Hydraulic Power (kW)} = \frac{(Q \cdot H \cdot SG) 9.81}{3600} \quad (4.1)$$

In general, the pump hydraulic power is a non-linear function of flow rate, Q .

The Net Positive Suction Head available (NPSH_A) reflects the fluid head loss in the suction piping system. It is independent of pump suction requirements and is entirely a process system characteristic. Net Positive Suction Head required (NPSH_R) defines NPSH required for a specific flow rate. The NPSH is given by Equation (4.2):

$$\text{NPSHA (meters)} = \frac{[P_s + P_a - P_v] \cdot 2.31}{9.81 \text{ SG}} + \frac{[V_o^2 - V_i^2]}{2g} \quad (4.2)$$

where P_s is pump suction pressure in psig, P_a is local atmospheric pressure, and P_v is fluid vapor pressure. V_i and V_o are the velocities of the fluid at the inlet and outlet. These two equations show that there is a relationship between the pump power, flow and pressure [87]. Figure 4.1 shows the typical pump performance plots for a centrifugal pump.

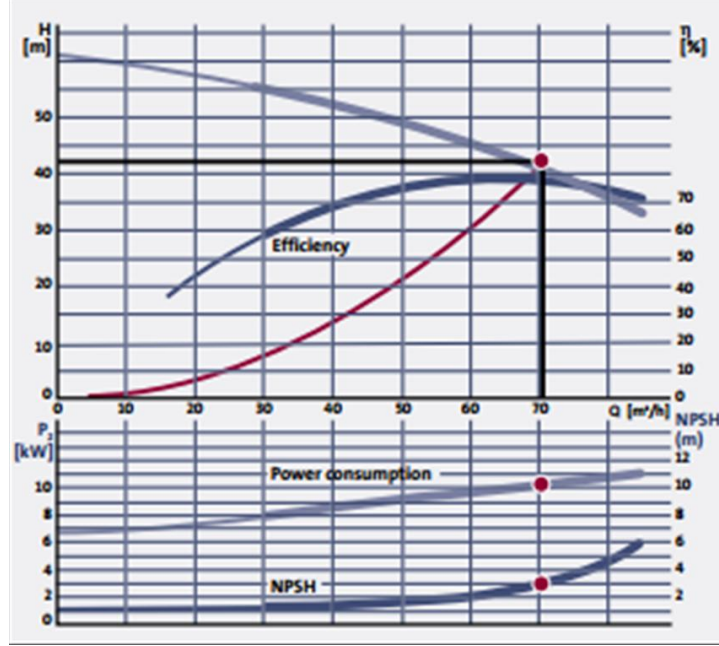


Figure 4.1: Example of pump performance [87].

The plot details the Q-H curve which relates the head with the volumetric flow rate. This graph indicates how the pump is able to perform at a given fluid flow rate. Head is measured in 'meter' and thus the performance curve is true for any fluid.

The pump efficiency is the ratio between the pump hydraulic power and the break horsepower or the power input to the pump shaft. This is given by

$$\eta_p = \frac{P_H}{P_s} = \frac{\rho g Q H}{\omega T} \quad (4.3)$$

Where ω is the shaft speed (rad/sec) and T is the torque (N-m) imparted to the pump shaft. The power delivered to the pump is proportional to the power drawn by the induction motor. This power can be calculated by measurements of three phase currents and voltages. Thus, within a factor (which may change, in general) the hydraulic power is proportional to the power delivered to the pump shaft.

4.3. Motor Power Calculation

The apparent motor power is calculated using the RMS values of phase currents and voltages. For a three-phase Y-connection induction motor, the apparent power is calculated as:

$$\text{Motor Power (apparent)} = \frac{1}{\sqrt{3}} [I_{1,rms} V_{1,rms} + I_{2,rms} V_{2,rms} + I_{3,rms} V_{3,rms}] \quad (4.4)$$

Pump motor power can be defined as the combination of the actual and the apparent power. The power factor is the ratio of the actual and the apparent power in the circuit, and can also be referred to as a practical measure of the efficiency of a power distribution system. Apparent power is the product of the root mean square values of the voltage and the current. Actual power is the portion of power that is averaged over a complete cycle of the AC waveform results in net energy transfer in one direction. The power factor is unity when the voltage and the current are in phase with each other. For a balanced three-phase motor, the actual power is calculated as:

$$\text{Motor Power (actual)} = \sqrt{3} [I_{rms} V_{rms}] \cos \phi \quad (4.5)$$

$\cos(\phi)$ is the power factor, indicating the phase shift between the phase voltage and the current. This angle is calculated from the actual measurements of current and voltage. In this calculation the power in each phase is assumed to be the same.

4.4. Characterizing Pump Power, Flow Rate, and Pump Discharge Pressure

In order to calculate the pump power, the voltage and current of all three phases were recorded. The efficiency of the pump is affected when the pump rotational frequency changes. The change in the frequency will cause the load on the motor to change, and thus alter the power factor. Experiments were performed to show the direct relationships between the measured power and the flow rate, therefore, it was assumed the power factor is constant throughout the experimental runs.

The root-mean-squared (RMS) values of all three phases are calculated estimate the RMS power. Power and flow rate are plotted at various motor frequencies to establish the relationship between the variables as changes occur. The relationship between flow and power is also explored by changing the valve (MOV) position in order to determine how load changes on the system affect the pump power. The R-squared statistic is used to define the goodness of fit of the model and provides a measure of how well the observed outcome fits the model. The R-squared statistic is a value between 0 and 1; if the value is closer to 1, it means that the fit is good

and the predictions are accurate. It is calculated by finding the sum of squares of the residuals and the total sum of squares, and is given by:

$$R\text{-squared} = 1 - (SS_{\text{res}} / SS_{\text{total}}) \quad (4.6)$$

where SS_{res} is the residual sum-of-squares which is the discrepancy between the estimated model and the data. SS_{total} is the total sum-of-squares which is the sum-of-squares of all the observations with the mean value subtracted from the measurements.

In order to test the feasibility of determining the flow rate using the power drawn by the pump, the relationship between power and flow was first explored. In this experimental run, the inlet valve was kept closed and the flow of water was only allowed through the bypass valve so the only variables of concern were the pump power, bypass flow rate, and pump discharge pressure. The input frequency was altered in steps of 0.1Hz from 60.0 Hz to 59.0 Hz. The RMS power drawn by the pump was found to be linearly related to its rotational frequency with an R-squared value of approximately 0.97 (Figure 4.2). As is seen in the figure, the relationship is fairly linear, primarily because of limited changes in process conditions.

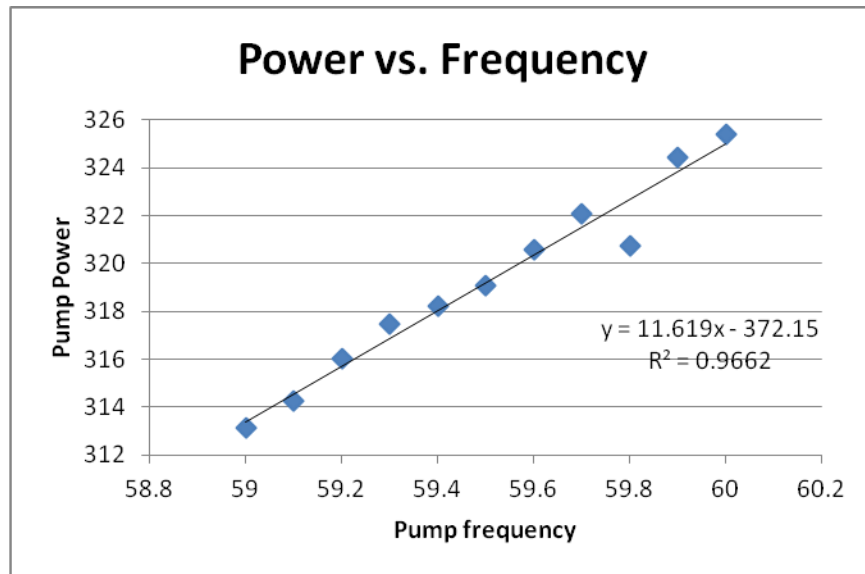


Figure 4.2: RMS power and motor frequency relationship.

The relationship between the motor power and the outlet pressure was also studied from this experiment and shows that as the frequency of the pump increased, pressure also increased in a linear fashion (Figure 4.3).

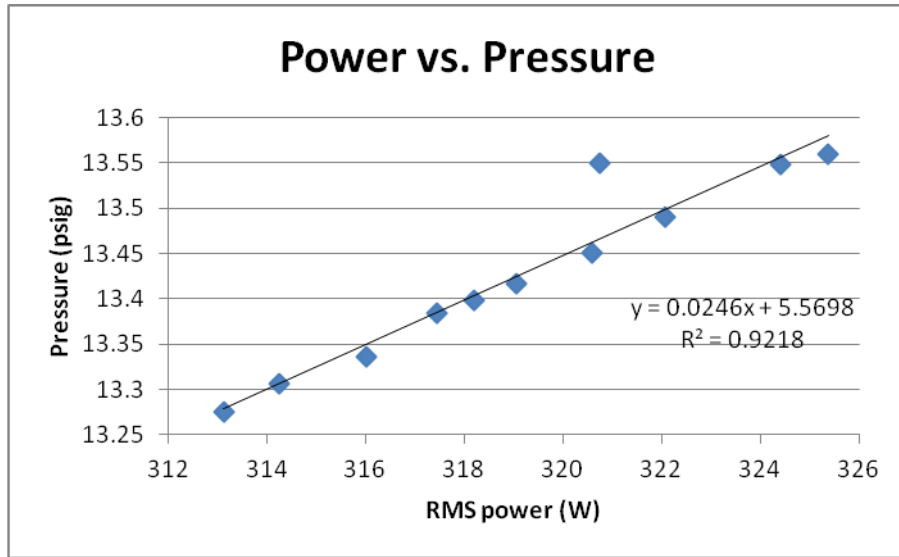


Figure 4.3: RMS power and pressure relationship

Once it was established that the motor power directly follows the pump rotational speed (frequency), the relationship between flow rate and power was then investigated. The flow rate was measured using the turbine flow meter on the bypass part of the loop, and the frequency was changed in 0.1 Hz increments and the flow rate at each frequency was recorded (Figure 4.4). An R-squared value of approximately 0.87 was found, proving that the flow rate and power are linearly related.

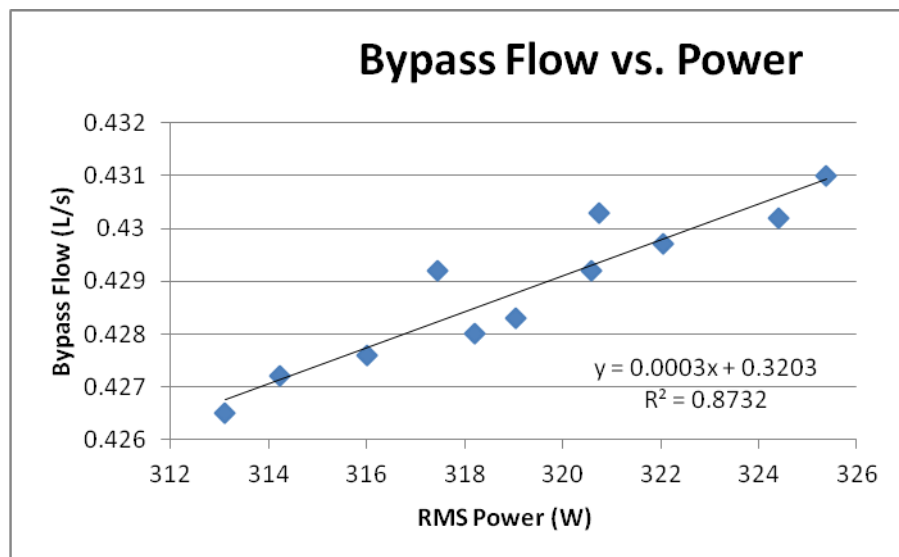


Figure 4.4: Average flow rate increases with the RMS power

In the next set of experiments, the pump motor frequency was kept constant at 60 Hz, and the flow rate to the vertical column was measured when the control valve was opened to different positions (Figure 4.5).

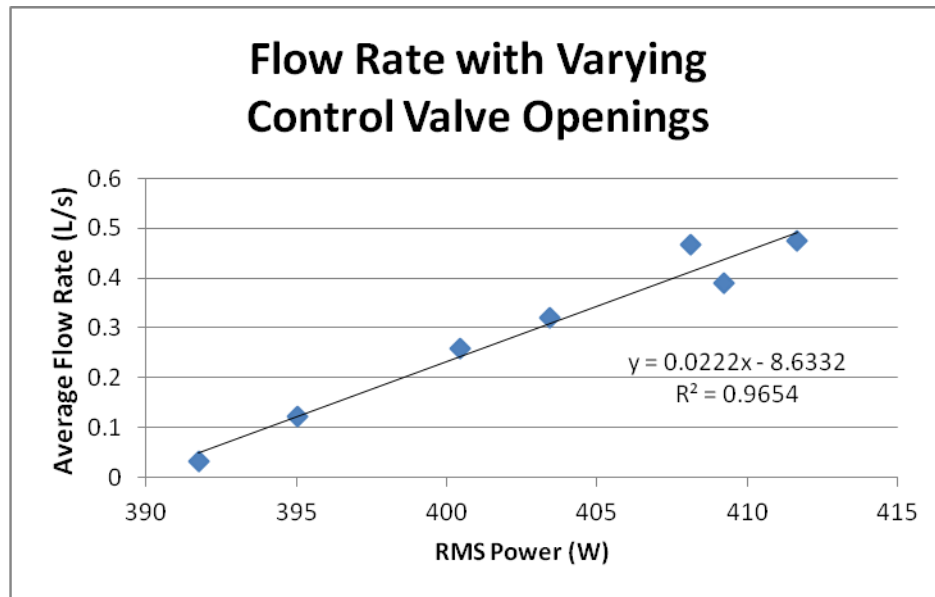


Figure 4.5: RMS power increases as the flow rate increases

A linear relationship between the pump discharge pressure and RMS power was also apparent from the experiment (Figure 4.6).

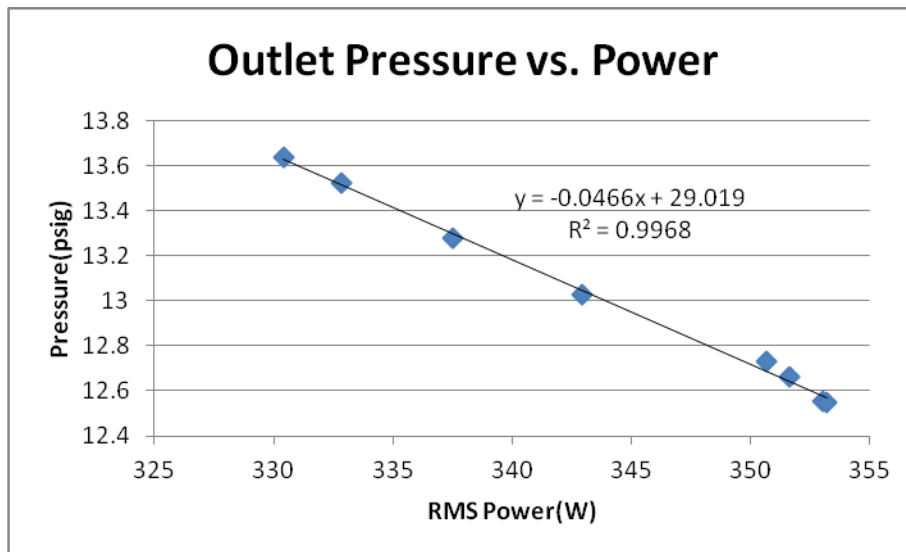


Figure 4.6: Power and pressure at various valve openings

In this experiment it was shown that as the control valve is opened more, the outlet pressure decreases and the pump power increases. The high R-squared values indicate a linear relationship between the flow rate through the control valve and the RMS power of the pump as well as between the pressure and power.

Experiments with transient changes in the control valve changes were also performed. The valve operates via a user supplied voltage signal from the computer of 0 – 5 V, zero being completely closed, and five being completely open. Flow through the valve does not actually occur until the input to the control valve is at approximately 2 V. Changes to the valve opening were performed while taking data continuously and plotting the changes in flow rate and RMS power (Figure 4.7).

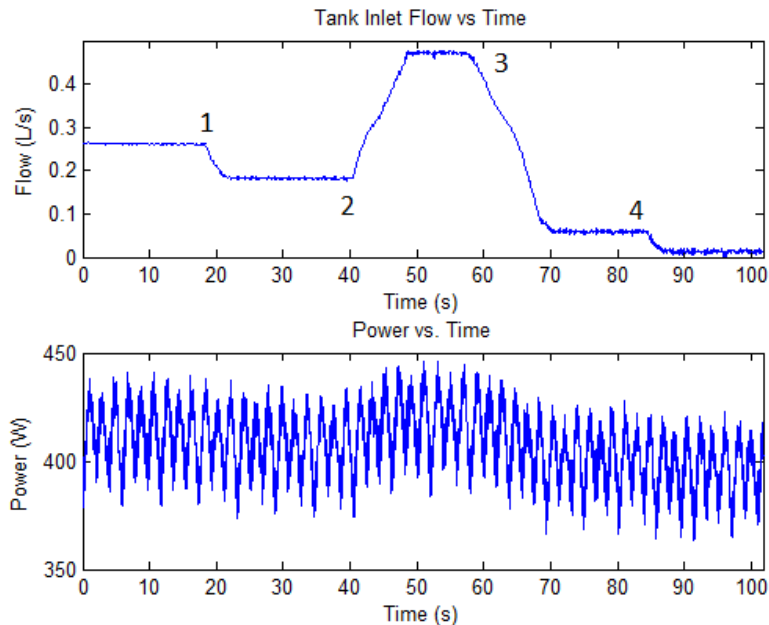


Figure 4.7: Varying flow rates and power drawn due to control valve changes

The test began with a constant flow and control valve input set to 3 V. At event 1 on the graph, the input was changed to 2.5 V. At event 2, the input was changed to 5 V. Event 3 occurred when the input was changed back to 2 V, and finally at event 4, the valve was closed. The power followed these changes well, increasing and decreasing with the flow.

After observing the relationships among motor power, flow rate, and pressure, an experiment was performed to determine the behavior of the process variables based on user-induced faults. Leakage was induced in the system by considering the system to consist only of the one vertical tank by assuming that the bypass valve was always closed. With this setup,

water was only allowed to flow to and from the vertical tank and not through the bypass valve. In order to simulate leakage, the tank inlet valve was kept open at a fixed position and then leakage was introduced in the system by opening the bypass valve at different positions (Figures 4.8 & 4.9).

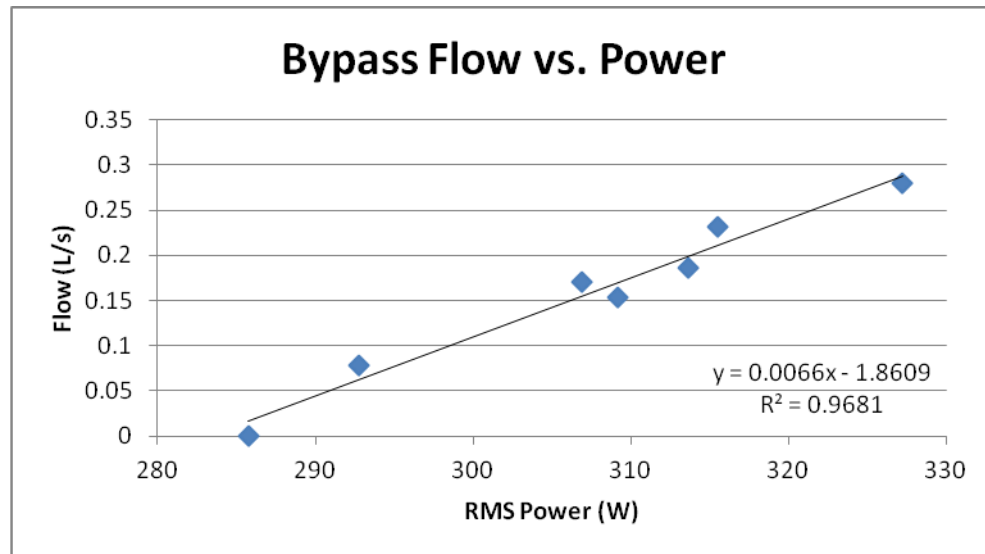


Figure 4.8: Flow and power relationship for different rates of leakage

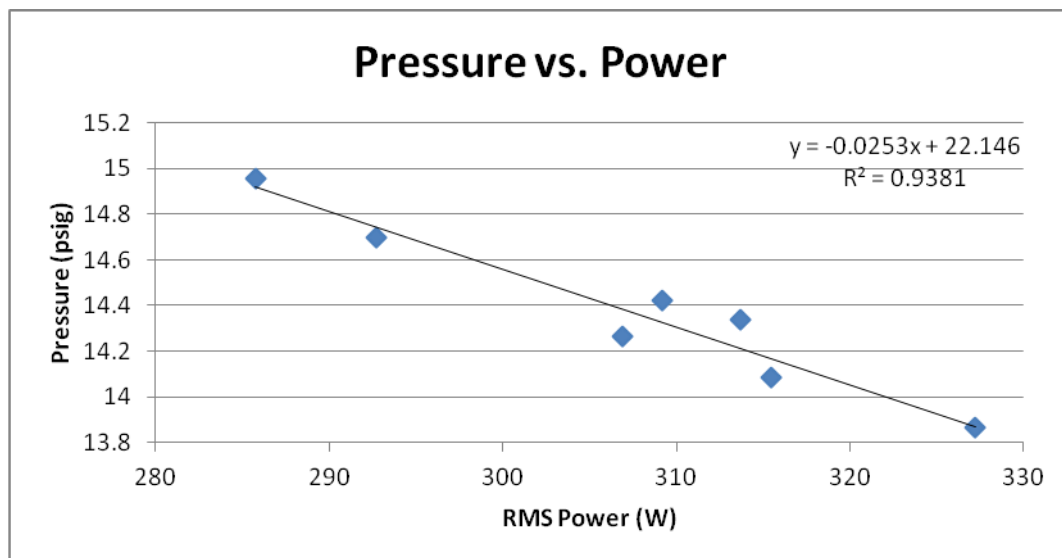


Figure 4.9: Pressure and power relationship for different rates of leakage

The opening of the bypass valve causes the pressure in the system to decrease and the motor power to increase.

These experiments show that there is a very good relationship between motor power (current) and pressure, and motor power and flow. These relationships can be used to train data-based models to detect faults in the system.

4.5. Remarks on Experimental Results

The experiments relating changes in pump flow and motor power clearly indicate that the motor power is able to track the changes in pump flow. With proper calibration, this relationship can be used to estimate pump output indirectly, and thus monitor its performance. In such a scenario, it is necessary to assume that the electric motor itself is operating without any fault. For a complete system diagnostics it is necessary to have measurements of multiple variables, such as motor power, pressure, flow rate, valve position, and others.

4.6. Repeatability of Experimental Data

As discussed in the above sections, extensive data acquisition was performed to determine the relationships among motor power, pressure, and flow in the experimental flow loop. To ensure that the results of the experiments were repeatable, the same tests were repeated ten separate times on the flow loop and the results of these separate tests were compared. The testing involved collecting data from frequencies between 60 and 55 Hz in one Hz increments. The average flow, pressure, and power were calculated for each frequency and the resulting data were plotted to observe the relationships. The test runs were repeated ten separate times for each motor frequency in the range 55 – 60 Hz. The results of the tests were all plotted on the same graph where the error between different results at the same frequency could then be calculated. The purpose of this was to ensure the repeatability of the experiments that were run.

The first relationship that was observed was the relationship between flow rate and RMS motor power. To analyze this relationship, the flow rate and RMS power at each frequency increment of each test was plotted (Figure 4.10).

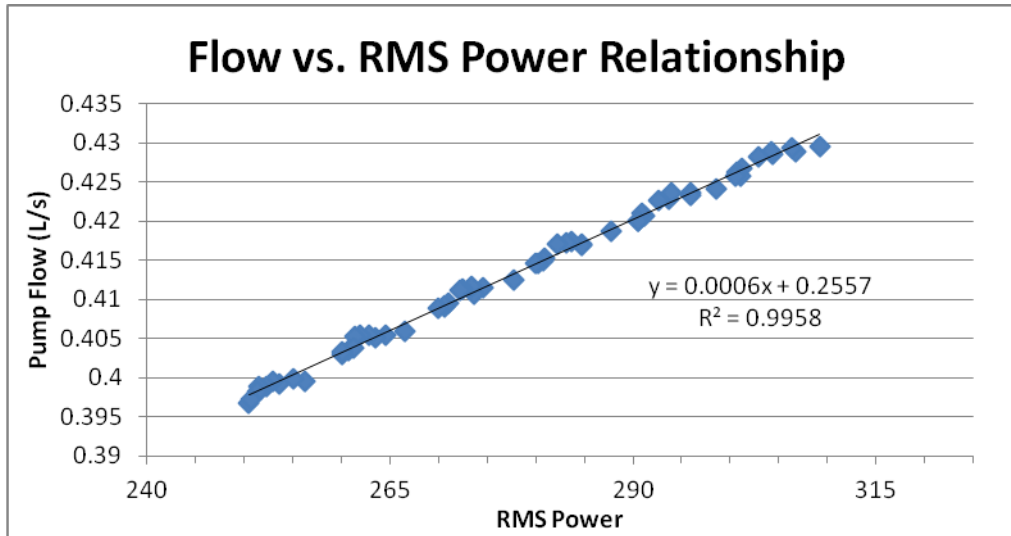


Figure 4.10: Flow rate versus motor power at different rotational frequencies

The error in the measurements at each frequency increment was then calculated by finding the standard deviation of 10 different values for the RMS power and flow at each frequency value. These results showed that the experiment was highly repeatable and that the values from different tests could be trusted (Figure 4.11).

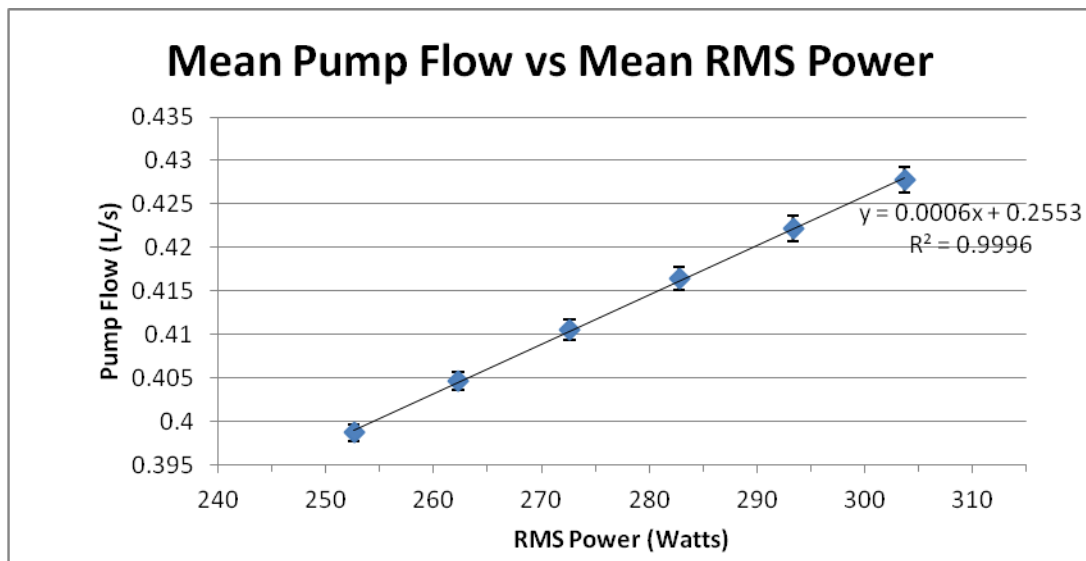


Figure 4.11: Deviation of flow rate (with respect to mean) at each experimental condition

The next relationship studied was the correlation between the pump discharge pressure and the RMS power of the pump. Sixty different data points were plotted, 10 for each power and pressure at each frequency increment value (Figure 4.12).

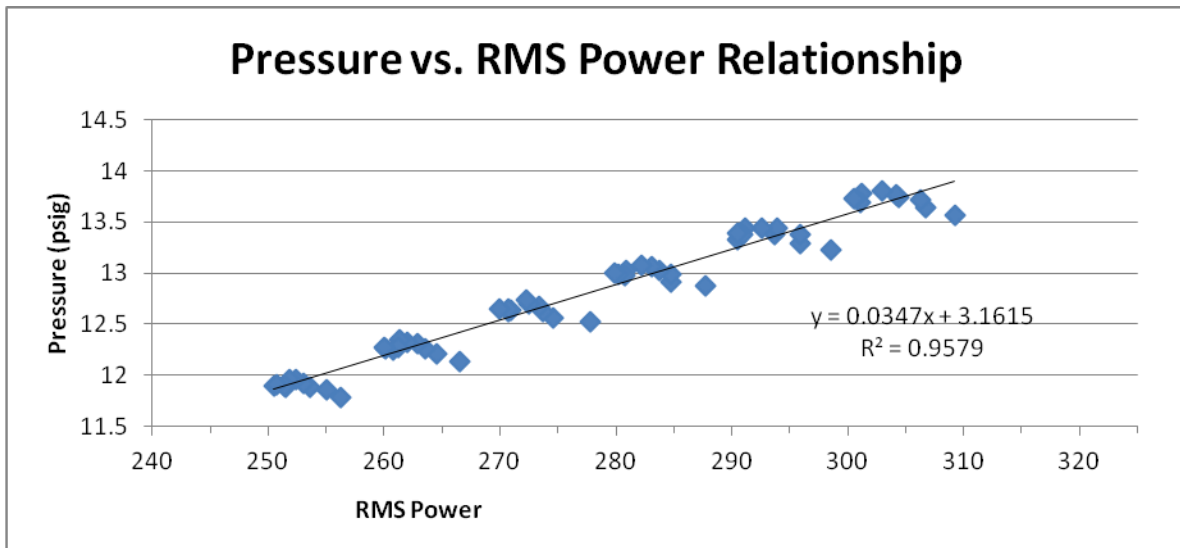


Figure 4.12: Pump discharge pressure as a function of motor power for different frequencies.

The standard deviation was then calculated for pressure and power using the 10 different data points at each frequency increment (Figure 4.13).

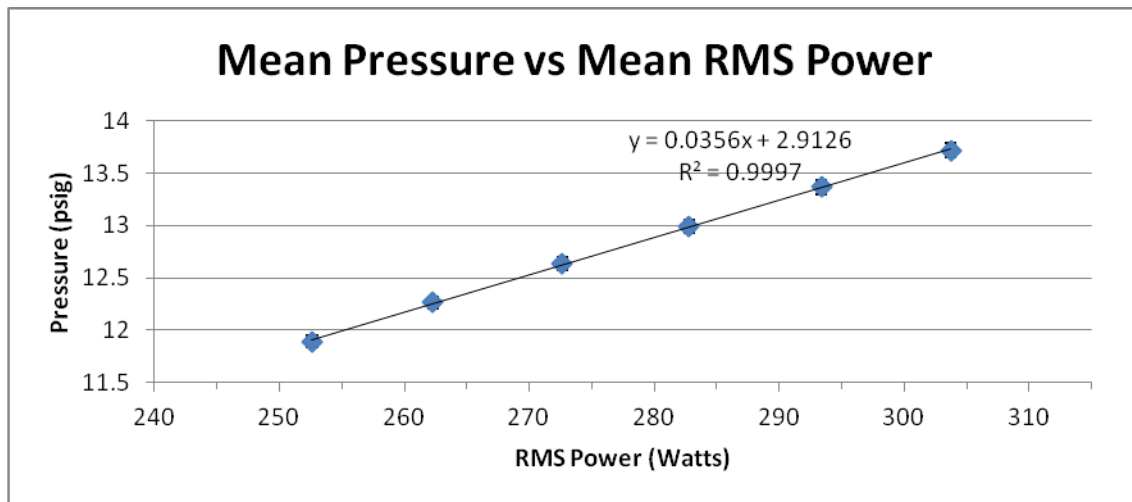


Figure 4.13: Deviation of pump discharge pressure (with respect to mean) at each experimental condition

The results for pressure vs. power were also repeatable, but it seems that there is a slight deviation in the relationship at each frequency value which is assumed to derive from a decrease in the pump efficiency over time as it heats up. A summary of the mean and standard deviation of these measurements is given in Table 4.1.

Table 4.1: Mean and standard deviation of measurements at different frequencies

Frequency (Hz)	Mean RMS Power (W)	Standard Deviation (W)
60	303.7	2.83
59	293.4	2.62
58	282.8	2.37
57	272.6	2.22
56	262.3	1.98
55	252.6	1.79
	Pressure	Std. Dev.
60	13.72	0.065
59	13.37	0.068
58	12.99	0.059
57	12.64	0.059
56	12.26	0.058
55	11.89	0.051
	Power_Factor	Std. Dev.
60	0.845	0.0038
59	0.835	0.0037
58	0.821	0.0038
57	0.807	0.0031
56	0.792	0.0038
55	0.777	0.0037
	Bypass flow	Std. Dev.
60	0.428	0.0014
59	0.422	0.0015
58	0.416	0.0013
57	0.411	0.0012
56	0.405	0.0011
55	0.399	0.0010

5. TIME-FREQUENCY ANALYSIS OF TRANSIENT DATA

5.1. Non-Stationary Data and Short-Time Fourier Transform (STFT)

In general, a random signal is defined to be a stationary signal if its statistical properties do not change with time. A necessary and sufficient condition for a signal to be stationary is that its probability density function (or distribution) does not change with time. The Fourier transform of a stationary signal is often used to estimate the energy in the signal at different frequencies. The Fourier transform breaks the signal into a set of sinusoidal components. Thus, the sine and cosine functions form a complete set of basic functions for this expansion. Note that a sine or a cosine function is a continuous wave, and theoretically extends to infinite time. For discrete data, a finite Fourier transform of a block of data is performed, and is then used to compute the power spectral density (PSD) at discrete frequency points. This is estimated by averaging over several blocks of data.

In the above Fourier analysis, the time information is lost. That is, the variation in the frequency as a function of time, the time of occurrence of an event or changes in the signal characteristics over short periods of time, are not available. Thus, the classical Fourier transform and the PSD analysis are suitable for *stationary signals*. The use of the short-time Fourier transform (STFT) or the wavelet transform (WT) [64] may overcome this drawback. The STFT uses a finite-length window, which is then translated along the data to compute the Fourier transform. The window size is fixed, and therefore the frequency resolution of the transform is also fixed. The transient variability in the signal may not be captured by the STFT. This drawback may be overcome by using the wavelet transform. A wavelet is a *small wave* “which has its energy concentrated in time to give a tool for the analysis of transient, non-stationary, or time-varying” signals. In analogy with the Fourier series, the wavelet basis functions may be used to represent a signal or a function.

In this section the STFT was used in order to explain the characteristics of transient data. This technique was applied to data to find whether changing the motor frequency was reflected in the subsequent frequency signals of pressure, vibration or current. The data under observation is the transient data obtained from the experimental loop; transient here means the change in motor frequency while recording data.

5.2. Description of Transient Data

Experiments were performed by changing the motor frequency to observe the changes in the current, pressure, and flow rate. It was observed that the pressure, motor current, and the fluid flow rate show close correlation with each other. The motor was started at 55 Hz, and then the pump frequency was decreased to 45 Hz. Motor frequency was then increased in steps of 5 Hz to 60 Hz, and then was decreased gradually to 50 Hz. Pump was then shut down after increasing the speed back to 55 Hz. This operation is explained by dividing the entire experiment into four regions as illustrated in Figures 5.1 through 5.3.

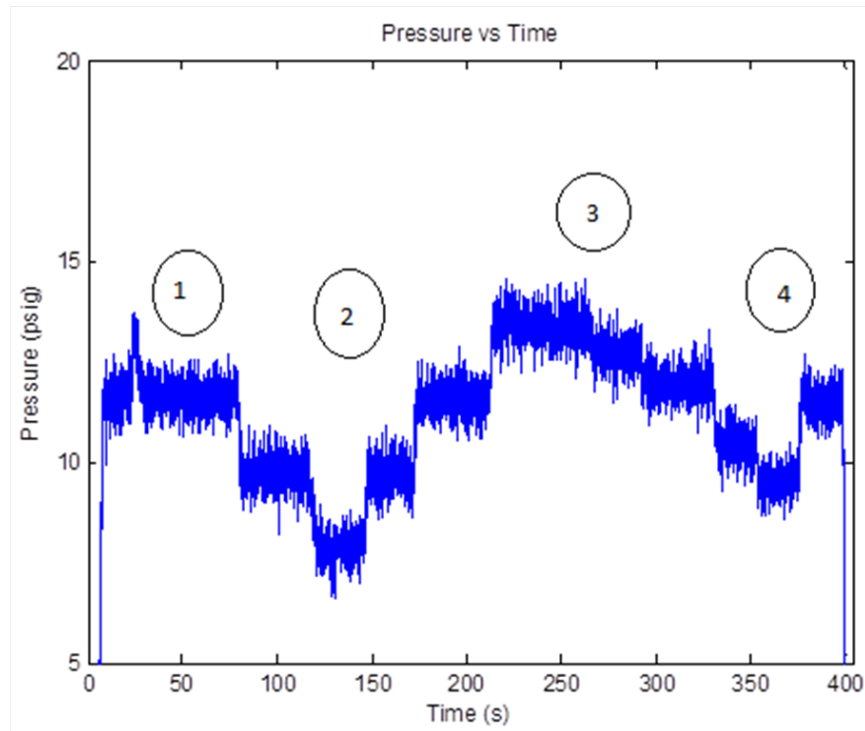


Figure 5.1: Pressure signal throughout experiment

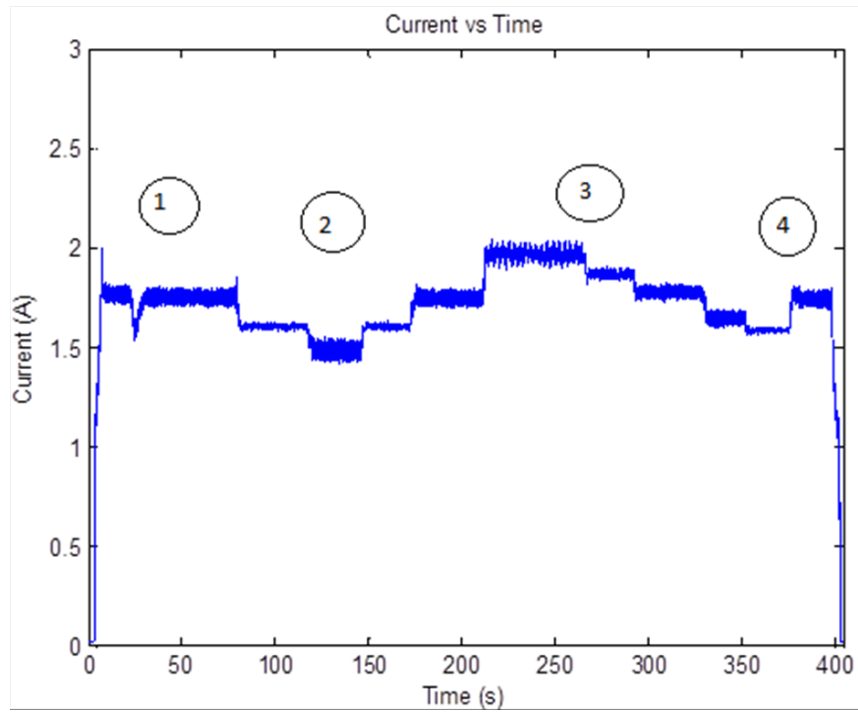


Figure 5.2 Motor current signal throughout experiment

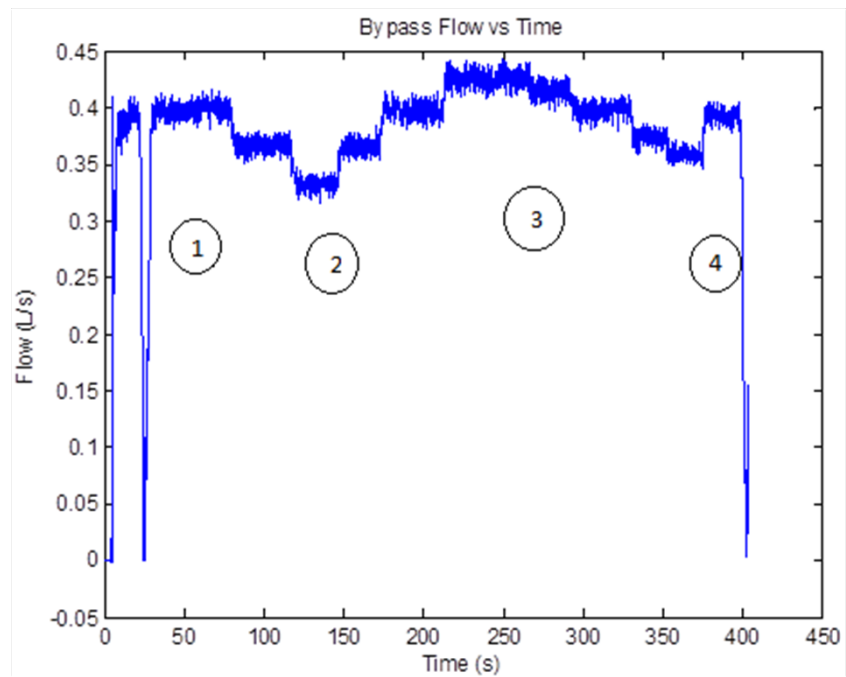


Figure 5.3: Bypass flow rate throughout experiment

Region 1:

This region involves initial start up of the pump at 55 Hz, and also removing air bubbles from the loop. The bypass valve was closed to remove air bubbles in the loop. During this time there was an increase in the pressure but the motor current goes down and as expected the bypass flow goes to 0. Pressure increases to nearly 14 psig and current goes down to 1.45Amps. After the air bubbles are removed the bypass valve is opened completely and the flow increases to 0.4 L/s.

Region 2:

In this region the pump speed is first decreased to 45 Hz, and then increased to 60 Hz in increments of 5 Hz to see its effect on the current and pressure. The motor current decreases to 1.4 Amps at 45 Hz from 2 Amps at 60 Hz, whereas the pressure goes as low as 7.5 psig at 45 Hz and reaches its maximum value of 15 psig at 60 Hz. Water flow rate decreases as expected to 0.33L/s and then increases back to 0.45 L/s at 60 Hz.

Region 3:

This region involves reducing the speed in steps to 5 Hz. The change in pressure here can be clearly related to the change in flow and the current. As seen, the pressure change of 15 psig to 8.5 psig is also reflected in the current which decreases to 1.5 Amps from 2 Amps. Bypass flow also decreases to 0.35 L/s. This region shows that even a small change in pressure is reflected in the current and the bypass flow.

Region 4:

This region deals with shutdown of the motor. First, the speed was increased to the speed at which the pump began operation, and was then shut down. As expected, all three process variables reach zero at the same time.

Correlation coefficients were calculated for the three process variables to check whether a relation could also be shown statistically. It is observed that the correlation coefficients also show very strong relationship of pressure with current and bypass flow. Current has the correlation of 0.90 whereas flow has the correlation 0.77 with the pressure in the loop.

As the pump speed was decreased, the current drawn decreased which also reduces the pressure and flow in the loop. It was also observed that if the water is not allowed to exit the loop by closing the bypass valve there is a decrease in the current and increase in the pressure in the loop. These two observations show that based on the changes in process variables and electrical signatures, the condition in the loop can be determined. In other words, the change in the current

drawn by the motor can determine whether the pressure and flow in the loop are changing due to a blockage or due to a change in the speed.

The nature of the transient and the time scale greatly affect the type of analysis that is used. In the experimental setup the sampling rate (1652 Hz) is much higher than the speed of the transient. Low frequency signal monitoring such as monitoring maximum and minimum signal values of the transient may yield valuable information about the signal.

5.3. Short-Time Fourier Transform (STFT)

The drawback of the Fourier transform can be partially overcome by using a finite data window. This is achieved by multiplying the signal by the window function, and then performing a Fourier transform to derive the time-frequency analysis. This was first adapted by Gabor (1946) using a Gaussian window function.

$$G_x(t, f) = \int_{-\infty}^{\infty} e^{-\pi(\tau-t)^2} e^{-j2\pi f\tau} x(\tau) d\tau \quad (5.1)$$

Where, x is the signal, f is the frequency, and τ is the transform parameter. It is similar to the Fourier transform, with a moving window. This transform works best if the segments are made smaller to make the signals look stationary in each segment. A note should also be made about the tradeoff between frequency and time resolution. A higher time resolution is achieved with a smaller window, but at a cost of having fewer data samples for STFT [79]. By decomposing a single signal into an overlapping series of Fourier transforms, the Gabor transform allows the evolution of frequencies over time to be more directly analyzed. The STFT has a fixed time-frequency resolution and may not provide information about the signal that may require a higher frequency and time resolution. In the Gabor transform, the frequency features are captured by a frequency modulation of the Gaussian window; however, the window size is kept constant.

In the experiments, the STFT was used in order to calculate frequency information from process signals. The motor frequency in the loop was adjusted in steps of 1Hz from 60Hz to 45Hz and then back to 55 Hz. The STFT was performed on the accelerometer signal to determine the frequencies of motor vibration (Figure 5.4).

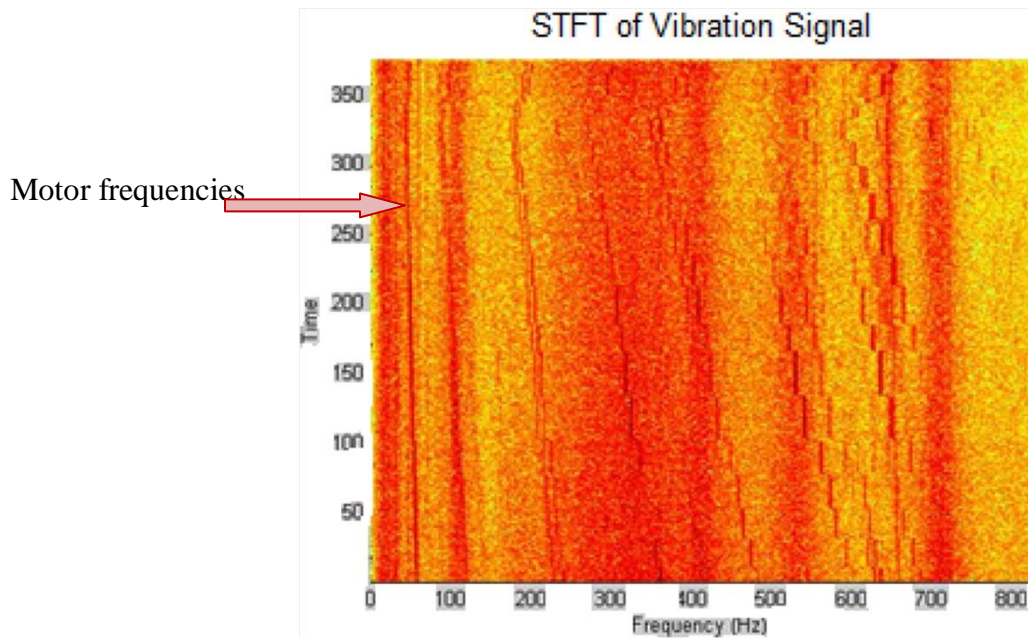


Figure 5.4: STFT of the motor vibration data

Frequency changes are clearly observed where the motor frequency and its harmonics show a decreasing trend due to the slowing rotation of the motor as adjusted with the frequency drive. The STFT of the pressure signal was also calculated (Figure 5.5).

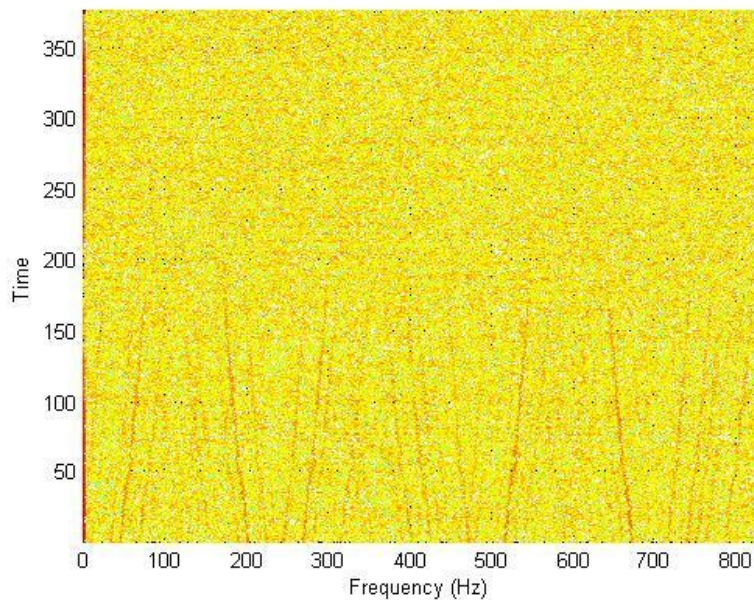


Figure 5.5: STFT of the pressure signal

The submersible pump used in the experimental loop has 4 vanes, resulting in a vane pass frequency of four times the line frequency. The dark red lines are prominent at the vane pass frequencies and its harmonics. In case of the pressure sensor, the same relation is found at the third harmonic of the vane pass frequency. Finally, the STFT of the motor current was calculated (Figure 5.6).

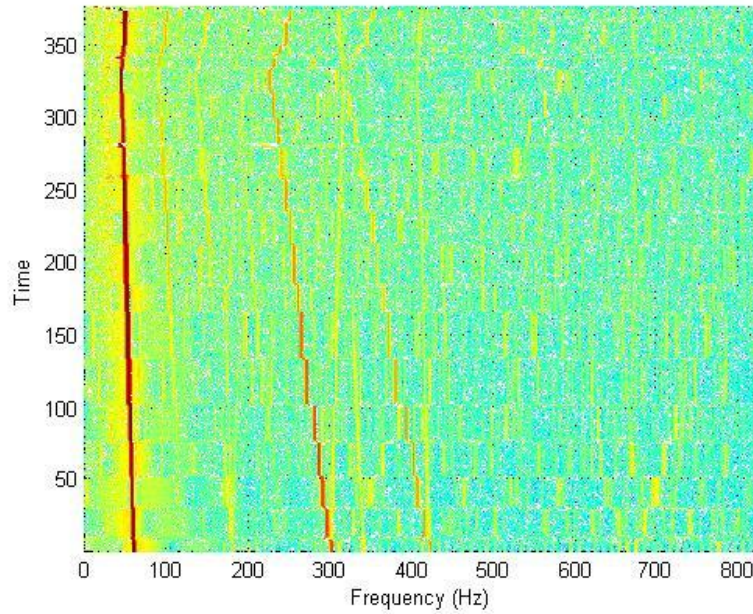


Figure 5.6: STFT of motor current signal

The STFT of one phase of the motor current shows a strong frequency relation at the supply voltage frequency as expected. As the pump frequency is changed, the same change is observed in the current characteristics. The motor current and vibration signals have a close relationship when it comes to relating the line frequency and the vane pass frequency.

5.4. Transient Data Analysis Using Hilbert-Huang Transform

The Hilbert-Huang Transform (HHT) is a method used to convert a signal into intrinsic mode functions (IMFs). Hilbert Transform (HT) is then applied to IMFs to obtain instantaneous frequency and amplitude information. Each IMF can be defined as, the number of extrema and the number of zero-crossings that must differ by no more than one, and at any point, the mean value of the envelope defined by the local maxima, and the local minima is zero. After calculating the IMFs from the signal, the instantaneous frequency can be found by applying the Hilbert transform [79].

$$X(t) = \text{Real} \sum_{j=1}^n a_j(t) e^{i \int \omega_j(t) dt} \quad (5.2)$$

Non-stationary signals are analyzed using this algorithm as it provides instantaneous frequency information and also gives better resolution than the other tradition time-frequency decompositions. The HHT provides multi-resolution in various frequency scales and takes the signal's frequency content and variation into consideration. HHT can not only provide the frequency information, but the information regarding power and amplitude as well. Though HHT can be computationally costly to calculate, the information it provides can be invaluable. Analytic amplitude of the HHT is simply the absolute value of each IMF from the HHT, and the instantaneous frequency is calculated by looking at the first derivative of the phase angle for each IMF [79].

The HHT is a mathematical method to successively derive empirical, non-parametric sinusoidal modes of a function, which are based on the outer envelope of each progressive layer of that function [27]. In an attempt to analyze the current of a motor with the HHT, an empirical mode extraction algorithm taken from the first steps of the HHT was implemented on this data. A full decomposition of data yielded over eleven IMFs for a given current or pressure signature. Depending on the form of the data under analysis, a given decomposition could lead to differing numbers of IMFs, and usually this difference will not be more than one [79].

When the Hilbert-Huang transform is applied to individual signals from the loop, it is found that the results are similar to those obtained using the STFT. Only first four modes are shown in the figures as they have the dominant information about the frequencies. As shown in the Figure 5.7 the first and second modes of the IMF show dominant frequency close to the first harmonic frequency of the vane pass frequency whereas the third mode shows the vane pass frequency.

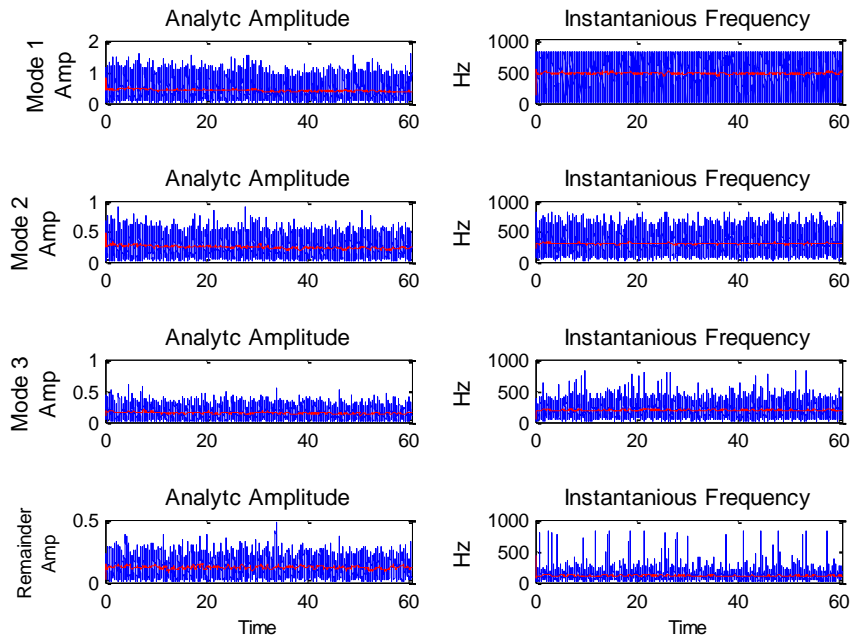


Figure 5.7: HHT of Vibration Signal (first four modes)

The third mode from the pressure signal (Figure 5.8) and the vibration data display appear to have similar frequency characteristic, which is near the vane pass frequency of the pump being used. This observation matches with the results from the STFT.

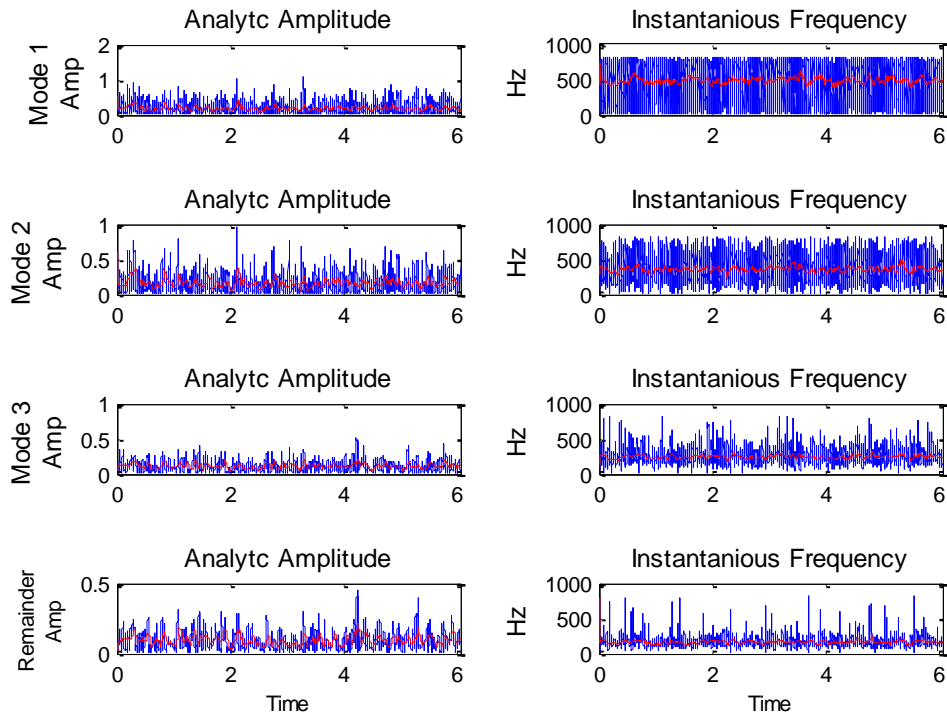


Figure 5.8: HHT for Pressure signal (First four modes)

Figure 5.9 shows the HHT performed on the motor current signal. For this signal, the first two modes are the most significant ones, which have features near the line frequency at which the motor was operated, and the third and fourth modes do not contain much information. These results can be considered as typical of the relationship in the frequency domain for pressure and vibration signals.

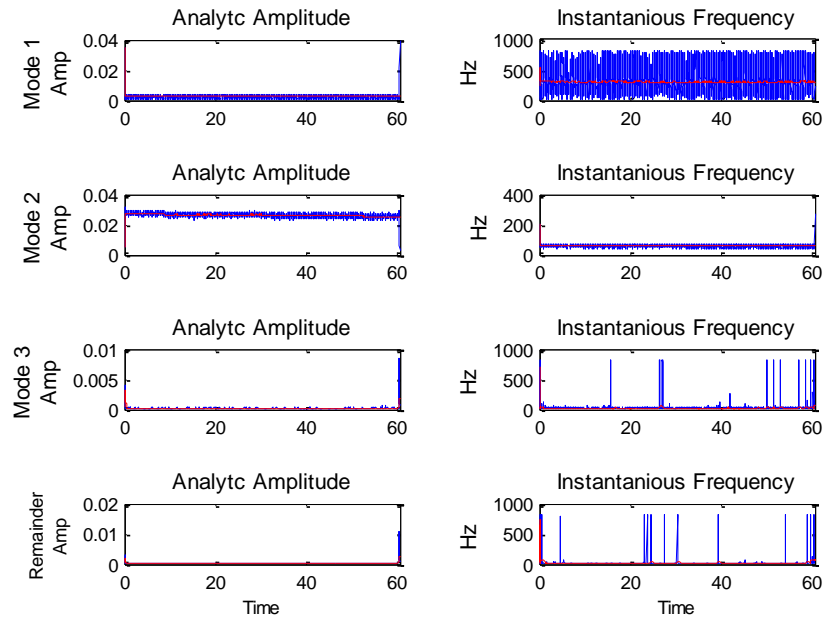


Figure 5.9: HHT for current (first four modes).

These experiments demonstrate the applicability of time-frequency analysis of transient data in extracting information during equipment operation. Examples of transient data include pump start-up, shut-down, load changes, and external disturbances.

6. CONDITION MONITORING BY USING STOCHASTIC TIME SERIES MODELS

6.1. Discrete-Time Stochastic Modeling of Wide-Band Signals

Random signals generated by finite bandwidth systems can be characterized by discrete-time auto-regression models and used to estimate the spectral-domain and time-domain signatures. The models generally fall under the category of auto-regression moving average (ARMA) models. The auto-regression (AR) models are often used to characterize the dependency of band-limited signals. An example of the univariate AR model is given in Equation (6.1)

$$y(t) = \sum_{i=1}^n a_i y(t-i) + v(t) \quad (6.1)$$

In Equation (6.1), $\{y(t)\}$ is a sequence of discrete signal or measurement; $v(t)$ is assumed to be a wide-band noise (approximating white noise) with zero mean and finite variance σ_v^2 , and $\{a_1, a_2, \dots, a_n\}$ are time-invariant parameters. There are situations where AR models with changing parameters can be developed in order to characterize non-stationary or transient data. An example is the case of pump start-up or coast-down sequence.

The AR parameters are estimated using either a one-step prediction error minimization or by solving the Yule-Walker equations [77] for the parameter set $\{a_1, a_2, \dots, a_n\}$. The Yule-Walker equations are derived directly from the AR model, and for a model of order, n , have the form

$$R_{yy}(k) = \sum_{i=1}^n a_{ni} R_{yy}(k-i), k = 1, 2, 3, \dots, n \quad (6.2)$$

In Equation (6.2), $R_{yy}(k)$ is the autocorrelation function of $y(t)$ at time lag k (or $k\Delta t$) where Δt is the data sampling interval (second). The normalized autocorrelation of $x(t)$ at lag k is computed for a data block of sample size N as

$$R(k) = \frac{\sum_{i=1}^{N-k} \{y(i) - y_{mean}\} \{y(i+k) - y_{mean}\}}{\sum_{i=1}^N \{y(i) - y_{mean}\}^2} \quad (6.3)$$

Where y_{mean} is the mean value of the signal $y(t)$ for the given block of data.

The sampling frequency ($f_s = 1/\Delta t$, Hz) depends on the bandwidth of the signal being processed. The Yule-Walker equations can be solved recursively, for successively higher order models. That is, the parameters of AR(n+1) model are estimated from the parameters of AR(n) model and an additional autocorrelation function. This facilitates fast computation of AR models up to a certain maximum order, and the determination of optimal model order, n^* . The optimal order corresponds to minimum model prediction error. The details of the recursive parameter estimation algorithm are given in Upadhyaya *et al.* [119]. A model-recursive algorithm has been developed and implemented in MATLAB. The recursive algorithm provides accurate and fast computation of successively higher order AR models. Once an optimal AR model is determined, the model may be used to estimate frequency spectrum of the signal. The AR parameters can be used to determine the power spectrum of the signal $y(t)$ using the relationship

$$S_{yy}(f) = |H(f)|^2 \cdot S_{vv}(f) \quad (6.4)$$

The estimate of the power spectrum of $y(t)$ is given by

$$S_{yy}(f) = \frac{\sigma_v^2 \Delta t}{\left| 1 - \sum_{k=1}^n \hat{a}_k e^{-j 2\pi f k \Delta t} \right|^2} \quad (6.5)$$

The frequency f (Hz) has a maximum value of $f_{Nyquist} = \frac{1}{2\Delta t}$ Hz.

Since the model is fitted to a given data length, it provides the best estimate of the frequency spectrum, especially when the data size is limited. If the signal is quasi-stationary, the spectral estimates may be computed for short data lengths by moving a data window, thus providing a quick estimate of the spectrum during slow transients. In reactor applications, time

domain signatures are often used to estimate sensor time constant, ramp delay time, decay ratio from the impulse response function, and stability margin. The frequency spectrum estimate contains information about the signal bandwidth, changes in the frequency peaks in the signal, and other features. The AR model can also be used to detect possible faults by using a baseline AR model to estimate the prediction error during the test phase. Alternately, comparison of frequency or time domain signatures from the baseline model and the test model would also provide information about incipient anomalies [77].

The optimal model in the given class of autoregressive models is decided by plotting the Final Prediction Error (FPE) as a function of the model order, n . The error is calculated using

$$\underline{FPE = E \{y_N - \hat{y}_N\}^2} \quad (6.6)$$

where \hat{y}_N is the estimated value of y_N . The FPE is given by

$$(FPE)_n = \frac{N+n}{N-n} \sigma_v^2 \quad (6.7)$$

where σ_v^2 is variance of the prediction error, v . The noise variance is estimated as

$$\hat{\sigma}_v^2 = \frac{1}{N} \sum_{k=1}^N \hat{v}_k^2 \quad (6.8)$$

where the residual sequence is estimated by

$$\hat{v}_k = y_k - \sum_{i=1}^n \hat{a}_i y_{k-i}, k = 1, 2, 3, \dots, N \quad (6.9)$$

The optimal model corresponds to the value where the error is a minimum, or when the error goes to a low value without significant decrease with increasing model order [77]. Other minimization criteria, such as the Akaike Information Criterion (AIC), and the total prediction error [77], should also be computed and compared to determine the best model fit. The AIC is given by

$$AIC = N \ln(\sigma_v^2) + 2n \quad (6.10)$$

6.2. Data Pre-processing Using Wavelet Transform

In many applications it may be necessary to pre-process the digitized data to delete either low-frequency or high-frequency components, or both. This could be achieved by the implementation of digital filters. Digital filter operation tends to distort the signal near the cut-off frequencies. A more effective technique is to employ the wavelet transform that successively divides the signal into bands of desired bandwidth.

Wavelet transform is a time-frequency analysis tool which interprets the signal as the sum of scaled and shifted wavelets. It was first introduced with Continuous Wavelet Transform (CWT) using continuous scaling (a) and shifting (b) parameters. The CWT is defined by [102] Equation (6.11), where $f(t)$ is a square integrable function, $\psi(t)$ is a mother wavelet and $\psi(a, b) = \psi\left(\frac{t-b}{a}\right)$.

$$W(a, b) = \int_{-\infty}^{+\infty} f(t) \frac{1}{\sqrt{a}} \psi^*(a, b) \quad (6.11)$$

Then Wavelet Transform is interpreted again on dyadic scale by discretizing scaling and shifting parameters only, and is often referred to as the Discrete Wavelet Transform (DWT). The discretization is performed as $a = 2^k$ and $b = 2^k m$, where k and m are integers. The expression in Equation (6.12) is helpful to understand this concept.

$$f(t) = \sum_{k=-\infty}^{\infty} \sum_{l=-\infty}^{\infty} d(k, m) 2^{-\frac{k}{2}} \psi(2^{-k}t - m) \quad (6.12)$$

Here the terms $d(k, m)$ are related to values of CWT of $f(t)$ at $a = 2^k$ and $b = 2^k m$. With this, it is easy to see that the wavelet coefficients for an orthonormal DWT are samples of CWT on a dyadic grid.

At this point the scaling function $\phi(t)$ definition is introduced related to the mother wavelet to simplify the multi-scale (multi-resolution) representation [103, 104].

$$\psi(t) = \sum d(n)\phi(2t - n) \quad (6.13)$$

Then the main goal becomes expressing the $f(t)$ function by the basic sum of scaling and wavelet functions, where d_j 's are the detail coefficients at different scale and c_0 is the approximation coefficient at the last scale.

$$f(t) = \sum_k c_j(k)\phi(t - k) + \sum_k \sum_{j=0}^{J-1} d_j(k)2^{j/2}\psi(2^j t - k) \quad (6.14)$$

This process is represented by convolution of the expansion coefficients (c_j and d_j) with the wavelet function and the scaling function followed by decimation (down-sampling by 2). And the wavelet coefficients, which are seen in Equation (6.14), can be represented by high-pass filters whereas scaling coefficients can be represented by low pass filters [103]. Relevant schematic can be seen in Figure 6.1.

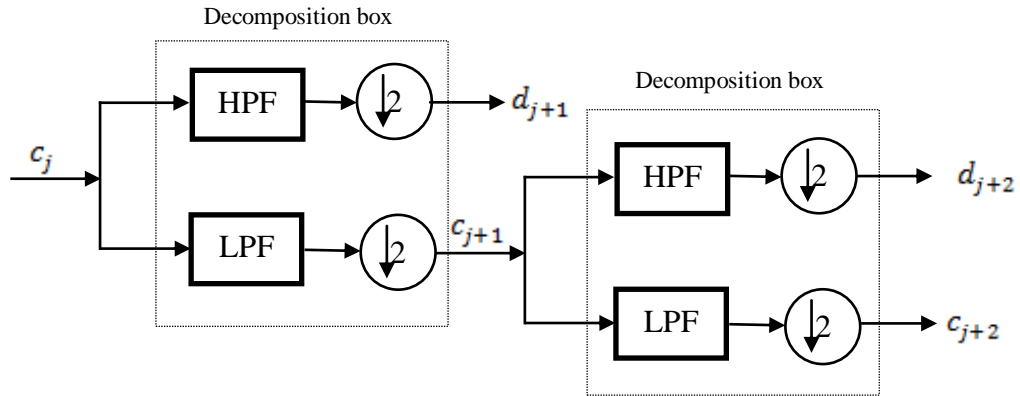


Figure 6.1: Multi-Resolution Wavelet Decomposition.

In order to get the approximated version A_k and detailed version D_k of the original signal $f(t)$ the expansion coefficients should be reconstructed.

It should be noted that each approximation and detail contain different frequency band information.

6.3. Analysis of Operational Data from a PWR

To further confirm the authentication of the functions, they were tested on a data received from Analysis and Measurement Services Corporation (AMS). The data set is from a 4-loop pressurized water reactor (PWR) plant and consists of transmitter data sampled from 9 sensors while the plant was operating. AMS used the data to determine the dynamic response of the various pressure transmitters [109]. The data for each sensor consists of 208,400 samples which are sampled at 200 Hz. Table 6.1 shows the transmitter identification and where it is used.

Table 6.1: List of sensors from an operating PWR

Sensor No.	Sensor Name	Service
1	FEED FLOW	FEEDWATER FLOW
2	PZR LVL	PRESSURIZER LEVEL
3	PZR PSR	PRESSURIZER PRESSURE
4	STM FLOW	STEAM FLOW
5	SG LVL NR1	STEAM GENERATOR LEVEL NARROW RANGE
6	SG LVL NR2	STEAM GENERATOR LEVEL NARROW RANGE
7	SG LVL WR1	STEAM GENERATOR LEVEL WIDE RANGE
8	STM PSR	STEAM PRESSURE
9	RCS PSR	RCS PRESSURE

The data from the sensors measuring the feed water flow and the pressurizer pressure are used to process the measurements. The results are compared with the those observed by AMS.

The functions explained in Section 6.1 are used to study the signals and their characteristics. The recorded feed water signal is shown in Figure 6.2. The output of the pressure sensor is in volts.

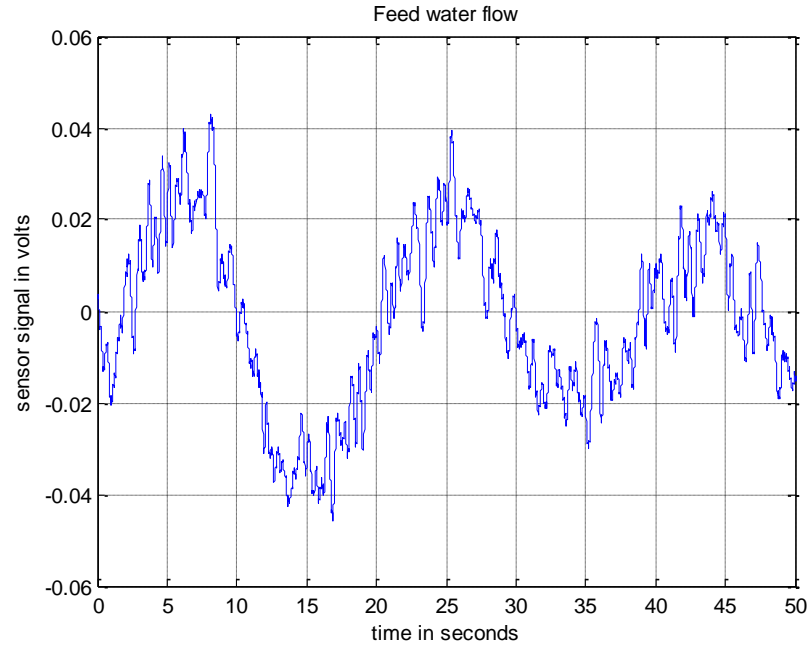


Figure 6.2: Feed water flow sensor signal

The AR model order needs to be estimated in order to choose the best AR fit. The Final prediction error (FPE) (Figure 6.3) and the Akaike Information Criterion (AIC) (Figure 6.4) were used to determine the optimal model order for the feed water flow signal.

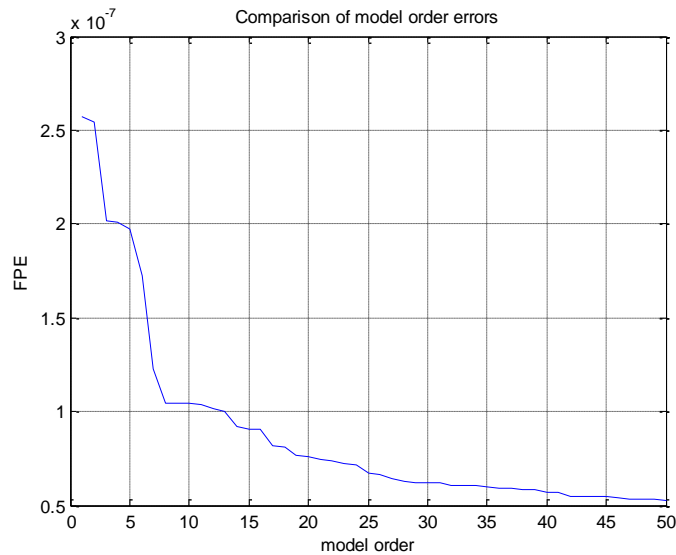


Figure 6.3: FPE criterion for different model orders

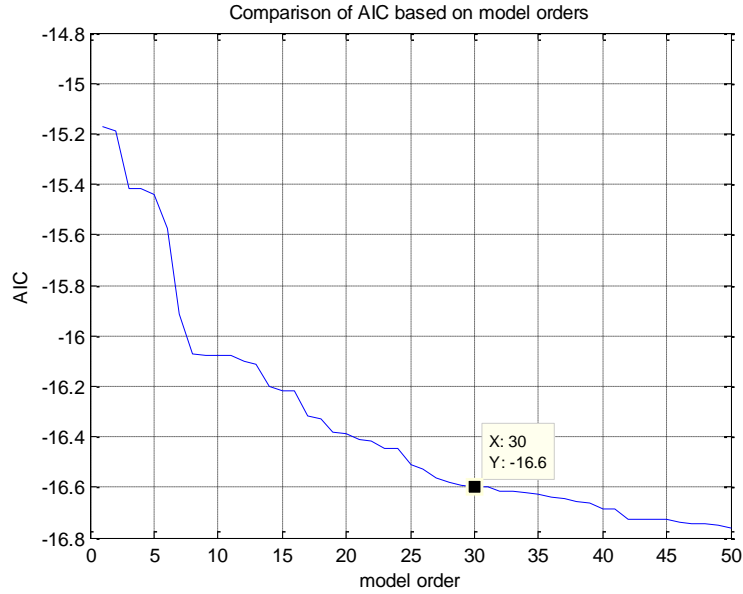


Figure 6.4: Akaike information criterion as a function of the model order

The inspection of AIC and FPE shows that they attain the lowest value at model order 30. Both the parameter values reach an almost constant value after order 30. After an optimal order is estimated the power spectrum is generated using the model parameters.

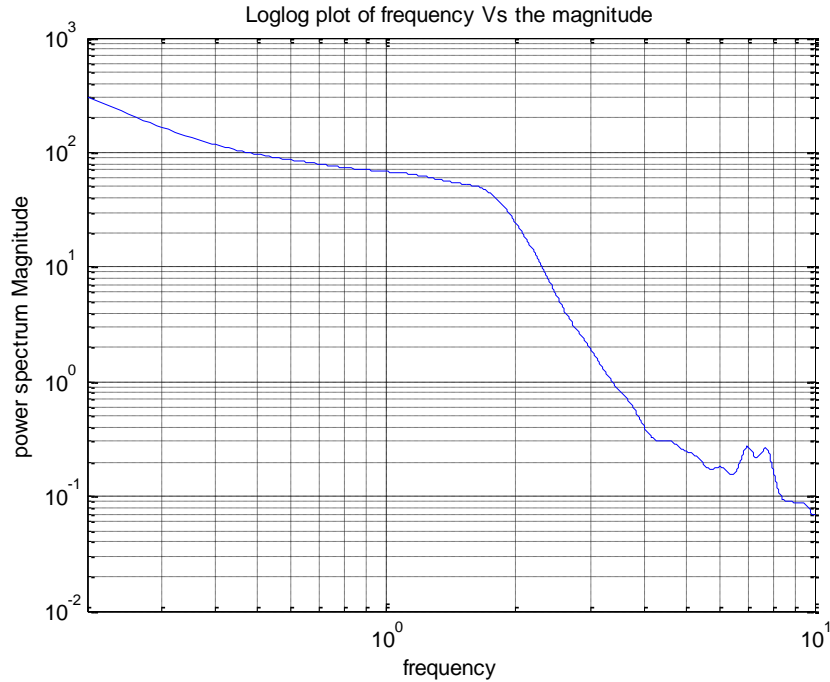


Figure 6.5: Power spectrum of the Feed water flow sensor

Power spectrum (Figure 6.5) of the feed water flow signal shows that the break frequency of the sensor is equal to 1.87 Hz. This is approximately equal to the break frequency that was estimated

by AMS and was $\sim 1.5\text{Hz}$. Thus using the real plant data the applicability of the AR model functions were validated.

Wavelet transform can be used to remove the frequencies that are not required for study or are not important. Basically, the data can be used to perform band-pass filter operations. This is useful in studying the characteristics of a signal in a particular frequency range. This operation is performed on the data set to remove the frequencies lower than 0.2, which can be seen in Figure 6.6. The filtered signal is shown in red, and the unfiltered signal is shown in blue.

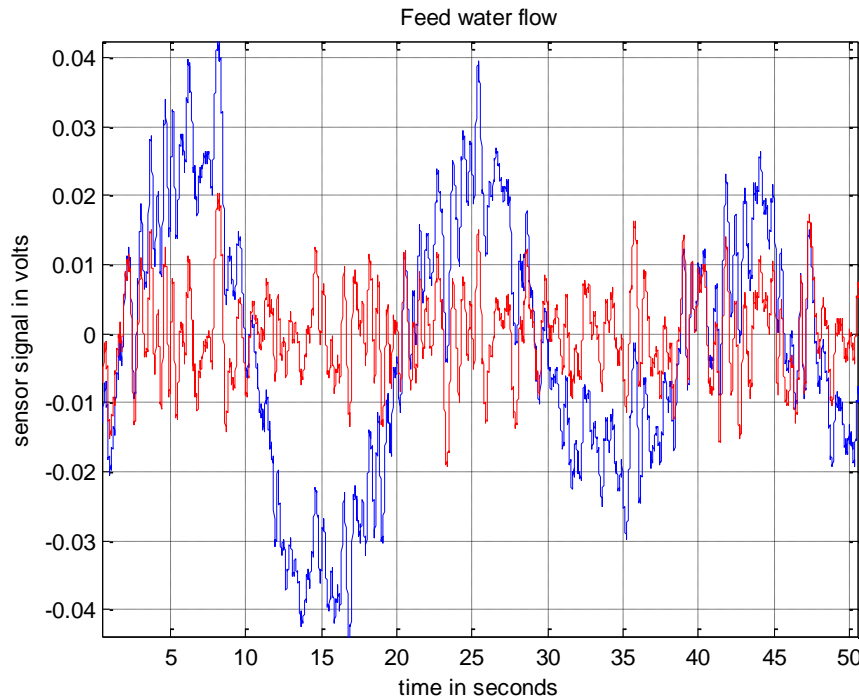


Figure 6.6: Data before and after filtering

The power spectral density of the filtered data (Figure 6.7) is cleaner than the previous attempt. The break frequency is also closer to the one estimated by AMS. Break frequency is calculated by observing the intersection of the high frequency and the low frequency asymptotes. The break frequency is calculated to be at 1.46 Hz.

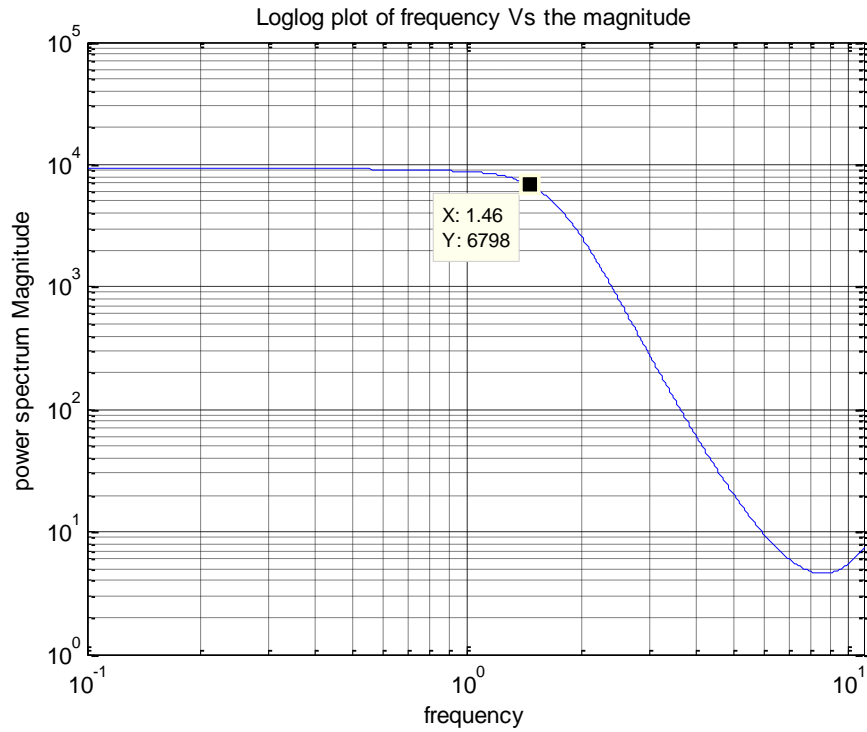


Figure 6.7: Power spectral density plot using the filtered data

The pressurizer signal is then used to verify the functions. Figure 6.8 shows the power spectrum of the raw signal. The block size used for generating the spectrum is 4096 which gives a frequency resolution of 0.05. The break frequency is observed at 0.48Hz.

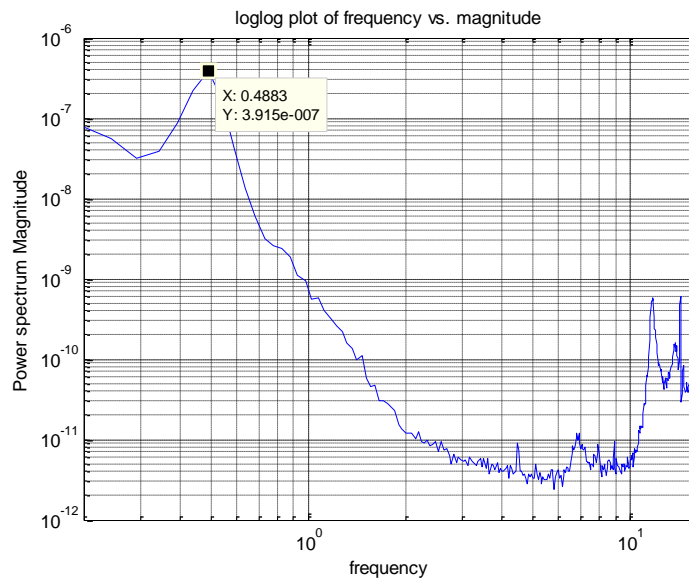


Figure 6.8: Power spectral density of the unfiltered pressurizer pressure data

The spectrum is then generated using the auto-regression model of the pressurizer pressure signal. Figure 6.9 shows the spectrum generated which is more smoother after the frequencies greater than 6.25 and less than 0.2 Hz are removed from the signal. This break frequency calculated is still around the 0.47 Hz, which is close to the one that was calculated earlier.

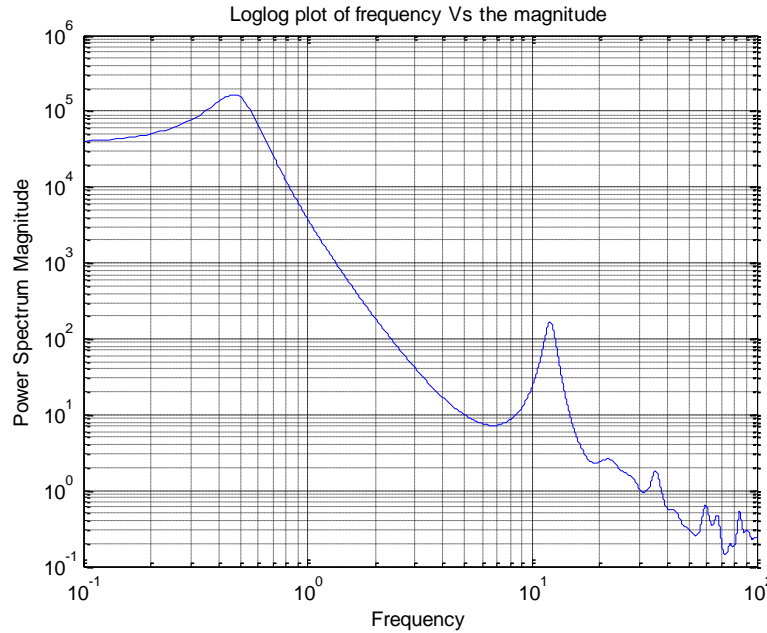


Figure 6.9: Power spectral density of the filtered pressurizer pressure data

These results verify the functions in the toolbox. There will be more functions that will be added in the toolbox.

6.4. Estimation of Response Time of Process Transmitters

The response characteristic of a process sensor is represented by its 'time constant'. The time constant of a sensor or a device is defined (for a first order dynamic approximation) as the time it takes for the step response of the sensor to reach 63.2% of its steady-state value. In general, this definition of the time constant is adapted, even if the device response is not described by a pure first order dynamics. The time constant indicates how fast the sensor responds for a change in the process variable being measured. Figure 6.10a is a plot of the step response of a first order system with a time constant of 1 sec. The figure shows the definition of the time constant.

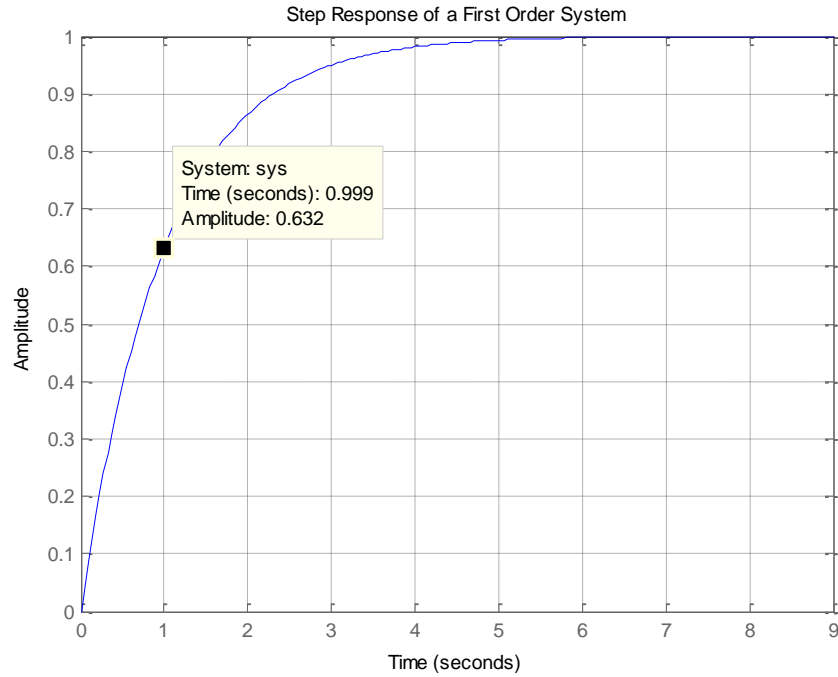


Figure 6.10a: Illustration of the step response of a first-order system with a time constant of 1 sec corresponding to 63.2% of its steady-state value of 1.

The model impulse response may be calculated using the AR processes by recursively calculating the y_k using the equation

$$y_k^I = \sum_{i=1}^n a_i \cdot y_{k-i}^I, y_0 = \text{constant}, y_{-1} = 0 \quad (6.15)$$

For real cases y_0 is taken 0, as the impulse response has the value 0 for the systems with more than one pole. Integrating the impulse response gives the step response.

$$y_s(t) = \int_0^t y_I(\tau) d\tau \quad (6.16)$$

Figure 6.10b shows that the feed water flow signal takes almost 5 seconds before reaching the steady state value. This is due to the involvement of the lower frequencies in the signal. Response time is calculated by finding out when the sensor reaches the 63.2% of the steady state value. The response time for this sensor was calculated as 0.95 sec.

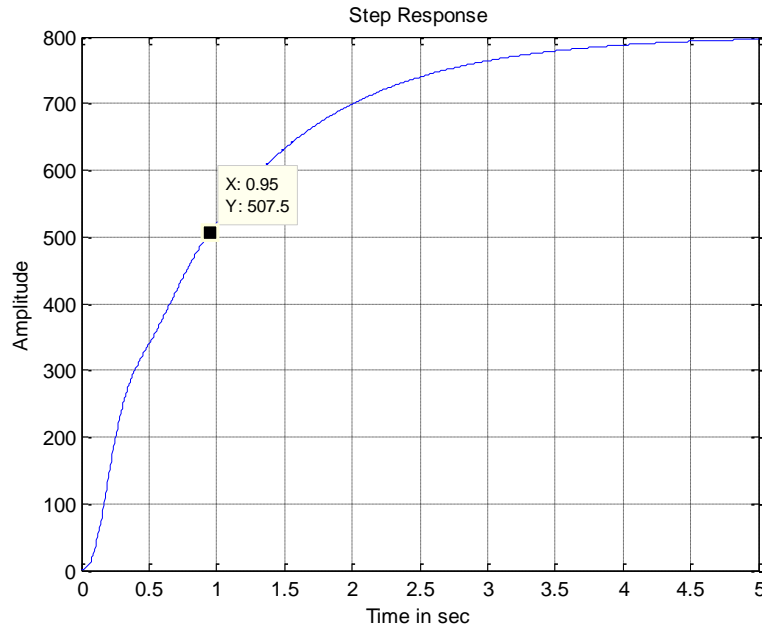


Figure 6.10b: Step response of unfiltered feed water flow signal

The filtered data are then used to estimate the response time of the PWR plant sensors (Figure 6.11). It was found that eliminating the lower frequency components filters out process related information from the sensor data.

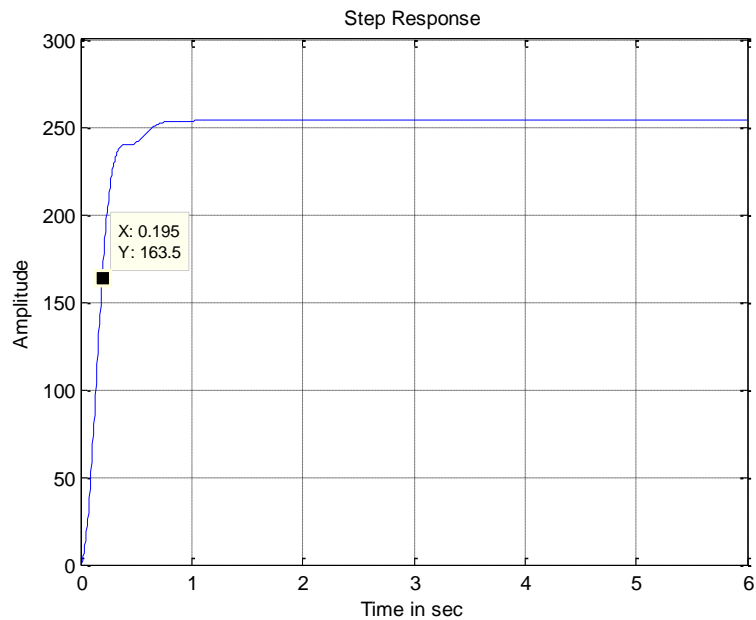


Figure 6.11: Step response of filtered feed water flow signal

The response time is calculated to be approximately equal to 0.20 sec. This shows that the sensor was earlier showing a higher response time because of the lower frequency that was associated with the data.

One of the advantage of AR modeling technique is that even small data samples can be used to estimate the characteristics of the sensors. This property was tested by using just 2500 data points from the original data. This data was also band passed between the same frequencies. Figure 6.12 shows that the response time calculated is still close to 0.2, even though the data acquisition time is only 12.5 seconds.

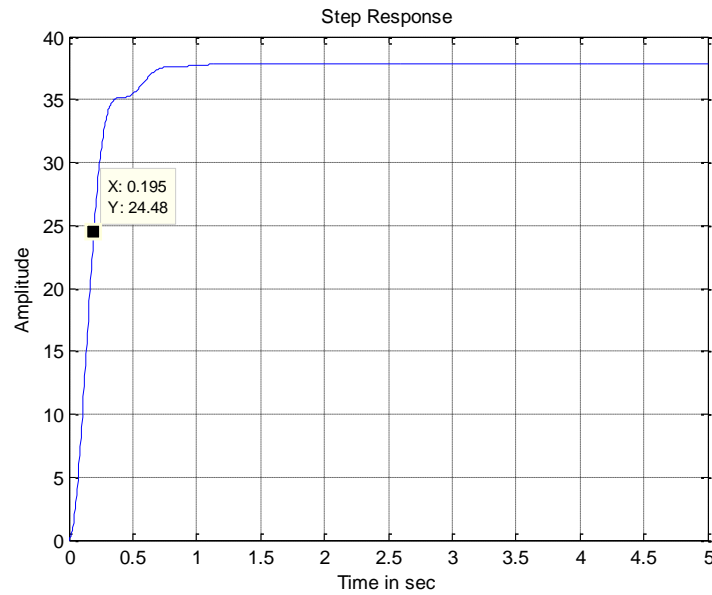


Figure 6.12: Step response of short filtered data

This feature can be used in the case of a signal that is changing on the course of time. Small sets of data can be taken and the responses can be calculated to verify the sensors performance.

Using a similar procedure the response times of all the sensors were calculated. Table 6.2 lists the estimated time constants and provides a comparison of estimates with original data and with pre-processed (band-pass filtered) data.

Table 6.2: Estimated time constants of pressure transmitters

<i>Sensor Name</i>	<i>Response time (Without filtering)</i>	<i>Response time (Filtered)</i>
Feed Flow	0.9	0.20
Pressurizer level	0.29	0.24
Pressurizer pressure	0.72	0.57
Steam Flow	0.15	0.15
Steam Generator Level Narrow Range1	0.73	0.62
Steam Generator Level Narrow Range2	0.4	0.34
Steam Generator Level Wide Range1	0.2	0.2
Steam Pressure	0.48	0.06
RCS Pressure	0.33	0.27

This comparison clearly shows that the response time after the data is filtered clearly gives a better estimate of the response time of the sensors as the values are closer to the expected value of the response time of the pressure sensors. The two redundant steam generator narrow range sensors show that the first sensor is comparatively slower than the second one. The sluggishness of the sensor was due to the fault that was introduced in the sensing line. This example illustrates that auto-regression modeling of wide-band data can provide information about possible faults in the sensors.

7. DATA-BASED MODELING OF PROCESS AND ELECTRICAL MEASUREMENTS IN THE FLOW CONTROL LOOP

7.1. Introduction

Data-based modeling could be an attractive proposition for monitoring components and sensors in SMRs due to the reduced space available for sensor placement. The integral layout presents many challenges with sensor type and placement. Sensor redundancy might also be an issue as there might simply not be enough space for the typical number of sensors in a large reactor. Therefore, it is important to consider a data-based modeling approach to ensure the safe operation of components housed within the reactor vessel. The development empirical models could help provide sensor redundancy and ensure sensors are operating within their acceptable ranges and are not drifting. For these reasons, a data-based modeling technique was considered in this project to determine if it was capable of identifying user-generated faults in the experimental flow control loop.

This section includes the theory of auto-associative kernel regression (AAKR) modeling and its implementation to the experimental flow control loop. The tools for building an AAKR model and for performing fault detection using the Sequential Probability Ratio Test (SPRT) are described in detail and are included in the MATLAB Process and Equipment Monitoring toolbox. The entire process of building an AAKR model and how it interfaces with the fault detection algorithm is described. Several experiments were performed with user-generated faults to demonstrate the ability of the model to identify when faulty conditions were experienced.

7.2. Tools for Empirical Model Development

This section details some of the tools used for building data-based models using measurements taken from the experimental flow control loop.

7.2.1 Auto-Associative Kernel Regression (AAKR)

AAKR is a non-parametric technique wherein historical, fault-free data are used to build a local model. Each time a new set of predictions is made for new queries to the model, a new model is built using the historical data. The non-parametric model builds a temporary parametric model using a weighted sum of historical values to form predictions [115, 116].

In order to build an AAKR model, the first step is selecting the data to be a part of the model training data set. Only historical data, that are similar to the query data set, as determined by a distance function, are used in the model training data set. The most common distance function used is the Euclidean distance or L^2 -norm and is given by Equation (7.1) where X_i is the value of the historical data and x is the value of the query data:

$$d_i(X_i, x) = \sqrt{(X_i - x)^2} \quad (7.1)$$

The AAKR model uses a weighted average of similar historical data to perform predictions. Once the training data set has been selected, each observation is assigned a weight based on its similarity to the query data. Similar observations receive a higher weight while less similar observations receive a smaller weight. The weight function is determined by using the Gaussian Kernel given by the following formula, where h is the kernel bandwidth and d is the Euclidian distance between the historical and query observations:

$$K_h(d) = \frac{1}{\sqrt{2\pi} h} e^{\frac{-d^2}{2h^2}} \quad (7.2)$$

The kernel's bandwidth determines the relationship between distance and the weighting factor. A small bandwidth only generates high weights when the distance is close to zero while a higher bandwidth generates low weights for larger distances. The optimal bandwidth is selected by testing the model with several different bandwidths and minimizing the uncertainty [116].

When training an AAKR model, it is important to select a normal operation data set that is free of faults and covers the full range of future expected operating conditions. The historical data set should be de-noised with a median filter and standardized to remove the mean values and give the data unit variance so that each signal has an equal chance to contribute to the model. The historical data should also be split up into training, testing, and validation sets where the training set should comprise roughly half the points and the remaining points split between the testing and validation sets. The training set is used to train the AAKR model while the testing set is used to optimize the model. Finally, the validation set is used to characterize the uncertainty of the AAKR model's predictions. The testing, validation, and faulty data sets should all be standardized with the same mean and standard deviation as the training data set.

Once the model has been properly trained and optimized, a faulty data set is used as a query to the AAKR model and the similarities between the training data and faulty data are calculated using a Gaussian Kernel to assign weights to the query data. The model then makes predictions based on the query vector which are then used to compute the residuals between the AAKR predictions and the faulty data to see where any faults have occurred.

7.2.2 Sequential Probability Ratio Test (SPRT)

The Sequential Probability Ratio Test (SPRT) was the method chosen for fault detection in sensors and water level controllers for this research. The SPRT method detects changes in the residuals from model predictions and actual measurements such as standard deviation and mean value. SPRT assumes that residuals generated from measurement noise should be normally distributed (Gaussian distribution) with a mean of zero, and that the changes in the residuals can be due to a fault in the system. SPRT analyzes a sequence of residuals and calculates the log likelihood ratio to determine if the residuals are normal or faulted and uses the following formula to check for faulty data where m_i is the mean, S_m is the residual at time m , and σ^2 is the variance:

$$\lambda_m = \lambda_{m-1} + \frac{m_i}{\sigma^2} * (S_m - \frac{m_i}{2}) \quad (7.3)$$

If λ is within specified bounds, the residuals are determined to be from normal operational data. The statistical decision-making bounds are calculated by specifying a false alarm rate, α , and a missed alarm rate, β .

$$A = \ln\left(\frac{\beta}{1-\alpha}\right), \quad B = \ln\left(\frac{1-\beta}{\alpha}\right) \quad (7.4)$$

If λ is less than A , the residuals are assumed to be from measurement noise and are normal, while if λ is greater than B , the residuals are assumed to be from a fault. If λ is between A and B , the test is inconclusive. Instead of computing a new mean and variance at each new observation in the data, SPRT monitors the residuals in a sequential fashion where a group of residuals are used to generate a log likelihood ratio based on the statistical properties of a new sequence of residuals when compared to the previous sequence. Essentially, SPRT compares the

statistical properties of a new sequence of residuals with the previous sequence to identify any changes that might indicate a fault [116].

7.2.3 Process and Equipment Monitoring (PEM) Toolbox

The Process and Equipment Monitoring (PEM) Toolbox, a set of MATLAB based tools previously developed at the University of Tennessee, was used in this research to support the development of an AAKR model with SPRT for fault detection [118]. The toolbox includes many functions used in this research to pre-process data, build auto associative kernel regression models, and perform fault detection.

7.3. AAKR Modeling without Water Level Control

Two auto-associative kernel regression models were developed for fault detection purposes without the use of the water level controller. The two faults included a bypass flow rate fault and a motor frequency fault.

7.3.1 Bypass Flow Rate Fault

A set of normal operational data was generated using the flow control loop to determine if an AAKR model would be capable of detecting a fault in the bypass flow. The normal data were taken by adjusting the frequency in increments of 0.5 Hz from 58 Hz to 60 Hz (Figure 7.1). The bypass valve was kept open at a half turn throughout the entire normal data set. The predictor variables used in this AAKR model included the motor current, bypass flow rate, pressure, and inlet flow rate.

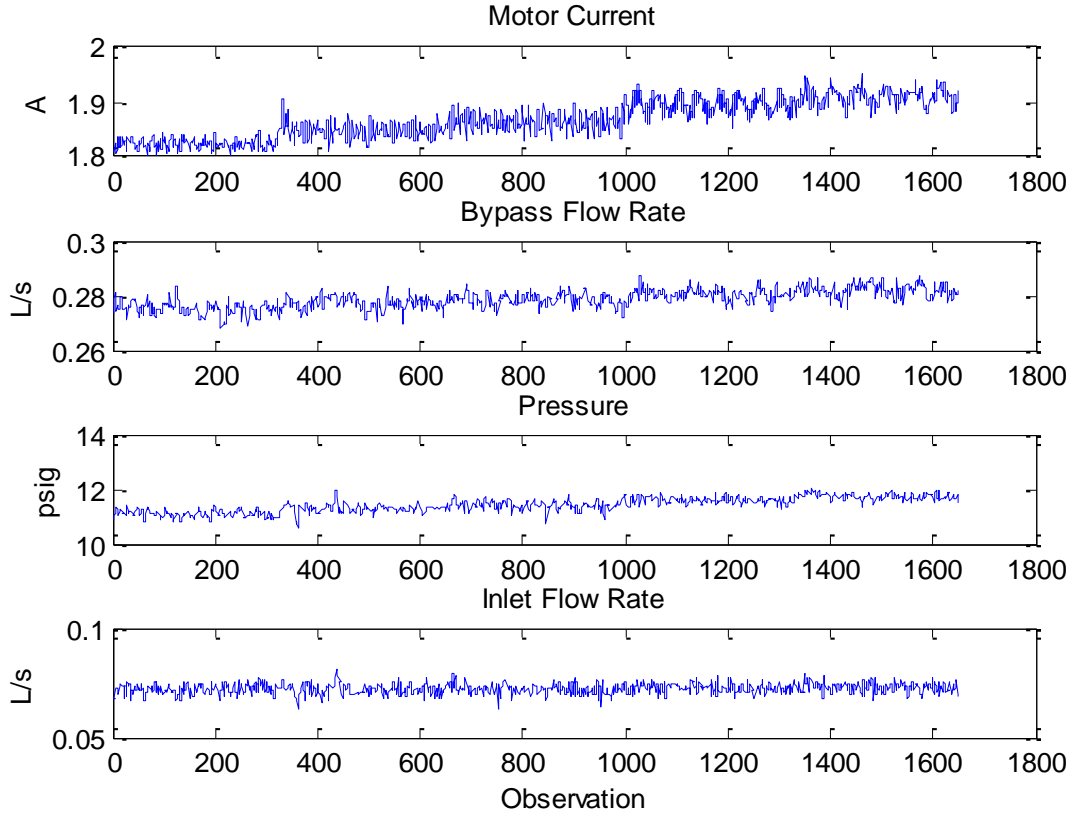


Figure 7.1: Plots of predictor variable under normal operation

The ability of the AAKR model to predict the sensors outputs was determined by comparing the predicted values of the AAKR model with the testing data set of actual measured sensor values. In order to assess the accuracy of the predictions, the mean absolute percent error (MAPE) was evaluated for each sensor. The MAPE measures the accuracy of a set of predictions to the measured values of the sensors and was calculated using Equation (7.5).

$$MAPE = \frac{1}{N} \sum_{i=1}^N \left| \frac{Actual(i) - Predicted(i)}{Actual(i)} \right| \quad (7.5)$$

Figures 7.2-7.5 show the results for the AAKR prediction versus the measured values, and Table 7.1 summarizes the MAPE for each predictor variable.

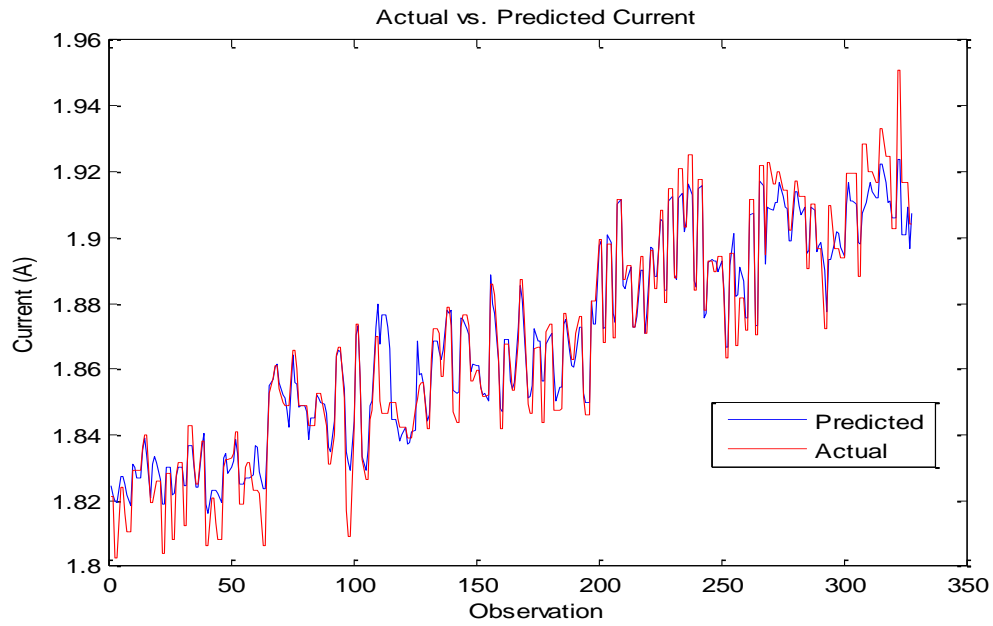


Figure 7.2: Measured vs. predicted motor current

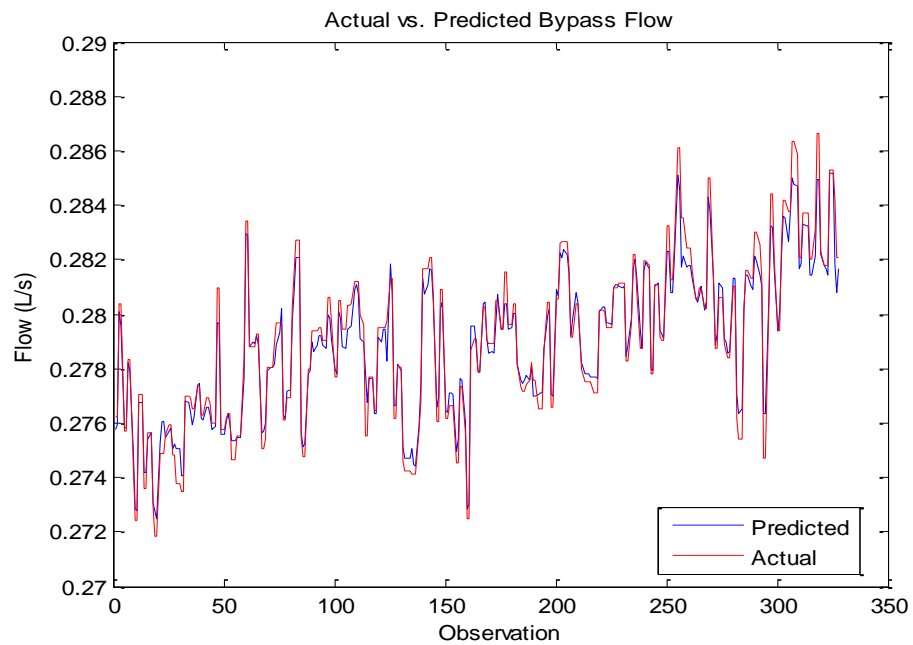


Figure 7.3: Measured vs. predicted values of bypass flow rate

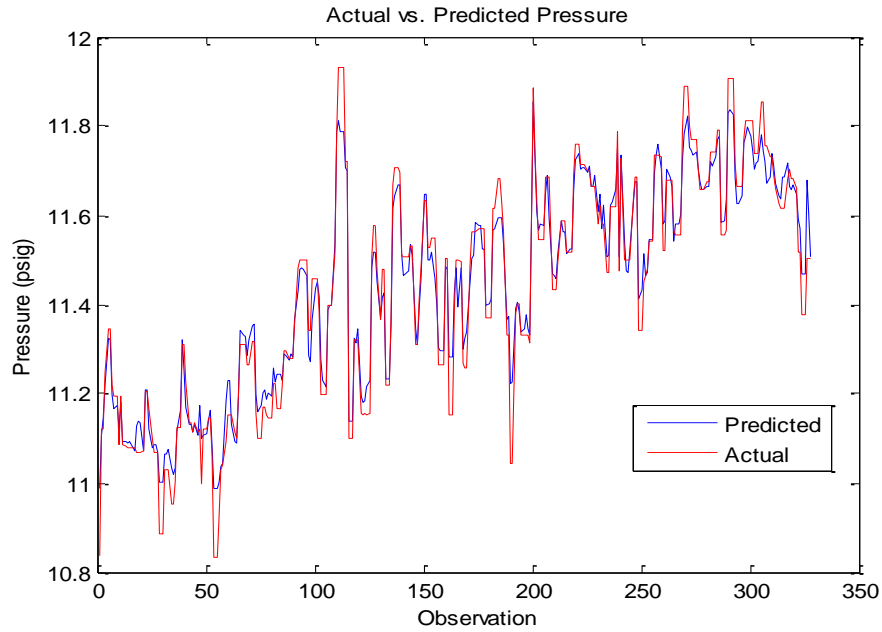


Figure 7.4: Measured vs. predicted values of loop pressure

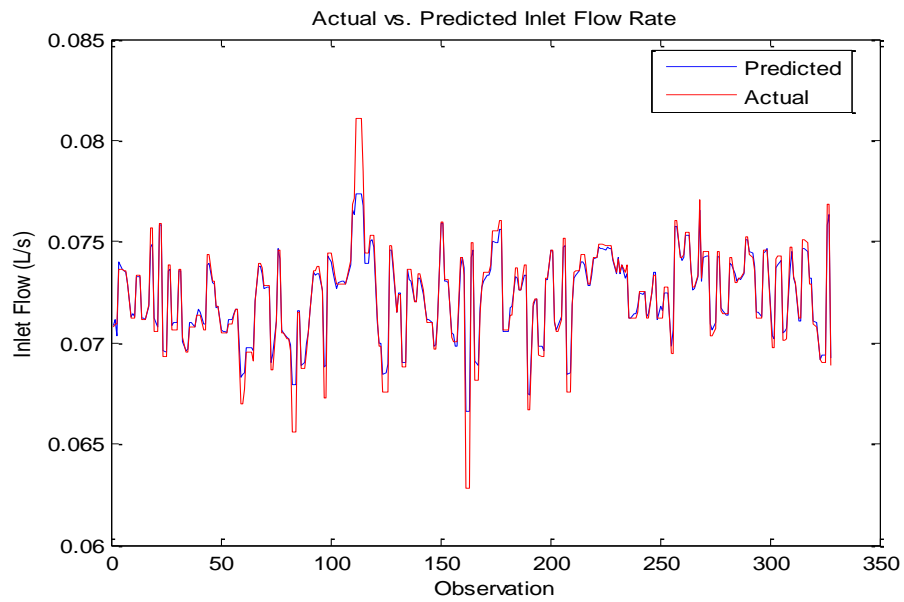


Figure 7.5: Measured vs. predicted inlet flow rate

Table 7.1: MAPE for AAKR Model for Bypass Flow Rate Fault

Sensor	MAPE
Current	0.29 %
Bypass	0.16 %
Pressure	0.32 %
Inlet Flow	0.46 %

In order to simulate a fault in the bypass flow rate, a data set was generated by operating at the same conditions as the previous data set, except at 59 Hz, the bypass valve was opened up another half turn until the motor's frequency was changed back to 60 Hz where the bypass was returned to its normal operating condition at one full turn (Figure 7.6).

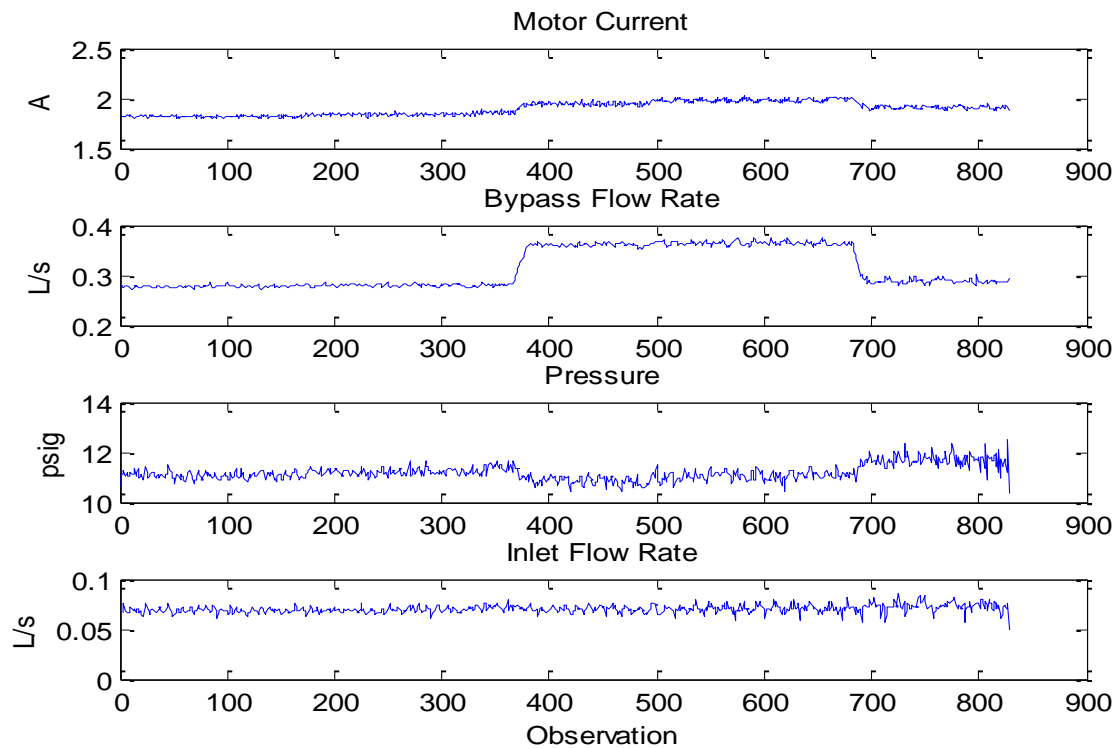


Figure 7.6: Plots of predictor variables for user-generated bypass flow rate fault

The fault-free data set was broken up into training, testing, and validation sets where the training set contained half of the observations while the rest of the data was split evenly between testing and validation sets. The PEM toolbox was then used to median filter the data to remove outliers and smooth the data as well as to standardize and mean center the data and give it unit variance.

All of the subsequent data sets were then standardized using the same mean and standard deviation as the training set. The optimal kernel bandwidth was determined by building several models using the testing data set and choosing the bandwidth which minimized the error. The optimal kernel bandwidth was then used to construct an AAKR model with the training data set. The faulty data set was then used as a new query to the AAKR model to test its ability to detect a fault with a simple thresholding method applied to the residuals. It was found that both the bypass flow and pressure predictor variables were able to detect the fault (Figures 7.7, 7.8).

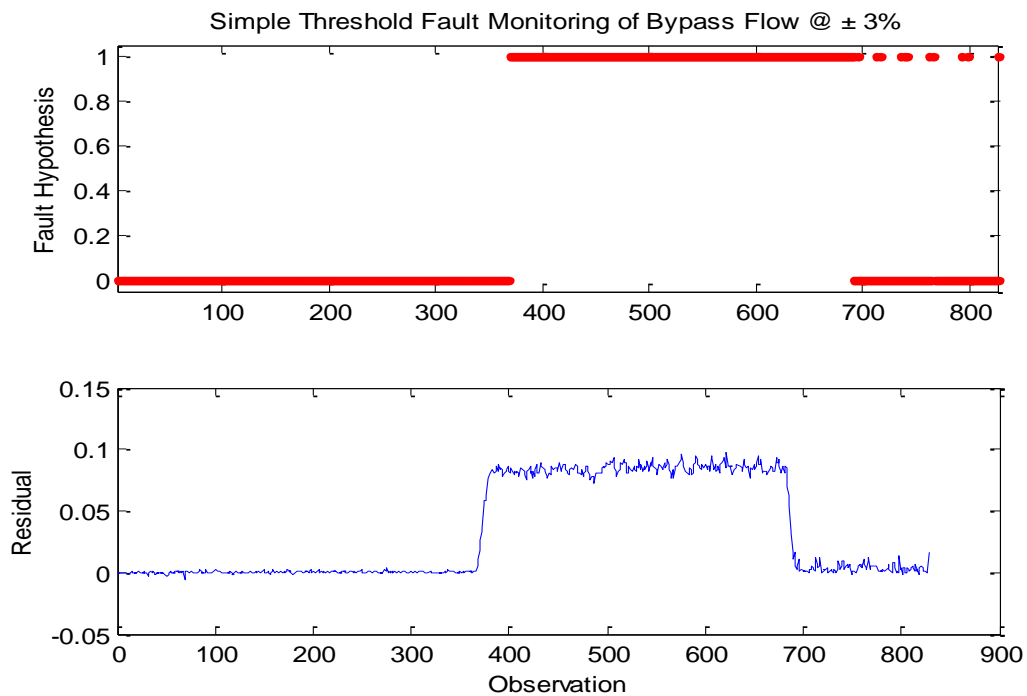


Figure 7.7: Residuals and simple threshold fault hypothesis for bypass flow rate

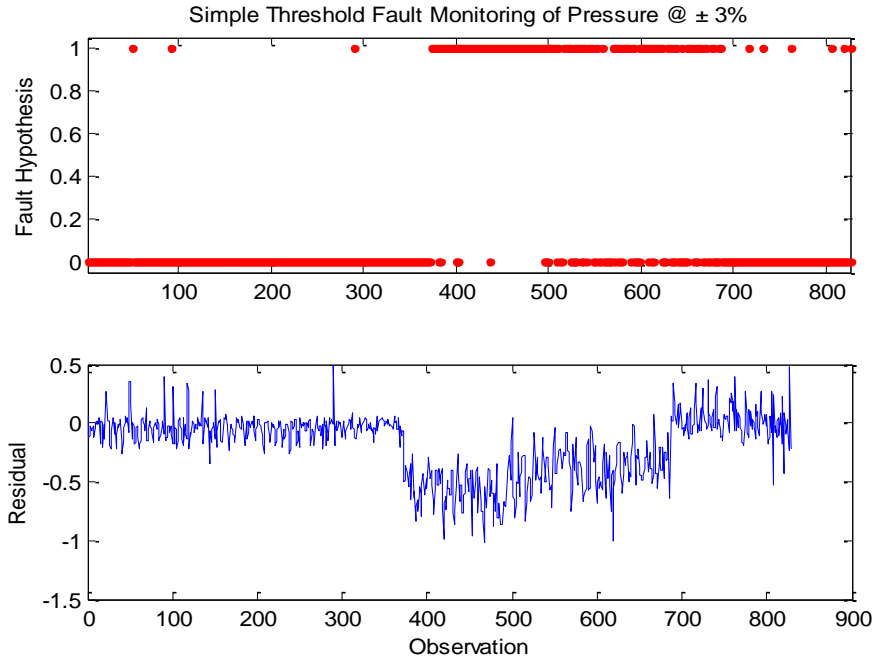


Figure 7.8: Residuals and simple threshold fault hypothesis for pressure

The bypass flow sensor was able to correctly identify the faulty observations with only a few outliers by a simple threshold of $\pm 3\%$. The pressure sensor was also able to detect the change in the bypass flow rate with a simple $\pm 3\%$ threshold, however, the pressure sensor residuals were low and the threshold did not catch every faulty observation and misidentified many of the observations as faulty. However, visual inspection can be used to identify the clear spike in residuals to determine that a fault has occurred. The inlet flow rate and current sensor measurements were unable to detect the faulted condition because the change in bypass is small and does not affect these signals enough to result in a faulted condition.

7.3.2 Motor Frequency Fault

A set of normal operation data was generated using the flow control loop to determine if an AAKR model would be capable of detecting a fault in the pump motor's rotational frequency. Normal data were taken by adjusting the inlet MOV to three different levels (Figure 7.9).

Again, the capability of the AAKR model to predict the values of the sensors was determined by comparing the predicted values of the AAKR model with the testing data set of actual measured sensor values with the MAPE criterion (Figures 7.10 -7.13).

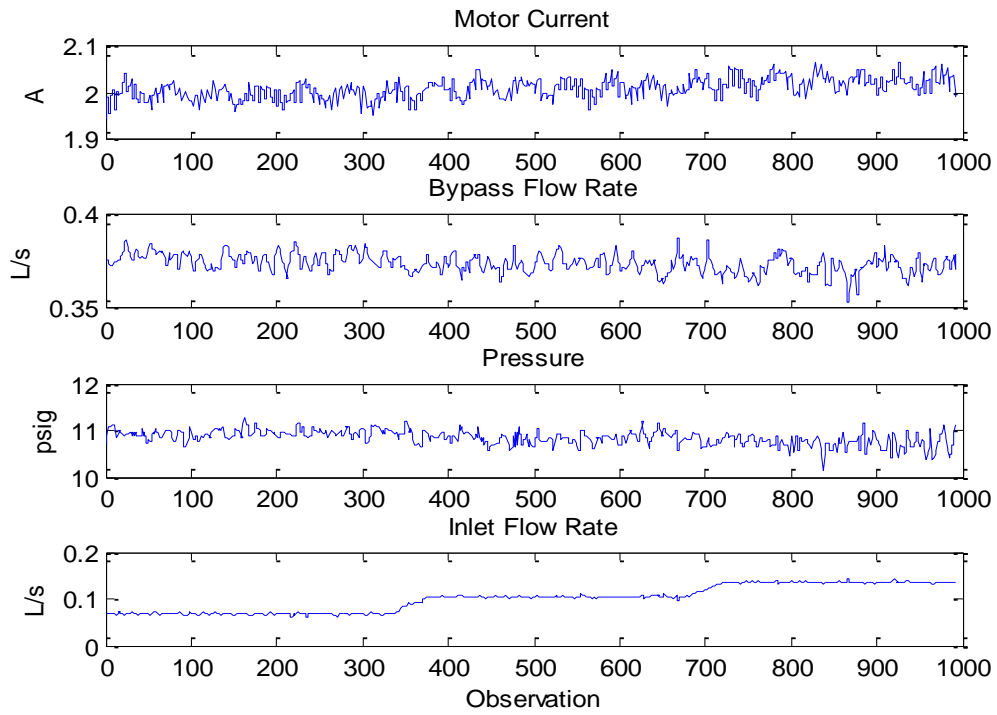


Figure 7.9: Plots of predictor variable under normal operation

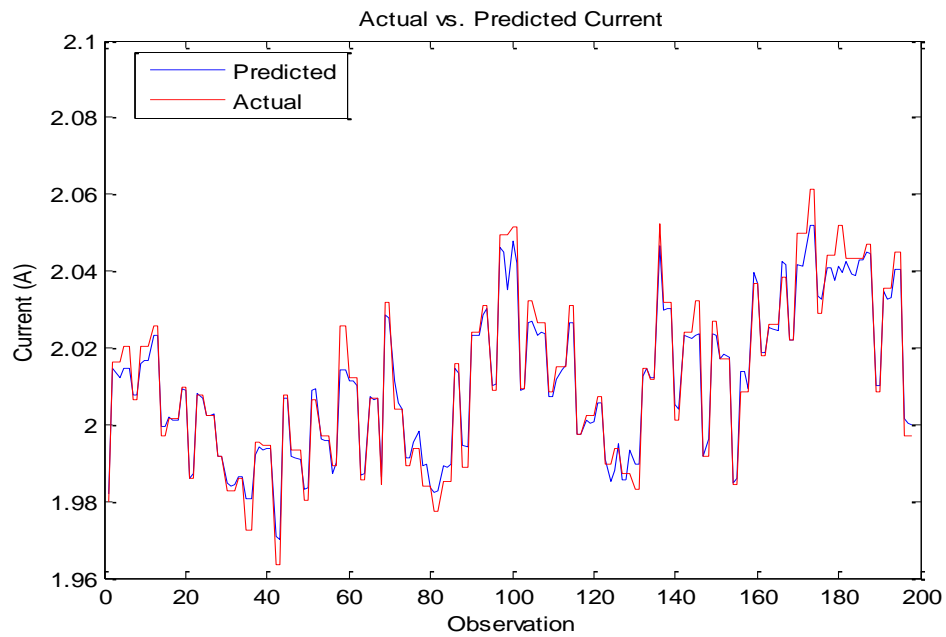


Figure 7.10: Measured vs. predicted values of motor current

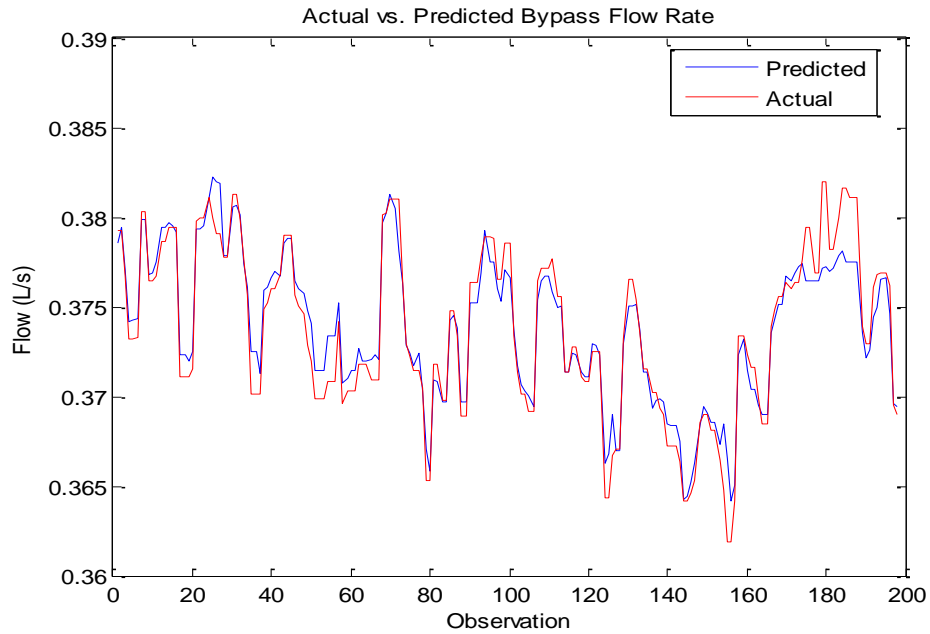


Figure 7.11: Measured vs. predicted values of bypass flow rate

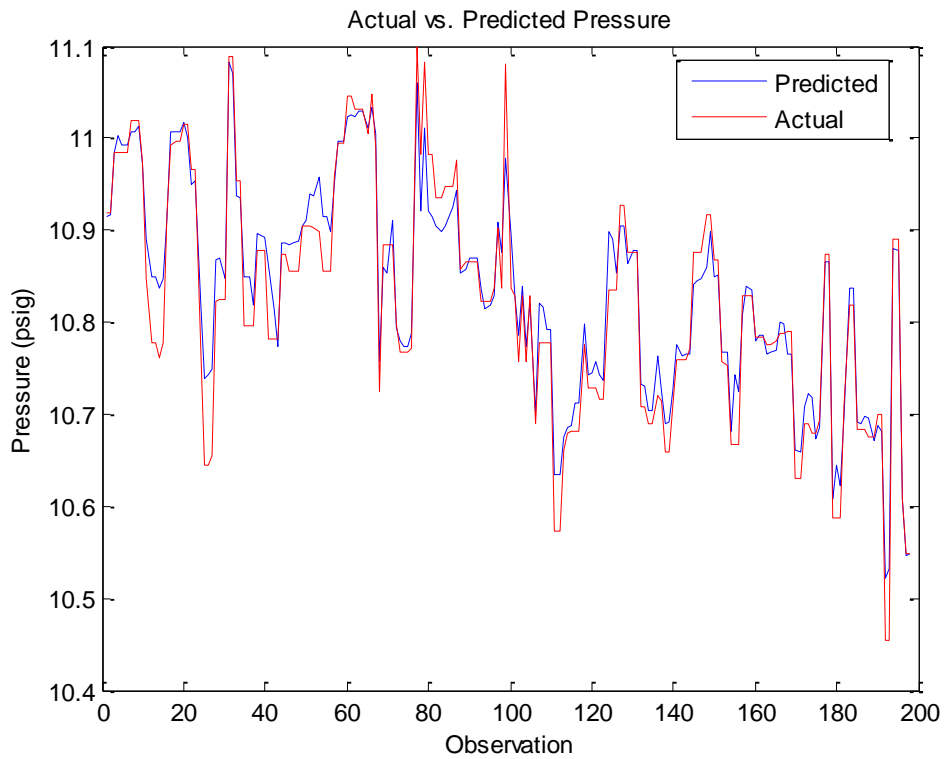


Figure 7.12: Measured vs. predicted values of loop pressure

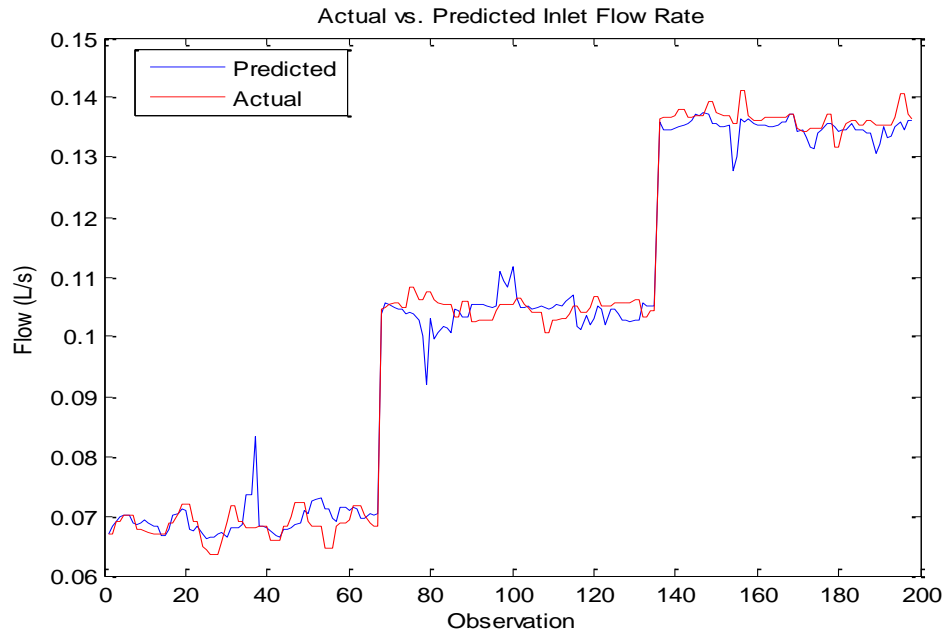


Figure 7.13: Measured vs. predicted values of inlet flow rate

Table 7.2 provides a summary of the MAPE for each predictor variable.

Table 7.2: MAPE for AAKR Model for Motor Frequency Fault

Sensor	MAPE
Current	.14 %
Bypass	.26 %
Pressure	.22 %
Inlet Flow	2.34 %

In order to simulate a fault in the motor's rotational frequency, a data set was generated by altering the pump rotational frequency by 1 Hz. At the start of the data set, the motor's rotational frequency was reduced to 59 Hz and then returned to 60 Hz halfway through the 2nd MOV opening position at approximate observation #250 (Figure 7.14).

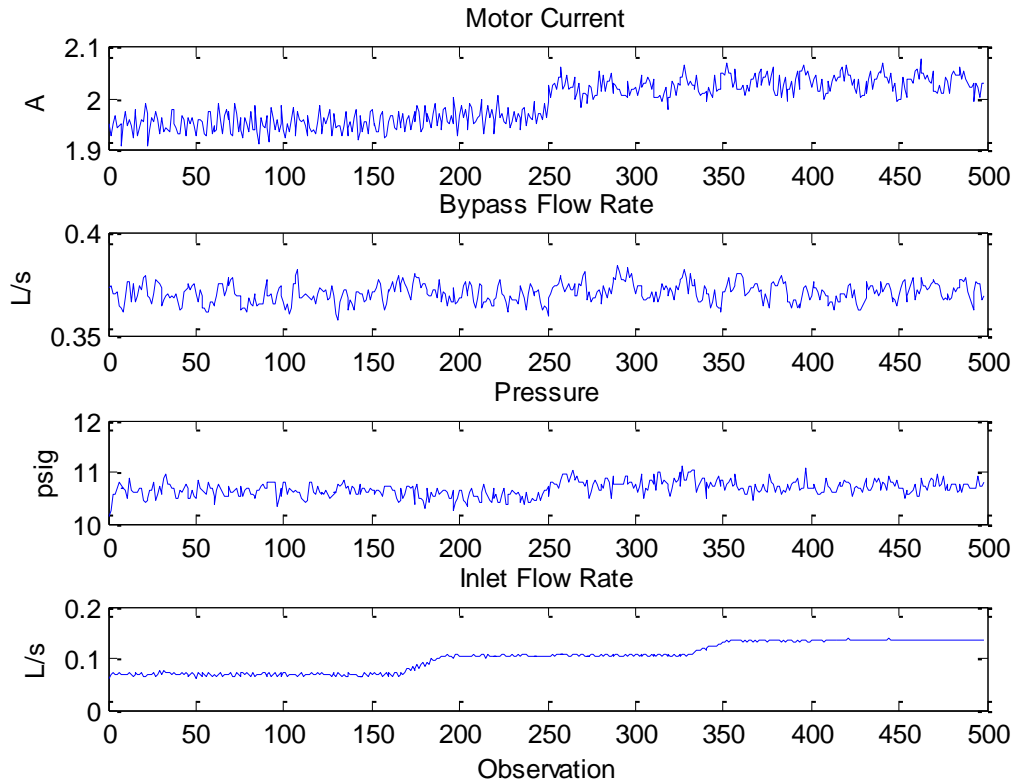


Figure 7.14: User-generated motor rotational frequency fault dataset

The predictor variables selected for this model included the current, bypass flow rate, pressure, and inlet flow due to their correlation with each other. The same AAKR modeling method implemented earlier was again used to test the ability of the model to detect the fault in motor rotational frequency. It was found that previously implemented simple signal thresholding was partially capable of identifying a fault in the current due to the change in motor speed (Figure 7.15).

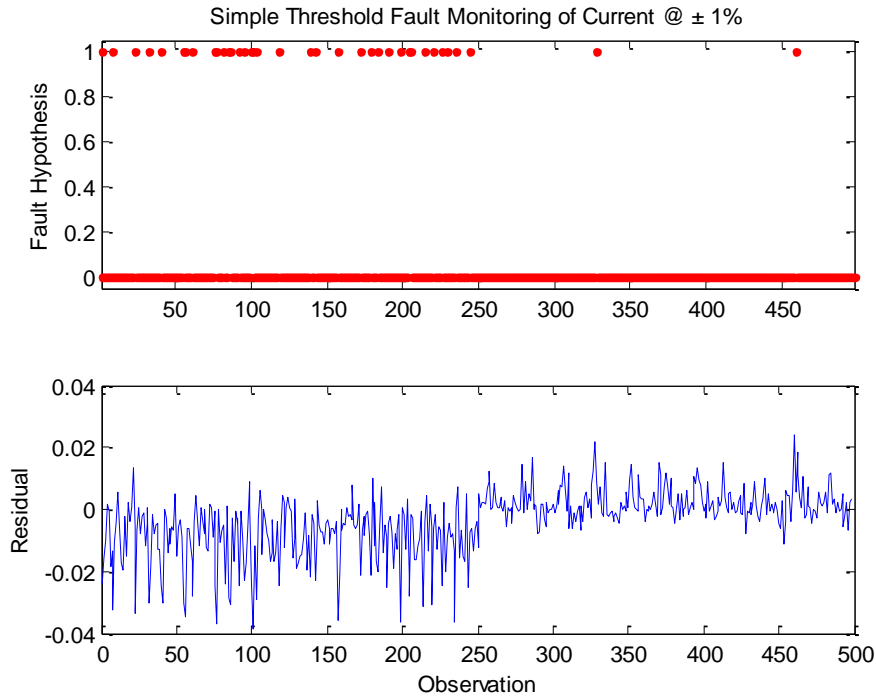


Figure 7.15: Residuals and simple threshold fault hypothesis for motor current

A check of the residuals shows that the first 250 observations are clearly a cause for concern. However, due to the small magnitude of the residuals and the noise in the current sensor, the thresholding technique was unable to recognize many of these observations as faulted. The thresholding method for the bypass residuals also exhibited similar results (Figure 7.16).

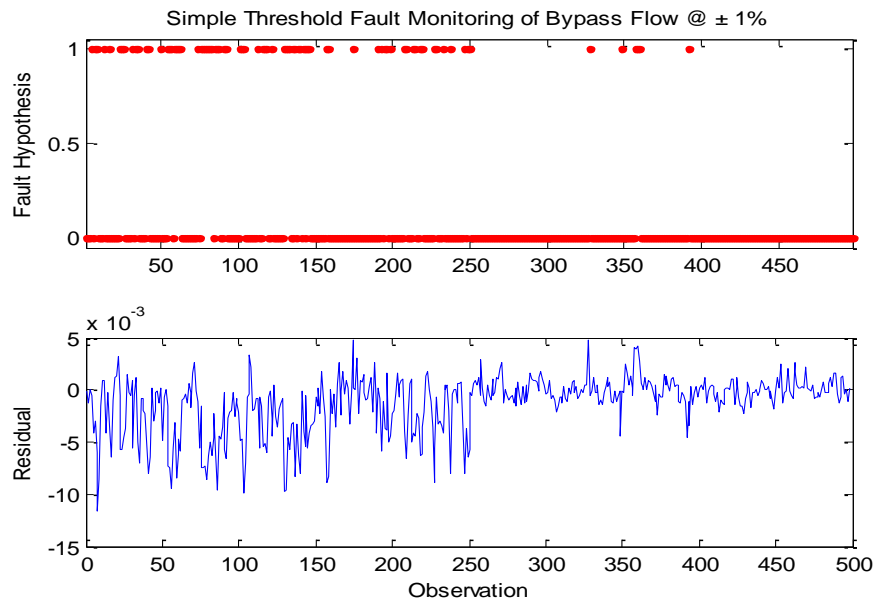


Figure 7.16: Residuals and simple threshold fault hypothesis for bypass flow rate

Again, the method was unable to correctly identify each faulty observation. The small magnitude of the residuals and noise of the signal was again the source of the problem. Although the method was unable to correctly identify each fault, the fault can still be observed by studying the residuals. For the case of a change in the motor's operation, a change in the residuals could signal a cause for concern and be investigated further. Frequency domain analysis on the pump motor via vibration or current signatures could be evaluated based on the residuals produced by the AAKR model.

7.4. AAKR Modeling with Water Level Control

This section provides an in-depth description of the process of building an AAKR model, generating a faulty dataset, and utilizing SPRT to detect the user-generated faults. All of the experiments were performed with water level control to further simulate conditions expected in a SMR.

7.4.1 AAKR Model Development

This section describes the process of developing the AAKR model with normal, fault-free operational data.

7.4.1.1 Training data set generation

For this research, a training dataset under normal operating conditions was recorded in order to train the AAKR model. This training data set was taken with the PI controller in order to regulate the water level in the tank. Several set points were chosen from 20 to 50 % full and the water level was allowed to settle for a pre-determined length of time (Fig. 7.17). The water level set points were chosen in order to cover the full range of expected operation in future experiments. The variables recorded in the experiment for data-based modeling are summarized in Table 7.3 and the process of obtaining the AAKR model is listed in the next section.

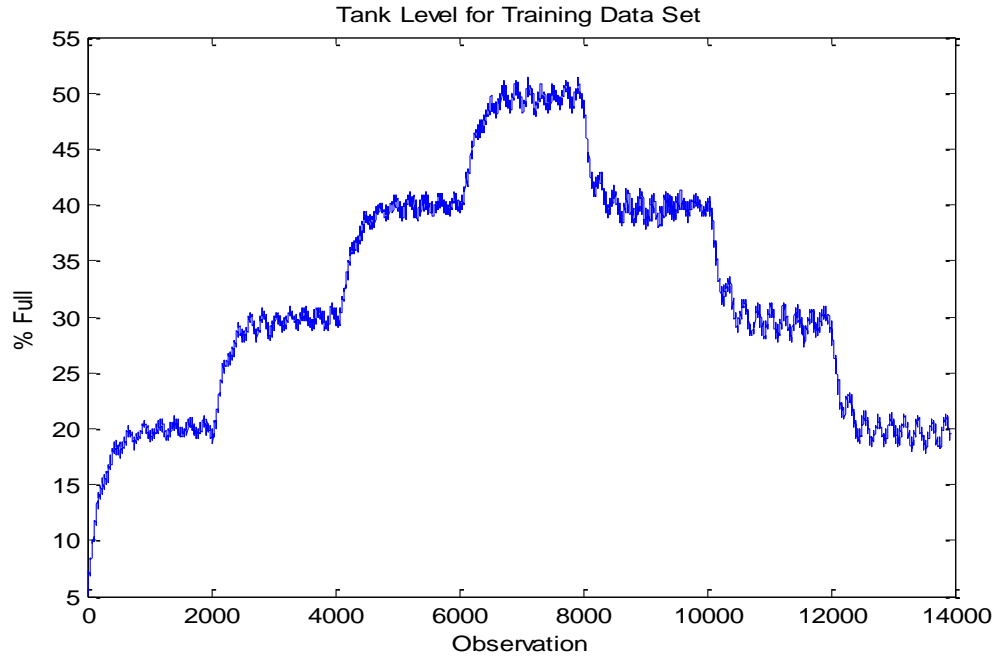


Figure 7.17: Water level set points used for training data set generation

Table 7.3: Recorded variables from the experimental flow control loop

Variable	Unit
Tank Inlet Flow Rate	L/s
Bypass Flow Rate	L/s
Tank Level	% Full
Tank Outlet Flow Rate	L/s
Motor Current	Amperes
Pressure	Psig
Controller Output	V
Valve Position	V

7.4.1.2 Variable selection and process of obtaining AAKR model

When building an AAKR model, only variables that are correlated should be used. If variables that are uncorrelated are included in the model, the accuracy of the model will decrease [116]. Furthermore, the model should use predictor variables that represent the loop dynamics. Therefore, only variables that were correlated with each other and represent the loop behavior

were incorporated in the AAKR model. The correlation coefficients, which are the zero-th lag of the normalized covariance function, were calculated to determine the relationship between the selected predictor variables (Table 7.4). The normalized correlation coefficient may have an absolute value between 0 and 1 where the closer the value gets to 1, the more related the two variables are.

Table 7.4: Correlation Coefficients between Predictor Variables

Variable:	Motor Current	Pressure	Inlet Flow Rate	Controller Output	Control Valve Position
Motor Current	1.00	-.260	.470	.173	.434
Pressure	-.260	1.00	-.454	-.145	-.448
Inlet Flow Rate	.470	-.454	1.00	.258	.866
Controller Output	.173	-.145	.258	1.00	.582
Control Valve Position	.434	-.448	.866	.582	1.00

Based on the correlations between the variables and knowledge of the loop dynamics, several conclusions about the predictor variable relationships can be made:

- The control valve position is the most highly correlated predictor variable as it regulates the inlet flow rate through the valve and into the tank. Therefore, it is highly related with the flow rate and other variables.
- The inlet flow rate is well related with the other predictor variables because of the simple relationships between flow rate and pressure.
- The motor current is well related to the inlet flow rate and the valve position because as the valve position is increased, the inlet flow rate will increase and the motor will draw more power in order to pump more water through the valve.

Plots of the selected predictor variables recorded for the training data set of the AAKR model under normal operation are plotted in Figures 7.18-7.22.

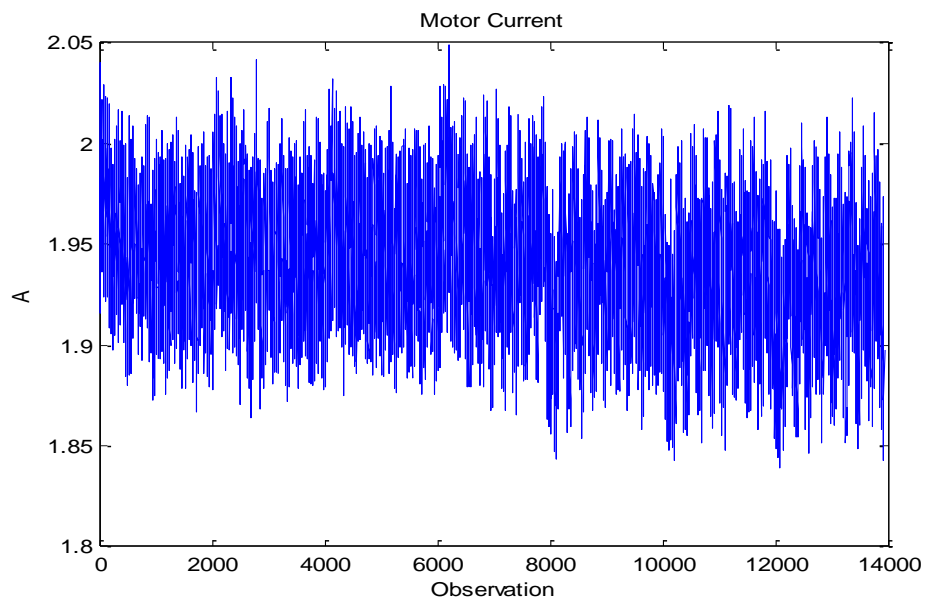


Figure 7.18 Motor Current for AAKR Training dataset

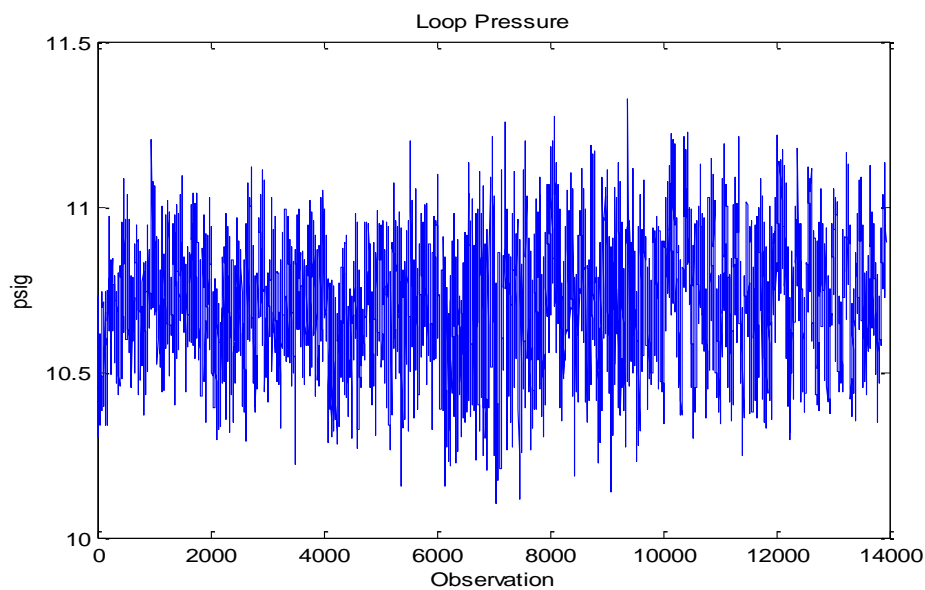


Figure 7.19: Pressure for AAKR Training dataset

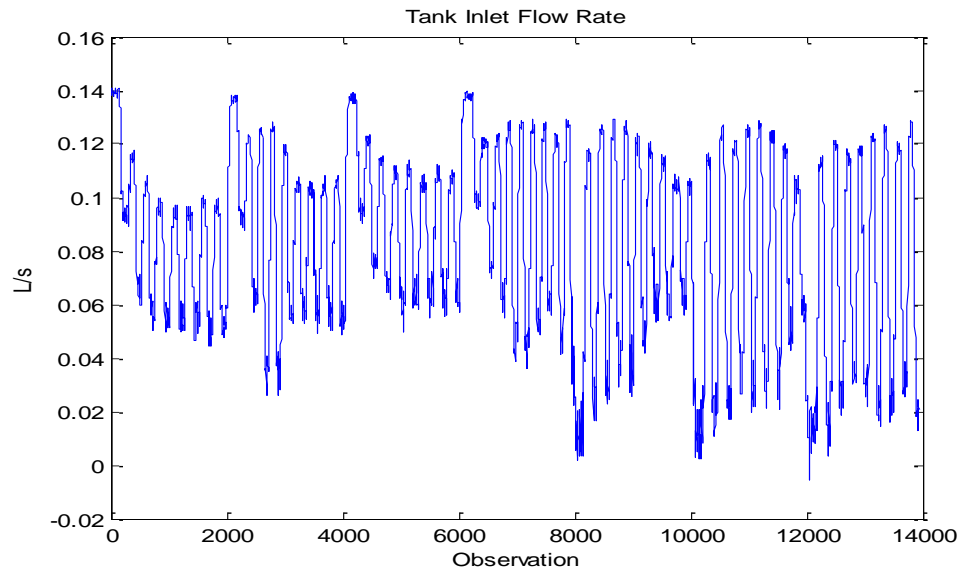


Figure 7.20: Inlet Flow Rate for AAKR Training dataset

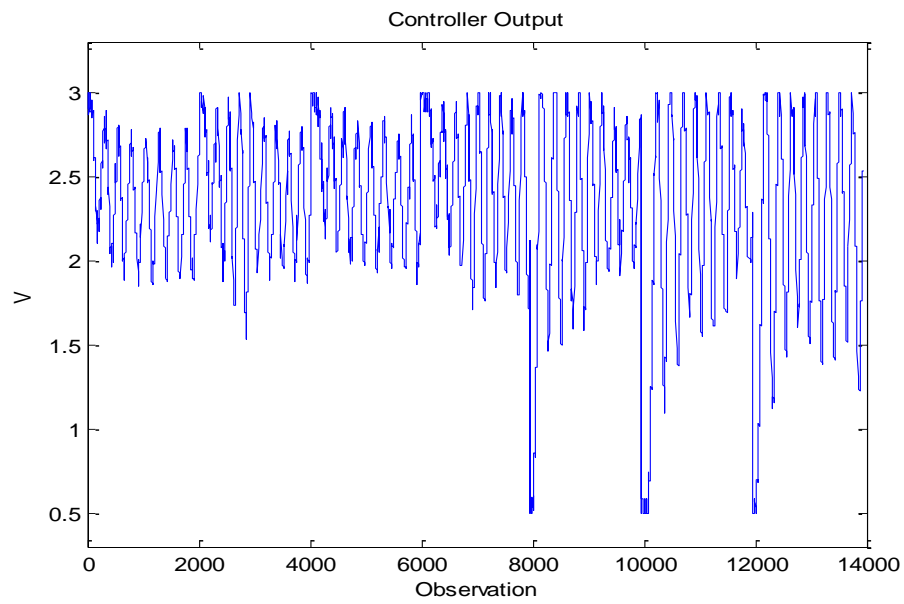


Figure 7.21: Controller Output for AAKR Training dataset

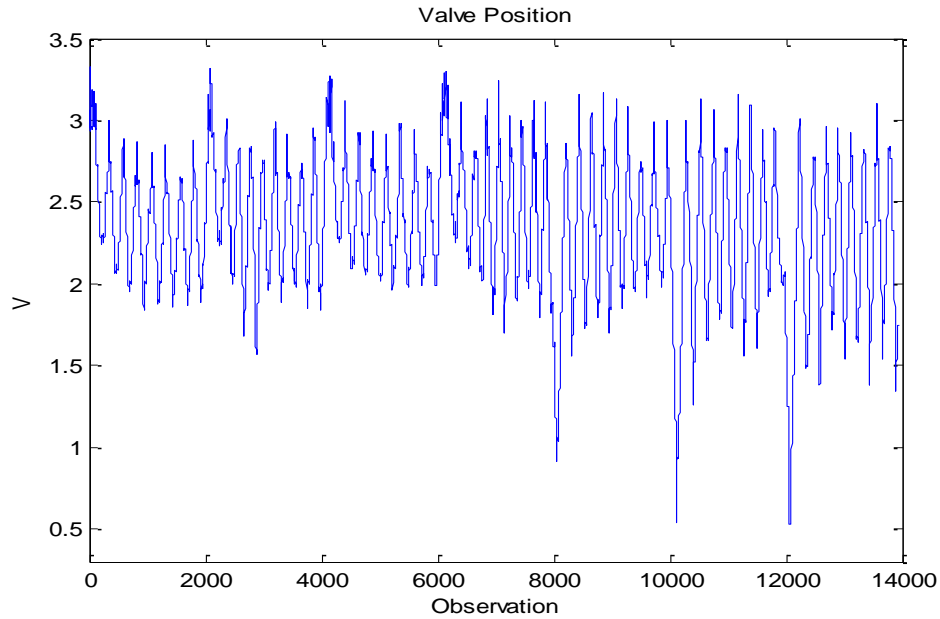


Figure 7.22: Control Valve Position for AAKR Training dataset

The next step in training the AAKR model is to use the PEM and NEUP project toolbox to clean and pre-process the noisy data. The data was mean-centered, and unit variance scaled to give each variable the same importance and ability to contribute to the model. The scaled dataset was then divided up into three different blocks using the venetian blind sampling function *DataBreakup*. The training block contains the most amount of information as it contains the lowest and highest values from each variable to ensure the entire variance of the dataset is included. The testing dataset was used to test the accuracy of the model, and finally, the validation dataset was used to determine how the model performs with new, unseen data.

7.4.1.3 AAKR Model Performance with Similar Data

Once the AAKR model was properly trained with normal, fault-free data, a different dataset was acquired with the same set points as the original training set in order to test the accuracy of the AAKR model. The new measurements were used as queries to the model and the results comparing the actual and predicted sensor values were plotted (Figures 7.23-7.27).

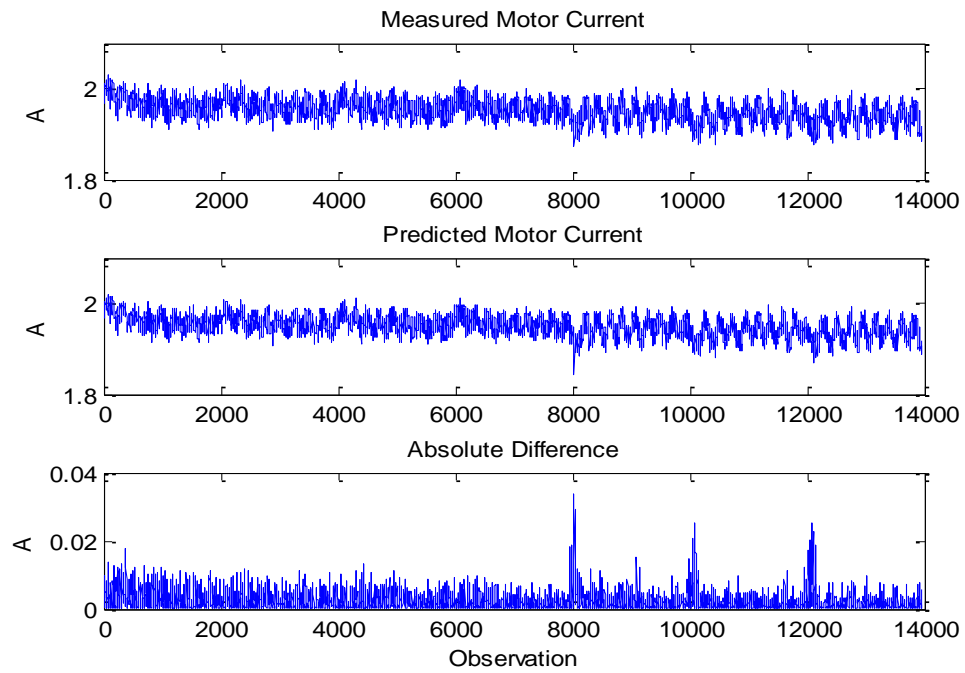


Figure 7.23: Measured motor current versus AAKR predictions

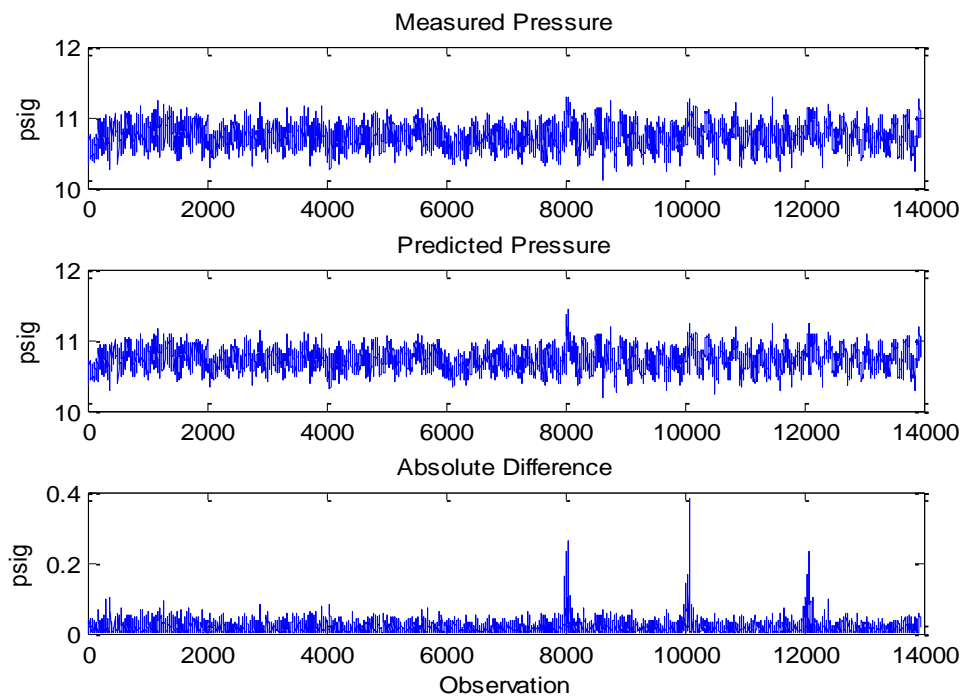


Figure 7.24: Measured pressure versus AAKR predictions

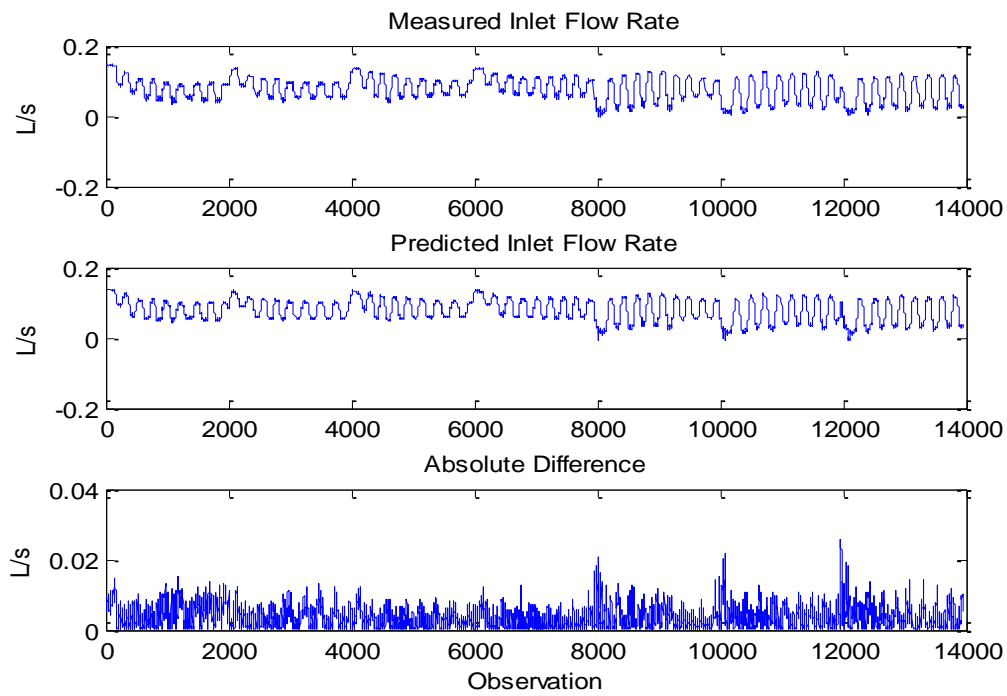


Figure 7.25: Measured inlet flow rate versus AAKR predictions

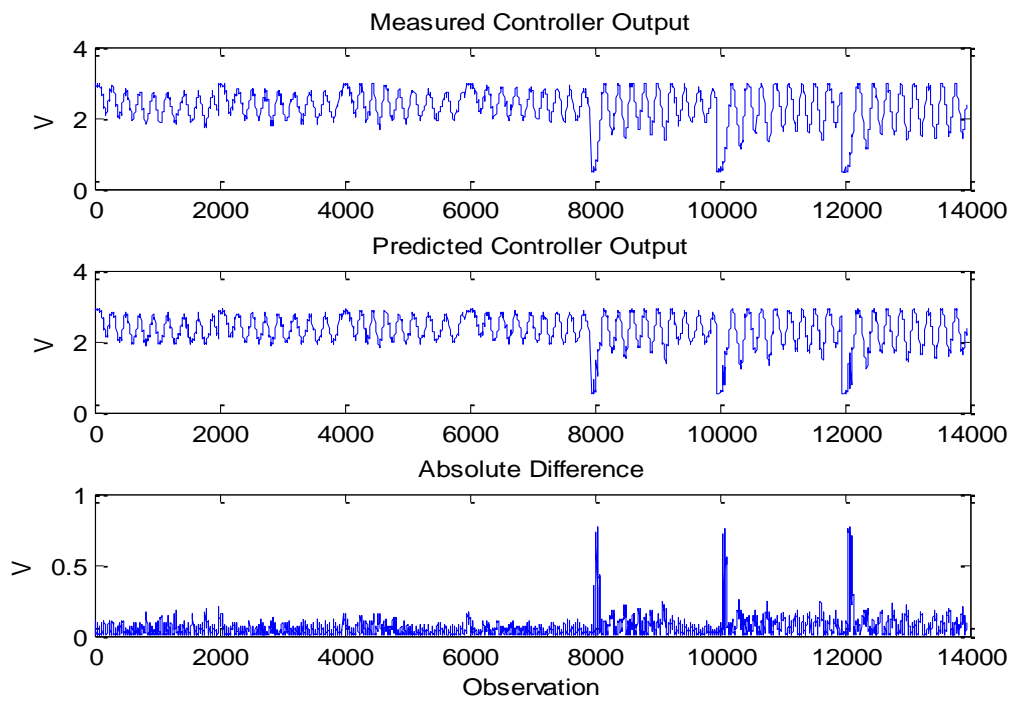


Figure 7.26: Measured controller output versus AAKR predictions

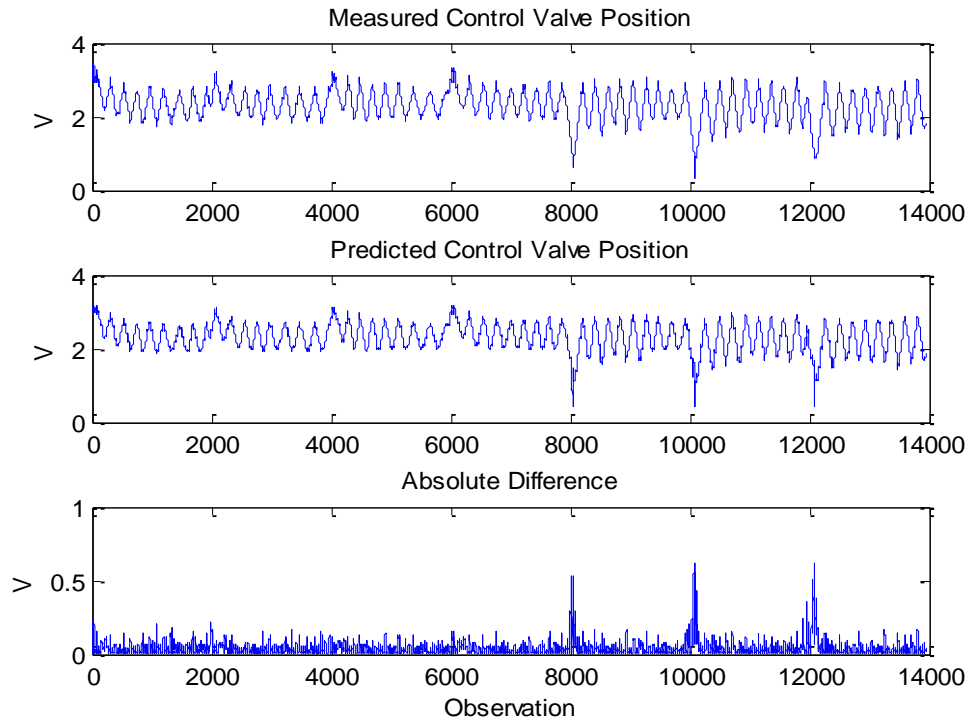


Figure 7.27: Measured control valve position versus AAKR predictions

The accuracy of the AAKR model predictions were again evaluated using the MAPE and is summarized in Table 7.5.

Table 7.5: MAPE of AAKR Model for each Predictor Variable

Variable	MAPE
Motor Current	.11 %
Pressure	.15%
Inlet Flow Rate	8.74 %
Controller Output	3.11 %
Valve Position	2.01 %

7.4.2 Design of Experiments

A set of user-generated faults were introduced to the normal operation of the experimental flow loop to test the capabilities of the AAKR model to identify the faults. The faults involved

different degrees of drifts in the sensor readings. Every experiment was performed with the PI controller to keep the water level at the desired set point. A summary of the faulty experiments investigated are listed below:

- Inlet Flow Rate
 - A slow drift of 50, 25, and 10 % were added to the inlet flow rate sensor readings over 3 minutes
- Controller Output
 - A slow drift of 40, 20, and 10 % were added to the controller voltage output sent to the control valve regulating the inlet flow rate over 3 minutes

Experiments adding varying amounts of sensor drift to the inlet flow rate sensor were performed to test the ability of the AAKR model and SPRT to identify when the sensor drifted outside of its normal operation based on the measurements of the loop variables. The faulty experiments were performed by operating under steady state conditions at a water level of 40 % for 3 minutes and then a slow drift of varying percentages was added to the actual sensor measurement over 3 minutes (Figures 7.28-7.30).

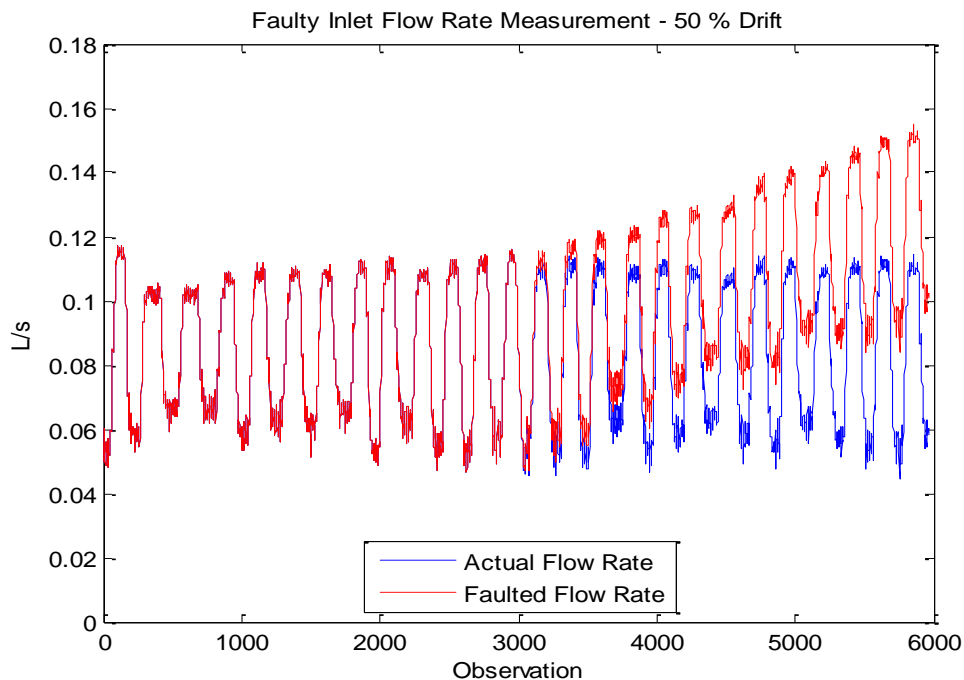


Figure 7.28: Faulty inlet flow rate measurement with slow 50 % sensor drift

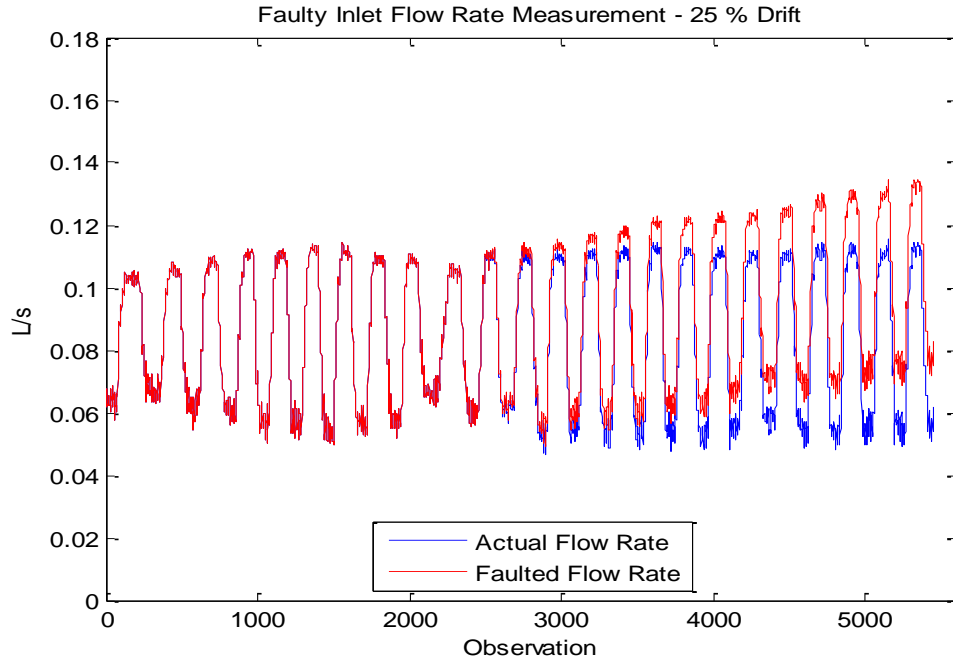


Figure 7.29: Faulty inlet flow rate measurement with slow 25 % sensor drift

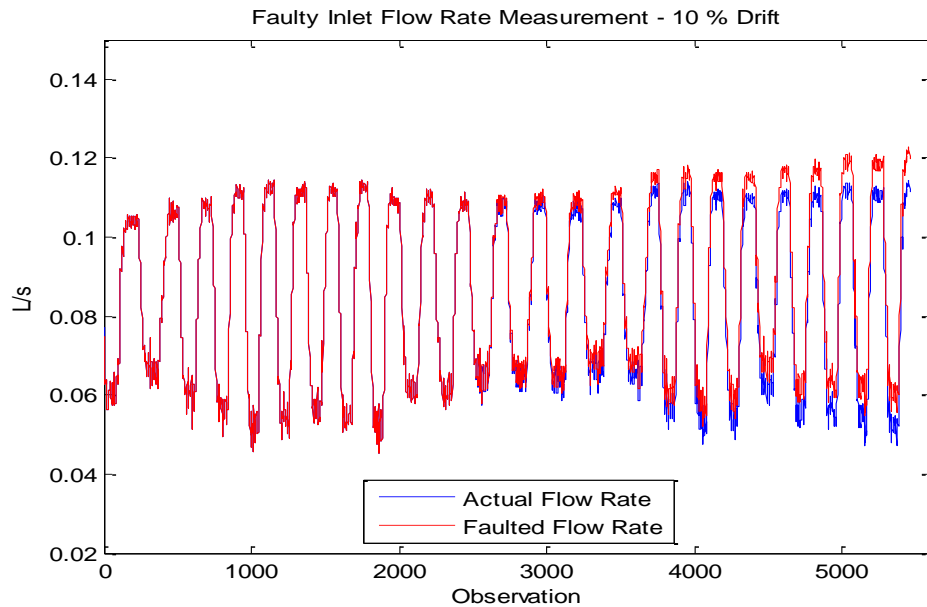


Figure 7.30: Faulty inlet flow rate measurement with slow 10 % sensor drift

The three percentages were chosen to determine the smallest amount of drift that the AAKR model could detect.

Another set of drift experiments were performed that altered the actual output of the controller to simulate a faulted water level controller. Slow drifts in the controller voltage output

were added to the controller output over 3 minutes to determine when the AAKR could detect the faulty conditions. The experiments were run at a 40 % water level for 3 minutes under steady state conditions and then a slow drift was added over 3 minutes at varying percentages for each different experiment (Figures 7.31-7.33). The drift in the controller output was added to the voltage output which represents the position of the control valve regulating the tank inlet flow rate. The drift in the voltage was positive, therefore, the controller begins to output a lower voltage than it should. The change in the controller output alters the valve position which in turn alters the inlet flow rate and other variables.

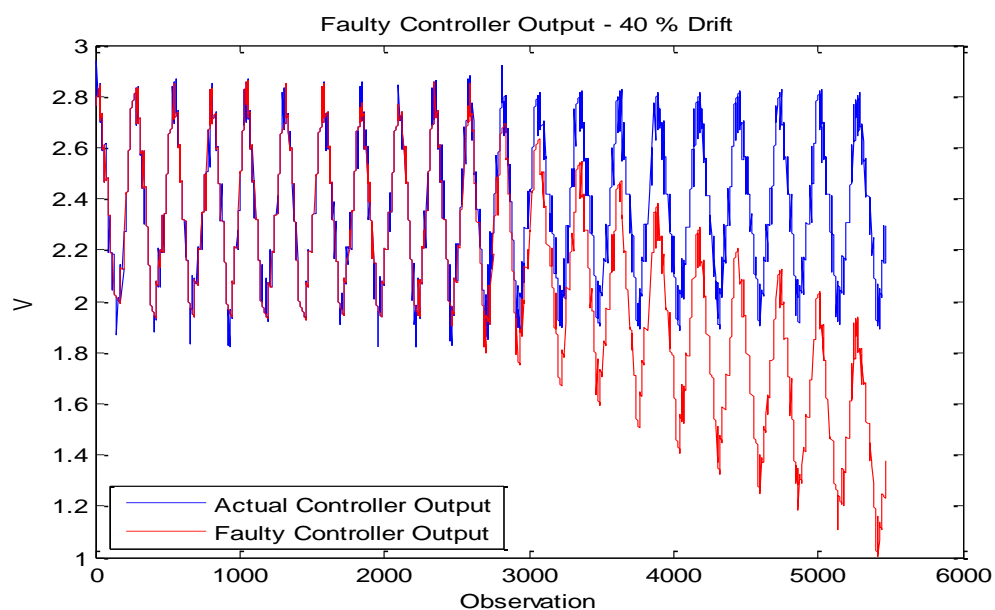


Figure 7.31: Faulty controller output with slow 40 % sensor drift

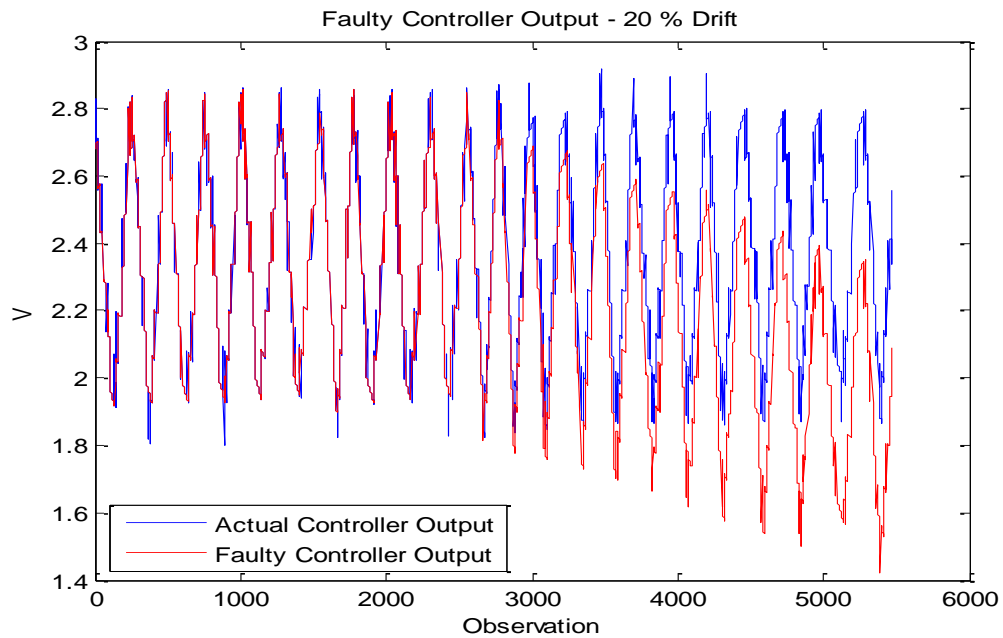


Figure 7.32: Faulty controller output with slow 20 % sensor drift

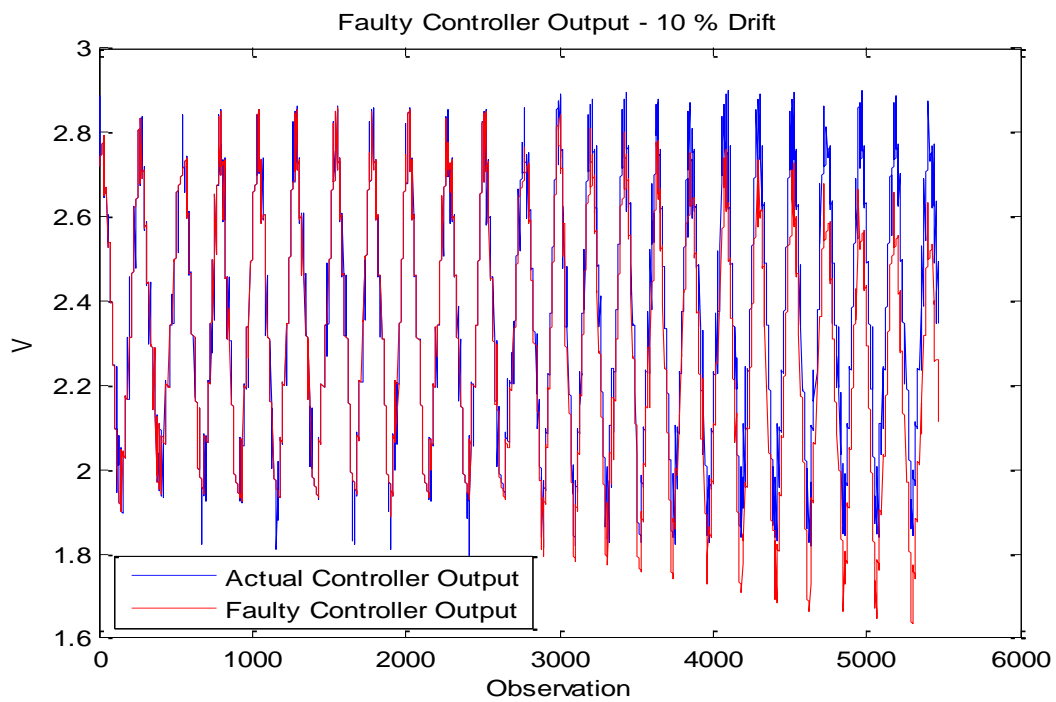


Figure 7.33: Faulty controller output with slow 10 % sensor drift

7.4.3 Results of Fault Detection

7.4.3.1 Inlet flow rate experiments

The 10 % drift in the inlet flow rate sensor was undetectable using the AAKR model and the SPRT because the drift was too small. However, the AAKR model along with SPRT was able to detect both the 25 and 50% drift in the inlet flow sensor readings with two different predictor variables. The inlet flow rate variable was able to predict the fault as expected (Figures 7.34, 7.35) as well as the valve position indicator (Figures 7.36, 7.37).

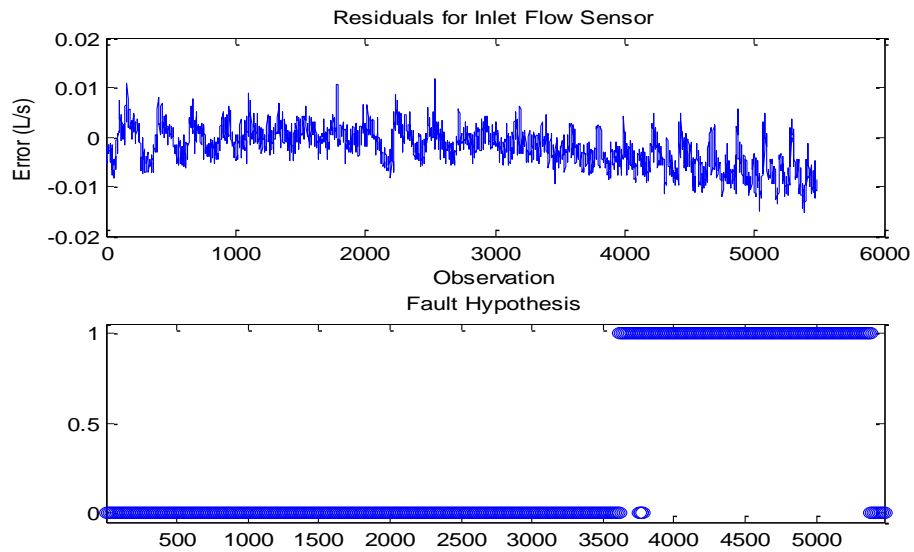


Figure 7.34: Residuals and fault hypothesis for inlet flow rate with 25 % sensor drift

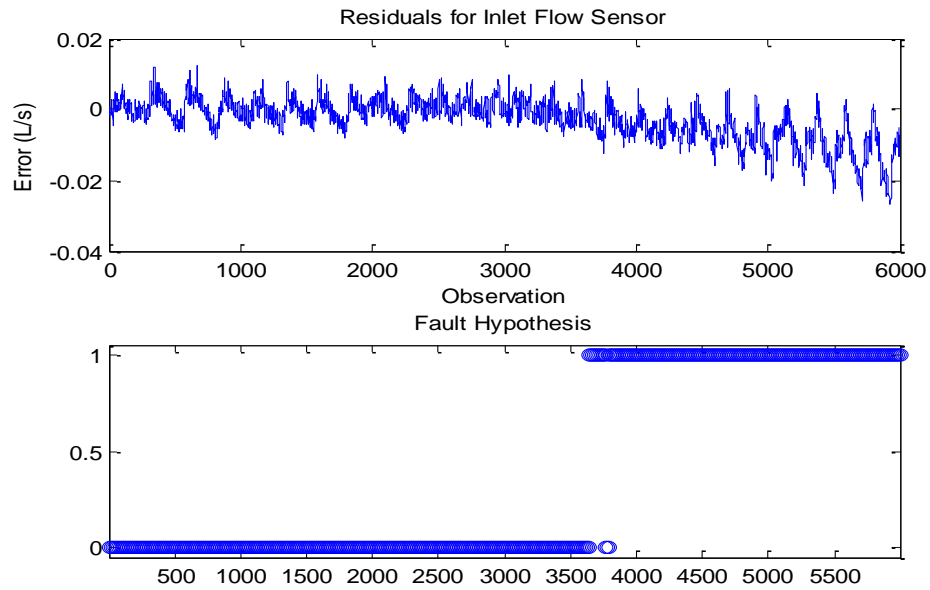


Figure 7.35: Residuals and fault hypothesis for inlet flow rate with 50 % sensor drift

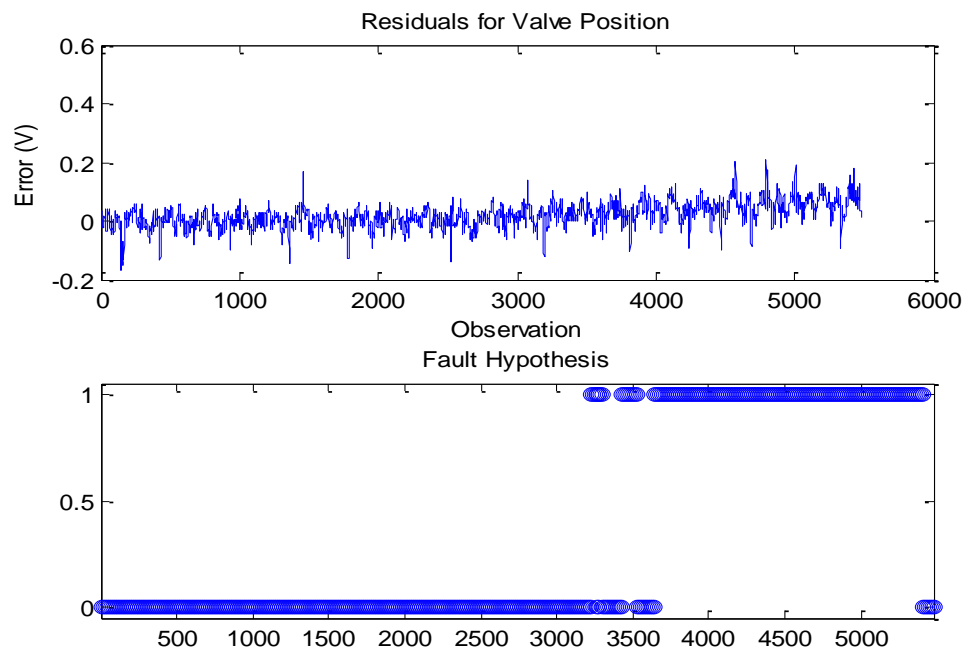


Figure 7.36: Residuals and fault hypothesis for valve position with 25 % sensor drift

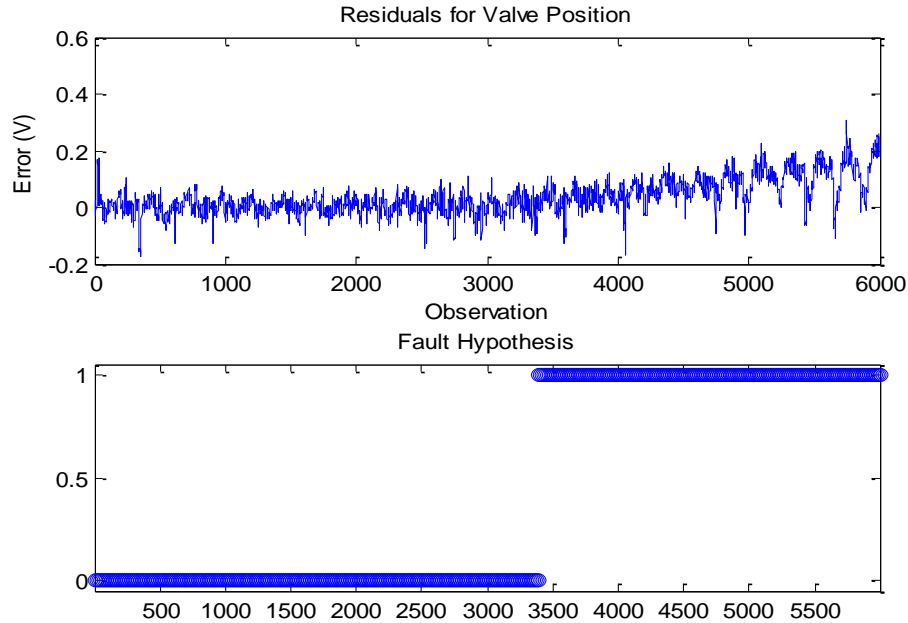


Figure 7.37: Residuals and fault hypothesis for valve position with 50 % sensor drift

The AAKR model easily identified the drifted sensor readings for the inlet flow rate once the residuals between the predicted and actual flow rate pass the SPRT threshold. In order to reduce the number of false alarms, a sequence of observations was only deemed faulted if 10 residuals in a sequence of 250 were faulted. The large sequence analyzed was chosen due to the noise of the signal. Along with the inlet flow rate predictor variable, the valve position signal was also able to identify the faulted sensor providing robustness to the AAKR model. The position of the valve is directly related to the inlet flow rate as the position of the valve determines the flow rate through it. Therefore, a certain inlet flow rate is expected for a particular valve position. The actual flow rate through the valve is not changing, only the measured flow rate, therefore, the AAKR model predicts the valve position to be higher than the measured for the artificially increased flow rate readings. Since the AAKR model was capable of detecting the 25 % drift in the sensor readings early on in the experiment, it was evident that it would also be capable of detecting the 50 % drift. Furthermore, SPRT was able to detect the fault earlier in the 50 % drift as the increase in the sensor readings was higher. The motor current, pressure, and controller output were unable to detect the fault because these variables do not undergo much change due to only the sensor readings being affected and not the operation of

the loop. However, the valve position was able to identify the faulty operation providing robustness to the model as more than one variable was capable of identifying the fault.

7.4.3.2 Controller output experiments

The next set of experiments involved adding a slow drift to the water level controller output. The AAKR model and SPRT was unable to detect the 10 % drift in the controller output because the overall change was too small. However, the AAKR model and SPRT was capable of identifying the fault with three different predictor variables. The controller output (Figures 7.38, 7.39), control valve position (Figures 7.40, 7.41), and inlet flow rate (Figures 7.42, 7.43) were all capable of identifying the fault for the 20 and 40 % drift in the controller output.

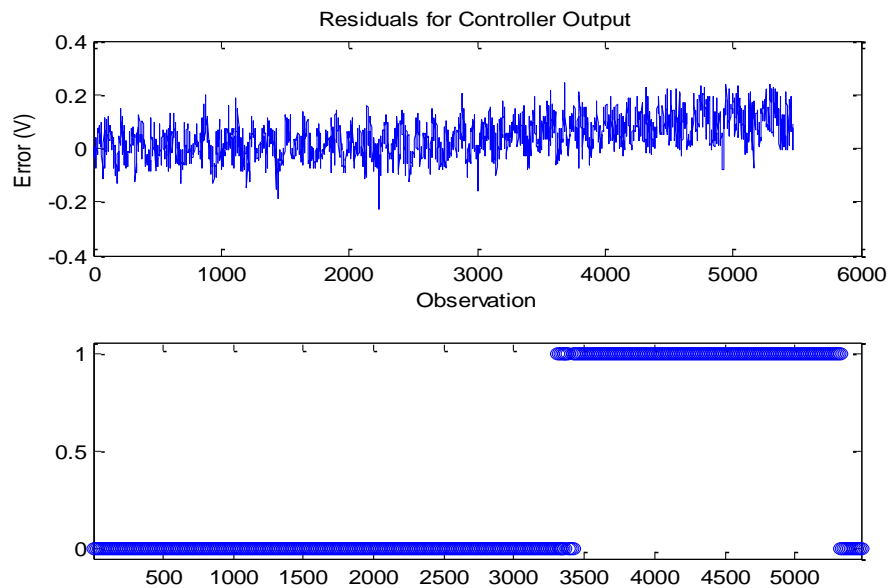


Figure 7.38: Residuals and fault hypothesis for controller output with 20 % drift in controller output

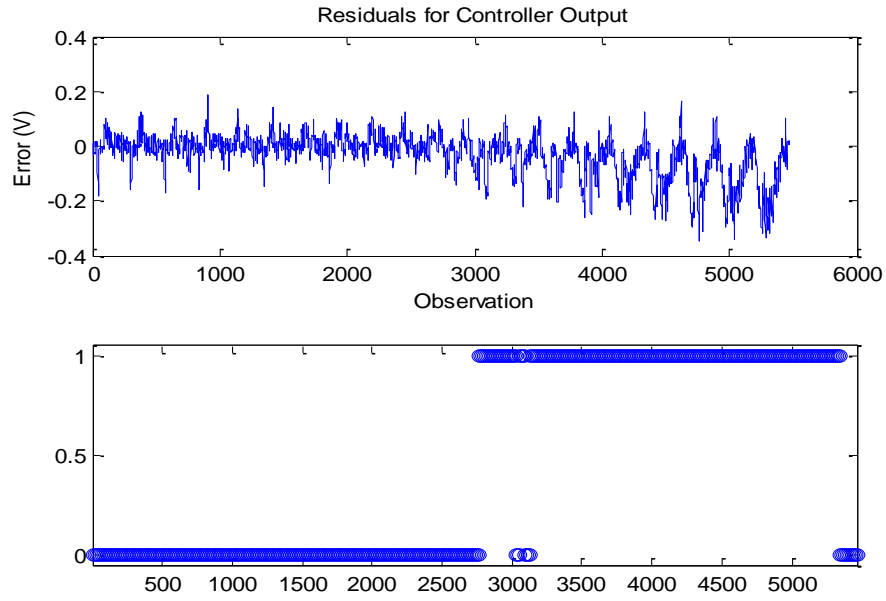


Figure 7.39: Residuals and fault hypothesis for controller output with 40 % drift in controller output

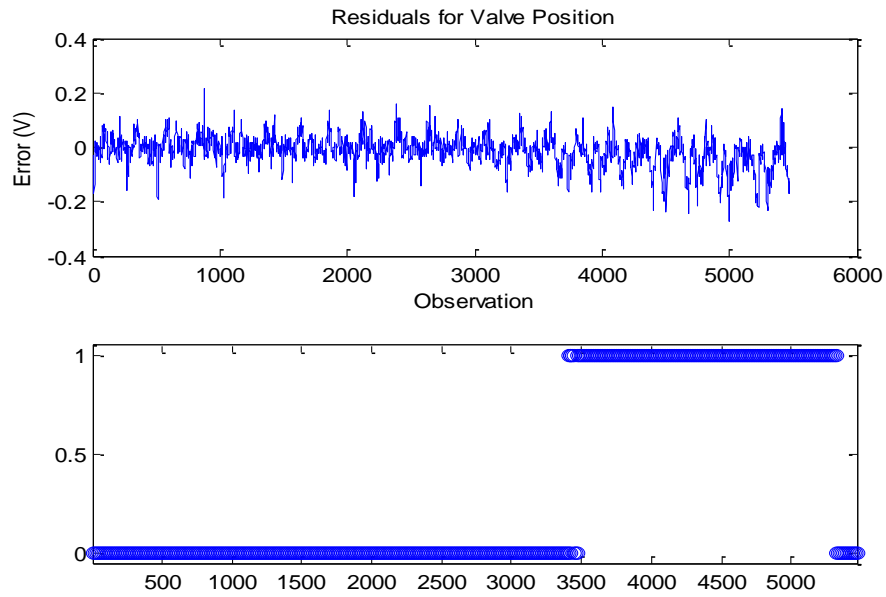


Figure 7.40: Residuals and fault hypothesis for valve position with 20 % drift in controller output

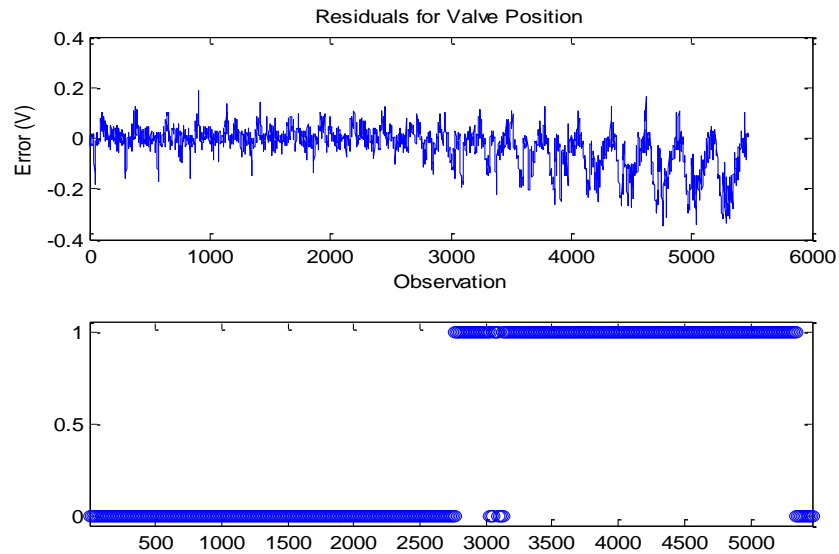


Figure 7.41: Residuals and fault hypothesis for valve position with 40 % drift in controller output

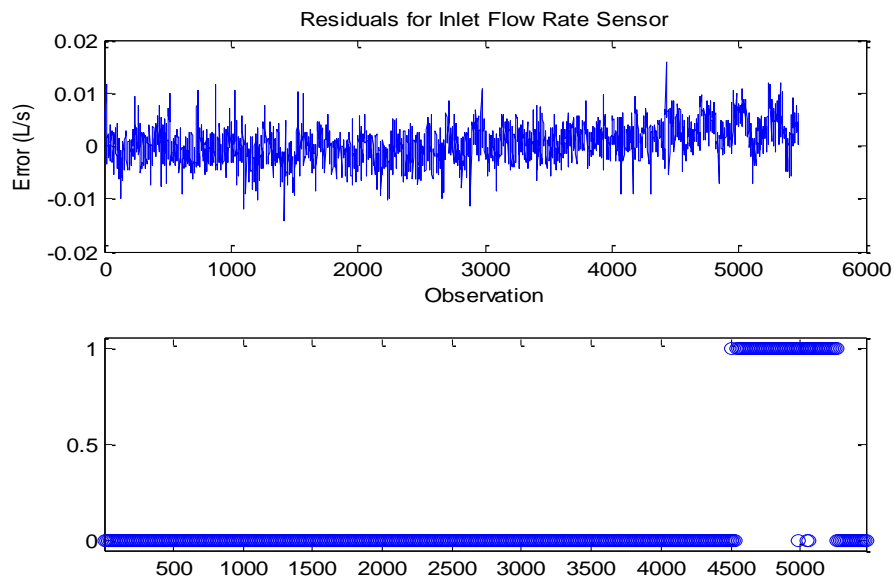


Figure 7.42: Residuals and fault hypothesis for inlet flow rate with 20 % drift in controller output

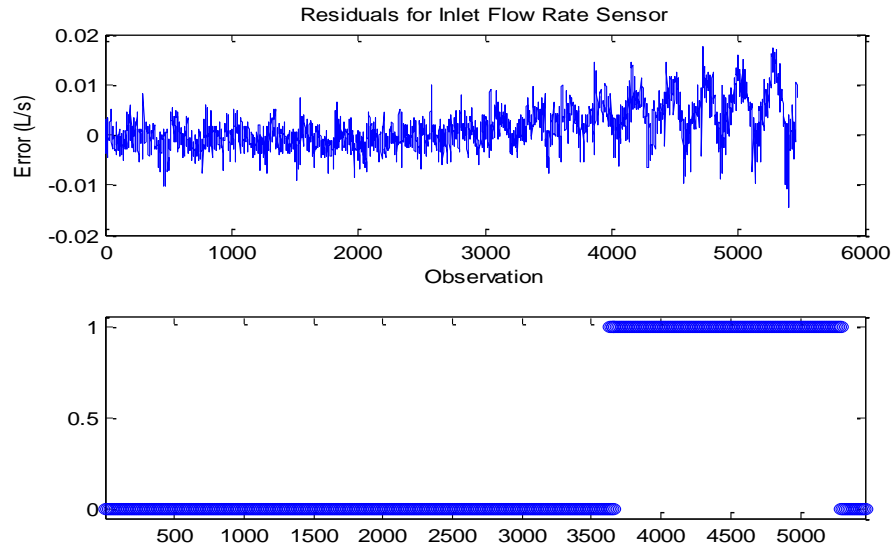


Figure 7.43: Residuals and fault hypothesis for inlet flow rate with 40 % drift in controller output

The AAKR model easily identifies the drifted controller output with 3 predictor variables once the residuals between the predicted and actual sensor values cross the SPRT threshold. The residuals between the measured and actual controller output signal were easily able to identify a fault in the controller output because the model predicted a different signal based on the behavior of the other signals. The valve position also easily identifies the fault as it is directly related to the controller output. Finally, the inlet flow rate sensor was also capable of identifying the faulty condition. However, the inlet flow rate sensor was not able to pick up the fault as early as the other two variables. This is due partly because of the noise of the sensor, but also because the change in the controller output is small at first and then becomes enough to alter the inlet flow rate noticeably. As the sensor drift was increased, the inlet flow rate sensor was able to identify the faulty condition sooner and more reliably due to the larger change in the inlet flow rate. In order to reduce the number of false alarms, a sequence of observations was only deemed faulted if 10 residuals in a sequence of 250 were faulted⁷. The large sequence analyzed was again chosen due to the noise of the signals.

7.5. Remarks on Data-based Modeling

The AAKR model developed for the experimental flow control loop measurements was capable of predicting when a user-generated fault was added to the normal operation. The AAKR model

uses the motor current, pressure, inlet flow rate, PI controller output, and the valve position indicator for its inputs. The model was able to identify drifted inlet flow rate sensor readings as well as a fault in the PI controller output. For each user-generated fault, multiple predictor variables were capable of identifying the fault providing a robust system for identifying deviations in the loop's normal behavior.

While the AAKR model used in this research was applied to a small flow control loop, the principles are the same for use in a nuclear power plant. The implementation of an empirical modeling technique such as auto-associative kernel regression could be attractive for SMR designs. Once a model could be trained with the normal operating conditions of the reactor, an on-line monitoring system could be developed to monitor sensor residuals to ensure the safe operation of the reactor. Sensor drift is a common problem in reactor that affects both safety and economics and could easily be monitored using an AAKR model. Furthermore, if SMR designs are to keep their proposed longer operating cycles, sensor drift must be monitored and kept to a minimum throughout the operating cycle.

8. DEVELOPMENT OF A LABORATORY WIRELESS DATA ACQUISITION AND COMMUNICATION SYSTEM

8.1. Introduction

This task is included in the project as part of the laboratory demonstration of data acquisition and communication using wireless networks. Recently, there has been growing interest in designing and developing wireless systems in nuclear power plants, starting with implementation in non-safety systems [88]. In light of the accident at the Fukushima Dai-ichi nuclear station, there is increased interest in incorporating such systems for applications during severe accidents and post-accident recovery. Benefits of wireless systems include lower installation costs, improved safety, and improved awareness of the condition of equipment throughout nuclear power plants.

The goal of this research task is to demonstrate that wireless communication is competitive with current wired systems of data acquisition and communication and can be used to reliably and safely monitor conditions throughout a nuclear power plant. These wireless systems can easily be installed in power plants to monitor equipment that is not currently monitored due to cost concerns.

The first part of the research involved assessing the requirements that a successful wireless system would need to have in order for it to be trusted for installation. Next, a list of different forms of wireless communication was compiled that met the criteria for a successful system and they were compared to decide which form of wireless communication would work best for use with instruments in reactors. Once a form of communication was selected, a system was designed that could be installed in the laboratory setting for extensive testing. The wireless system was designed to acquire data from several instruments and wirelessly communicate the acquired data from the instruments to a computer in the local area where the data are then processed. After the system was designed, the wireless hardware and the accompanying software were installed in the experimental flow control loop where it acquires the data for comparison with the wired system. Effectiveness of wireless communication through this system is the focus of the research. For this research a series of different types of tests are run on both the new wireless instrumentation system as well as the fully wired system. The resulting data from the two systems are then compared to verify that the wireless system operates as efficiently and accurately as the wired system.

8.2. Overview of Wireless Communication

Wireless communication is used in every industry in modern day society because of its versatility and flexibility in implementation. Most of the wireless communication in industry use different wavelengths of electromagnetic waves to communicate data from one point to another. The electromagnetic waves must go through a process called modulation where the waves are customized to the data.

The modulation alters the wave in one of several ways. For example, an AM radio transmits data through amplitude modulation where the amplitude, or height, of a wave is either increased or decreased to communicate the data. An FM radio uses frequency modulation where the frequency of a wave is increased and decreased depending on what data is transmitted. When a signal is received from a modulated wave it is demodulated to recover the original signal. Demodulation reverses the waves amplitude or frequency back to a form that can be read and understood by a computer. There are many different forms of modulation, making wireless communication very versatile. Home routers, for example, use a much more complicated form of modulation to communicate data effectively. Another aspect of variety in wireless communication lies in the overall architecture of the set-up of transmitters and receivers.

The architecture of a wireless system can be tailored to the specific needs of each system. A simple system may only have one transmitter communicating to one receiver, while a much more complicated system can integrate countless receivers and transmitters in a seemingly endless web of communication. For research purposes there are several options available: A wired system (illustrated in Figure 8.1) uses wires to communicate data from several sensors to a central hub (or chassis) where the signals are digitized and communicated to a computer where they can be analyzed. The downside of having a fully wired system, however, is that the wires are very expensive and not easily adaptable.

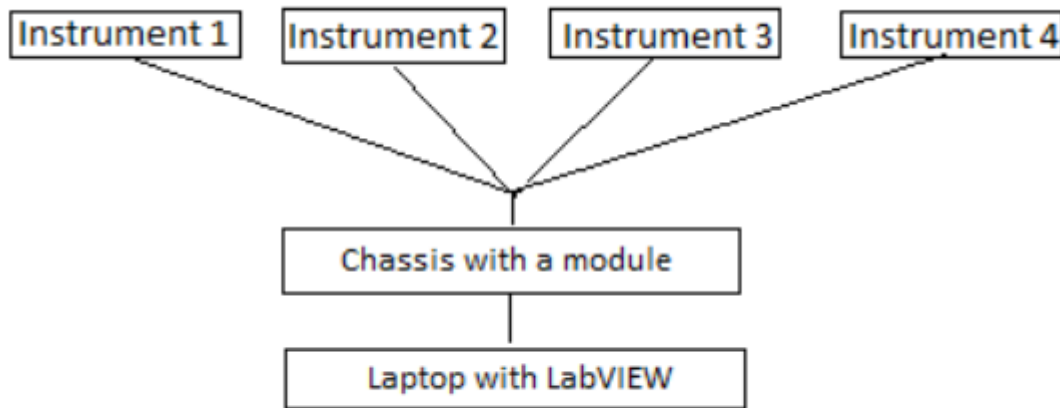


Figure 8.1: Wired Data Acquisition system

A fully wireless system of communication in (see Figure 8.2) is commonly used by many industrial processes and research laboratories. The instruments wirelessly communicate data to a hub where the data are collected and sent to a computer wirelessly where they can be analyzed.

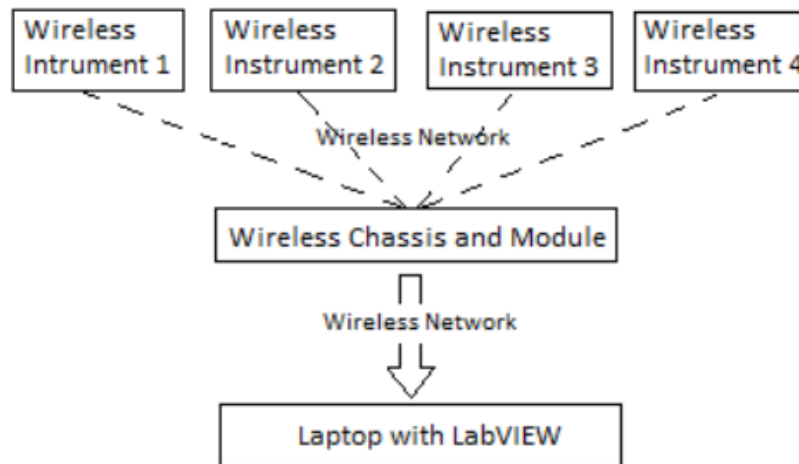


Figure 8.2: Fully Wireless Data Acquisition System

A system that is partly wireless and partly wired (Figure 8.3) is also very common in research because it only requires the replacement of a wired chassis with a wireless chassis when converting a wired system to a wireless system. This eliminates the need for a computer to be located right next to the equipment in a lab and gives researchers many more options.

A complicated form of wireless communication architecture is commonly called a mesh

network where all of the instrumentation can also act as a receiver (Figure 8.4). This drastically improves the safety and reliability of a wireless system. Each instrument works as a receiving hub as well as a transmitter, which means that the information from other instruments can be directed through one individual instrument if another hub fails.

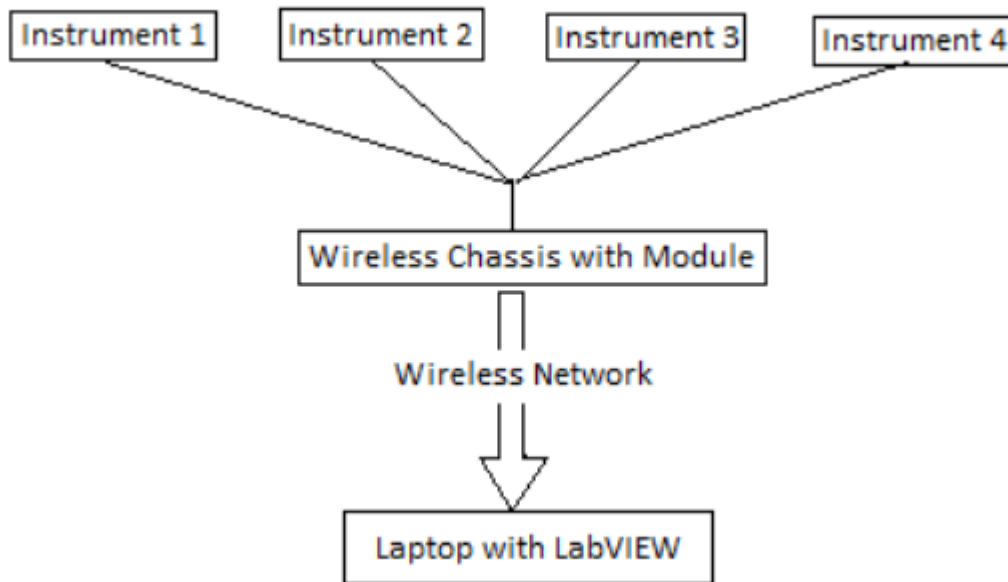


Figure 8.3: Wired data routing from sensors and wireless data transmission.

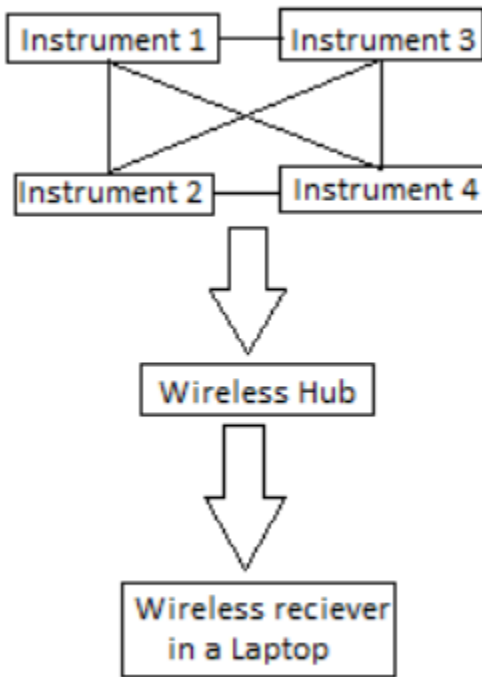


Figure 8.4: Wireless sensor network with cross-communication

8.3. Literature Review and Summary of System Development

The following steps were performed to accomplish the laboratory wireless data acquisition and transmission:

- A. Determined the necessary properties of a wireless data acquisition and communication system in a nuclear power plant
- B. Determined which form of wireless communication would be best suited for the nuclear power plant environment
- C. Designed the system architecture that would be most practical for laboratory testing of the effectiveness of wireless communication
- D. Selected and purchased the necessary hardware and software
- E. Installed the wireless system on the flow control loop in the laboratory
- F. Installed LabVIEW on a laptop and wrote programs to read and present the data
- G. Ran initial tests of the wireless system with one instrument until fully operational

- H. Set up system with four instruments
- I. Ran a few different tests on both the wired and wireless systems and compared the data to show how closely the two systems correlate
- J. Ran both systems simultaneously during a variety of tests and compared the resulting data
- K. Made conclusions on how well wireless communication performed compared to wired communication

Several reports on wireless communication were reviewed to get an understanding of what specifications a successful system would need. The main document used for this was a report by Analysis and Measurement Services Corporation (AMS) [88], *Wireless Sensors for Predictive Maintenance of Rotating Equipment in DOE's Research Reactors*. The document reviewed the use of wireless communication in non-safety applications.

The goal of research and development at AMS was to design and build an Equipment Health Monitoring System (EHMS), a wireless data acquisition and communication system that monitored the rotating equipment at Oak Ridge National Laboratory's High Flux Isotope Reactor (HFIR), and analyzed the condition of the equipment. The EHMS collected vibration data from several instruments located on the equipment and used that data to predict when the equipment needed maintenance. The EHMS helps increase the safety of the reactor by ensuring that faulty equipment gets replaced or fixed before they reach a point where they fail completely during the operation of the reactor. One example of equipment monitoring on rotating equipment in the HFIR is the monitoring of the cooling tower fan motors. Vibration and ultrasound sensors are installed on the fan motor bearings, and the acquired data can help reveal the condition of each fan motor. The sensors are connected to a wireless transmitter from National Instruments, where the data is communicated to a wireless repeater that in turn communicates it to a receiver connected to the data acquisition and analysis workstation. The data are analyzed by software at the workstation and the staff at HFIR can assess the condition of the fan. The report by AMS gave a good understanding of what types of wireless systems are used and how they are set up. Once that was established, research could be done on how well those systems worked compared to wired alternatives.

The form of wireless communication that was used in the report by AMS as well as many other industrial wireless systems is known as IEEE 802.11. It was clear that this form of

communication would work the best due to the fact that it is versatile, secure, and reliable. There are however several subcategories of IEEE 802.11 that include 802.11a, b, g, and n. The differences between these subcategories come from differences in their data rates, band widths, and modulation techniques. The subcategory that was chosen for implementation in the laboratory was the newest, most advanced standard, IEEE 802.11n.

The next step in the research process was assessing and determining which wireless system architecture would work best with research. For research purposes the most effective system architecture is a system that has instruments that are wired to a chassis where the data are digitized and wirelessly communicated over a wireless network to a receiver in a laptop as seen in Figure 8.5. The selected system is better than a fully wireless system simply because it eliminates the use of separate sensors which could affect the quality of the data.

The specific hardware devices that are used in the wireless data acquisition and communication system include:

- a. Wireless transmitter- NI cDAQ-9191
- b. Wireless Router- Netgear N600 Wireless Dual Band Router WNDR3400
- c. Wireless modules- NI 9201 and NI 9234
- d. Instrumentation- Orifice Flow Meters, Turbine Flow Meter, and Accelerometers.

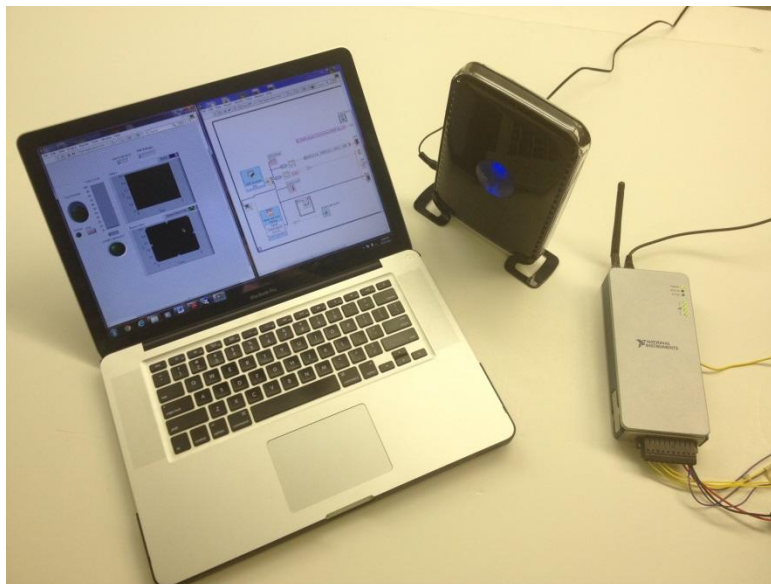


Figure 8.5: Wireless System Equipment

8.4. Testing the Wireless Data Acquisition and Transmission System

After the system was fully installed, several initial tests were run on both the new wireless system and the wired system. The data from these tests were compared to see how closely the wireless system matched with the wired system.

The tests that were run during this quarter involved taking different types of measurements on an experimental flow loop. The first test that was run involved fixing the inlet flow into a tank and measuring the tank level over the time it takes to fill up with both the wired and wireless systems (Figure 8.6). This helps to show how close the two systems actually match in a basic measurement situation.

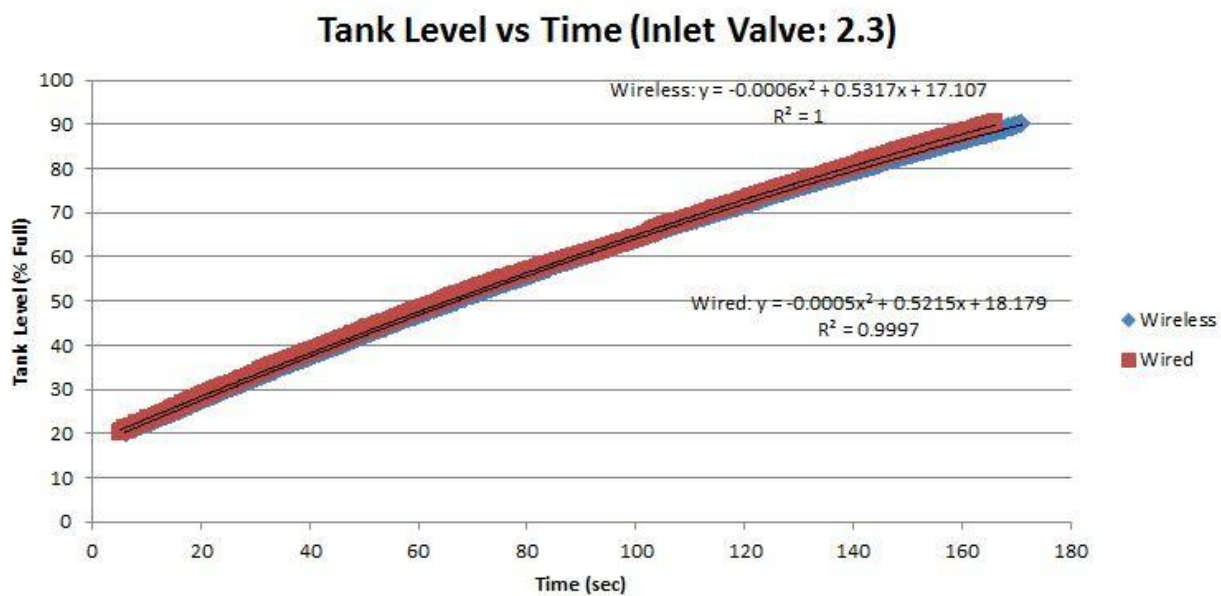


Figure 8.6: Tank Level vs. Time Initial Test

The next test that was conducted involved slightly changing the pump frequency and observing the resultant change in flow through the flow loop. The flow was measured with a turbine flow meter and the average flow rate was calculated for frequencies between 55.0 Hz and 60.0 Hz (Figure 8.7). After testing both the wired and wireless systems it became clear that the performance of the wireless system was close to that of the wired system. The slight difference between the two plots came from calibration differences between the two systems. The calibration that works with the wired system is not compatible with the wireless system, however the difference between the wired and wireless plots are insignificant if you consider the scale of the measurements taken.

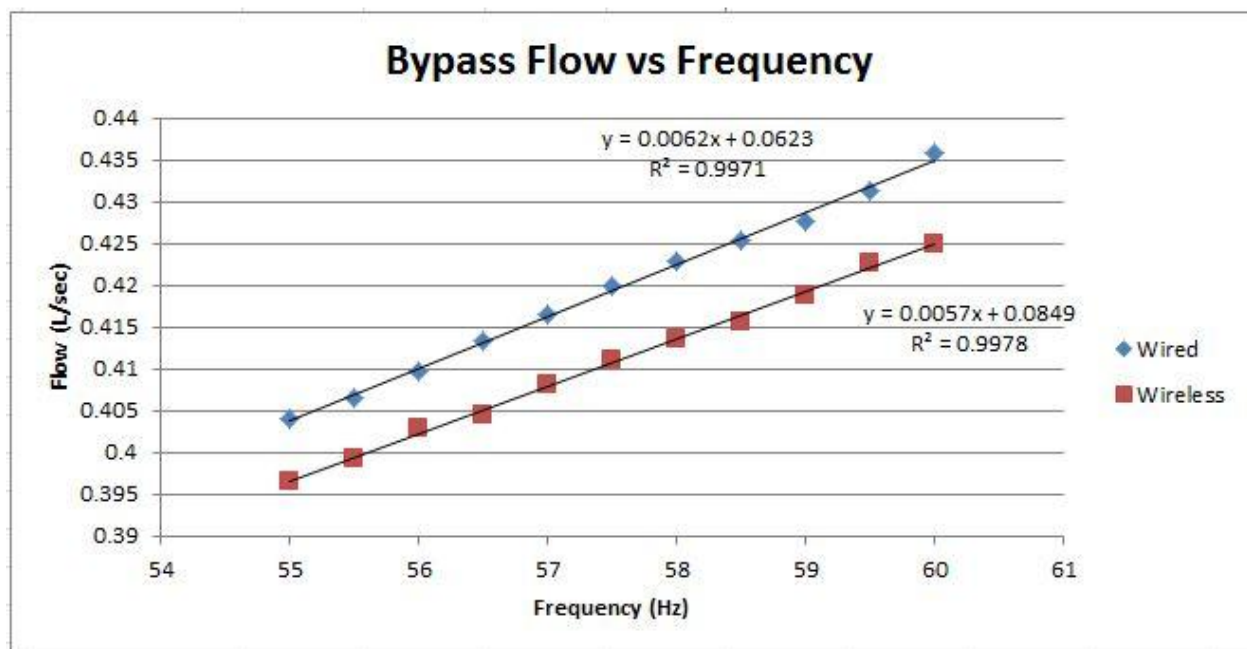


Figure 8.7: Bypass Flow vs. Frequency

The next test was much more demanding on both the wired and wireless systems. The flow loop uses a submersible pump to circulate the water through the piping. This submersible pump has accelerometers attached to the top and to the side that measure the vibrations of the pump while it is operating. The vibration data (Figures 8.8. and 8.9) were taken over several minutes while the pump was operating and the wireless system performed very well compared to the wired system.

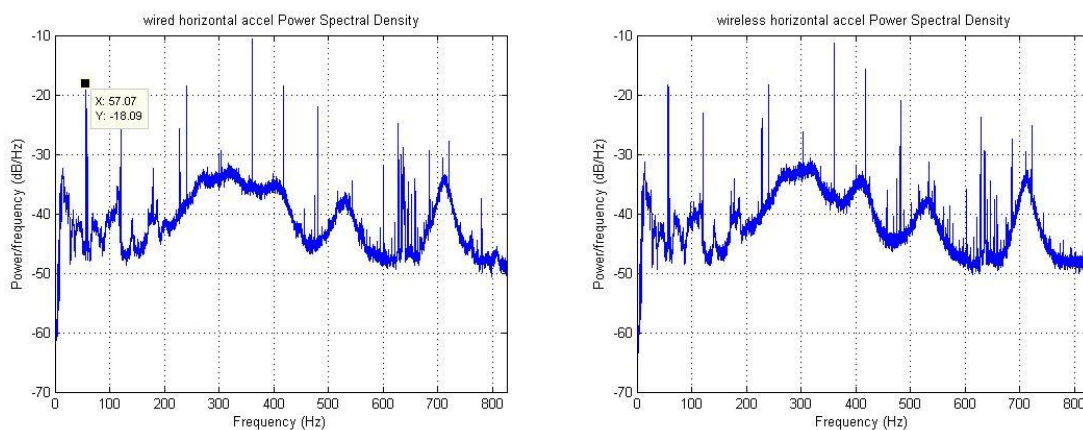


Figure 8.8: Power Spectral Density of Horizontal Acceleration

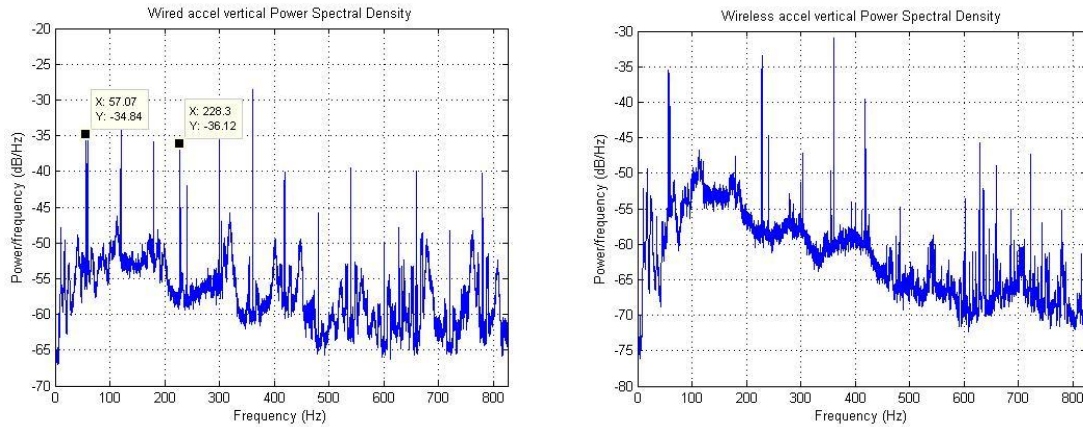


Figure 8.9: Power Spectral Density of Vertical Acceleration

The next tests were run simultaneously on both the wired and wireless systems at the same time. The first simultaneous test involved opening the inlet valve to allow the tank level to rise to above ninety percent and then the inlet valve was closed allowing the tank to drain. This helped show how well the two systems measured the tank level signals as well as the inlet flow signals. The graphs help show that the two systems were very similar in performance (Figures 8.10 and 8.11).

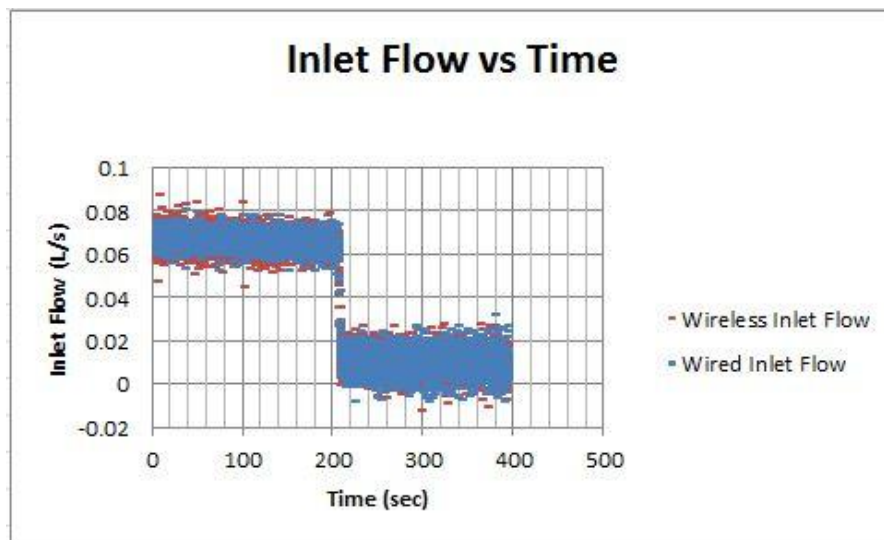


Figure 8.10: Inlet Flow vs. Time

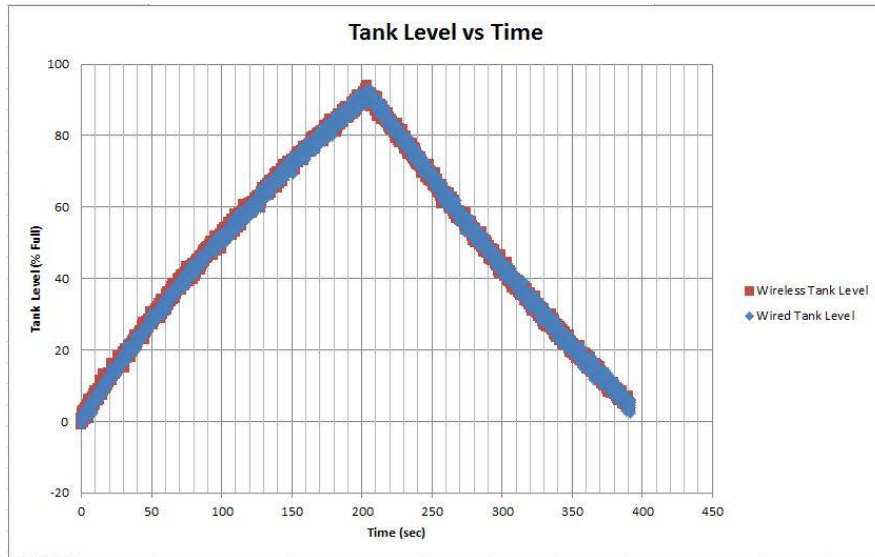


Figure 8.11: Tank Level vs. Time

The final test that was completed tested the dynamics of both the wireless and wired systems. This was done by manually opening and closing the bypass valve to random points and observing the how well the systems react to these changes. The bypass flow, inlet flow, and tank level were measured to observe how well the data acquisition systems performed (Figures 8.12, 8.13, and 8.14).

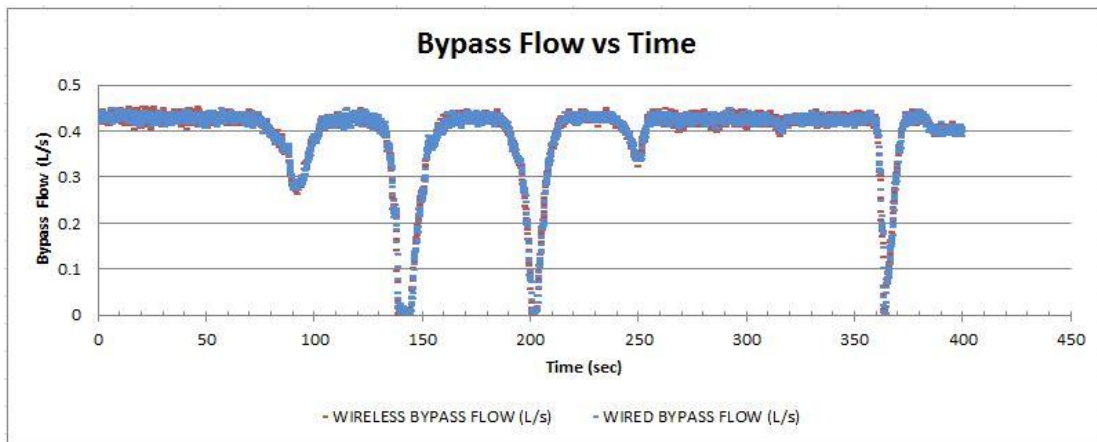


Figure 8.12: Dynamic Test: Bypass Flow vs. Time

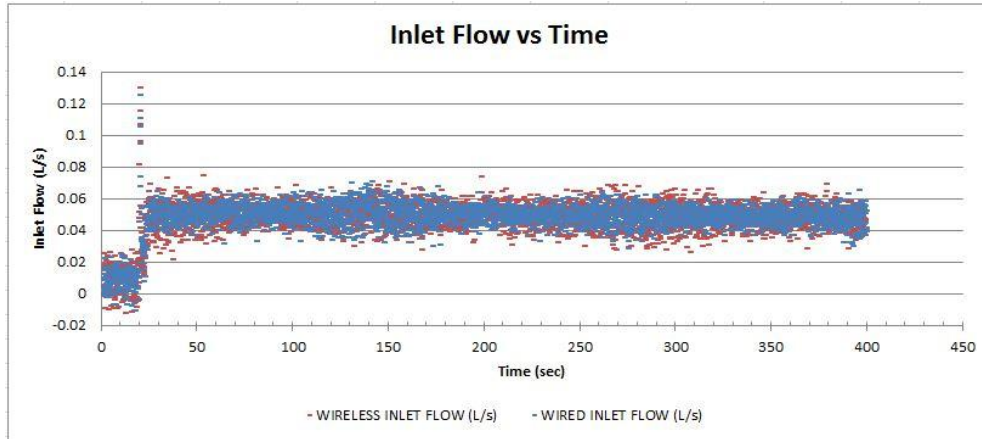


Figure 8.13: Dynamic Test: Inlet Flow vs. Time

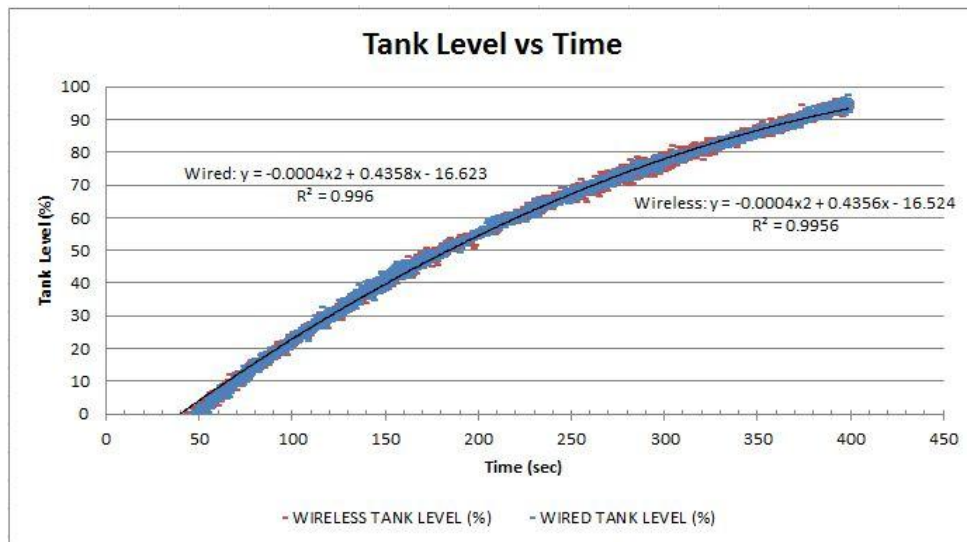


Figure 8.14: Dynamic Test: Tank Level vs. Time

8.5. Remarks on the Implementation of Wireless Data Acquisition

After extensive testing of both the wireless and wired data acquisition systems, it was determined that wireless communication can be just as accurate, dynamic, and reliable as wired communication. Wireless communication has the potential to completely and effectively replace wired communication in data acquisition systems. These tests had proven that it was possible, with further research and development, to make wireless communication the main form of communication in nuclear power plants as well as any other industry where system monitoring is

necessary. Although regulations may prevent wireless communication from being implemented as a primary data acquisition system, wireless data acquisition systems could be added to non-safety systems in power plants to help add redundancy and increase reliability. These systems could be installed much quicker and at a much lower cost than wireless equivalents.

9. DEVELOPMENT OF A LOW-COST MICROCONTROLLER-BASED EQUIPMENT MONITORING SYSTEM

9.1. Introduction to Microcontrollers

During this project research was conducted into using microcontrollers as a cost effective data acquisition system. Microcontrollers are small, powerful computers that allow for several analog and digital inputs that can then be processed in a variety of ways. For this research the BeagleBoard XM microcontroller was chosen due to its superior processing power and 16-bit analog to digital converter (ADC). The BeagleBoard XM (BBXM) is a Linux-based embedded system that contains a 1 GHz ARM processor. This allows the microcontroller to process high frequency data such as accelerometer signals. The microcontroller is capable of monitoring a large variety of different signals with ease. To test the data acquisition system against the current data acquisition system installed in the experimental flow loop, it was decided to test the most demanding of signals, the accelerometer signal.

9.2. Setting up and Testing the BeagleBoard XM Device

Working with the microcontroller involved a full understanding of how to properly install the BBXM in a data acquisition environment and acquire data, which can then be processed. The BBXM needs an interface to receive and display commands. For this, software called PuTTY was used to allow Linux to be run in parallel with another computer's windows operating system.

The system that was used with the BBXM included connecting four different cables to the microcontroller. The first cable that was connected was the Serial-to-USB cable. This cable connected to the serial port on the BBXM and the USB port on the computer running Windows with the PuTTY software installed. The second cable was the Ethernet cable that connected to the Ethernet port on the BBXM and the Ethernet port that connects it to the network. The third cable that was used connected the BBXM to the accelerometer (see Figure 9.1). This cable was a BNC-to-Audio cable that plugged into the Audio In port on the BBXM. The BNC connector side of the cable was connected to a PCB Piezotronics Model 482C Signal Conditioner, which was in turn connected to the accelerometer on the submersible pump. The last cable that gets plugged

into the BBXM is the power cord. The power supply for the BBXM must be a 5 Volt, 2 Amp power supply. If the power supply is incorrect the BBXM will not accept it.



Figure 9.1: BBXM with all cords properly connected

Once all of the hardware is properly connected the PuTTY software is opened and a serial connection is selected. The Serial-to-USB cable is connected to a USB port that has a specific COM number. This number as well as the speed of the cable can be found using the device manager in Windows. The COM number and the speed of the cord are entered into the PuTTY main screen, where the user then clicks Open. This opens Linux command window that lets you communicate with the BBXM.

At this point the power supply can be plugged in and the BBXM would run its boot up

screen. The username and password can then be entered and the BBXM is ready for any commands. The next step is to find the IP address to connect the BBXM through the Ethernet cable. The “ifconfig” command is used to find the IP address, which is written as:

```
“inet addr:####.##.#.###”
```

This number is noted and the PuTTY window can then be closed and reopened. This time the connection type “SSH” is selected to connect the BBXM through the Ethernet cord that is connected to the same Internet network as the computer with Windows. The IP address is entered and the port number should be 22. Once this is completed and the BBXM boots up, the username and password are entered once again and it’s ready to be used to acquire data.

The BeagleBoard XM records data through the Audio In port using the “arecord” command this command allows you to customize which type of file to save the data as, how many channels, the sampling rate, the duration of the data acquisition, as well as the name of the file and many additional choices. Using “arecord –help”, or looking up the “man” pages on the Internet explains all these options. An example of a command input to acquire data:

```
“arecord -t wav -f S16_LE -c 2 -r 4000 -d 1 test.wav”
```

Once the data are acquired, they need to be moved over to the computer with windows where the data are processed using MATLAB. To transfer the data, the command window on the computer with Windows is opened. This can be done by searching for “cmd.exe” and opening it. Once it is opened the directory needs to be changed to the same directory that contains the PuTTY software by using the “cd” command followed by the location of the directory. In order to securely transfer a file, a file named “pscp.exe” may be used, that allows a file to be copied securely from the BeagleBoard XM to the computer with Windows. To actually transfer a file the following command can be used:

```
“pscp.exe root@####.##.#.###:/home/root/test.wav C:/LOCATION_OF_PSCP.EXE”
```

The first term following the pscp.exe command is the location of the file on the BeagleBoard XM where the pound signs represent the IP address found using the “ifconfig” command. This location may be different on different Beagleboards. The second term following the pscp.exe command is the location that you would like the file to be copied to, preferably the

same file that contains the pscp.exe file. This entire second term can sometimes be replaced by a simple “.”, which tells the computer to copy the file to the current directory.

In order to compare the two different data acquisition systems, a test was run with the National Instruments data acquisition system. This test involved operating the pump under normal conditions at a frequency of 60 Hz. The NI DAQ acquires data at a sampling rate of 165Hz. The pump was allowed to run for a minute while data was acquired. These data were processed and the accelerometer was then connected to the BeagleBoard XM.

The Beagleboard XM is capable of acquiring data at any sampling rate between 4,000 Hz and 48,000 Hz. The pump was once again operated under the same conditions with the minimum sampling rate of 4,000 Hz for a period of 60 seconds. This data was also processed and the performance of the two systems was compared.

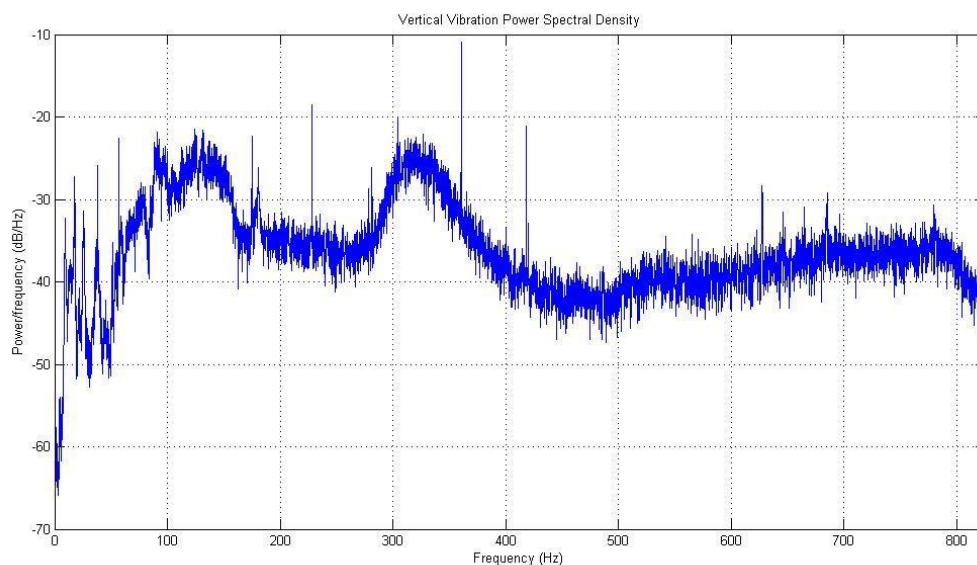


Figure 9.2: Power Spectral Density of accelerometer data using NI DAQ system.

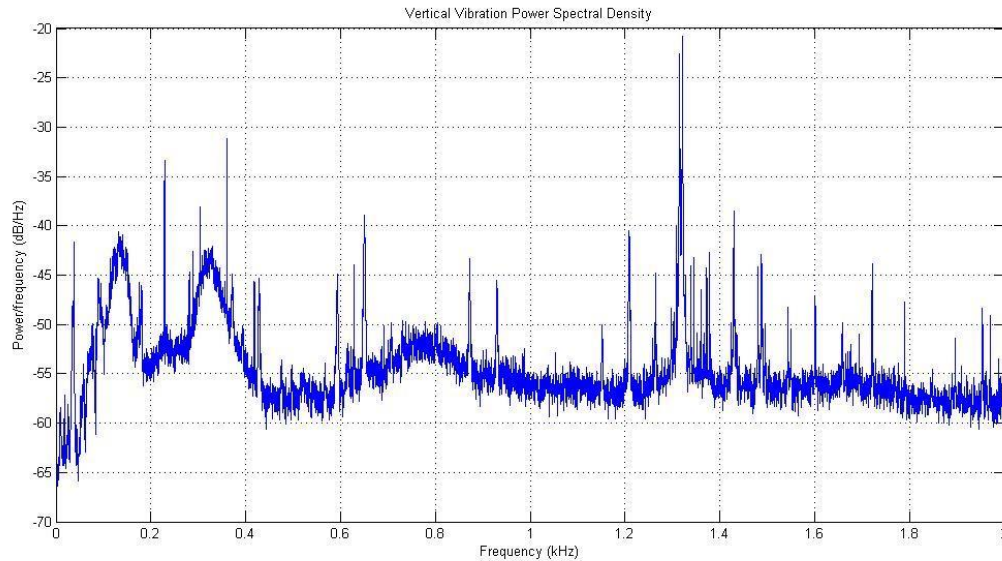


Figure 9.3: Power Spectral Density of accelerometer data using BBXM DAQ system.

The frequency spectra of the data acquired using the NI-DAQ and the BeagleBoard devices are shown in Figures 9.2 and 9.3, respectively. Comparing the data up to the frequency of 800 Hz, the performance looks very similar. The BBXM is a high quality data acquisition system that comes at a fraction of the cost of the currently implemented data acquisition system. These microcontrollers would be ideal for monitoring equipment in almost any scenario. The implementation of such systems may take some time to complete due to fact that they are not yet commonly used, but a competitive, low-cost data acquisition system could be developed for a large variety of situations.

9.3. Evaluation of a Consumer Electronics-Based Data Acquisition System for Equipment Monitoring (ORNL)

9.3.1 Introduction

A preliminary evaluation of the performance of a consumer electronics-based data acquisition system (DAS) has been performed by ORNL as part of the NEUP project *In-situ Condition Monitoring of Components in Small Modular Reactors (SMR) Using Process and Electrical Signature Analysis*. The motivation for this evaluation was the potential for drastically reduced per-channel costs of these systems compared to systems that use conventional DAS

electronics and instrumentation. While it was not anticipated that systems using consumer grade electronics would be suitable for use in nuclear applications, there exists the possibility that these systems could be used in balance of plant monitoring applications.

The evaluation was performed by assembling a 20 channel DAS using a combination of development level board CPUs, MEMs accelerometers, and consumer grade electronics. Four conventional PCB accelerometers were included in the system. The DAS was installed on a Central Engineering Plant (CEP) chiller and cooling water pump in ORNL Building 5600 – these components are part of the chiller system used to cool ORNL’s Titan supercomputer.

9.3.2 Consumer Electronics-Based DAS Architecture Description

The DAS system is based on several inexpensive consumer electronic components. Yet, while the costs are relatively low, the capabilities of each component yield a system design that is remarkably robust and provides high-performance and radical scalability. The system consists of three main functional subsystems as shown in Figure 9.4; the data source, the data stream manager, and the analytics. All three subsystems are integrated over a standard Ethernet network using secure SSH tunnels and NFS file mounting methods.

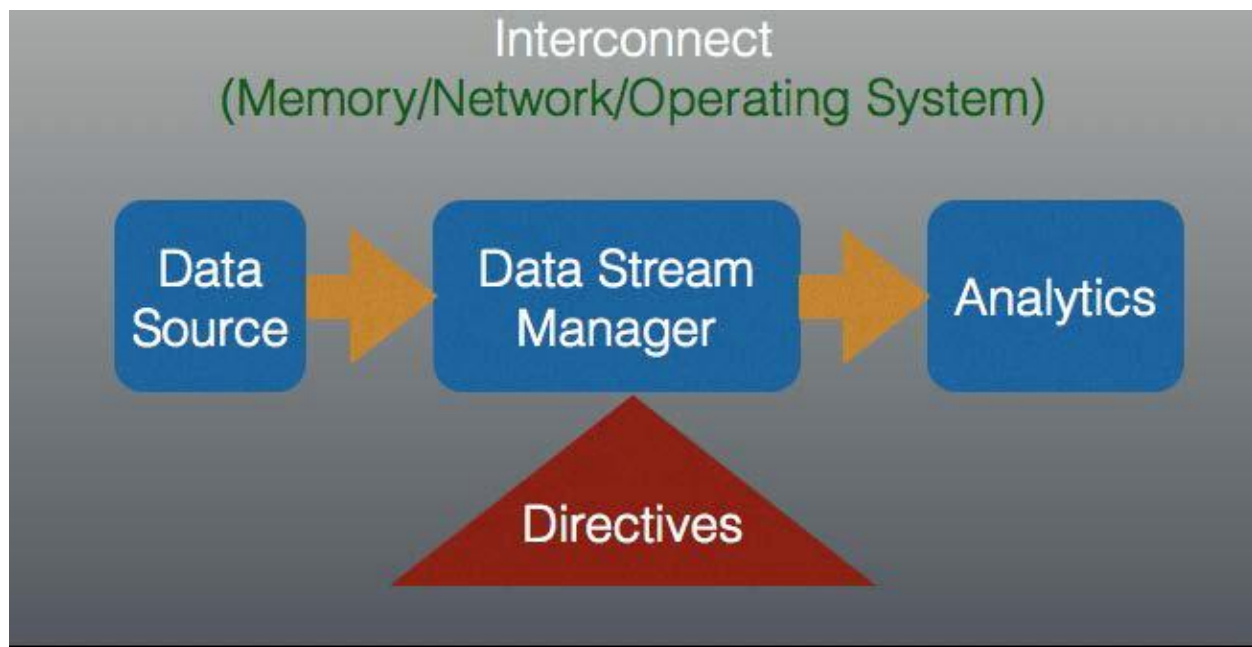


Figure 9.4: The three main functional subsystems.

The data source subsystem is the heart of the DAS where the signal digitization takes place. The basic system design was replicated twice to provide the twenty-channel capacity. The main part of the data source subsystem is a pair of BeagleBoard-XM boards. Each board provides one integrated audio CODEC stereo channel pair. The channel count is expanded to ten for each BeagleBoard-XM by adding four additional stereo audio CODEC USB-7.1 modules. These interface to the BeagleBoard-XM via four USB ports.

Signal conditioning for the system is implemented two ways. Each BeagleBoard-XM processes two channels of PCB accelerometers that are conditioned by PCB amplifiers. Eight additional channels for each BeagleBoard-XM are implemented using Analog Devices MEMS accelerometers along with signal conditioning provided by Texas Instrument instrumentation amplifiers. The BeagleBoard-XM's operate under the Angstrom Linux operating system that is configured and stored on a micro-SD memory card. The onboard Ethernet connection is used to connect to the ORNL network. The remaining items are various terminal blocks, internal connection wiring, signal cables, and three power supplies.

The data stream manager is a software application written in Python that is responsible for the flow control of the sampled data. It receives the incoming stream of sampled data from the audio CODEC, buffers the data inside a five-minute ring buffer, exports the data to several types of output files, and monitors for operating system directives that specify actions to be taken with the data. The data stream manager produces a number of data products in the form of files.

A monitor file is continuously updated that contains the last second of sampled data. Other programs can access the monitor file for the purpose of real-time monitoring. Figure 9.5 shows one example of how the monitor file was used at ORNL. The spectra from all twenty channels are displayed in an array of subplots that are updated each second.

The data stream manager also produces a large data file that contains 300 seconds of data. This file is produced when an operating system trigger is received. Two forms of trigger are currently implemented; on-demand trigger and interrupt trigger where the data file is produced such that the time of the triggering event is in the middle of the data file.

The third type of data product is called the historical assessment file. It contains four-second snapshots of each channel taken hourly. These snapshots are appended into a file and retained over the entire operational life of the system.

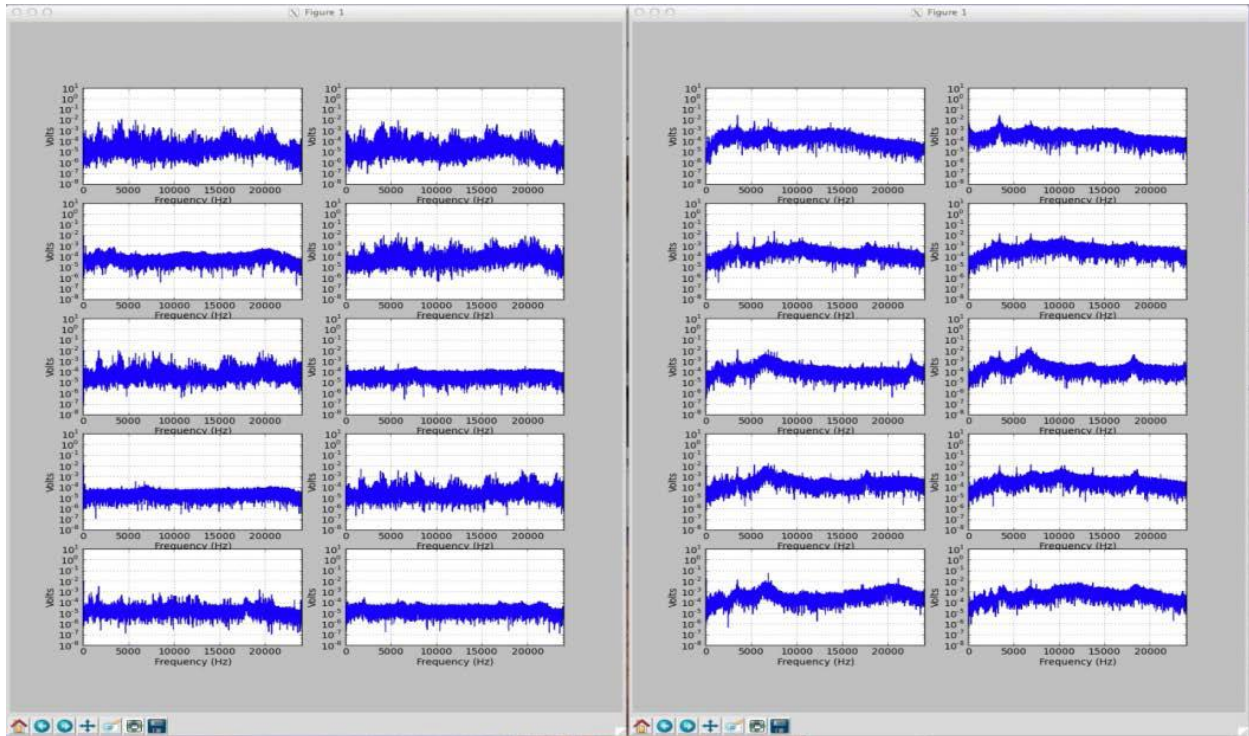


Figure 9.5: Frequency plots of all 20 channels in the CEP acquired remotely over the ORNL network

The last remaining subsystem of this design is the analytics. The analytics provides all required signal processing and data presentation functionality, both for real-time monitoring and display as well as any numerically intense post-processing. Like the data stream manager, the analytics is implemented with standard desktop PC hardware. However, more choices are available for which operating system is used in the analytics subsystem as well as the applications. Linux, Windows, and Mac-OS were successfully used at ORNL. Python and MATLAB were also used for the data processing application.

The overall design of the DAS can be further expanded in scale by adding more data source subsystems and more data stream managers. This distributed architecture was chosen intentionally so the DAS design could scale and accommodate a deployment of over 11,000 data source subsystems as required by one sponsor.

9.3.3 System Installation Description

Transducer selection is a critical step in building an effective monitoring system. Solid state accelerometers were developed as a cost effective sensor for applications such as air bag

deployment and other similar binary operations. The emergence and maturity of micro-electronic mechanical systems (MEMS) accelerometers presented an opportunity to evaluate and re-purpose these low cost sensors in a typical balance of plant monitoring scenario. Within this DAS system 16 Analog Devices MEMS sensors² were used as well as four Standard IEPE piezoelectric industrial accelerometers from IMI, a division of PCB.

The 1,200 ton chiller shown in Figure 9.6 and the standard 3,000 GPM chilled water pump shown in Figure 9.7 are typical of almost any large industrial facility. The pump spans the range of most industrial/commercial rotating equipment with an electrical driving component, shaft and coupler, and a driven component on a common base; the chiller provides a more specialized example of a piece of industrial rotating equipment. This equipment was a good pairing for evaluating the entire system from sensor, to digitizer, to processor boards, to Ethernet connection, to final data stream available for detailed analysis.



Figure 9.6: 1,200 ton chiller



Figure 9.7: Chilled water pump

Sensor placement was done per typical machinery diagnostic methodology i.e. radial at each inboard and outboard bearing location and at least one thrust load measurement point on the structure. Mounting was accomplished with magnetic attachment as an acceptable means of temporary mounting on the equipment. The MEMS sensors were procured as demonstration boards from Analog Devices.

The sensors required different signal conditioning. The IMI sensors required a power supply and amplifier to supply 4-20 mA at 24 volts; the amplifier drives a high impedance analog-to-digital converter with an AC coupled signal. The MEMS sensor required a TI amplifier to provide sufficient current to drive the analog-to-digital converters. Figure 9.8 shows the electronics enclosure in a standard Hoffman box. At top left is the IMI signal conditioning on a DIN rail mount, directly below that are the two stacked BeagleBoard-XM boards. The green boards in the center are the TI amplifiers for the MEMS devices, and the pink boxes below them are the audio two-channel USB analog-to-digital devices. Power supplies are on the bottom of the box and the rest of the wiring are the input and output cables. The system is installed in close

proximity to the chiller and supports 20 channels of sensors with cable runs of 100 feet or less.

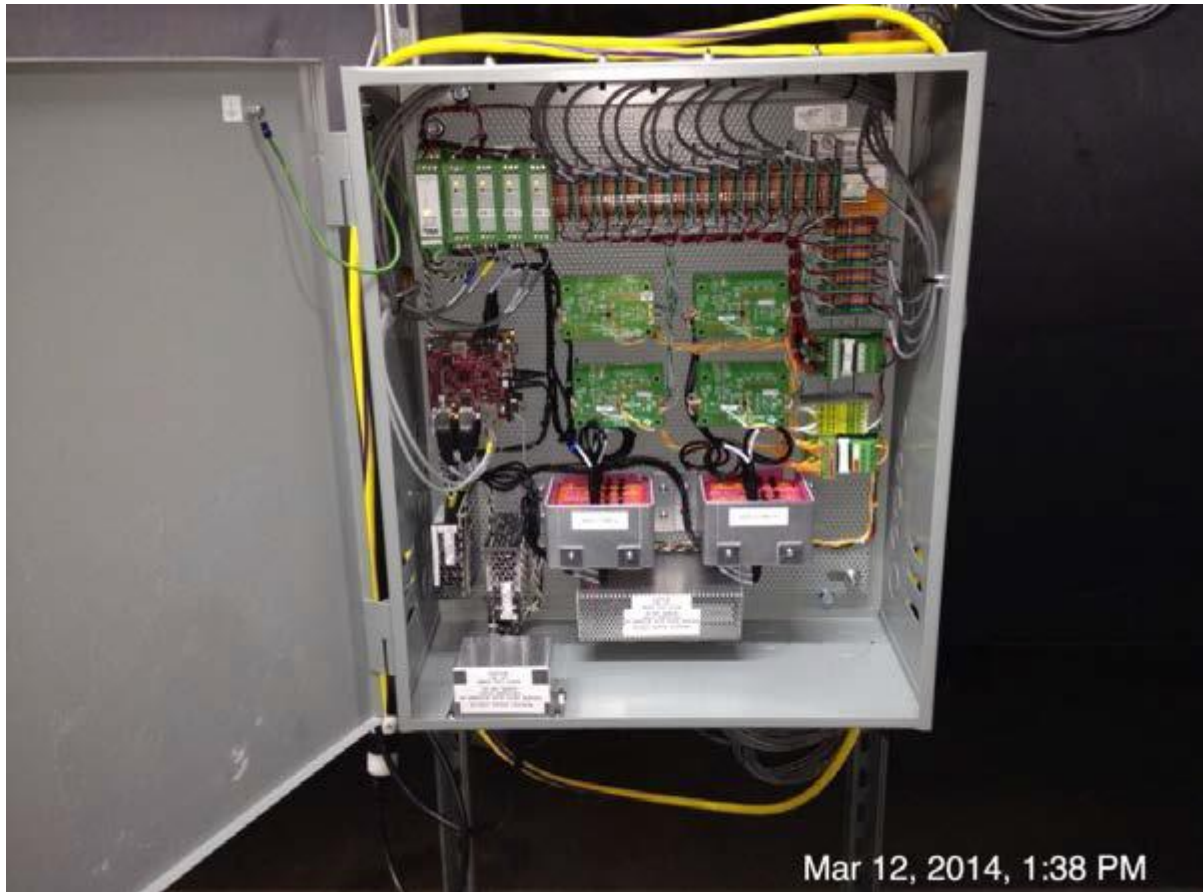


Figure 9.8: DAS electronics enclosure.

9.3.4 Data Analytics for Routine Machine Health Assessment

The system produces three types of data product. The monitor file is a one second snapshot of the current data buffer and is overwritten each second. Its sole purpose is to allow implementation of real-time monitoring for easy assessment of channel behavior. A Python display application was developed that generates a screen like that shown in Figure 9.9; this screen is particularly useful when installing the system because it allows easy verification of sensor and channel performance. Two other file types are produced that are intended for post-acquisition analysis.

For detailed analysis, a 300 second long file can be produced. This file contains over 14 million samples for each sensor at a rate of 48,000 samples per second. Commercial analysis

tools such as MATLAB were found to be very effective to perform this more in-depth processing.

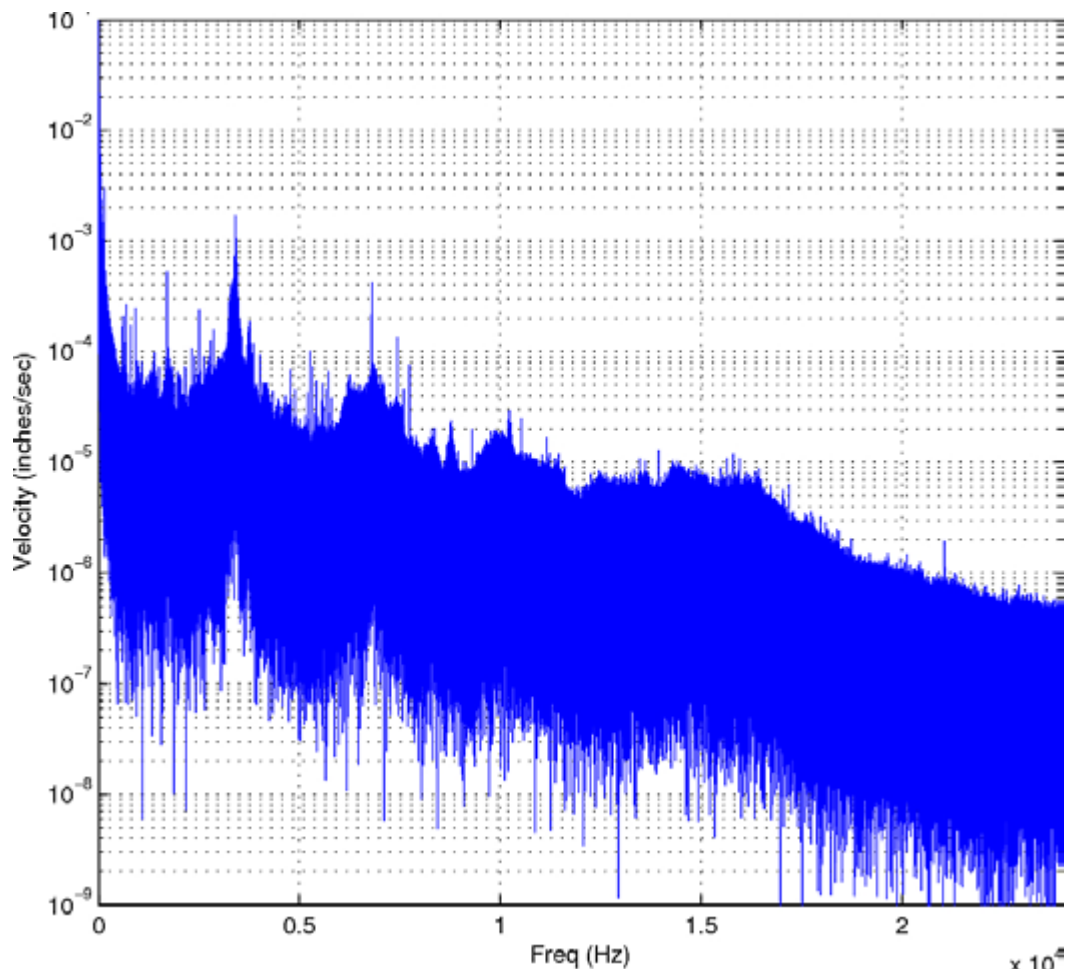


Figure 9.9: Narrow band plot of entire spectrum (7 M+ points)

A historical assessment file is also produced. This file contains a time-ordered sequence of four-second snapshots of a channel pair taken at one hour intervals with each successive sample appended to the end of the file. The data from the historical assessment file can be displayed as a waterfall plot; an example is shown in Figure 9.10. The lower part of the plot reflects data that was acquired on March 12, 2014 while the upper portion of the plot reflects data acquired on August 25, 2014. Individual tones show up as vertical lines. White gaps in the plot are gaps in the data. These gaps were caused by electrical power outages to the service supplying power to the DAS.

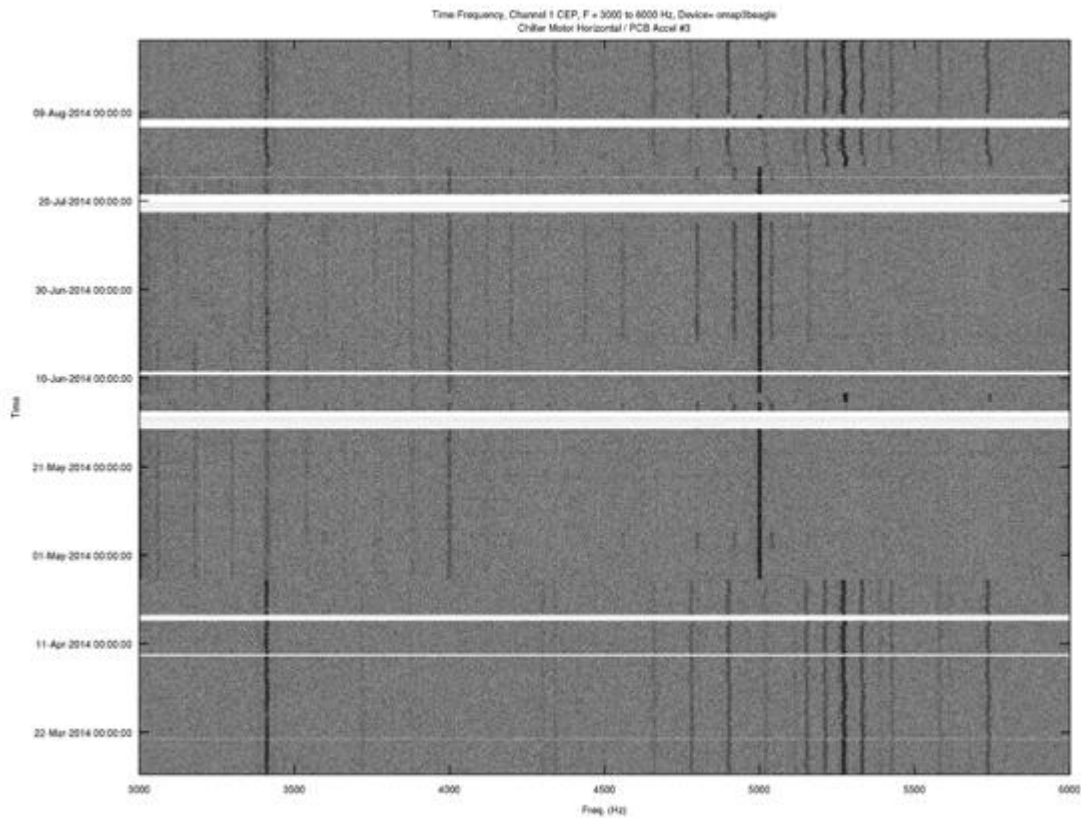


Figure 9.10: Time-frequency plot of a PCB accelerometer attached to the 1,200 ton compressor

Energy band trend line plots are also produced from the data. An example is shown in Figure 9.11. The trend lines shown for two sensors are for the 2 KHz band, which is 2 KHz wide.. Currently, this may be the most important reporting from our data analysis because it shows quite effectively how energy content in the vibration signal is trending over the operating history of the machine.

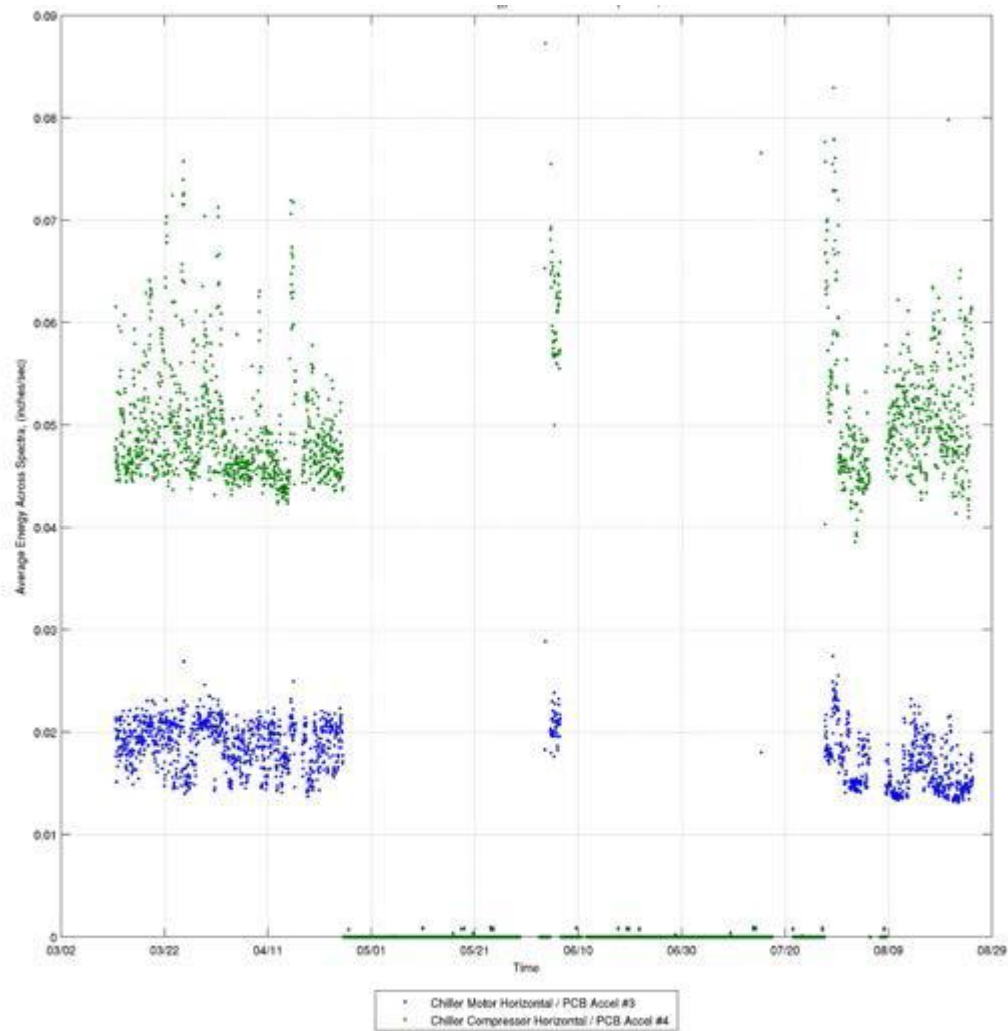


Figure 9.11: Band-average energy trend, Band 2 (centered at 2 KHz)

9.3.5 Evaluation of Consumer Electronics-based DAS Performance

The consumer electronics-based system exhibits remarkably good performance even though it is a 16 bit system. Being a consumer audio system, its maximum input is limited to 1-volt RMS instead of 10-volt RMS; this limitation immediately results in a loss of 30 dB of dynamic range. This dynamic range loss immediately requires that the system designer carefully consider the type and output range of transducers during system design. The sample rate for the audio system has been standardized for 44 kHz or 48 kHz, considerably slower than the higher rates typically used by instrumentation grade hardware.

Phase matching between the IMI sensors, whose two channel analog-to-digital hardware

share a common clock, appears to be very good. Because there is no master clock or synchronous buss in the consumer grade system, these data channels have no phase relationship, making techniques such as Operating Deflection Shape Analysis or Modal Analysis unavailable. This lack of phase information presents an area for improvement in future system design.

Comparison of the IMI sensors and the MEMS sensors showed that the frequency responses of the two sensors differ. Figure 9.12 shows snapshot FFTs from both sensor types at the same geometric location and the same instance in time. The plots differ in overall characteristics as well as noise floor. Signal processing such as averaging may eliminate some of these differences; however the MEMS sensor selected is only one of many different types of MEMS on the market. The major frequency peaks are in both signals and the individual sensor characteristics will require further evaluation and testing to fully quantify the absolute differentials between them.

Instrument grade data acquisition systems average costs range from \$800 to \$2,000 per channel depending on speed, overall data rate and throughput, and system options. These costs do not include sensors or cabling or outboard signal conditioners, or any software to operate the system or analyze the data. Additional costs for networked data storage and multiple user access for commercial systems begin in the \$20K - \$100K price range and have significant yearly maintenance fees.

The consumer grade system has a hardware cost of less than \$5,000 for the entire 20 channel system including the sensors and cabling. The software is based on public domain based resources and is configurable from one system to another. Thus, once a monitoring system is developed and installed for a specific application, it can be efficiently duplicated or modified to expand the monitoring effort to multiple machines.

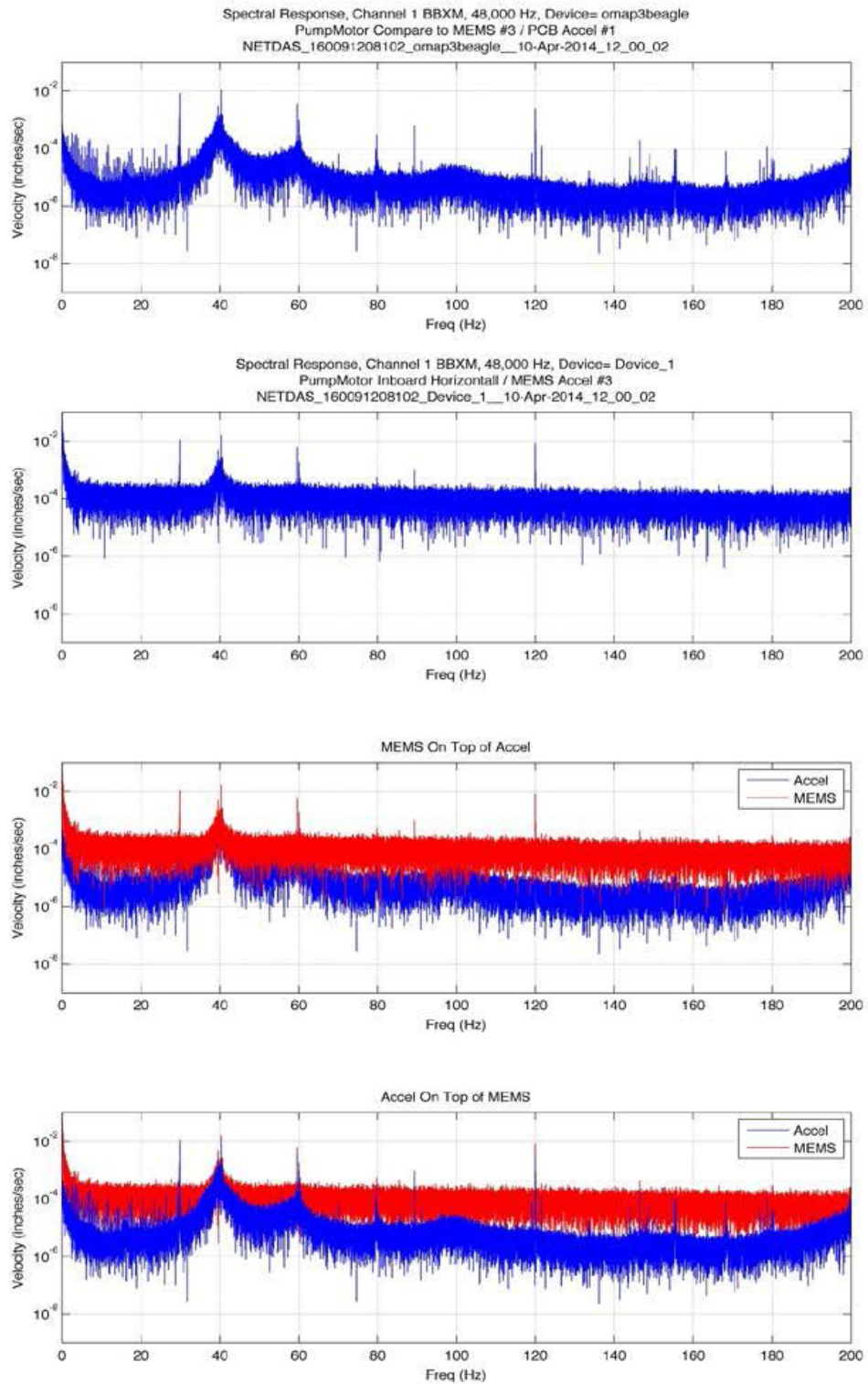


Figure 9.12: Snapshot FFTs from both sensor types at the same location and instance in time

9.3.6 Concluding Remarks

A preliminary evaluation of the performance of a consumer electronics-based data acquisition system (DAS) has been performed by ORNL as part of the NEUP project *In-situ Condition Monitoring of Components in Small Modular Reactors (SMR) Using Process and Electrical Signature Analysis*. Evaluation of the data provided by the consumer electronics-based system leads to the conclusion that for many industrial processes this system could form the basis for a cost effective means of obtaining operating health data in real time. While it is not anticipated that monitoring systems using consumer grade electronics will be suitable for use in monitoring reactor operating or safety systems, the possibility exists to apply these systems to monitor the operating health of balance of plant components.

The main advantage of these systems compared to conventional instrumentation grade systems is cost; instrument grade data acquisition systems average costs range from \$800 to \$2,000 per channel compared to a range of \$200 - \$400 per channel for a consumer electronics-based system. The potential low cost of these systems, combined with their reasonable monitoring performance and ease of upgrading, makes them an attractive alternative to conventional systems for industrial monitoring applications.

10. CONCLUDING REMARKS, SUMMARY AND RECOMMENDATIONS FOR FUTURE R&D

All the research and development tasks under this project (11/2011 – 10/2014) were completed. A summary of significant contributions of the project tasks presented in Volume 1 of the report is given in Section 10.2. Suggestions for future R&D work are outlined in Section 10.3.

10.1. Concluding Remarks

The primary goal of this NEUP funded research and development project was to develop and demonstrate in-situ equipment monitoring methods for small modular reactors (SMRs) with applications to reactor internals such as coolant pumps, valve-actuators, and control rod drive mechanisms. The overall objective was to integrate electric signature analysis (ESA) and process measurements to perform remote monitoring of SMR components. The primary reactor vessel in a typical SMR has limited space for the installation of control, safety, and system monitoring instrumentation. The focus of this research is to develop monitoring and diagnostics methods using easily accessible measurements. Both experimental and physics-based modeling approaches were developed to establish the feasibility of implementing such techniques and incorporate them during the SMR design phase.

Recent activities by light water reactor SMR vendors and developers (NuScale Power, Generation mPower, Westinghouse SMR, CAREM in Argentina, SMART design by KAERI, and others) have indicated an increased interest in the development of integral pressurized water reactors for deployment by 2025. SMRs in the 25-200 MWe range are useful for power supply in remote areas, especially in locations with limited infrastructure. SMRs can also be used for co-generation, combining electricity production and process heat for industrial applications, including water desalination. Because of the modular nature of SMRs and limited vessel penetrations, safety and security of such installations are greatly enhanced.

The research and development under this project was focused on the following three major objectives:

Objective 1: Identification of critical in-vessel SMR components for remote monitoring and development of their low-order dynamic models, along with a simulation model of an integral pressurized water reactor (iPWR).

Objective 2: Development of an experimental flow control loop with motor-driven valves and pumps, incorporating data acquisition and on-line monitoring interface.

Objective 3: Development of stationary and transient signal processing methods for electrical signatures, machinery vibration, and for characterizing process variables for equipment monitoring. This objective includes the development of a data analysis toolbox.

The project tasks were performed in collaboration with the Measurement Sciences and Systems Engineering Division of ORNL. All the tasks and deliverables were completed by the end of the project execution period. Volume 1 of the Final Report describes the results of R&D tasks under objectives 2 and 3.

10.2. Summary of Significant Contributions Reported in Volume 1

The following is a list of significant contributions of the project tasks described in Volume 1 of the Final Report:

- A detailed literature review of various SMR types and electrical signature analysis of motor-driven systems was completed. A bibliography of literature is provided at the end of this report. Assistance was provided by ORNL in identifying some key references.
- An existing flow control loop was upgraded with new instrumentation, data acquisition hardware and software. The upgrading of the experimental loop included the installation of a new submersible pump driven by a three-phase induction motor. All the sensors were calibrated before full-scale experimental runs were performed.
- A frequency controller was interfaced with the motor power supply in order to vary the electrical supply frequency. The experimental flow control loop was used to generate operational data under varying motor performance characteristics. Coolant leakage events were simulated by varying the bypass loop flow rate. The accuracy of motor power calculation was improved by incorporating the power factor, computed from motor current and voltage in each phase of the induction motor.
- A variety of experimental runs were made for steady-state and transient pump operating conditions. Process, vibration, and electrical signatures were measured using a submersible pump with variable supply frequency. High correlation was seen between motor current and pump discharge pressure signal; similar high correlation was exhibited between pump motor power and flow rate. Wide-band analysis indicated high coherence (in the frequency domain) between motor current and vibration signals.

- Wide-band operational data from a PWR were acquired from AMS Corporation and used to develop time-series models, and to estimate signal spectrum and sensor time constant. All the data were from different pressure transmitters in the system, including primary and secondary loops. These signals were pre-processed using the wavelet transform for filtering both low-frequency and high-frequency bands. This technique of signal pre-processing provides minimum distortion of the data, and results in a more optimal estimation of time constants of plant sensors using time-series modeling techniques.
- The experimental loop data indicate a clear relationship between motor power and pump discharge (flow rate). This relationship can be used to infer pump flow rate using the computed motor power.
- A laboratory scale wireless data acquisition and transmission network was developed and demonstrated successfully.
- A micro-controller based data acquisition and analysis module was developed and tested for monitoring machinery vibration. Such low-investment devices are attractive for monitoring a large number of similar plant equipment.
- A data analysis toolbox was developed for processing both the experimental loop operational data and wide-band sensor data. It includes all the computational functions that were developed and used in the project; these are classical data analysis and modern digital signal processing (DSP) techniques.

Other contributions include the participation by both graduate and undergraduate research assistants and information dissemination in the form of journal papers, conference proceedings, and presentations at national and international meetings.

10.3. Recommendations for Future Research and Development

It is anticipated that the results and deliverables of this R&D project would be useful in further developing and implementing remote monitoring and intelligence maintenance technologies in future light water SMRs and other integral reactors. During the course of the project and discussion with various collaborators, suggestions were made and ideas were developed for future research activities in extending instrumentation and controls strategies for advanced reactors. Because of the limited in-vessel volume, it is necessary to develop optimal strategies for sensor placement and new instrumentation for certain measurements. An example

of the latter is the measurement of primary coolant flow rate which is of a greater significance during transient operations and accident conditions.

Digital I&C and wireless implementations add to increased attention to cyber security. Topics of interest relating to plant control include R&D in fault tolerant control and the incorporation of resiliency under system/equipment/device anomalies and accident conditions. In some applications model-based control strategies may be used as a back-up or parallel control action that have the characteristics of anticipating control actions over a finite future horizon [120].

REFERENCES AND BIBLIOGRAPHY

1. D.E. Holcomb, B.R. Upadhyaya, *et al.*, *Instrumentation, Controls, and Human-Machine Interface Technology Development Roadmap for Grid-Appropriate Reactors*, ORNL-GNEP-LTR-2008-041, Oak Ridge National Laboratory, June 2008.
2. C.N. Obiozor, “Selection of motor operated Valves (MOV) for Nuclear Power Plant applications,” IEEE Explore, 0-7803-2642, 1995.
3. S. Mukhopadhyay and S. Chaudhuri, “A Feature-Based Approach to Monitor Motor-Operated Valves Used in Nuclear Power Plants,” IEEE Transactions on Nuclear Science, Vol. 42, No. 6, December 1995.
4. IEEE Standards Board, IEEE Guide for Motor-Operated Valve (MOV) Motor Application, Protection, Control, and Testing in Nuclear Power Generating Stations, IEEE Standard 1290™, 1996 (R2005).
5. B. Lu, B.R. Upadhyaya, and R.B. Perez, “Structural Integrity Monitoring of Steam Generator Tubing Using Transient Acoustic Signal Analysis,” IEEE Transactions on Nuclear Science, Vol. 52, No. 1, pp. 484-493, February 2005.
6. J.W. Hines *et al.*, Technical Review of On-line Monitoring for Performance Assessment, Volumes 1, 2, 3, NUREG/CR-6895, 2008.
7. U.S. Department of Energy, Nuclear Energy Research and Development Roadmap, Report to Congress, April 2010.
8. IAEA Nuclear Energy Series: *On-line Monitoring for Improving Performance of Nuclear Power Plants*, Parts 1 & 2, IAEA Technical Report No. NP-T-1.1 & NP-T-1.2, 2008.
9. J. Coble and J.W. Hines, “Applying the General Path Model to Estimation of Remaining Useful Life,” International Journal of Prognostics and Health Management, 2010.
10. D.T. Ingersoll, “Deliberately Small Reactors and the Second Nuclear Era,” Progress in Nuclear Energy, Vol. 51, pp. 589-603, 2009.
11. W. Gunther and K. Sullivan, “Detecting and Mitigating Rod Drive Control System Degradation in Westinghouse PWRs,” IEEE Transactions on Nuclear Science, Vol. 38, No. 6, December 1991.

12. W. Gunther and K. Sullivan, Aging assessment on PWR Control Rod Drive Systems, BNL-NUREG-52232, Brookhaven National Laboratory. November 1990.
13. R.C. Kryter, Aging and Service Wear of Solenoid-Operated Valves Used in Safety Systems of Nuclear Power Plants –Volume II, Evaluation of Monitoring Methods, NUREG/CR-4819, ORNL/TM-12038, Vol. 2, July 1992.
14. D. Casada and S. Bunch, “The Use of the Motor as a Transducer to Monitor Pump Conditions,” Proceedings of the P/PM Technology Conference, Indianapolis, December 1995.
15. H.D. Haynes, D.E. Welch, D.F. Cox, and R.J. Moses, "Electrical Signature Analysis (ESA) as a Diagnostic Maintenance Technique for Detecting High Consequence Fuel Pump Failure Modes," Proceedings of the 6th Joint FAA/DOD/NASA Conference on Aging Aircraft, San Francisco, CA, September 19, 2002.
16. C. Maxey and H.D. Haynes, "Distributed Capacitance Motion Sensor Employing Electrical Signature Analysis," Proceedings of the Institute of Nuclear Materials Management (INMM), 46th Annual Meeting, Phoenix, Arizona, 2005.
17. H.D. Haynes, "Application of Signature Analysis for Determining the Operational Readiness of Motor-Operated Valves Under Blow-down Test Conditions," Proceedings of the 16th Water Reactor Safety Information Meeting, National Bureau of Standards (NBS), Gaithersburg, MD, October 1988.
18. D.M. Eissenberg, “Status of motor-operated valve aging assessment,” Conf-890373 presentation, 1989.
19. H.D. Haynes, "Evaluation of Check Valve Monitoring Methods," Proceedings of the 17th Water Reactor Safety Information Meeting, Rockville, MD, October 1989.
20. H.D. Haynes, "Recent Improvements in Check Valve Monitoring Methods," NUREG/CP-0114, Vol. 3, pp 403-430, Proceedings of the 18th Water Reactor Safety Information Meeting, Rockville, MD, October, 1990.
21. H.D. Haynes, Aging and Service Wear of Check Valves Used in Engineered Safety-feature Systems of Nuclear Power Plants - Volume II, Aging Assessments and Monitoring Method Evaluations, NUREG/CR-4302, ORNL-6193/V2, April 1991.
22. H.D. Haynes, “Check valve aging assessment,” Conf-9103142 presentation, 1991.
23. H.D. Haynes, "Electrical Signature Analysis (ESA) Developments at the Oak Ridge Diagnostics Applied Research Center," Proceedings of COMADEM '95, the 8th International

Congress on Condition Monitoring and Diagnostic Engineering Management, Kingston, Ontario, Canada, June 1995.

24. K.L. McElhaney, H.D. Haynes, D.F. Cox, P.J. Otaduy, R.H. Staunton, and W.E. Vesely, A Methodology for Evaluation of In-Service Test Intervals for Pumps and Motor-Operated Valves, NUREG/CR-6578, January 1999.

25. H.D. Haynes, D.E. Welch, D.F. Cox, and R.J. Moses, "Electrical Signature Analysis (ESA) as a Diagnostic Maintenance Technique for Detecting High Consequence Fuel Pump Failure Modes," Proceedings of the 6th Joint FAA/DOD/NASA Conference on Aging Aircraft, San Francisco, CA, September 2002.

26. H.D. Haynes, Aging and Service Wear of Electric Motor-operated Valves used in Engineered Safety-feature Systems of Nuclear Power Plants – Vol. 2, Aging Assessments and Monitoring Method Evaluation, NUREG/CR-4234, August 1989.

27. N.E. Huang, et al., "The empirical mode decomposition and the Hilbert transformation for nonlinear and non-stationary time series analysis," Proc. Roy. S. London, Vol. 454, pp. 903-995, 1998.

28. G. Damm, W. Krauthausen, and J. Wolters, Improvements to the Primary Circuit of the FRJ-2, Research Center Jülich, Germany, D-52425.

29. J.S. Park, J.I. Kim, C.W. Lee, J.H. Seo, and L. Wang, "A Rotor dynamic Analysis: Model for Rotor Shaft of SMART MCP," Transactions of the 15th International Conference on Structural Mechanics in Reactor Technology(SMiRT-15) Seoul, Korea, August,1999.

30. H. Huh, J.S. Park, and J.I. Kim, "Thermal Analysis of Canned Induction Motor for Main Coolant Pump in System-Integrated Modular Advanced Reactor," KIEE International Transactions on EMECS, Vol. 3-B, No. 2, pp. 1-6, 2003.

31. Instrumentation Needs for Integral Primary System Reactors (IPSRs), Westinghouse Electric Company LLC, Cooperative Agreement DE-FC07-05ID14690.

32. A.C.O. Barroso *et al.*, "IRIS Pressurizer Design," Proceedings of ICAPP '03, Córdoba, Spain, May 2003.

33. J.M. Kujawski, D.M. Kitch, and L.E. Conway, "The IRIS Spool Type Reactor Coolant Pump," Proceedings of ICONE-10, 10th International Conference on Nuclear Engineering, Arlington, VA, April 2002.

34. Westinghouse Electric Company LLC, AP 1000 design control document, Chapter 5 Reactor Coolant System and Connected Systems.
35. M.D. Carelli, Westinghouse Electric Company LLC, IRIS International Reactor Innovative and Secure, Final technical progress report, November 2003.
36. E. Grove, W. Gunther, and K. Sullivan, Effect of Component Aging on PWR Control Rod Drive Systems, BNL-NUREG-47470, June 1992.
37. D.E. Welch et al., "Electrical Signature Analysis (ESA) as a Diagnostic Maintenance Technique for Detecting the High Consequence Fuel Pump Failure Modes," Proceedings of the 6th Joint FAA/DOD/NASA Conference on Aging Aircraft, San Francisco, CA, September 2002.
38. H.D. Haynes and R.C. Kryter, "Motor Current Signature Analysis for Determining Operational Readiness of Motor-Operated Valves," Proceedings of the 4th Conference on Utility Experience in Reactor Noise Analysis, Hartford, CT, May 1987.
39. R.C. Kryter and H.D. Haynes, "Condition Monitoring of Machinery Using Motor Current Signature Analysis," Proceedings of the Seventh Power Plant Dynamics, Control, and Testing Symposium, Knoxville, TN, May 1989.
40. D. Casada, "Using the Motor to Monitor Pump Conditions," Proceedings of the Fourth NRC/ASME Symposium on Valve and Pump Testing, NUREG/CP-0152, July 1996.
41. E.M. Blake, "The year ahead: This time for sure?" Nuclear News, Vol. 55, No. 1, pp.44-47, January 2012.
42. R.J. Fetterman, A.W. Harkness, M.C. Smith, and C. Taylor, "An Overview of the Westinghouse Small Modular Reactor," Proceedings of the ASME 2011 Small Modular Reactors Symposium, SMR 2011, Washington, D.C., September 2011.
43. Westinghouse Nuclear, www.westinghousenuclear.com/smr
44. B.R. Upadhyaya and S.R.P. Perillo, Advanced Instrumentation and Control Methods for Small and Medium Reactors with IRIS Demonstration, Vol. 5: Multi-modular Integral Pressurized Water Reactor Control and Operational Reconfiguration for a Flow Control Loop. Final Report prepared for the U.S. Department of Energy, University of Tennessee. Report No. DE-FG07-07ID14895/UTNE/2011-7, May 2011.
45. Final Safety Evaluation Report for AP1000, 2004.
46. F. Pollak, Pump Users Handbook, Gulf Publishing Company, 1984.

47. B. Ozpineci and L.M. Tolbert, "Simulink Implementation of Induction Machine Model – A Modular Approach," IEEE Transactions on Power Systems, 2003.

48. National Instruments, "NI 9201." 8-Ch, $\hat{A}\pm 10$ V, 500 KS/s, 12-Bit Analog Input Module, C Series. National Instruments. Web. 30 Mar. 2012.

<http://sine.ni.com/nips/cds/view/p/lang/en/nid/208798> .

49. National Instruments, "NI 9227." 4-Channel Current Input C Series Module. National Instruments. Web. 30 Mar. 2012. <http://sine.ni.com/nips/cds/view/p/lang/en/nid/208794> .

50. National Instruments, "NI 9211." 4-Channel, 14 S/s, 24-Bit, $\hat{A}\pm 80$ MV Thermocouple Input Module. National Instruments. Web. 30 Mar. 2012.

<http://sine.ni.com/nips/cds/view/p/lang/en/nid/208787> .

51. National Instruments, "NI 9234." - 4-Channel, $\hat{A}\pm 5$ V, 51.2 KS/s per Channel, 24-Bit IEPE. National Instruments. Web. 30 Mar. 2012. <http://sine.ni.com/nips/cds/view/p/lang/en/nid/208802>

52. Gould Submersible Pump. Advertisement. KG Power Systems, March 2006. Web. <http://store.kgpowersystems.com/1dw51clea-goulds-pump-submersible-dewatering-1-2-hp-1-phase-3450-rpm-230-volts.aspx> .

53. Fluke, "I200s AC Current Clamp." I200s. Fluke. Web. 30 March 2012.

<http://www.fluke.com/Fluke/usen/Accessories/Current-Clamps/i200s.htm?PID=56289> .

54. G.P. Schultz, Transformers and motors: a single-source reference for electricians. Woburn, MA: Newnes, 1989.

55. HVAC Heating Ventilation & Air Conditioning, Department of Natural Resources, State of Louisiana. N.p., n.d. Web. 27 March 2012.

<http://dnr.louisiana.gov/assets/TAD/education/ECEP/hvac/d/d.htm> .

56. "Model of the dynamics of single phase asynchronous machine with squirrel-cage rotor – Simulink," MathWorks - MATLAB and Simulink for Technical Computing, March 2012.

<http://www.mathworks.com/help/toolbox/phymod/powersys/ref/singlephaseasynchronousmachine.html?nocookie=true> .

57. "Model the dynamics of three-phase asynchronous machine, also known as induction machine - Simulink." MathWorks - MATLAB and Simulink for Technical Computing. N.p., n.d. Web. 27 March 2012.

<http://www.mathworks.com/help/toolbox/phymod/powersys/ref/asynchronousmachine.html> .

58. J.W. Hines, B.R. Upadhyaya et al., Advanced Instrumentation and Control Methods for Small and Medium Reactors with IRIS Demonstration, Vol. 1: Executive Summary. Final Report prepared for the U.S. Department of Energy, University of Tennessee. Report No. DE-FG07-07ID14895/UTNE/2011-3, May 2011.

59. J.S. Bendat and A.G. Piersol, Random Data: Analysis and Measurement Procedures, Third Edition, Wiley Interscience, New York, 2000.

60. B.P. Lathi, *Signal Processing and Linear Systems*, Oxford University Press, New York, 1998.

61. S.M. Kay, Modern Spectral Estimation, Prentice-Hall, Englewood Cliffs, NJ, 1988.

62. R.B. Randall, Frequency Analysis, Bruel & Kjaer, Denmark, 1984.

63. S.L. Marple, Jr., Digital Spectral Analysis with Applications, Prentice-Hall, Englewood Cliffs, NJ, 1987.

64. O. Rioul and M. Vetterli, "Wavelets and Signal Processing," IEEE Signal Processing Magazine, Vol. 8, No. 4, pp. 14-38, October 1991.

65. D.E. Newland, An Introduction to Random Vibrations, Spectral & Wavelet Analysis, (Third Edition) Longman Group Limited, Essex, England, 1993.

66. B. Lu, B.R. Upadhyaya, and R.B. Perez, "Structural Integrity Monitoring of Steam Generator Tubing Using Transient Acoustic Signal Analysis," IEEE transactions on Nuclear Science, Vol. 52, No. 1, pp. 484-493, February 2005.

67. N.E. Huang et al., "The Empirical Mode Decomposition and the Hilbert Transformation for Nonlinear and Non-stationary time series analysis," Proc. Royal Society of London, A 454, pp. 903-995, 1998.

68. IMI Sensors Product Catalog, IMI, 2003, www.vitek.com.br. 2003. Web. 05 June 2012.

http://www.vitek.com.br/imi/catalogo_imi.pdf .

69. "Pressure Transducers." Pressure Transducers. Omega, n.d. Web. 12 June 2012.

<http://www.omega.com/prodinfo/pressuretransducers.html> .

70. "Accelerometer Concepts." PCB Piezotronics, Inc. - Tech Support. PCB, 2012. Web. 18 June 2012. http://www.pcb.com/techsupport/tech_accel.php .

71. "ILK Dresden - Durchfluss Berechnung Nach ISO 5167." ILK Dresden - Durchfluss Berechnung Nach ISO 5167. 8 Oct. 2009. Web. 25 May 2012.

<http://www.ilkdresden.de/iso5167/index.html> .

72. M. Naghedolfeizi and B.R. Upadhyaya, *Dynamic Modeling of a Pressurized Water Reactor Plant for Diagnostics and Control*, Research Report prepared for the U.S. Department of Energy, University of Tennessee, DOE/NE/88ER12824-02, June 1991.

73. I. Karassik and R. Carter, *Centrifugal Pumps*, McGraw-Hill, New York, 1976.

74. F. Pollak, *Pump Users Handbook*, Gulf Publishing Company, 1981.

75. Final Safety Evaluation Report for the Westinghouse AP1000 Reactor, 2004.

76. Technical Review No. 3, Bruel & Kjaer, Hilbert Transform, Denmark, 1984.

77. B. R. Upadhyaya and T. W. Kerlin, "Estimation of Response Time Characteristics of Platinum Resistance Thermometers by the Noise Analysis Technique," *ISA Transactions*, Vol. 17, pp. 21-38, 1978.

78. B. R. Upadhyaya and M. Kitamura, "Stability Monitoring of Boiling Water Reactors by Time Series Analysis of Neutron Noise," *Nuclear Science and Engr.*, Vol. 77, No. 4, pp. 480-492, 1981.

79. B.R. Upadhyaya, O. Glockler, and J. Eklund, "Multivariate Statistical Signal Processing Technique for Fault Detection and Diagnostics," *ISA Transactions*, Vol. 29, No. 4, pp. 79-95, 1990.

80. K.M. Kim, B.I. Lee, D. Lee, H.H. Cho, and K.H. Jeong, "Experimental and numerical study on local pressure distributions in a system-integrated modular reactor," *Annals of Nuclear Energy*, Vol. 47, pp. 216-224, 2012.

81. J.N. Reyes, Jr., "NuScale Plant Safety in Response to Extreme Events," *Nuclear Technology*, Vol. 178, pp. 153-163, May 2012.

82. J. Eklund and B.R. Upadhyaya, "An Automated System for Motor-Operated Valve Diagnostics," *Power Engineering*, pp. 38-41, December 1991.
83. M. Sharp, *Prognostic Approaches Using Transient Monitoring Methods*, Doctoral Dissertation, University of Tennessee, Knoxville, 2012.
84. J.J. Jelovich and G. Werber, "Application of the Digital Rod Drop Indication for Establishment of Control Rod Drive-Line Dynamic Characteristics of a PWR," *IEEE Transactions on Nuclear Science*, Vol. NS-25, No. 1, February 1978.
85. W. L. Dufek, J.J. Jelovich, and J.A. Neuner, "A Fault Tolerant, Multiplexed Control Rod Position Detection and Indication System for Nuclear Power Plants," *IEEE Transactions on Nuclear Science*, Vol. NS-24, No. 1, February 1977.
86. Grundfos Management, *Pump Handbook*, Grundfos Management A/S, 2004.
87. S.T. Shiels, "Centrifugal Pump Application: Key Hydraulic and Performance Criteria," Imperial Oil Ltd., Dartmouth, Nova Scotia, Canada, 1995.
88. H.M. Hashemian, E. Riggsbee, and R. O'Hagan, *Wireless Sensors for Predictive Maintenance of Rotating Machinery in DOE's Research Reactors*, Final Project Report prepared for DOE by Analysis and Measurement Services Corp., December 2012.
89. H.M. Hashemian, "Wireless Sensors for Predictive Maintenance of Rotating Equipment in Research Reactors," *Annals of Nuclear Energy*, Vol. 38, pp. 665-680, 2011.
90. H.M. Hashemian, C.J. Kiger, G.W. Morton, and B.D. Shumaker, "Wireless Sensor Applications in Nuclear Power Plants," *Nuclear Technology*, Vol. 173, No. 1, pp. 8-16, 2011. 91. H.M. Hashemian, *Wireless Sensors for Predictive Maintenance of Rotating Equipment in DOE's Research Reactors*, DOE Phase I Final Report, AMS Corp., DE-FG02-08ER85004, May 2009.
92. *Guidelines for Wireless Technology in Power Plants, Volume 1: Benefits and Considerations*, 1003584, Electric Power Research Institute, 2002.
93. *Guidelines for Wireless Technology in Power Plants, Volume 2: Implementation and Regulatory Issues*, 1007448, Electric Power Research Institute, 2002.
94. B.J. Kaldenbach et al., *Assessment of Wireless Technologies and their Application at Nuclear Facilities*, NUREG/CR-6882, July 2006.
95. *Revised Guidelines for Wireless Technology in Power Plants, Volume 1: Benefits and Considerations*, EPRI Report 1013485. Project Manager: A Hussey, December 2006.

96. D. Shull and J. Cordaro, "Careful, hot wireless," InTech Magazine, January 2008.
97. E.F. Policastro, "Driving Data Node to Node," ISA InTech Magazine, pp. 32-35, June 2005.
98. Wireless Sensor Networks, National Instruments, <http://www.ni.com/wsn/>
99. C.B. Jacobsen, The Centrifugal Pump, Grundfos Research and Technology, 2004.
100. J.M. Doster, IRIS Pump Characteristics, Private Communication, 2012.
101. U.S. Nuclear Regulatory Commission, Cyber Security Programs for Nuclear Facilities, Regulatory Guide 5.71, January 2010.
102. I. Daubechies, Ten Lectures in Wavelets, Society for Industrial and Applied Mathematics, Philadelphia, PA, 1992.
103. G. Strang and T. Nguyen, Wavelets and Filter Banks, Wellesley-Cambridge Press, Wellesley, Massachusetts, 1996.
104. C.S. Burrus, R.A. Gopinath, and H. Guo, Introduction to Wavelets and Wavelet Transforms, Prentice-Hall, Upper Saddle River, NJ, 1998.
105. O. Rioul and M. Vetterli, "Wavelets and Signal Processing," IEEE Signal Processing Magazine, Vol. 8, No. 4, pp. 14-38, October 1991.
106. R.M. Rao, *Wavelet Transforms: Introduction to Theory and Application*, Addison-Wesley, Canada, 1998.
107. A.M. Gaouda *et al.*, "Monitoring HVDC systems using wavelet multi-resolution analysis," IEEE Transactions on Power Systems, Vol. 16, pp. 662-670, 2001.
108. M. Young, The Technical Writer's Handbook. Mill Valley, CA: University Science, 1989.
109. International Atomic Energy Agency (IAEA), *Advanced Surveillance, Diagnostic and Prognostic Techniques in Monitoring Structures, Systems and Components in Nuclear Power Plants*, IAEA Nuclear Energy Series No NP-T-3.14, Vienna, Austria, September, 2013.
110. Isotope Cross sections: E.M. Baum, *Nuclides and Isotopes: Chart of the Nuclides*. Chart. 16th ed. Lockheed Martin, pp. 56-58.

111. S.F. Mughab, M. Divadeenam, and N.E. Holden, "Neutron Cross Sections from Neutron Resonance Parameters and Thermal Cross Sections," *The Isotopes Project*. LBNL, 1981. Web. <http://ie.lbl.gov/ngdata/sig.htm#A=231>
112. "Chart of Nuclides." *National Nuclear Data Center*, BNL.
<http://www.nndc.bnl.gov/chart/>
113. J.L. Duderstadt and L.J. Hamilton, Fission Product Burnup: Analysis of Core Composition Changes. In *Nuclear Reactor Analysis*, John Wiley, pp. 566-600, 1976.
114. N.E. Todreas, "Chapter 3: Reactor Heat Generation." *Nuclear Systems I: Thermal Hydraulic Fundamentals*, New York: Taylor & Francis, 1990.
115. J.W. Hines *et al.*, *Technical Review of On-line Monitoring for Performance Assessment*, Volumes 1, 2, 3, NUREG/CR-6895, 2008.
116. J. Henkel, *Development of a Safeguards Monitoring System for Special Nuclear Facilities*, Doctoral Dissertation, University of Tennessee, August 2011.
117. B.R. Upadhyaya, C. Mehta, V.B. Lollar, J.W. Hines, and D. de Wet, "Approaches to Process Monitoring in Small Modular Reactors," Proceedings of the ASME 2014 Small Modular Reactors Symposium, Washington, D.C., April 2014.
118. J.W. Hines and D. Garvey, "Development of a Process and Equipment Monitoring (PEM) Toolbox and its Application to Sensor Calibration Monitoring," *Fourth International Conference on Quality and Reliability (ICQR4)*, Beijing, PRC, 2005.
119. B.R. Upadhyaya, C. Mehta, and D. Bayram, "Integration of Time Series Modeling and Wavelet Transform for Monitoring Nuclear Plant Sensors," IEEE transactions on Nuclear Science, Vol. 61, No. 5, pp. 2628-2635, October 2014.
120. J. Richalet, "Industrial Applications of Model-Based Predictive Control," *Automatica*, Vol. 29, No. 5, pp. 1251-1274, 1993.

APPENDIX A

MATLAB-based Data Analysis Toolbox

A.1. Introduction

One of the tasks outlined in the project proposal was to develop a MATLAB toolbox to use for the analysis of experimental data to perform monitoring and diagnostics. One module of the toolbox focuses on wide-band signal analysis algorithms for both stationary and transient signals from the experimental loop such as calculation of motor power phase angle. The second module analyzes operational data (both electrical and process measurements) from the loop to perform monitoring and fault detection. The MATLAB code for all functions discussed herein can be found in the appendices.

A.2. Toolbox Module One

The first module of the toolbox includes functions that were created to process operational data to find the characteristics of the signals.

A.2.1 Auto-Correlation Function

A function for computing the auto-correlation between two signals was developed to determine the similarity between the observations as a function of separation of time between them. The function can be used to find repeated patterns and the dependence of the signal itself as well as being incorporated into auto-regression time series modeling. The function is entitled *autocorrelation* and requires a data and lag input where the auto-correlation is calculated up to the value of the desired lag. The normalized auto-correlation function is given by,

$$R(k) = \frac{\sum_{i=1}^{N-k} \{y(i) - y_{mean}\} \{y(i+k) - y_{mean}\}}{\sum_{i=1}^N \{y(i) - y_{mean}\}^2} \quad (A.1)$$

where, k is the lag, N is the number of observations, y are the observations, and y_{mean} is the mean value of the signal y (t). To demonstrate the function, it was tested using a known equation of a second order system [68]. The time-series data was generated with the equation:

$$y(k) = 0.75*y(k-1) - 0.5*y(k-2) + v(k), \quad (A.2)$$

where $v(k)$ is the white Gaussian noise and k is again the lag. The equation was used to generate 4000 data points and the autocorrelation function was then used for analysis (Figure A.1).

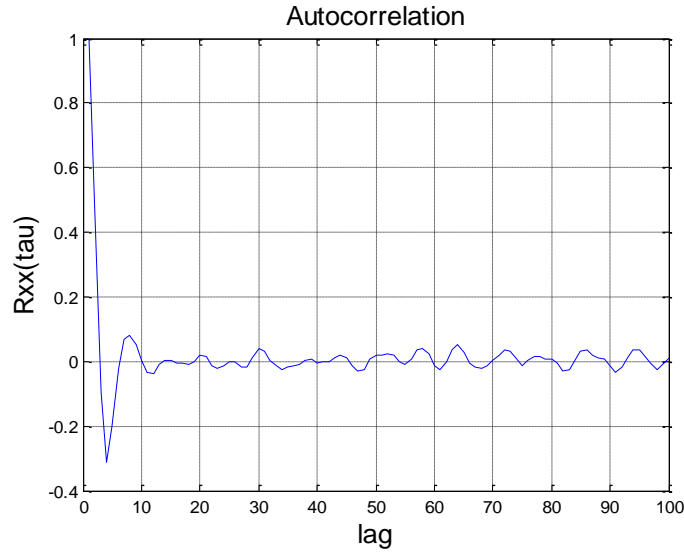


Figure A.1: Auto-correlation plot for test data

The result from the function was normalized based on the auto-correlation at lag zero and the estimates match the actual values closely. The normalized correlation at lag zero was equal to one.

A.2.2 Auto-Regression (AR) Modeling

Linear discrete-time models generally fall into the category of auto-regression moving average (ARMA) models. Auto-regression (AR) models are often used to characterize the dependency of band -limited signals. An AR model using the equation,

$$y(t) = \sum_{i=1}^n a_i y(t-i) + v(t) \quad (A.3)$$

where $y(t)$ is a sequence of discrete signals or measurements, $v(t)$ is assumed to be wideband noise (approaching white noise) with zero mean and finite variance, and $\{a_1, a_2, \dots, a_n\}$ are time-invariant parameters. There are situations where AR models with changing parameters can be developed in order to characterize non-stationary or transient data. An example is the case of pump start-up or coast-down sequence.

The AR parameters are estimated using either a one-step prediction error minimization or by solving the Yule-Walker equations [77] for the parameter set $\{a_1, a_2, \dots, a_n\}$. The Yule-Walker equations are derived directly from the AR model, and for a model of order, n , has the form:

$$R(k) = \sum_{i=1}^n a_{ni} R(k-i), k = 1, 2, 3..n. \quad (A.4)$$

where $R(k)$ is the autocorrelation function of $x(t)$ at time lag k (or $k\Delta t$ where Δt is the data sampling interval).

The sampling frequency ($f_s = 1/\Delta t$, Hz) depends on the bandwidth of the signal being processed. The Yule-Walker equations can be solved recursively, for successively higher order models. That is, the parameters of AR($n+1$) model are estimated from the parameters of AR(n) model and an additional autocorrelation function. This facilitates fast computation of AR models up to a certain maximum order, and the determination of optimal model order, n^* . The optimal order corresponds to minimum model prediction error. A model-recursive algorithm was developed and implemented in MATLAB. The recursive algorithm provides accurate and fast computation of successively higher order AR models. The autoregressive modeling function can be called using the function *autoregression*. The inputs to the function include the data, lag, and order. The lag is used to calculate the autocorrelation of the data set, and the order is the value up to which the model coefficients are calculated recursively. Once an optimal AR model is determined, the model may be used to estimate the frequency spectrum of the signal or to compute time-domain signatures.

The optimal model in the given class of autoregression models is decided by plotting the Final Prediction Error (FPE) as a function of the model order, n . The error is calculated using,

$$(FPE)_n = \frac{N+n}{N-n} \sigma_v^2 \quad (A.5)$$

where σ_v^2 is the white noise variance. The noise variance, calculated by,

$$\hat{\sigma}_v^2 = \frac{1}{N} \sum_{k=1}^N \hat{v}_k^2 \quad (A.6)$$

where the residual sequence is estimated by,

$$\hat{v}_k = y_k - \sum_{i=1}^n \hat{a}_i y_{k-i}, k = 1, 2, 3.., N \quad (A.7)$$

The optimal model corresponds to the value where the error is a minimum, or when the error goes to a low value without significant decrease with increasing model order. Other minimization criteria, such as the Akaike Information Criterion (AIC), and the total prediction

error, should also be computed and compared to determine the best model fit. This procedure provides a robust model order determination. The AIC is given by [73].

$$AIC = N \ln(\sigma_v^2) + 2n \quad (A.8)$$

where, σ_v^2 is the variance of the noise sequence $\{v(k)\}$; n is the number of AR parameters. Similar to FPE, the model order, n , is selected such that AIC has the minimum value. To demonstrate the function, the autocorrelation function was used to estimate the parameter values using the previous data set. The Yule Walker recursive method was then used to estimate the parameters of the second order model. The estimate of the parameters were found to be,

$$a = \begin{bmatrix} .5047 & 0 \\ .7586 & -.5030 \end{bmatrix} \quad (A.9)$$

The parameters of the second order equation were close to the parameters used to generate the data.

A.2.3 Spectral Density

The spectrum of a signal is a positive real function of a frequency variable associated with a stationary process. The spectrum decomposes the stochastic process into the different frequencies of that process. The AR parameters can also be used to estimate the power spectrum of the signal $y(t)$ using,

$$S_{yy}(f) = |H(f)|^2 S_{vv}(f) \quad (A.10)$$

The estimate of the power spectrum of $y(t)$ is given by,

$$S_{yy}(f) = \frac{\sigma_v^2 \Delta t}{|1 - \sum_{k=1}^n \hat{a}_k e^{-j2\pi f k \Delta t}|^2} \quad (A.11)$$

where $S_{yy}(f)$ is the power spectrum of y_k , $H(f)$ is the linear transformation from the AR model, $S_{vv}(f)$ is the power spectrum of the noise v_k , and $S_{vv}(f)$ is equal to $\sigma_v^2 \Delta t$ and f is in Hz. The MATLAB function, entitled *spectraldensity* and requires function inputs of the AR parameters of the optimal AR model, and F_s is the sampling frequency. Since the model is fit to a given data length, it provides the best estimate of the frequency spectrum, especially when the data size is limited. If the signal is quasi-stationary, the spectral estimates may be computed for short data lengths by moving a data window, thus providing a quick estimate of the spectrum during slow transients. In reactor applications, time domain signatures are often used to estimate sensor time

constant, ramp delay time, decay ratio from the impulse response function, and stability margin. The frequency spectrum estimate contains information about the signal bandwidth, changes in the frequency peaks in the signal, and other features. The AR model can also be used to detect possible faults by using a baseline AR model to estimate the prediction error during the test phase. Alternately, comparison of frequency or time domain signatures from the baseline model and the test model would also provide information about incipient anomalies. To demonstrate the function's operation, the spectral density function was used with the AR parameters from the user-generated data (Figure A.2).

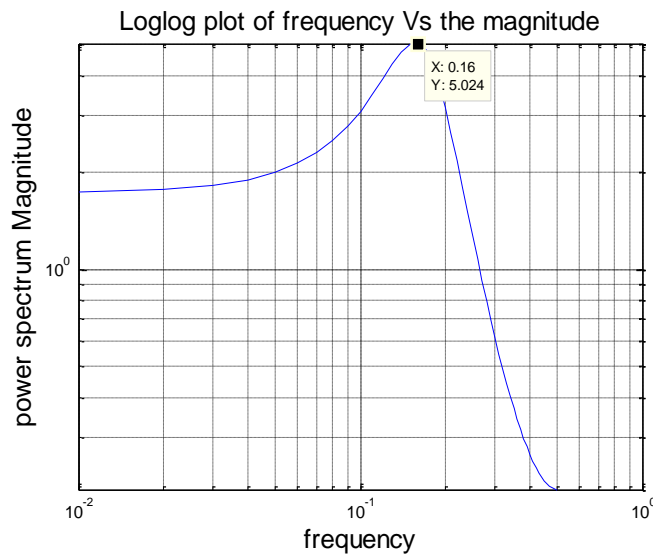


Figure A.2: Power spectral density plot for user-generated data

The spectral peak is expected to be around 0.16 Hz for a sampling frequency of 1Hz, which is where the function also calculates the peak [68].

A.2.4 Testing of Functions with Nuclear Power Plant Data

Once these functions were tested on simulated data, data from a nuclear power plant was provided by AMS. The data set was from a 4-loop PWR plant and consists of transmitter data sampled from 9 sensors during plant operation. The data for each sensor consists of 208,400 samples which are sampled at 200 Hz. Table A.1 provides a description of the list of sensors.

Table A.1: List of Sensors

S.no	Sensor Name	Service
1	FEED FLOW	FEEDWATER FLOW
2	PZR LVL	PRESSURIZER LEVEL
3	PZR PSR	PRESSURIZER PRESSURE
4	STM FLOW	STEAM FLOW
5	SG LVL NR1	STEAM GENERATOR LEVEL NARROW RANGE
6	SG LVL NR2	STEAM GENERATOR LEVEL NARROW RANGE
7	SG LVL WR1	STEAM GENERATOR LEVEL WIDE RANGE
8	STM PSR	STEAM PRESSURE
9	RCS PSR	RCS PRESSURE

The data from the transmitters measuring feed water flow was used to test the functions (Figure A.3). The results were then compared to those calculated by AMS.

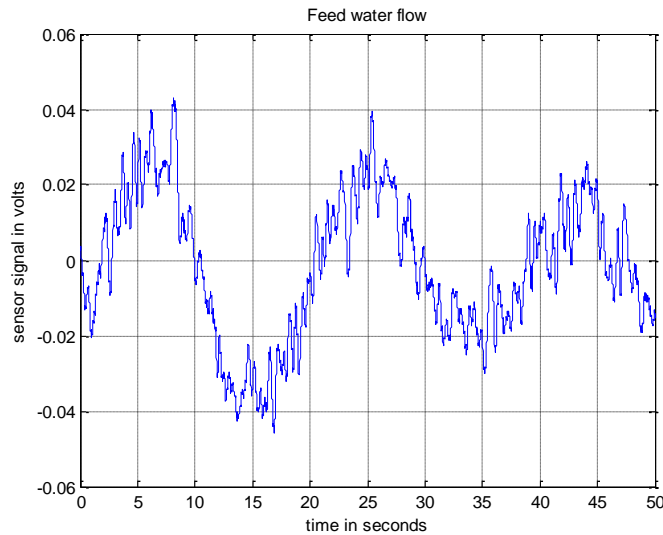


Figure A.3 Feed Water Flow Sensor Signal

The model order needs to be decided in order to move forward with the best AR fit. The Final prediction error (FPE) (Figure A.4) and the Akaike Information Criterion (AIC) (Figure A.5) were used to determine the optimal model order for the feed water flow signal.

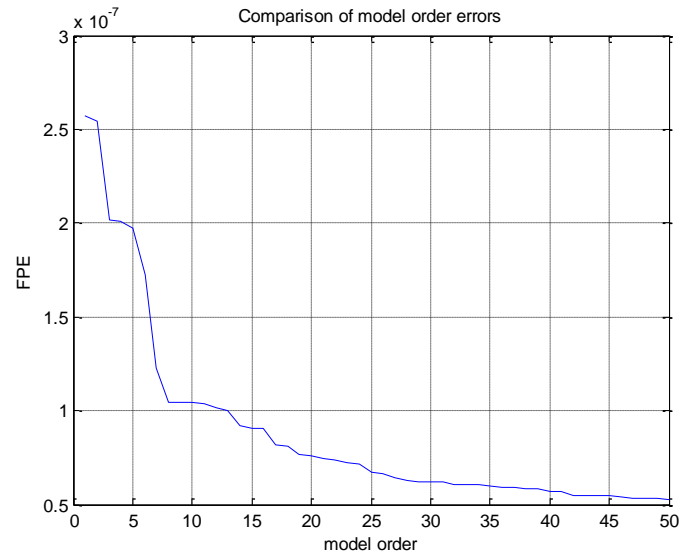


Figure A.4: FPE criterion for different model orders

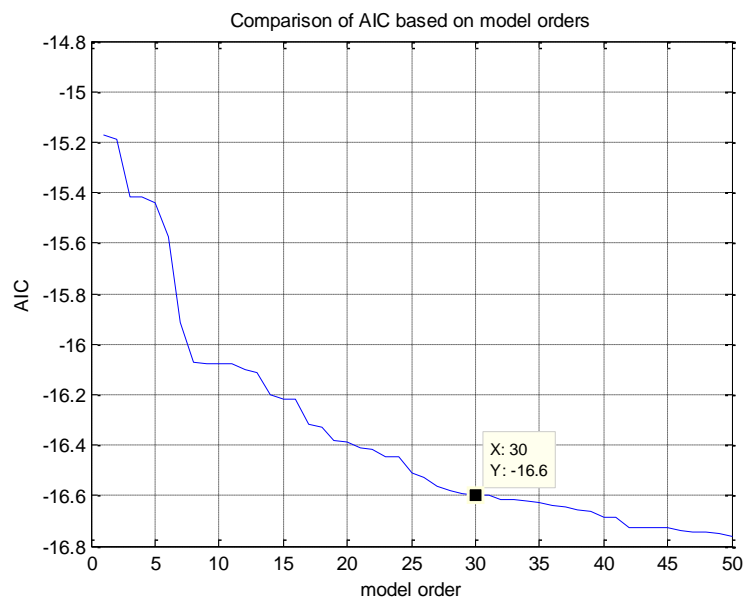


Figure A.5: Akaike information criterion versus model order

Observing the AIC and FPE, they attained the lowest value at a model order of 30. Both the criteria reach an almost constant value after order 30. After an optimal order was estimated, the power spectrum was generated using the model coefficients.

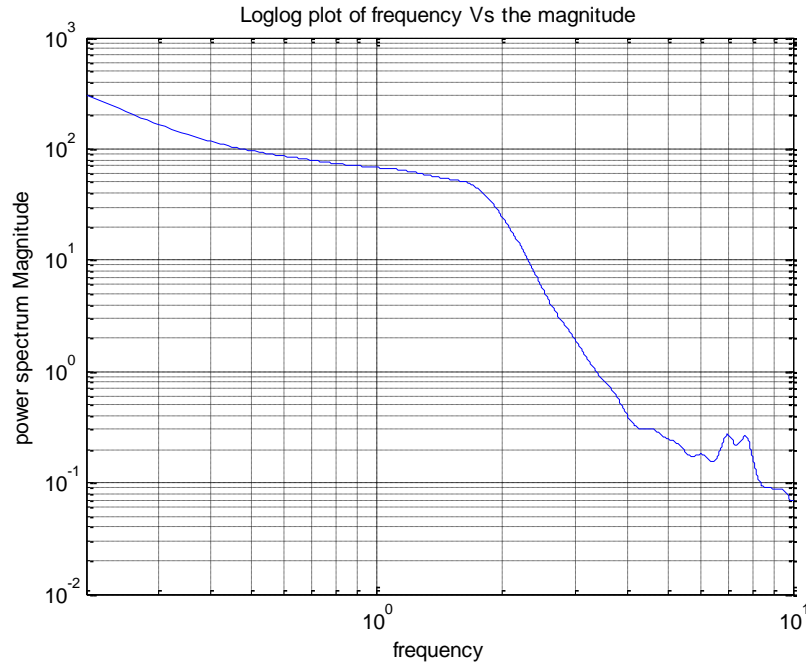


Figure A.6: Power spectrum of the feed water flow sensor

The power spectrum of the feed water flow transmitter (Figure A.6) showed that the break frequency of the sensor was ~ 1.87 Hz. This is close to the frequency calculated by AMS at ~ 1.5 Hz. The accuracy of the predictions provides confidence in the use of the signal processing functions.

A.2.5 Estimation of Phase Angle and Power Factor

The AC power of a pump has three components including real power (P) as measured in watts, apparent power (W) as measured in volt-amperes, and reactive power (Q) measured in reactive volt-amperes. The power factor of an electrical system is the ratio of the real power flowing to the load and the apparent power in the circuit. The phase angle is required to calculate the real power of the motor which is calculated as,

$$|P| = |S| |\cos\phi| \quad (\text{A.12})$$

The phase angle between the voltage and current of a phase will be enough to calculate the power factor of the operating conditions. Power factor is calculated from experiments when the load and frequency of the motor is changed during different testing conditions. The function *phased* reads in the motor voltage and current to return the phase angle between the voltage and current.

A.3. Toolbox Module Two

The second module of the toolbox includes functions that were created to determine the relationship between process variables and motor electrical signatures as well as to perform monitoring and fault detection. This module includes functions for both data pre-processing and data-based modeling techniques.

A.3.1 Window Averaging Function

A function for averaging a subsequent number of user-defined points was developed in order to smooth the experimental data. The function is entitled *WindowAverage* and reads in a data set that breaks it into windows with each window including the desired number of points. Each window is then averaged and the resultant data set is returned. For example, if the user selects a window size of 10, the function will average each subsequent set of 10 data points and return the average of each set. Therefore, if a user has a data set with 1000 points and a window size of 10, the new data set will consist of 100 points.

To demonstrate the results of using the function, the motor current from an experiment will use the window averaging function with block sizes of 5 and 10 and compare the results to the original data set (Figs. A.7-A.9). The original signal is quite noisy and could benefit from averaging. As the block size increases, the number of subsequent points that are averaged increases and the data becomes smoother. It is noted however that too high of a window size could result in loss of information from a data set. Therefore, care must be taken when choosing the window size in order to avoid this.

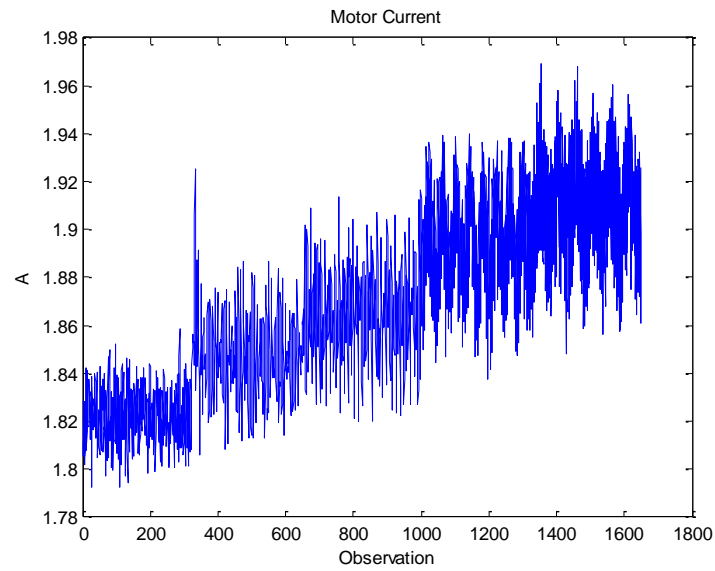


Figure A.7: Original Motor Current Data

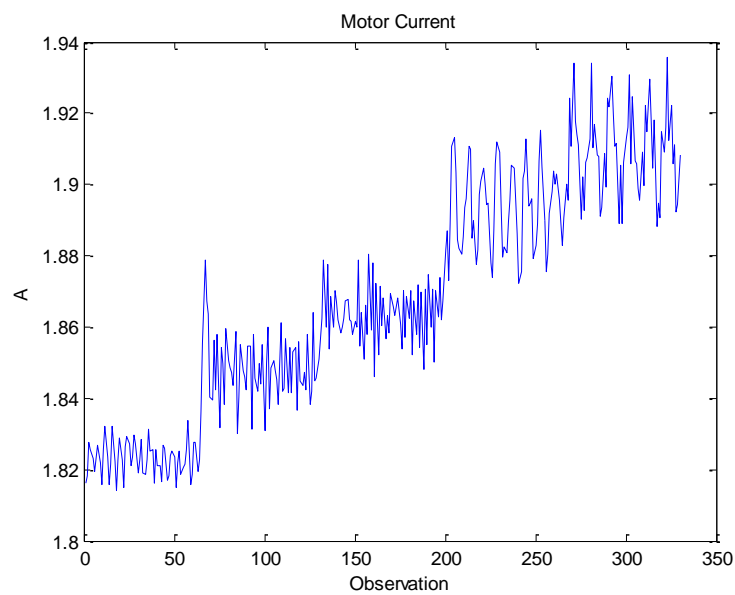


Figure A.8: Motor Current Data with block size of 5

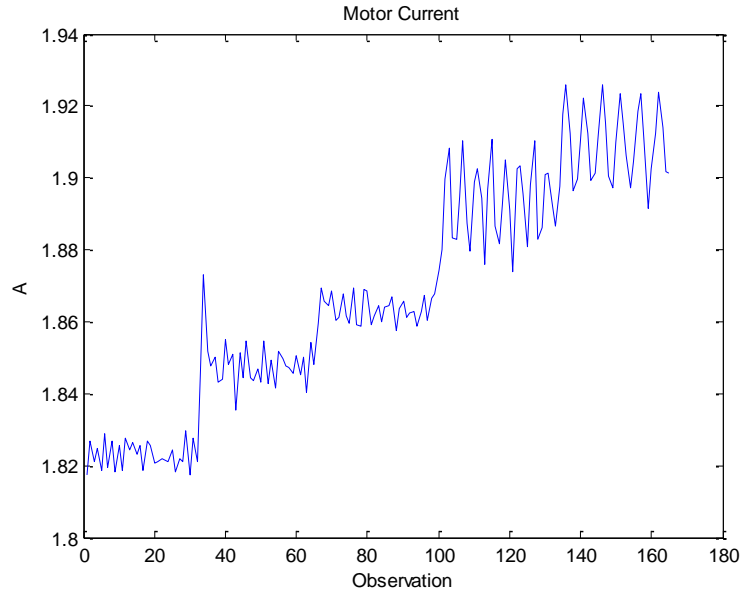


Figure A.9: Motor Current Data with block size of 10

A.3.2 Venetian Blind Sampling Function

In order to construct correct empirical models using AAKR, experimental data must be broken up into three sets referred to as the training, testing, and validation sets. A function for breaking a data set into these required parts was built and uses the venetian blind sampling method to decide which data points are included in each new set. The venetian blind sampling method is widely accepted as a robust and effective way to separate time-dependent experimental data. The method works by splitting the data into successive blinds of equal length. These blinds are then allocated into either the training, testing, or validation sets. The function selects select 60% of the observations for the training set and split the remaining 40% between the testing and validation sets. The training set is the largest set because it should always contain the largest number of points and contain the full range of operational data. An illustration of the venetian blinds can be seen in Figure A.10 where each rectangle represents one venetian blind.

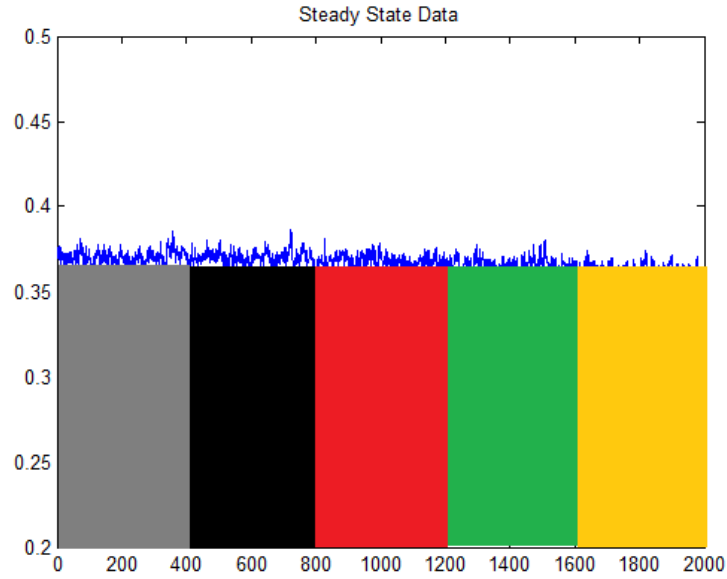


Figure A.10: Example of the Venetian Blind Sampling Method

The training, testing, and validation data sets must contain data points from each region of operation to avoid any potential problems that could occur late when building any models. These regions of operation can be seen when the motor rotational frequency is varied from 58 Hz to 60 Hz (Figure A.11).

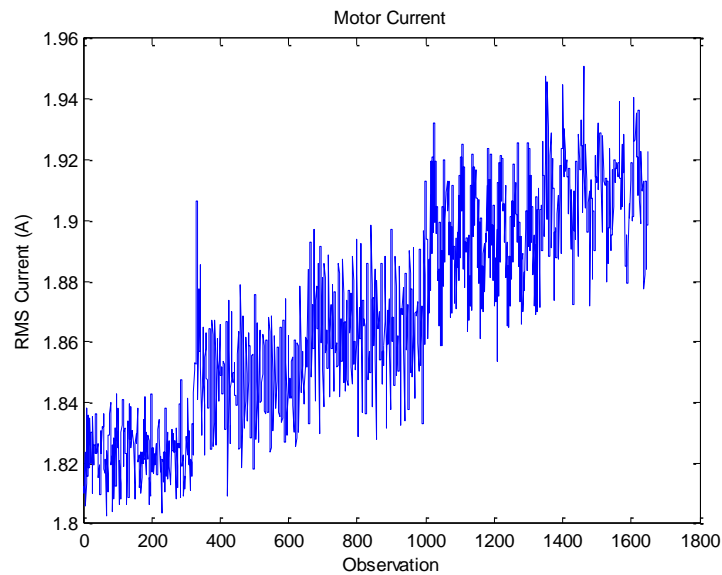


Figure A.11: Motor Current from 58 Hz to 60 Hz Rotational Frequency

The distinct regions are observed when performing experiments under transient conditions where certain parameters are varied throughout. Another example can be seen when varying the position of the MOV (Figure A.12).

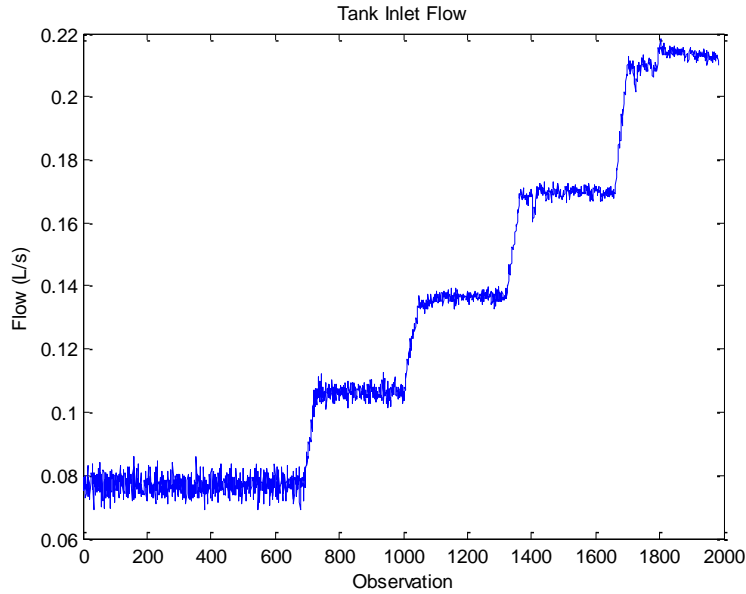


Figure A.12: Tank Inlet Flow while Varying MOV Position

In order for the function to break up the full data set into its three required sets and include information from each region of operation, the user must supply the function with the endpoints of the each region. For example, for the varying MOV position, the user would select the endpoint of the first region (~700), the endpoint of the second region (~1050), repeating the process until the beginning point of the last region (~1700). The function will then split each region of operation into five venetian blinds. Blinds one, three, and five of each region will be dedicated to the training set while blind two will be allocated to the testing set, and blind four will be for the validation set. The function is robust and can be used to break the original data set into any number of different regions of operation. The user must simply specify the endpoints of the region as required by the function. It can also be used for steady state data where there is only one large region of operation. In order to provide an appropriate number of blinds, the user should select several endpoints equally spaced out throughout the observations in order to get enough data points into the training, testing, and validation sets.

In-situ Condition Monitoring of Components in Small Modular Reactors Using Process and Electrical Signature Analysis

Final Report – Volume 2 Development of Dynamic Models and Simulation of Operational Anomalies for a Small Modular Pressurized Water Reactor

**Report No. NEUP-11-3212-Y3Q4-2014-2
NEUP Contract Number: 00120767
DE-AC07-05IDPS07-07ID14517**

**Belle R. Upadhyaya
(Principal Investigator)
J. Wesley Hines
(Co-Principal Investigator)
Brian Damiano
(Collaborator, Oak Ridge National Laboratory)**

**Price Collins, Chaitanya Mehta, Matthew Lish, Brian Cady
(Graduate Research Assistants)
Victor Lollar, Dane de Wet
(Undergraduate Research Assistants)**

**The University of Tennessee
Department Nuclear Engineering
Knoxville, TN 37996-2300
E-mail: bupadhya@utk.edu**

**TPOC: Richard Wood
Federal Manager: Tim Beville**

December 2014



EXECUTIVE SUMMARY

In-situ Condition Monitoring of Components in Small Modular Reactors Using Process and Electrical Signature Analysis

1. Background and R&D Objectives

For reliable and economic long-term operation of Small Modular Reactors (SMRs), it is imperative that continuous in-situ monitoring of critical equipment must be developed and incorporated in the reactor design phase. This capability is attractive for remote deployment of SMRs with longer fuel cycle duration and for minimizing forced outages, thus enhancing the utilization of these power generating systems in small electric grid environments. These technologies contribute to smart condition-based maintenance, reduced human resources, remote monitoring of reactor components, and autonomous operation. In integral pressurized water reactors (iPWR) and other designs of SMRs, the pressure vessel incorporates most of the critical equipment used for power generation. Examples of such plant components include: steam generators, motors, coolant circulation pumps, motor-operated valves, control rod drive mechanisms (CRDM), in-core instrumentation, and reactor internal structures.

The development of these techniques is also important in monitoring critical parameters during severe accidents and for post-accident recovery. Small integral light water reactors have in-vessel space constraints and many of the traditional instrumentation are not practical in actual implementation. In order to resolve this issue, research is being performed to develop techniques for indirect measurement of process parameters. Examples of some of the process measurements of interest are primary coolant flow rate in the reactor vessel, characteristics of motor-driven coolant pumps, water levels in steam generators where the secondary water flows through the steam generator tubing, in a once-through steam generator configuration, and others.

The purpose of this NEUP funded research and development project was to develop and demonstrate in-situ equipment monitoring methods for small modular reactors (SMRs) with applications to reactor internals such as coolant pumps, valve-actuators, and control rod drive mechanisms. The overall objective was to integrate electric signature analysis (ESA) and process measurements to perform remote monitoring of SMR components. The primary reactor vessel in a typical SMR has limited space for the installation of control, safety, and system monitoring

instrumentation. The focus of this research is to develop monitoring and diagnostics methods using easily accessible measurements. Both experimental and physics-based modeling approaches were developed to establish the feasibility of implementing such techniques and incorporate them during the SMR design phase.

Recent activities by light water reactor SMR vendors and developers (NuScale Power, Generation mPower, Westinghouse, CAREM, KAERI, and others) have indicated an increased interest in the development of integral pressurized water reactors for deployment by 2025. SMRs in the 25-200 MWe range are useful for power supply in remote areas, especially in locations with limited infrastructure. SMRs can also be used for co-generation, combining electricity production and process heat for industrial applications, including water desalination. Because of the modular nature of SMRs and limited vessel penetrations, safety and security of such installations are greatly enhanced.

The research and development under this project was focused on the following three major objectives:

Objective 1: Identification of critical in-vessel SMR components for remote monitoring and development of their low-order dynamic models, along with a simulation model of an integral pressurized water reactor (iPWR).

Objective 2: Development of an experimental flow control loop with motor-driven valves and pumps, incorporating data acquisition and on-line monitoring interface.

Objective 3: Development of stationary and transient signal processing methods for electrical signatures, machinery vibration, and for characterizing process variables for equipment monitoring. This objective includes the development of a data analysis toolbox.

The project tasks were performed in collaboration with the Measurement Sciences and Systems Engineering Division of ORNL. All the tasks and deliverables were completed by the end of the project execution period.

2. Project Technical Summary

The following is a summary of the technical accomplishments under this project:

- A detailed literature review of various SMR types and electrical signature analysis of motor-driven systems was completed. A bibliography of literature is provided at the end of this report. Assistance was provided by ORNL in identifying some key references.

- A review of literature on pump-motor modeling and digital signal processing methods was performed.
- An existing flow control loop was upgraded with new instrumentation, data acquisition hardware and software. The upgrading of the experimental loop included the installation of a new submersible pump driven by a three-phase induction motor. All the sensors were calibrated before full-scale experimental runs were performed.
- MATLAB-Simulink model of a three-phase induction motor and pump system was completed. The model was used to simulate normal operation and fault conditions in the motor-pump system, and to identify changes in the electrical signatures.
- A simulation model of an integral PWR (iPWR) was updated and the MATLAB-Simulink model was validated for known transients. The pump-motor model was interfaced with the iPWR model for testing the impact of primary flow perturbations (upsets) on plant parameters and the pump electrical signatures. Additionally, the reactor simulation is being used to generate normal operation data and data with instrumentation faults and process anomalies.
- A frequency controller was interfaced with the motor power supply in order to vary the electrical supply frequency. The experimental flow control loop was used to generate operational data under varying motor performance characteristics. Coolant leakage events were simulated by varying the bypass loop flow rate. The accuracy of motor power calculation was improved by incorporating the power factor, computed from motor current and voltage in each phase of the induction motor.
- A variety of experimental runs were made for steady-state and transient pump operating conditions. Process, vibration, and electrical signatures were measured using a submersible pump with variable supply frequency. High correlation was seen between motor current and pump discharge pressure signal; similar high correlation was exhibited between pump motor power and flow rate. Wide-band analysis indicated high coherence (in the frequency domain) between motor current and vibration signals.
- Wide-band operational data from a PWR were acquired from AMS Corporation and used to develop time-series models, and to estimate signal spectrum and sensor time constant. All the data were from different pressure transmitters in the system, including primary and secondary loops. These signals were pre-processed using the wavelet transform for filtering both low-frequency and high-frequency bands. This technique of signal pre-processing provides minimum distortion of the data, and results in a more optimal estimation of time constants of plant sensors using time-series modeling techniques.

- The experimental loop data indicate a clear relationship between motor power and pump discharge (flow rate). This relationship can be used to infer pump flow rate using the computed motor power.
- The iPWR physics model was used to simulate normal operation data and operation with faulty sensors, primary coolant flow rate anomaly, and variations in process parameters such as heat transfer coefficients and reactivity feedback coefficients. The iPWR dynamic model was interfaced with the pump-motor model, and this feature was used to introduce variations in the electrical supply frequency and other anomalies in the equipment to simulate their degradation.
- The iPWR model was extended to include the dynamics of fission product poisoning and its long-term effect on reactor operation.
- A laboratory scale wireless data acquisition and transmission network was developed and demonstrated successfully. In addition, a micro-controller based data acquisition and analysis module was developed and tested for monitoring machinery vibration. Such low-investment devices are attractive for monitoring a large number of similar plant equipment.
- A data analysis toolbox was developed for processing both loop operational data and wide-band sensor data. It includes all the computational functions that were developed and used in the project; these are classical data analysis and modern digital signal processing (DSP) techniques.

3. Student Participation and External Collaboration

The NEUP grant was beneficial in training both graduate and undergraduate students, and in providing opportunities for parallel collaboration with other related projects.

The project PI and the Co-PI are engaged in three synergistic research projects. One of these is a DOE STTR Phase-1 and Phase-2 projects with the industrial partner, Analysis and Measurement Services (AMS) Corporation, with an emphasis on SMR on-line monitoring. The second is collaboration with Korea Atomic Energy Research Institute (KAERI) on a DOE I-NERI project, and is related to monitoring safety critical functions during beyond design basis accidents in light water reactors. The latter also addresses station blackout, remote sensing, self-

powered detectors, energy harvesting, and wireless communication. The third collaborative project is an IRP titled *Integral Inherently Safe Light Water Reactor (I²S-LWR)*, with Georgia Institute of Technology as the lead for this NEUP-IRP. These illustrate the value of this NEUP project in enhancing the safety and operational reliability of both existing and future nuclear power plants.

The following students and visiting scholars were engaged in making research and development contributions during the project period. These included 1 Ph.D. student, 3 MS students, 2 undergraduate research assistants, and two visiting scholars – from Istanbul Technical University (ITU) and from Korea Atomic Energy Research Institute (KAERI).

Graduate and Undergraduate Students:

- Matthew Lish (Ph.D., Dynamic modeling an iPWR with helical coil steam generators; currently engaged in I²S-LWR research funded by IRP)
- Chaitanya Mehta (M.S., Condition Monitoring of Equipment in Small Modular Reactors Using Electrical and Process Signature Analysis, 2013)
- Price Collins (M.S., Dynamic Analysis and Fault Simulation for Small Modular Reactors, 2014)
- Brian Cady (M.S., Modeling a three-phase induction motor and pump system; currently working for an engineering services company)
- Victor Lollar (B.S., Nuclear Engineering, 2014; currently M.S. student)
- Dane de Wet (B.S., Nuclear Engineering, junior)

Visiting Scholars:

- Seop Hur, Instrumentation, Controls, and Human Factors Division, KAERI, ROK.
- Duygu Bayram, Department of Electrical Engineering, Istanbul Technical University, Turkey.

Publications:

The following are journal and conference publications resulting from the NEUP project.

Journal Publications

1. B.R. Upadhyaya, C. Mehta, and D. Bayram, “Integration of Time Series Modeling and Wavelet Transform for Monitoring Nuclear Plant Sensors,” *IEEE Transactions on Nuclear Science*, Vol. 61, No. 5, pp. 2628-2635, October 2014.

2. B.R. Upadhyaya, C. Mehta, V.B. Lollar, and J.W. Hines, "Remote Monitoring of Equipment in Small Modular Reactors," Chemical Engineering Transactions, AIDIC, Italy, Vol. 33, pp. 841-846, August 2013.
3. *Monitoring Pump Parameters in Small Modular Reactors Using Electric Motor Signatures*, manuscript prepared for submission to ASME Journal on Nuclear Engineering and Radiation Science.
4. *Process Fault Simulation and Monitoring for an Integral Pressurized Water Reactor*, manuscript prepared for submission to IEEE Transactions on Nuclear Science.

Conference Publications

5. P.A. Collins and B.R. Upadhyaya, "Small Modular Reactor Response to Errors in Process Variables and Sensors," Transactions of the American Nuclear Society, Vol. 111, ANS Winter Meeting, Anaheim, CA, November 2014.
6. B.R. Upadhyaya, C. Mehta, V.B. Lollar, J.W. Hines, and D. de Wet, "Approaches to Process Monitoring in Small Modular Reactors," Proceedings of the ASME 2014 Small Modular Reactors Symposium, Washington, D.C., April 2014.
7. C. Mehta, V.B. Lollar, B.R. Upadhyaya, J.W. Hines, and D. Bayram, "Development of a Method for Monitoring Pump Parameters in Small Modular Reactors Using Motor Signatures," Transactions of the American Nuclear Society, Vol. 109, pp. 278-279, Washington, D.C., November 2013.
8. B.R. Upadhyaya, P. Collins, M.R. Lish, J.W. Hines, and C. Mitra, "Modeling and Dynamic Simulation of an Integral Pressurized Water Reactor," Transactions of the American Nuclear Society, Vol. 108, pp. 173-175, Atlanta, Georgia, June 2013.
9. B.R. Upadhyaya, C. Mehta, V.B. Lollar, J.W. Hines, and B. Damiano, "In-situ Condition Monitoring of Components in Small Modular Reactors," Transactions of the American Nuclear Society, Vol. 107, pp. 843-844, San Diego, California, November 2012.
10. V.B. Lollar, B.R. Upadhyaya, J.W. Hines, J.B. Coble, and D. de Wet, "Data-based Modeling for Monitoring and Fault Detection in Small Modular Reactors," accepted for conference presentation, NPIC&HMIT 2015, Charlotte, NC, February 2015.

11. R. Wetherington, B. Van Hoy, L. Phillips, B. Damiano, and B.R. Upadhyaya, “Evaluation of A Consumer Electronics-Based Data Acquisition System for Equipment Monitoring,” accepted for conference presentation, NPIC&HMIT 2015, Charlotte, NC, February 2015.
12. B.R. Upadhyaya, J.-T. Kim, and J.W. Hines, *Development of Diagnostics and Prognostics Methods for Sustainability of Nuclear Power Plant Safety Critical Functions*, Final Report prepared for the DOE I-NERI Project-ROK, 2011-004-K, November 2014; presented at the I-NERI Review Meeting, Washington, D.C., November 2014.

4. Final Report and Future Directions

The Final Report of the three-year project is presented in two volumes:

- Volume 1: Development of an experimental flow control loop with instrumentation, data acquisition, and analysis for demonstrating in-situ condition monitoring of SMRs.
- Volume 2: Development of dynamic models and simulation of anomalies for a small modular pressurized water reactor.

The report presents all the information related to the project, including technical work, computer codes, and the discussion of results.

It is anticipated that the results and deliverables of this R&D project would be useful in further developing and implementing remote monitoring and intelligence maintenance technologies in future light water SMRs and other integral reactors. During the course of the project and discussion with various collaborators, suggestions were made and ideas were developed for future research activities in extending instrumentation and controls strategies for advanced reactors.

DISCLAIMER

Any opinions, findings, and conclusions or recommendations expressed in this report are those of the authors, and do not necessarily reflect the views of the U.S. Department of Energy or the Oak Ridge National Laboratory.

CONTENTS

SECTION	PAGE
EXECUTIVE SUMMARY	1
1. INTRODUCTION	10
1.1. Background and Project Objectives	10
1.2. Summary of R&D Contributions Presented in Volume 2	12
1.3. Organization of the Report	13
2. REVIEW OF LITERATURE	15
2.1. Introduction	15
2.2. Use of Motor as a Transducer	15
2.3. On-line Monitoring of SMR Components	16
2.4. Overview of Integral Pressurized Water Reactors and SMRs	16
2.5. Comparison and Status of SMR Designs	21
3. DEVELOPMENT OF SIMULATION MODELS OF SMR COMPONENTS	23
3.1. Introduction to the IRIS MATLAB-Simulink Model	23
3.2. Components Modeled for Increased System Complexity.....	24
3.3. Comments on the Additional SMR Components	26
4. FAULT SIMULATION USING PUMP AND MOTOR MODEL	27
4.1. Subsystem Development and Necessity	27
4.2. Governing Physics of the Pump Motor Model (PMM)	28
4.3. Results of Coupled System Simulation	31
4.4. Remarks on the Pump and Motor Model	43
5. LOAD-FOLLOWING SIMULATIONS AND SYSTEM RESPONSE	44
5.1. Importance of Load-Following Maneuvers (LFM) in SMRs	44
5.2. Dynamics of Reactor Systems during Load-Following	44
5.3. Faults Introduced during LFM	45
5.4. Remarks on System Response during LFM	66
6. FISSION PRODUCT POISONING EFFECTS IN SMRs	68
6.1. Motivation for Fission Product Subsystem	68
6.2. Theory of Reactivity Poisoning in Thermal Reactors	68
6.3. Simulation of Fission Product Poisoning Effects	73
6.4. Remarks on Fission Product Poisoning Effects	77

7. EFFECTS OF DEVICE AND PROCESS FAULTS ON SMR PERFORMANCE	78
7.1. Overview of Sensor Faults	78
7.2. Steam Pressure Signal Faults	78
7.3. Faults in the P-I Controller	88
7.4. Remarks on General Process Faults	93
8. CONCLUDING REMARKS, SUMMARY AND RECOMMENDATIONS FOR FUTURE R&D	94
8.1. Concluding Remarks	94
8.2. Summary of Significant Contributions Reported in Volume 2	95
8.3. Recommendations for Future Research and Development	96
REFERENCES FOR VOLUME 2	97
REFERENCES AND BIBLIOGRAPHY	100

1. INTRODUCTION

1.1. Background and Project Objectives

The development of small modular reactors (SMRs) such as the NuScale Power, Westinghouse-SMR and the mPower reactor in the U.S., the operation of the research reactor, OPAL, in Australia, and the construction of the CARAM-25 reactor designed and developed by CNEA, Argentina, signify the importance of SMRs for power generation, process heat utilization, water desalination, and medical isotope production. Safe and economic long-term operation of these small reactors requires improved design of instrumentation and control systems, remote monitoring, and fault tolerant control for load-following scenarios. This is generally true of all integral reactor designs.

One of the advantages of small modular reactors (SMRs) is their possible deployment in remote locations and continued long-term operation with minimum downtime. In order to achieve this operational goal, the SMRs may require remote and continuous monitoring of process parameters. This feature is also important in monitoring critical parameters during severe accidents and for post-accident recovery. Small integral light water reactors have in-vessel space constraints and many of the traditional instrumentation are not practical in actual implementation. In order to resolve this issue, experiments were carried out on a flow test loop to characterize the relationship among process variables (flow rate, pressure, water level) and pump motor signatures. The Final Report presents the findings of this research with implications in relating electrical signatures to pump parameters. Additionally, the project scope included the development of a complete nodal model of an integral pressurized water reactor and the simulation and evaluation of various plant operational anomalies.

The objective of the R&D described in this volume was to develop a complete simulation model of a small pressurized water reactor and study the effects of various anomalies on plant operation. The anomalies included faults in sensors, devices, and equipment, and process-related anomalies. This R&D project focused on the following three major objectives. The R&D tasks were carried out in collaboration with the Measurement Sciences and Systems Engineering Division of ORNL.

Objective 1: Identification of critical in-vessel SMR components for remote monitoring and develop their low-order dynamic models, along with a simulation model of an integral pressurized water reactor (iPWR).

Objective 2: Development of an experimental flow facility with motor-driven valves and pumps, incorporating data acquisition and on-line monitoring interface. This objective includes the task of demonstrating wireless data acquisition and the implementation of microcontroller-based data acquisition and analysis for machinery monitoring.

Objective 3: Development of stationary and transient signal processing methods for electrical signatures, machinery vibration, and for characterizing process variables for equipment monitoring.

Volume 2 of the report addresses research tasks under objective 1. Some of the experimental data reported in Volume 1 of the report were used for validating pump-motor models. The simulations conducted demonstrate the performance of an SMR under normal and fault-related transients and the need to understand the effects of these faults on plant operation. A good understanding of the problems SMRs could potentially face in the field, along with solutions to these problems, would help with plant licensing as well as address safety and economic issues related to unplanned downtime due to these conditions.

Figure 1.1 shows the organizational diagram indicating the interaction among the project personnel. Table 1.1 shows the task schedule and milestones.

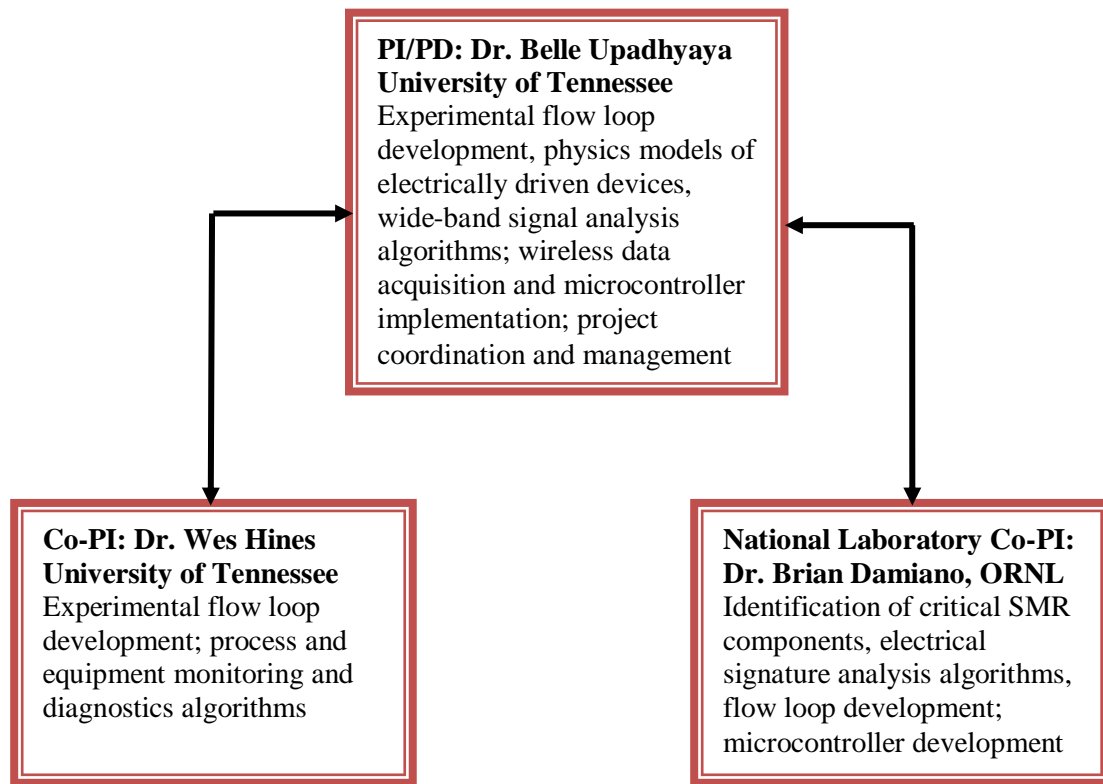


Figure 1.1: Project organizational chart and project coordination. Quality assurance is the responsibility of each of the partnering organizations.

1.2. Summary of R&D Contributions Presented in Volume 2

The following are the significant accomplishments of the project described in Volume 2 of the report.

- A detailed literature review of various SMR types, including integral pressurized water reactors (iPWR), and electrical signature analysis of motor-driven systems was completed. A bibliography of literature is provided at the end of this report.
- The iPWR physics model was used to simulate normal operation data and operation with faulty sensors, primary coolant flow rate anomaly, and variations in process parameters such as heat transfer coefficients and reactivity feedback coefficients.
- The iPWR dynamic model was interfaced with the pump-motor model, and this feature was used to introduce variations in the electrical supply frequency and other anomalies in the equipment to simulate their degradation. The relationship between pump flow rate and motor power was verified using experimental data reported in Volume 1.

- The iPWR model was extended to include the dynamics of fission product poisoning and its long-term effect on reactor operation.

The project PI and the Co-PI are engaged in three synergistic research projects. One of these is a DOE STTR Phase-1 and Phase-2 project with the industrial partner, Analysis and Measurement Services (AMS) Corporation, with an emphasis on SMR on-line monitoring. The second is collaboration with Korea Atomic Energy Research Institute (KAERI) on a DOE I-NERI project, and is related to monitoring safety critical functions during beyond design basis accidents in light water reactors. The latter also addresses station blackout, remote sensing, self-powered detectors, energy harvesting, and wireless communication. The third collaborative project is an IRP titled *Integral Inherently Safe Light Water Reactor (I²S-LWR)*, with Georgia Institute of Technology as the lead for this NEUP-IRP. These illustrate the value of this NEUP project in enhancing the safety and operational reliability of both existing and future nuclear power plants.

1.3. Organization of the Report

Volume 2 of the Final Report provides description and results of developing a simulation model of an integral pressurized water reactor and the simulation of various system faults. The focus of the report is on the tasks performed under objective 1. The following topics are described in Sections 2-8.

Section 2: Review of literature, providing a background on different SMRs in various stages of research as well as the specific system chosen for simulation.

Section 3: Development of models of plant components.

Section 4: Effects of pump and motor faults on the reactor performance.

Section 5: Load following maneuvers and the influence of sensor faults on plant operation.

Section 6: Study of the effects of fission product poisoning on reactor power production and other system parameters.

Section 7: Study of the effect of process-related faults on plant performance.

Section 8: Concluding remarks and future work.

A complete list of references and related bibliography is given at the end of the report.

Table 1.1: Schedule of tasks/milestones

→	T	I	M	E	---	---	M	O	N	T	H	S
Tasks/Milestones	1-3	4-6	7-9	10-12	13-15	16-18	19-21	22-24	25-27	28-30	31-33	34-36
Task 1: Identification of critical in-vessel SMR components; functional models	X	X	X	X	X	X	X	X				
Task 2: Development of Electrical Signature Analysis (ESA); relationship to process dynamics	X	X	X	X	X	X	X	X				
Task 3: Development of stationary and transient signal processing methods. Time-series modeling technique for sensor response monitoring		X	X	X	X	X	X	X				
Task 4: Development of an experimental flow loop with SMR-type devices and demonstration of relationship among process variables and electrical signatures	X	X	X	X	X	X	X	X				
Task 5: Development of a MATLAB toolbox for analysis of measurements; data-based modeling for condition monitoring			X	X	X	X	X	X	X	X		
Task 6: System integration and demonstration. Wireless data acquisition; low-cost microcontrollers for equipment monitoring					X	X	X	X	X	X	X	
Deliverables: Progress reports →	X	X	X	X	X	X	X	X	X	X	X	X
System demonstration →									X	X	X	X

2. REVIEW OF LITERATURE

2.1. Introduction

While SMRs are not a new research topic, several aspects relating to their deployment must be further understood in order for designs to be accepted by regulatory agencies. Many of the problems associated with SMR deployment are not unique to the small reactor field. This is important to consider since full scale reactors can experience some of the same issues and solutions have been found. In addition, other industries (defense, aerospace, etc.) have found satisfactory solutions to problems associated with sensitive electronics. One of the more modern tools used for this project as well as for other high-tech fields involves the use of Electrical Signature Analysis (ESA), a technique developed by researchers at the Oak Ridge National Laboratory around 1985 [4].

This project utilized ESA by using the embedded pump-motor model (PMM) for some simulations and allowing the motor to act as a transducer. This novel technique can “provide an improved means of detecting small time-dependent load and speed variations generated anywhere within an electro-mechanical system and converting them into revealing signatures that can be used to detect equipment degradation and incipient failure” [4]. SMRs discussed in this section are all of the pressurized type. There have been some research conducted for SMRs using gas or liquid metal coolants, but they will not be discussed in this report since fault simulations are designed for pressurized reactors. All the U.S SMRs being researched are of this type and as such stand to benefit most from simulations conducted with the IRIS model.

2.2. Use of Motor as a Transducer

Motor operated valves (MOV) are used in power and process plants to regulate fluid flow rate. Using the motor as a transducer, coupled with noninvasive probes like current and voltage sensors can be an invaluable tool for monitoring pump and motor systems for minimizing system downtime [5]. The experimental portion of the NEUP project used MOVs and ESA as a way of measuring system signals and subsequent system response to artificial faults added. The simulation component of the project had limitations owing to system complexities, and was unable to reproduce some conditions created in the experimental portion.

The system response of the IRIS model was measured through the subsequent change in the coolant flow pumped being modified in the PMM. This was the only variable coupled with the reactor model in the primary system. Results of the coupled simulations are presented in Section 4.

2.3. On-line Monitoring of SMR Components

Using the motor as a transducer is one way of on-line monitoring (OLM) of SMRs. Sensors send data to operators, allowing for decisions to be made on live data updates. Since fuel cycles of SMRs are envisioned to last between 24-48 months for some designs, the sensors providing data for OLM are bound to deviate from acceptable operational parameters. While a full scale reactor will have multiple redundancies in the monitoring of the primary system, SMRs do not have this luxury due to reduced size of pressure vessels and their integral design. For these reasons, bad data feed to operators or sensor failures can be a major problem during long term operation. It is estimated a single sensor calibration can cost \$3000 to \$6000; this occurs during planned downtimes [6]. Unplanned downtime, however, can greatly affect a plants bottom line. Unscheduled shutdowns not only reduce a plants revenue stream, but could also potentially affect customers since less power is available. OLM offers the ability for plant operators to not only determine whether the system is in an abnormal state through noise analysis but also for sensor health [7]. This allows for the possibility of determining whether a system is actually at fault or merely if bad data is being sent by sensors. The cost attributed to sensor calibration is small compared to the cost of unintended plant shutdowns. Typical downtimes of a full scale power plant can be as large as \$250,000 per day or more [8]. This cost will likely be smaller for an SMR, however.

2.4. Overview of Integral Pressurized Water Reactors and SMRs

This section focuses on several designs of proposed integral SMRs. What separates an integral reactor from a typical power reactor is all major primary loop components (coolant pumps, pressurizer, core, etc.) are contained inside the reactor pressure vessel (RPV). This creates several advantages typical PWRs do not have. Since the flow loops are self-contained in SMRs, the creation of a large scale loss of coolant accident is virtually eliminated since any break in flow would traverse to the bottom of the core and not to the containment building or the environment. The possibility of a control rod ejection is also removed in the integral SMR design

since the control rod drive mechanism (CRDM) is house inside the pressure vessel [9]. Another attractive feature of SMRs is their use of digital instrumentation and control; something the industry has yet to embrace. A vast majority of the reactors in the U.S fleet use aging analog components. These components are, for the most part, not manufactured anymore and in limited demand as plants extend their operating licenses for 20 years or more.

2.4.1 International Reactor Innovative and Secure

In terms of the SMR field, IRIS is more appropriately classified as a medium sized integral reactor. This is due in part to the 335 MWe electrical output. The Department of Energy classifies SMRs as “Nuclear power plants that are smaller in size (300 MWe or less) than current generation base load plants (1,000 MWe or higher). These smaller, compact designs are factory-fabricated reactors that can be transported by truck or rail to a nuclear plant site [10]. This PWR was designed through a Westinghouse led consortium to meet the needs of the Gen III+ reactor initiative. Figure 2.1 illustrates an overview of the IRIS primary system.

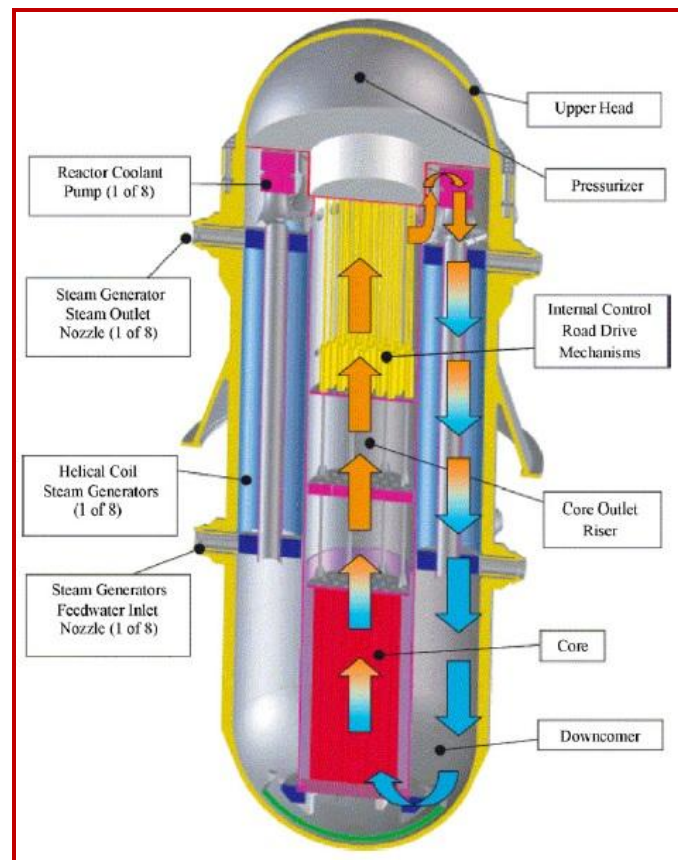


Figure 2.1: IRIS pressure vessel layout [11]

The IRIS reactor uses 8 spool type reactor coolant pumps for forced convection heat transfer. The steam generators produce superheated steam for the turbine. Fluid at the bottom of the core in the fuel region will flow downwards in an accident condition; a passive safety feature. This primary piping removal also allows for the reduction of size in containment. Figure 2.2 illustrates a comparison between the IRIS design and a typical 600 MWe PWR.

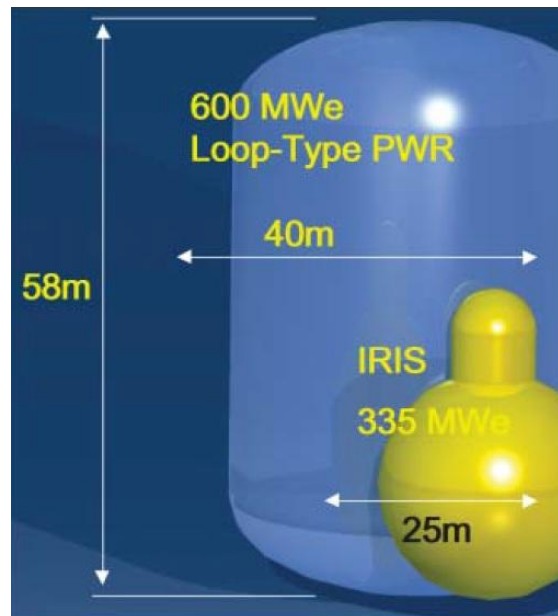


Figure 2.2: IRIS size in contrast to a 600 MWe PWR [12]

Much of the design work and lessons learned have been put into the newer 225 MWe Westinghouse SMR.

2.4.2 Babcock and Wilcox mPower Reactor

The mPower reactor was the first SMR design to receive funding from the Department of Energy's SMR development initiative [13]. Unlike the IRIS design, mPower utilizes a once-through steam generator design for production of 180 MWe. Figure 2.3 shows the location of primary components in the mPower reactor pressure vessel (RPV).

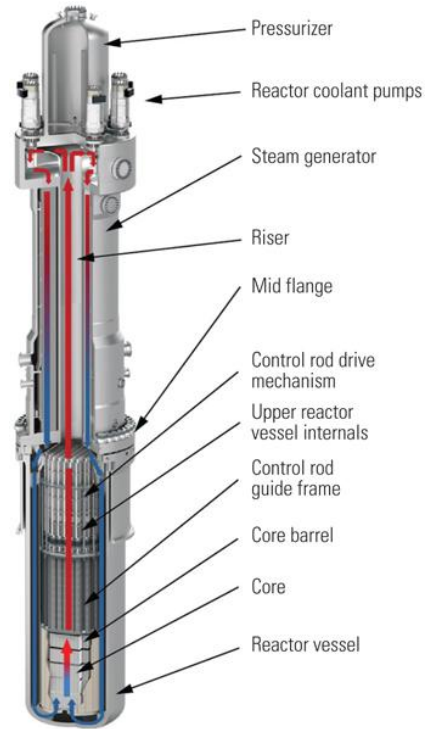


Figure 2.3: mPower Reactor Design [14]

The Tennessee Valley Authority (TVA) has signed a memorandum of understanding to build mPower reactors at the site of the former Clinch River Breeder Reactor. The reactor is designed to run for 4 years without refueling and utilizing less than 5% enriched fuel.

2.4.3 NuScale Reactor

The NuScale reactor is drastically different in terms of heat transfer from the B&W and Westinghouse designs. The reactor does not use reactor coolant pumps, instead utilizes natural circulation to drive the primary side heat transfer [15]. The plant produces 45 MWe and is designed for a 12 unit configuration for a plant site. Figure 2.4 illustrates the primary module of the NuScale design.

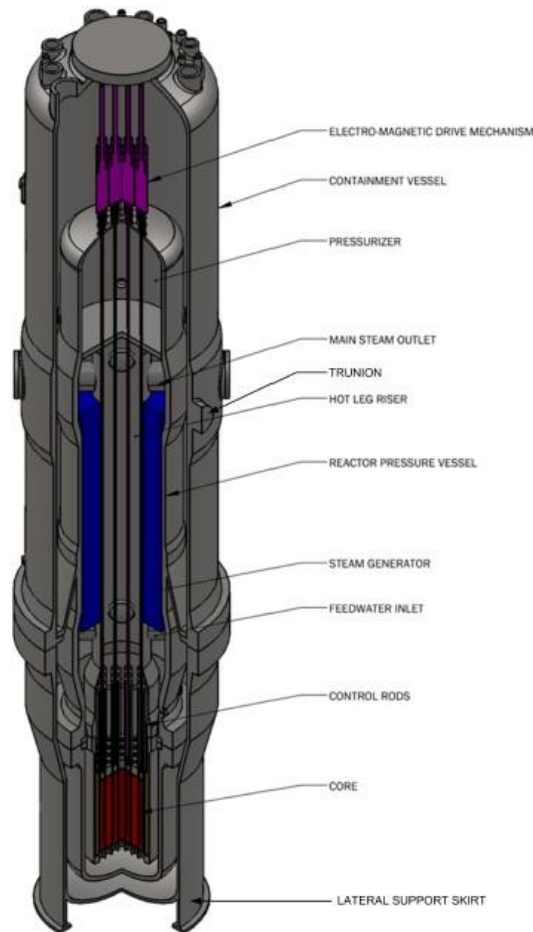


Figure 2.4: NuScale module overview [15]

NuScale was another company to benefit from the Departments of Energy's SMR initiative.

2.4.4 CNEA CAREM Reactor

The CAREM reactor is a natural circulation SMR developed by the Argentinian organization INVAP. The first prototype built will produce 27 MWe, while further iterations of the reactor could be built to produce 100-200 MWe [16]. In contrast to previously mentioned designs, the CAREM design utilizes hexagonal fuel assemblies.

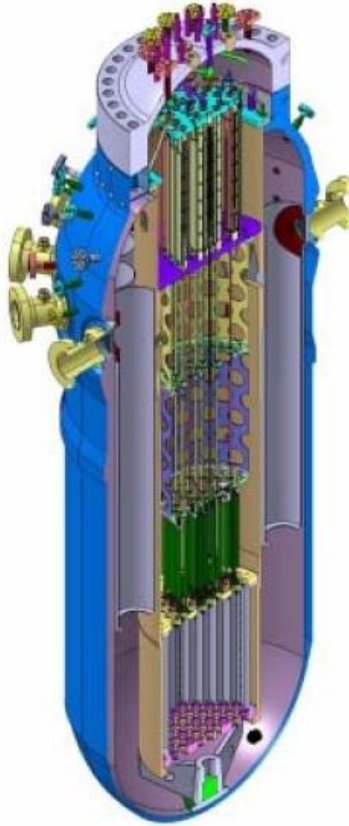


Figure 2.5: CAREM pressure vessel internal view [17]

2.5. Comparison and Status of SMR Designs

Table I presents a summary of major design parameters of the IRIS system and the two SMRs receiving the U.S. Department of Energy funding. As evident by some of the parameters, the SMRs have similar values. This is in part due to the basic dynamics of the PWR design. For example, feedback coefficients in PWRs will be the same for a range of temperatures and pressures. The U.S Nuclear Regulatory Commission (NRC) prefers new SMR designs to be based on well understood technology. PWRs, after all, have been in continuous operation in the U.S since the 1950s.

TABLE I
COMPARISON OF MAJOR SMR PARAMETERS [17, 18, 19, 20, 21]

Parameter	IRIS	NuScale	mPower
Core Thermal Power	1000 MW _{th}	160 MW _{th}	530 MW _{th}
Power Plant Output	335 MW _e	45 MW _e	180 MW _e
Steam Temperature	317 °C	N/A ^a	314 °C
Steam Pressure	5.8 MPa	N/A	5.67 MPa
Primary Coolant Flow	4700 kg/s	750 kg/s	3750 kg/s
Reactor Pressure	15.5 MPa	12.76 MPa	15.85 MPa
Core Inlet Temp	292 °C	269 °C	297 °C
Core Exit Temp	330 °C	309 °C	319 °C
Fuel Assembly Length	5.207 m	2 m	2.4 m
Fuel Inventory	48.5 tU	12 tU ^b	26.9 tU
Fuel Material	UO ₂	UO ₂	UO ₂
Enrichment	4.95% U ₂₃₅	4.95% U ₂₃₅	<5% U ₂₃₅
Avg. Burnup	60 GWd/tU	N/A	N/A
Total Height	21.3 m	24.38 m	25.3 m
Steam Generator Type	Helical coil	Helical coil	Once-Through
Number of SGs	8	2	8
Coolant Pump Type	Spool	-	Canned
Number of Pumps	8	-	8

^aSpecifications not available due to working number of parameters, or intentional withholding due to a proprietary nature

^bParameters estimated based on formulas from Todreas and Kazimi

The interest in SMR research has decreased in recent months. B&W has decided to decrease their research focus on SMRs due to a lack of corporate partnership. Similarly, Westinghouse has reduced its SMR commitment in order to focus on supplying orders for their AP1000 design. For the time being, NuScale is the only company with significant time invested in research and will likely be the first of the U.S designed SMRs constructed. Holtec has also decided to become involved in the SMR field, but still requires significant time and research before a design is ready for submission to the NRC.

3.1. Introduction to the IRIS MATLAB-Simulink Model

The screenshot displays the MATLAB R2014a environment. The main window is the Editor, showing a script named 'Parameters_IRIS.m' located at 'C:\Users\Price\Desktop\Volume II\Parameters_IRIS.m'. The script contains parameters for a reactor system, including a list of parameters (a1 through a16), a units converter (kk), and various physical constants (c1, c2, c3, c4, c5, c6, c7, c8, c9, c10, c11, c12, c13, c14, c15, c16, c17, c18, c19, c20, c21, c22, c23, c24, c25, c26, c27, c28, c29, c30, c31, c32, c33, c34, c35, c36, c37, c38, c39, c40, c41, c42, c43, c44, c45, c46, c47, c48, c49, c50, c51, c52, c53, c54, c55, c56, c57, c58, c59, c60, c61, c62, c63, c64, c65, c66, c67, c68, c69, c70, c71, c72, c73, c74, c75, c76, c77, c78, c79, c80, c81, c82, c83, c84, c85, c86, c87, c88, c89, c90, c91, c92, c93, c94, c95, c96, c97, c98, c99, c100, c101, c102, c103, c104, c105, c106, c107, c108, c109, c110, c111, c112, c113, c114, c115, c116, c117, c118, c119, c120, c121, c122, c123, c124, c125, c126, c127, c128, c129, c130, c131, c132, c133, c134, c135, c136, c137, c138, c139, c140, c141, c142, c143, c144, c145, c146, c147, c148, c149, c150, c151, c152, c153, c154, c155, c156, c157, c158, c159, c160, c161, c162, c163, c164, c165, c166, c167, c168, c169, c170, c171, c172, c173, c174, c175, c176, c177, c178, c179, c180, c181, c182, c183, c184, c185, c186, c187, c188, c189, c190, c191, c192, c193, c194, c195, c196, c197, c198, c199, c200, c201, c202, c203, c204, c205, c206, c207, c208, c209, c210, c211, c212, c213, c214, c215, c216, c217, c218, c219, c220, c221, c222, c223, c224, c225, c226, c227, c228, c229, c230, c231, c232, c233, c234, c235, c236, c237, c238, c239, c240, c241, c242, c243, c244, c245, c246, c247, c248, c249, c250, c251, c252, c253, c254, c255, c256, c257, c258, c259, c260, c261, c262, c263, c264, c265, c266, c267, c268, c269, c270, c271, c272, c273, c274, c275, c276, c277, c278, c279, c280, c281, c282, c283, c284, c285, c286, c287, c288, c289, c290, c291, c292, c293, c294, c295, c296, c297, c298, c299, c300, c301, c302, c303, c304, c305, c306, c307, c308, c309, c310, c311, c312, c313, c314, c315, c316, c317, c318, c319, c320, c321, c322, c323, c324, c325, c326, c327, c328, c329, c330, c331, c332, c333, c334, c335, c336, c337, c338, c339, c340, c341, c342, c343, c344, c345, c346, c347, c348, c349, c350, c351, c352, c353, c354, c355, c356, c357, c358, c359, c360, c361, c362, c363, c364, c365, c366, c367, c368, c369, c370, c371, c372, c373, c374, c375, c376, c377, c378, c379, c380, c381, c382, c383, c384, c385, c386, c387, c388, c389, c390, c391, c392, c393, c394, c395, c396, c397, c398, c399, c400, c401, c402, c403, c404, c405, c406, c407, c408, c409, c410, c411, c412, c413, c414, c415, c416, c417, c418, c419, c420, c421, c422, c423, c424, c425, c426, c427, c428, c429, c430, c431, c432, c433, c434, c435, c436, c437, c438, c439, c440, c441, c442, c443, c444, c445, c446, c447, c448, c449, c450, c451, c452, c453, c454, c455, c456, c457, c458, c459, c460, c461, c462, c463, c464, c465, c466, c467, c468, c469, c470, c471, c472, c473, c474, c475, c476, c477, c478, c479, c480, c481, c482, c483, c484, c485, c486, c487, c488, c489, c490, c491, c492, c493, c494, c495, c496, c497, c498, c499, c500, c501, c502, c503, c504, c505, c506, c507, c508, c509, c510, c511, c512, c513, c514, c515, c516, c517, c518, c519, c520, c521, c522, c523, c524, c525, c526, c527, c528, c529, c530, c531, c532, c533, c534, c535, c536, c537, c538, c539, c540, c541, c542, c543, c544, c545, c546, c547, c548, c549, c550, c551, c552, c553, c554, c555, c556, c557, c558, c559, c560, c561, c562, c563, c564, c565, c566, c567, c568, c569, c570, c571, c572, c573, c574, c575, c576, c577, c578, c579, c580, c581, c582, c583, c584, c585, c586, c587, c588, c589, c590, c591, c592, c593, c594, c595, c596, c597, c598, c599, c600, c601, c602, c603, c604, c605, c606, c607, c608, c609, c610, c611, c612, c613, c614, c615, c616, c617, c618, c619, c620, c621, c622, c623, c624, c625, c626, c627, c628, c629, c630, c631, c632, c633, c634, c635, c636, c637, c638, c639, c640, c641, c642, c643, c644, c645, c646, c647, c648, c649, c650, c651, c652, c653, c654, c655, c656, c657, c658, c659, c660, c661, c662, c663, c664, c665, c666, c667, c668, c669, c670, c671, c672, c673, c674, c675, c676, c677, c678, c679, c680, c681, c682, c683, c684, c685, c686, c687, c688, c689, c690, c691, c692, c693, c694, c695, c696, c697, c698, c699, c700, c701, c702, c703, c704, c705, c706, c707, c708, c709, c710, c711, c712, c713, c714, c715, c716, c717, c718, c719, c720, c721, c722, c723, c724, c725, c726, c727, c728, c729, c730, c731, c732, c733, c734, c735, c736, c737, c738, c739, c740, c741, c742, c743, c744, c745, c746, c747, c748, c749, c750, c751, c752, c753, c754, c755, c756, c757, c758, c759, c760, c761, c762, c763, c764, c765, c766, c767, c768, c769, c770, c771, c772, c773, c774, c775, c776, c777, c778, c779, c780, c781, c782, c783, c784, c785, c786, c787, c788, c789, c790, c791, c792, c793, c794, c795, c796, c797, c798, c799, c800, c801, c802, c803, c804, c805, c806, c807, c808, c809, c810, c81

23

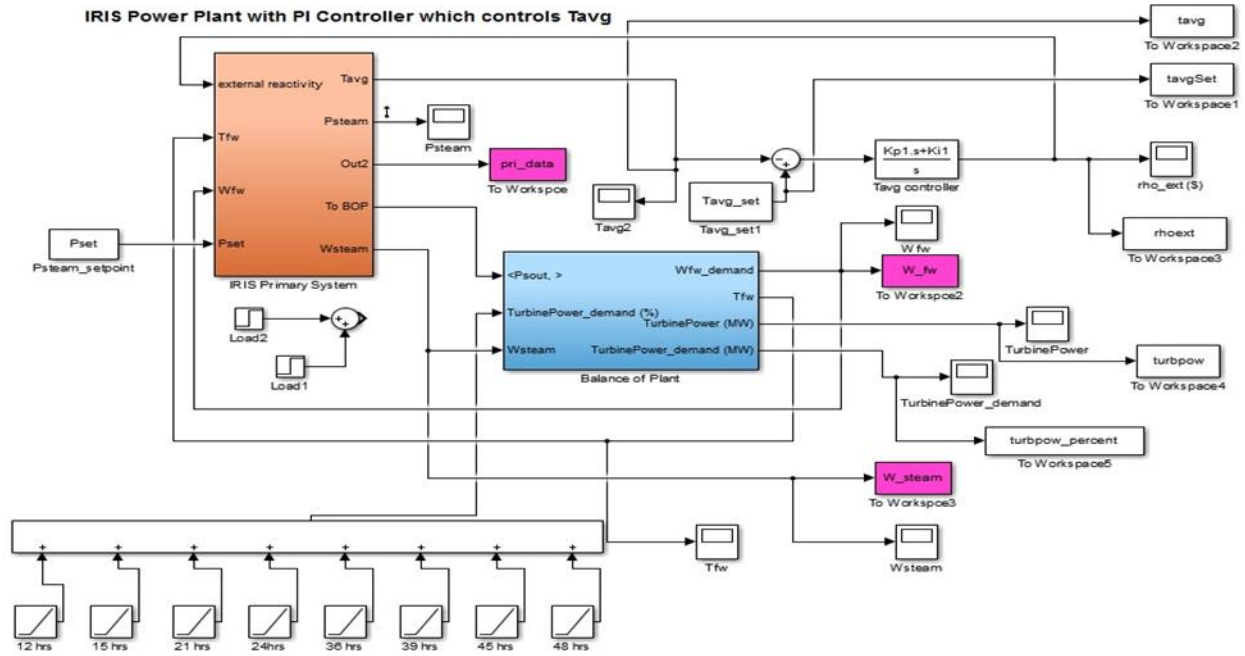


Figure 3.2: IRIS model overview with embedded subsystems

Once the input m-file and functions are run in MATLAB and stored in the workspace, the Simulink model is ready to be run.

The Simulink model was initially designed with expansion in mind. The main pieces of the model include: the reactor core, HCSG, and balance of plant (BOP). The BOP contains all the dynamic equations for turbine operation; important for load-following maneuvers (LFM). This project has seen the addition of other critical subsystems, and will be described in further detail in the next section. The basic reactor dynamics of the system are governed by Mann's Model [22]. Several controllers exist in the model to regulate reactor dynamics. The primary method of control in the primary side of the reactor is the average temperature (T_{avg}) controller. This controller is based on the difference in the measured average temperature between the hot leg and cold leg of the IRIS core and the predefined set point value. The error signal created then feeds into a proportional-integral (P-I) controller for adjusting the reactivity.

3.2. Components Modeled for Increased System Complexity

Several components have been added to the model. This is in addition to the adjustment of other parameters necessary for a specific simulation. For example, some LFMs are conducted for different periods of time and for different fractional changes in power. This requires adjustment

every time a simulation is conducted. Temperature sensor faults were simulated by the addition of step fault blocks to the hot leg temperature signal, and connecting the resulting signal back to the component blocks dependent on the original signal. For many simulations, faults were conducted during LFMs in order to measure abnormal system response during large transient conditions. Other simulations were only carried out during steady-state conditions. This allowed for creation of relationships based on a range of similar fault conditions.

3.2.1 Pump and Motor Model

The embedded subsystem created for the PMM was constructed based on specifications provided by Kujawski et al [22] and Doster [23]. The only true signal connecting the PMM and the IRIS core was the primary core coolant flow rate. This subsystem vastly increased the computational requirements of simulations when coupled with the IRIS. For this reason, simulations were unable to be conducted for long simulation times. For example; a 60 hour LFM without the PMM coupling might take 45 minutes of real time. The coupled simulation, however, would take almost the same amount of real time for a 300 second simulation. This did not allow for as complete a set of simulations as without the coupling, but none the less still provided good results. The results of the PMM coupled with the IRIS will be discussed in Chapter 4.

3.2.2 Fission Product Reactivity Effects

Fission products created during irradiation of UO_2 fuel can have profound reactivity effects on reactor operation and also during power start up following a shutdown. Traditional reactors overcome poisoning effects by control rod movement and use of dissolved neutron absorbers in primary coolant. Some fuels even make use of burnable absorbers mechanically blended into their fuel matrix to help control the reactivity and thus the power. The IRIS design does not utilize dissolved boron in the primary coolant for extra reactivity control. Instead, burnable absorbers are mechanically blended into the fuel and Westinghouse uses their proprietary MSHIM design [28]. MSHIM uses the controls rods for manual reactivity control and even burn up of fuel.

3.3. Comments on the Additional SMR Components

The additional components added to the base IRIS model greatly helped increase the realism of the model and allowed for simulation of a wider variety of conditions and faults. Should other types of simulations be necessary for data generation, the model is still easily adaptable. Some of the sensor faults were able to be completed without creating entirely new subsystems, such as for fission product poisoning and the PMM. This next chapter of this report will focus on the physics of the PMM as well as the effects perturbing the subsystem has on the coupled model.

4. FAULT SIMULATION USING PUMP AND MOTOR MODEL

4.1. Subsystem Development and Necessity

In order for basic ESA to occur and use a motor as a transducer, a motor powering a pump was required to be developed. The IRIS design uses 8 HCSGs and coolant pumps for circulation in the primary loop [9]. Simplifying the simplicity of the simulation led to the use of only one PMM block in the Simulink model. The coolant flow rate in the IRIS was assumed to be constant during operation. This would hold true during operation in general as well since pump health is greatly increased at nominal operation parameters e.g. prevent cavitation in the pumps. In a real plant setting, the pump and motor would also be connected to the system through a power signal and initiate a SCRAM if power was lost to the motor or other faulty criteria were met. Figure 4.1 illustrates the location of the PMM in relation to the IRIS model.

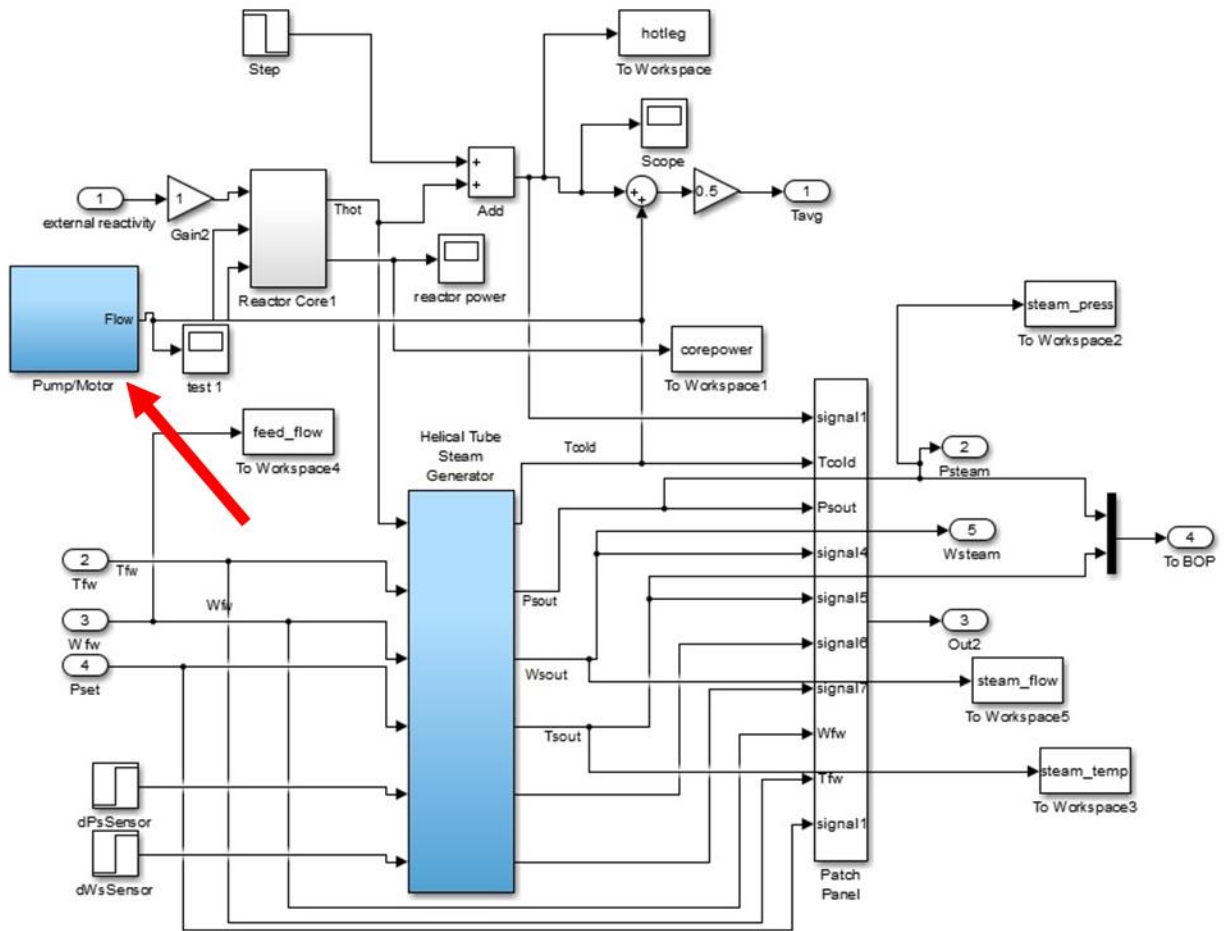


Figure 4.1: PMM embedded subsystem in the IRIS model

4.2. Governing Physics of the Pump Motor Model (PMM)

As described in the previous chapter, the dynamics of the PMM were provided by Doster [23] and Kujawski *et al.* [22] as well as general equations found in the Grundfos handbook [24]. Simulink allows the creation of models using block functions from its internal library. The first step in developing the IRIS PMM was by upgrading a previously developed .5 HP motor into the full-scale IRIS pump. This proved to be ineffective early during development, and a new model was created instead. Two versions of the PMM were created; one as a stand-alone and the embedded system coupled to the IRIS. This allowed for different sets of simulations to be conducted without generating extraneous information i.e. generating reactor parameters when it was only necessary to create data for the PMM. Figure 4.2 shows the overview of the embedded PMM model. The stand-alone is nearly identical, except the coolant flow was not sent to another portion of the model. The coupled model was computationally inefficient, yet still yielded interesting results.

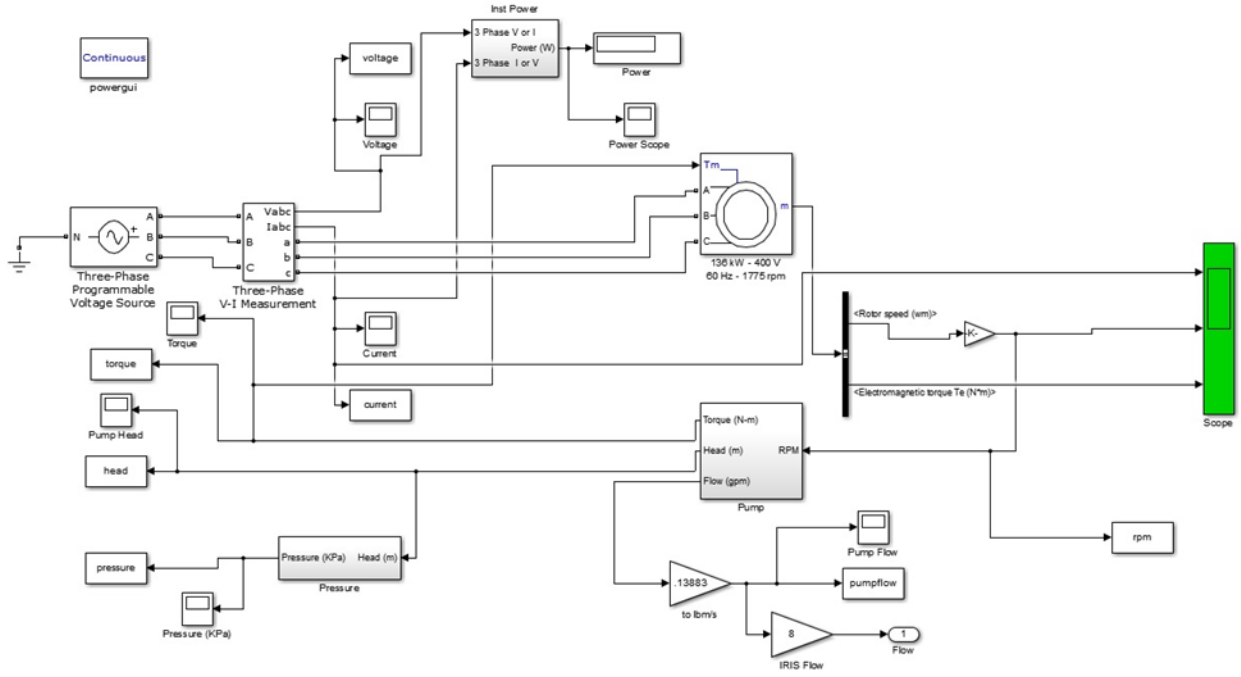


Figure 4.2: Full size view of the PMM embedded subsystem

The PMM governing equations simulate system dynamics during startup, steady-state, and other transient conditions. Some of the physics are made simple due to the nature of the Simulink blocks. Some blocks were as simple as entering two or three parameters, that is, the motor

frequency and the other parameters were automatically calculated. There are many equations, however, that must be manually modeled using math equation blocks. Equation (4.1) shows the pump shaft power input required for operating the pump at the desired flow rate and pump head [26].

$$\text{Pump Shaft Power (kW)} = \frac{\text{Pump Hydraulic Power}}{\text{Efficiency}} = \frac{(Q \cdot H \cdot SG) \cdot 9.81}{3600\eta} \quad (4.1)$$

Where:

Q = volumetric coolant flow rate (m³/hr)

H = pump head (meter) at flow rate Q

SG = specific gravity of the fluid at the pumped temperature

η = pump efficiency; the ratio between pump hydraulic power and pump shaft power

Some of the parameters in the Simulink code are in SI units while others are in English units [9]. Appropriate conversions are applied in order to achieve unit consistency and not introduce error into data generated. Simulink also requires SI units for some of the pre-defined blocks. The motor power required for an individual pump in the IRIS was found to be approximately 136 kWe. The dynamic pump head, shown in Equation (4.2), was provided by Doster [24]

$$H = H_R * \alpha^2 \left[a_0 + b_0 \left(\frac{v}{\alpha} \right) + c_0 \left(\frac{v}{\alpha} \right)^2 + d_0 \left(\frac{v}{\alpha} \right)^3 \right] \quad (4.2)$$

$$v = \frac{Q}{Q_R} \quad (4.2a)$$

$$\alpha = \frac{\Omega}{\Omega_R} \quad (4.2b)$$

Where:

H = pump head (ft)

H_R = rated pump head (78.5 feet)

Q = Volumetric flow rate (gpm)

Q_R = Rated flow rate (14,065 gpm)

Ω = Pump speed (RPM)

Ω_R = Rated pump speed (1775 RPM)

As shown in the Simulink diagram in Figure 4.2, pump shaft torque is a necessary parameter input to the motor block along with the 3-phase current signal. Creating a fault or change in the torque simulates the change in the pump load, therefor changing the current and voltage drawn for the power signal. Other equations used in the creation of the model include shaft power, torque, electrical power, and other associated PMM parameters.

$$Torque = \frac{Pump\ Hydraulic\ Power(Watts) * 30}{\pi * RPM} \quad (4.3)$$

$$P = \frac{QH\rho g}{\eta} \quad (4.4)$$

Where:

P = power (Watt)

Q = volumetric flow rate (m³/s)

ρ = fluid density (kg/m³)

H = dynamic pump head (meter)

The motor instantaneous electrical power is given by:

$$P_M = V_a I_a + V_b I_b + V_c I_c \quad (4.5)$$

Where:

$V_{a,b,c}$ = voltage of the 3-phases (Volts)

$I_{a,b,c}$ = current of the 3-phases (Amps)

The volumetric flow rate (m³/s) as a function of pump speed is given by:

$$Q' = Q \frac{N'}{N} \quad (4.6)$$

Q = base flow rate (m³/s)

N' = new pump speed (RPM)

N = base pump speed (RPM)

The relationship between the pump speed, N', and pump head has the form:

$$N' = N \sqrt{\frac{H'}{H}} \quad (4.7)$$

Where:

H' = new pump head (feet)

H = base pump head (feet)

N = base pump speed (RPM)

The dynamic speed is given by the first order differential equation:

$$\frac{dN_p}{dt} = \frac{P_d}{(2\pi)^2 N_p I} - \frac{\rho g Q_p H_p}{(2\pi)^2 N_p I} \quad (4.8)$$

Where:

P_d = motor power (W)

N_p = pump speed (RPM)

I = moment of inertia

Q_p = volumetric fluid flow (m³/s)

H_p = pump head (meter)

Other equations will be displayed in Appendix C for some of dynamics governing the circuitry of the 3-phase block.

4.3. Results of the Coupled System Simulation

Fault simulation in the PMM primarily dealt with changing the operational frequency (60 Hz) and indirectly creating desired faults. By this, a ramp frequency fault was used to change the voltage or current signals in the PMM which would in turn affect system parameters. Since the PMM is only directly coupled to the rest of the IRIS model through the coolant signal, determining where a fault stems from. For example, if power is changing in the reactor core without an LFM occurring and based on changes in other parameters, it could potentially be

traced backed to a faulty pump or motor. A comparison was also made with the experimental component of the project for a series of faults, and yielded similar results indicating the PMM is a good tool for use in simulation.

4.3.1 Power Signal Faults

The faults simulated in this section are in the motor and voltage and current signals As shown in Figure 4.3, two faults were conducted for this set; $+0.0175 \text{ Hz/s}$ and -0.015 Hz/s The ramp block added the faulty signal to the PMM over a 30 second period between 120 and 150 seconds. This allowed for the system to reach a steady state before the faults were added. The baseline signal is also included for all parameters in this section as a reference.

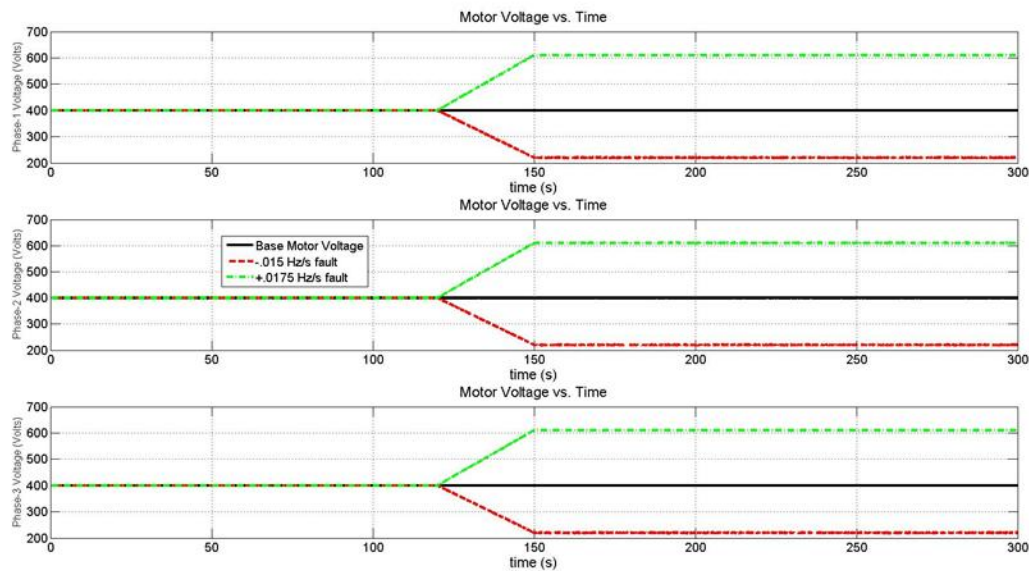


Figure 4.3: Three-Phase voltage fault profile

Figure 4.3 shows the voltage signal response to the signal frequency fault. Voltage is either increased or decreased by approximately 50% for the corresponding fault. In a real system, this is a very high voltage change and would likely cause a shutdown to prevent motor damage or create a dangerous operating condition. The time scale of the simulations should also be noted. Three hundred seconds is not a long time to truly see how system response occurs. Effects from the faults, however, are evident and suffice to monitor system response.

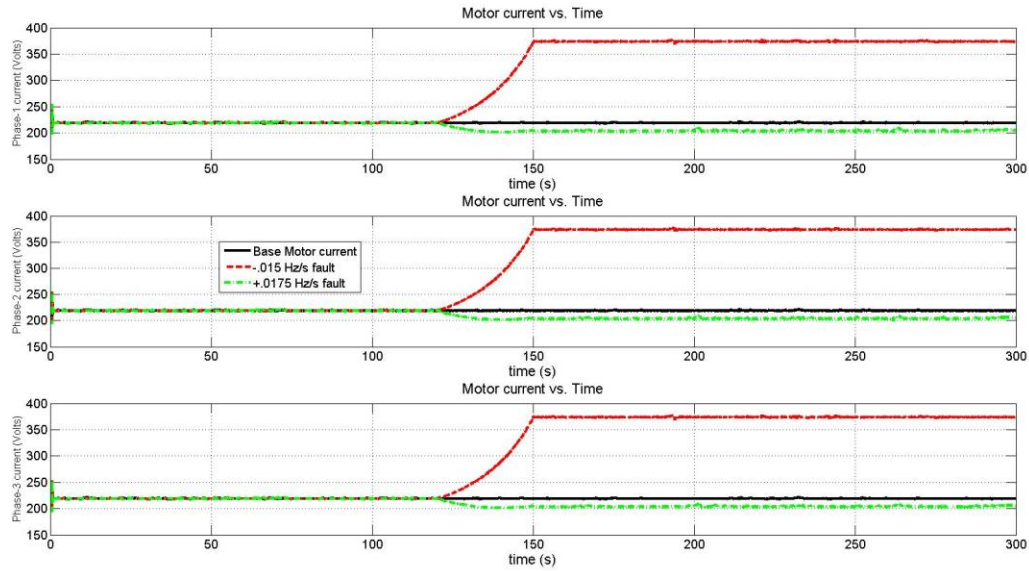


Figure 4.4: Three-phase current response to the frequency fault

The motor current in signal Figure 4.4 responds in a different fashion to the frequency faults. The decreased frequency fault leads to an increase by approximately 150 Amps, while the increased frequency leads to a drop in current by approximately 25 Amps. The response appears to be non-linear not in an equal and opposite effect in a manner the voltage signal responds. This will lead to non-linear responses in the rest of the monitored parameters shown in this section.

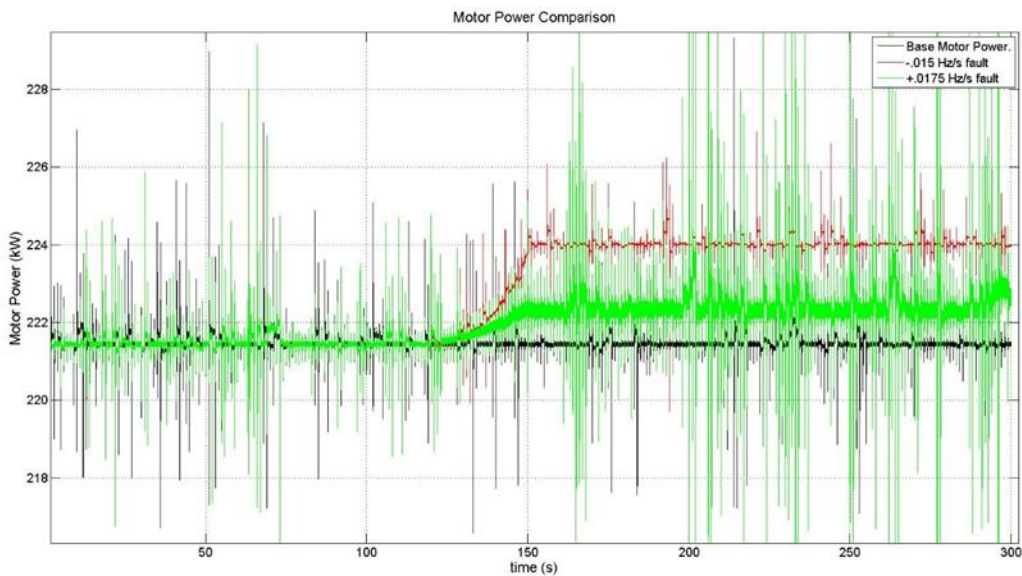


Figure 4.5: Motor power response to voltage and current faults

Even though the voltage and current signals experience opposite effects during the fault addition, the overall effect leads to an increase in the motor power for both the positive and negative frequency change. Figure 4.5 illustrates the effect for the frequency faults. The seemingly large spikes in the motor power signal are indicative of random noise fluctuations in the system and from the frequency faults. There were no faults simulated for the operational frequency or other types that could be experienced during operation; for example, a miscalibration.

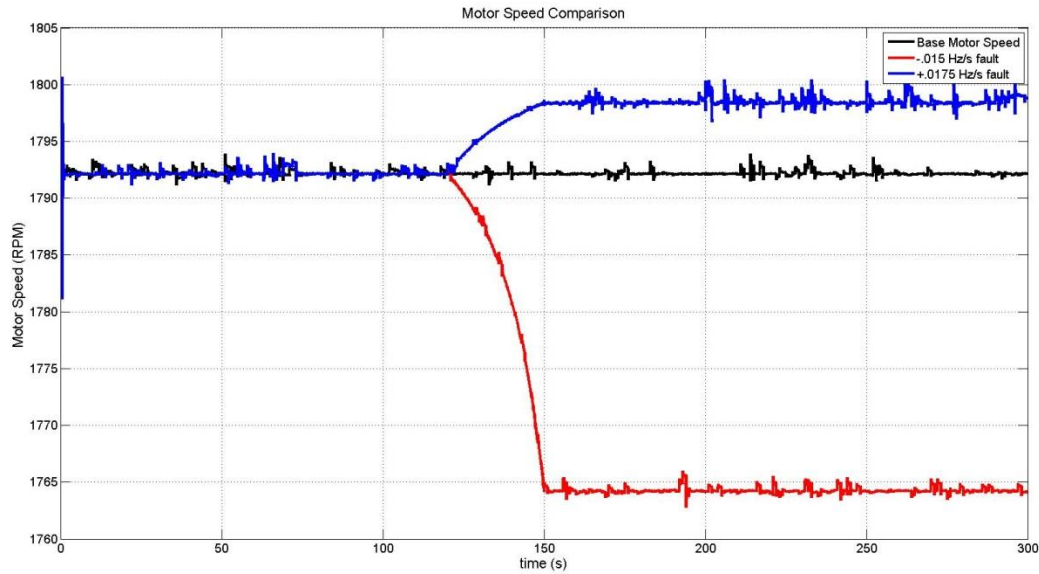


Figure 4.6: Motor speed response to voltage and current faults

The motor speed responds to fault changes in a similar fashion to the response of the voltage signal. Most of the parameters in the model are based upon one another i.e. a change in power will affect speed, head, flow, which in turn affect each other. These relationships between parameters can be seen in Equations (4.2) - (4.8).

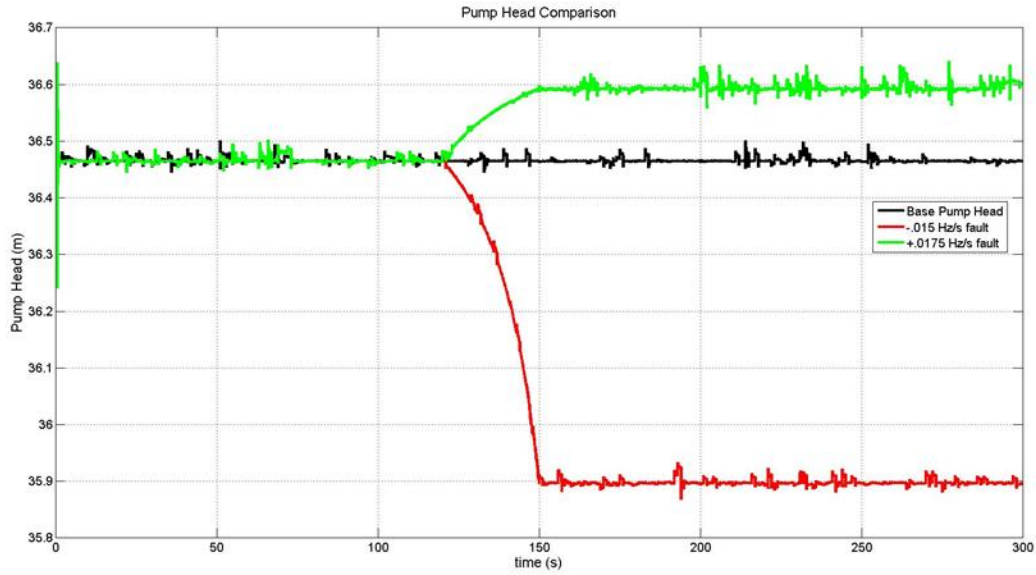


Figure 4.7: Pump fluid head response to voltage and current faults

The changes in the pump head appear to be rather large; the scale of Figure 4.7 is misleading. The positive frequency fault corresponds to a change in the pump head by approximately 0.13 m while the negative fault creates a drop in head by almost 0.57 m.

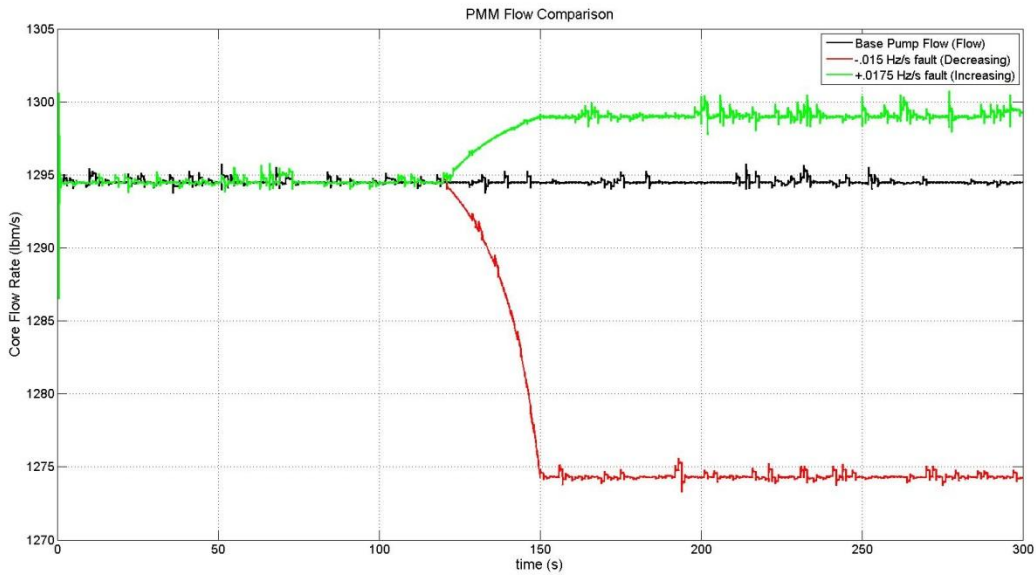


Figure 4.8: Coolant flow response to voltage and current faults

The responses in Figures 4.7 and 4.8 are nearly identical from the frequency faults. This seems counter intuitive to how pump head and coolant flow should respond i.e. a decrease in flow should lead to an increase in head and vice-versa. Since the motor power is increasing for both cases of frequency change but speed changes in an opposite manner, the results in Figure 4.8 respond in a correct fashion.

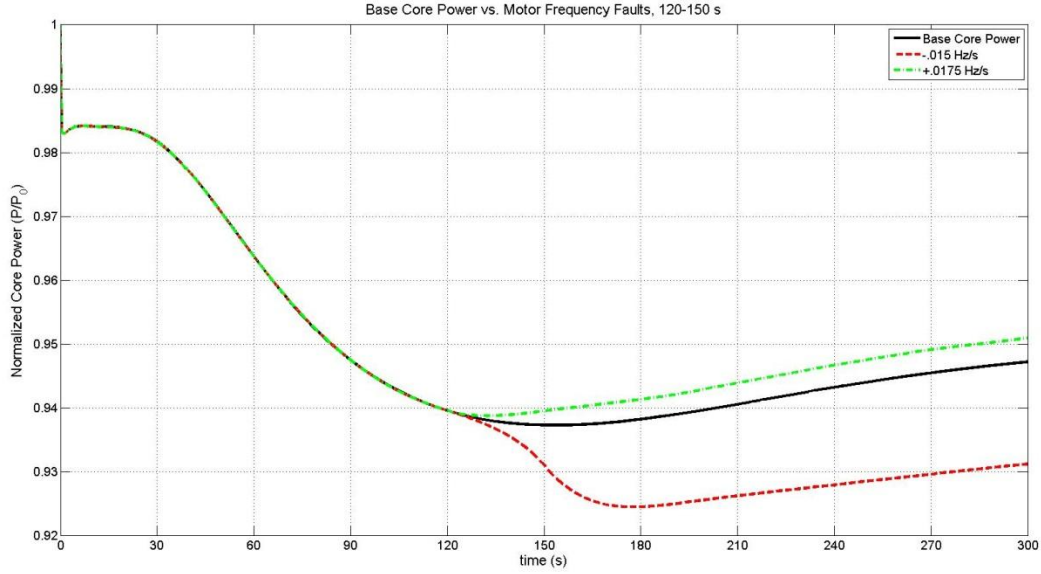


Figure 4.9: Reactor core power response to current and voltage faults in the PMM

The changes in the IRIS parameters from the PMM faults all related to changes in the primary coolant flow rate. Figure 4.9 illustrates the change in flow rate has on reactor core power. The basic relationship with power and flow rate is based on Equation 4.9, while in the larger scale affects the dynamic response in Mann's model [22]. The change in reactor core power is not very large when the frequency increases, but affects output by approximately 1.6% when the frequency decreases. This significant decrease in power would likely be detected by reactor operators and require action in order to return power output to the desired level.

$$\dot{Q} = \dot{m}c_p\Delta T \quad (4.9)$$

Where:

\dot{Q} = Reactor power (MWth)

\dot{m} = Mass coolant flow rate (kg/s)

c_p = Heat transfer coefficient (kJ/kg-°C)

ΔT = Change in primary coolant temperature (°C)

This means assuming other parameters hold constant, a change in the coolant flow is proportional to a change in the reactor core power.

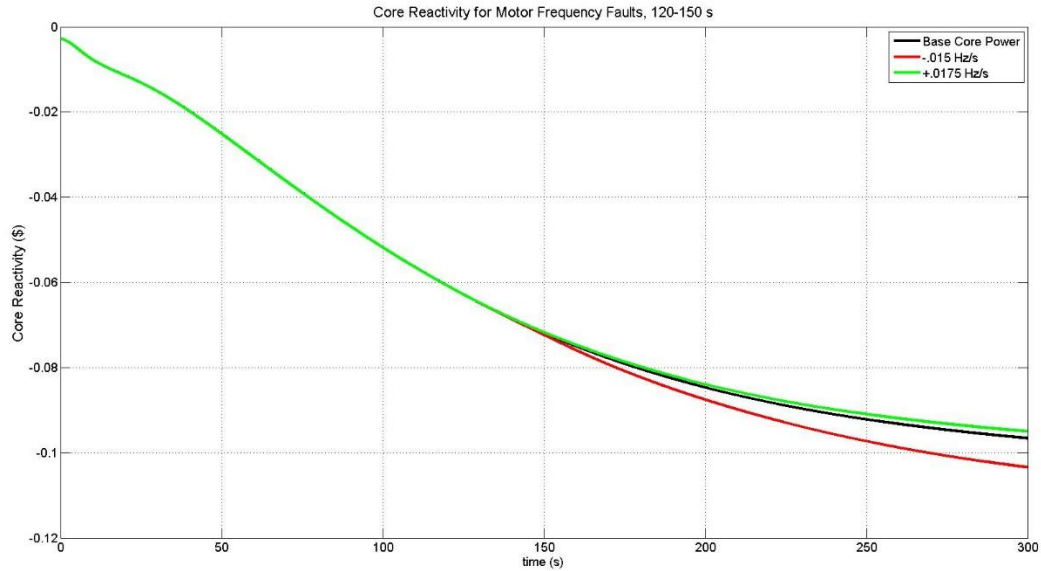


Figure 4.10: Core external reactivity response to current and voltage faults in the PMM

Figure 4.10 shows the change in external reactivity in the IRIS core. The change in reactivity is very small. While the increases in reactivity are small when the coolant flow increases, it should be noted the value is still negative. This response is important to consider since the negative reactivity indicates the system will stabilize; an important safety feature.

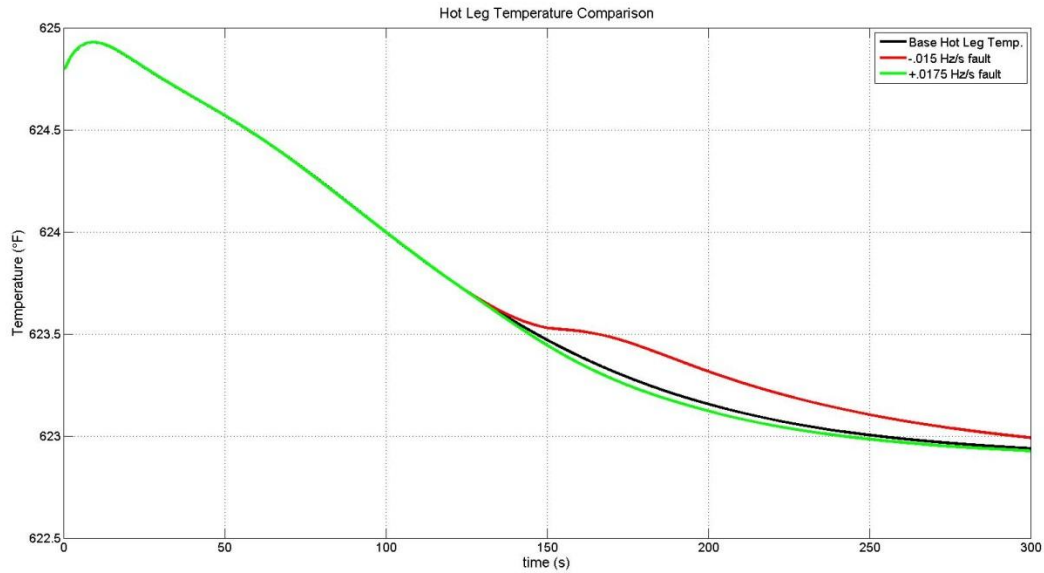


Figure 4.11: Hot leg temperature response to current and voltage faults in the PMM

Figures 4.11 and 4.12 show the changes in the primary coolant inlet and outlet temperatures, respectively. When the coolant temperature increases, the coolant density also increases and becomes a less effective neutron moderator. This is due to the negative temperature coefficient of reactivity; a critical, passive safety feature in PWRs. The actual changes in the temperature values are fractional values of degrees, however. As can be seen in Figure 4.11, the temperatures resulting from the frequency faults are returning to the baseline value within a relatively short time period. This indicates two to key pieces of information: the controller can handle faults well and the primary coolant temperatures are not a good place to look or perform cross-checks during fault monitoring. Should the controller not handle the fault in a correct fashion yet the temperature deviations are similar to those found at 200 seconds, it is still unlikely to detect a fault from this signal since it may naturally have fluctuations in the tenths of degrees to a full degree or two; the change is essentially trivial.

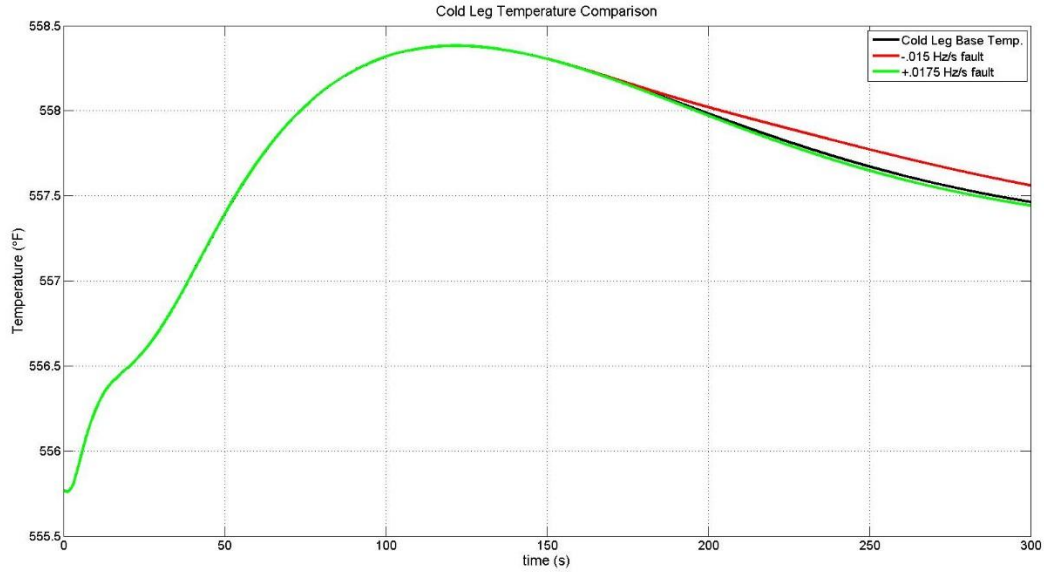


Figure 4.12: Cold leg temperature response to current and voltage faults in the PMM

In the IRIS model, the inlet temperature is fixed in Mann's Model [22]. Since the primary controller in the system is based on the difference in the T_{avg} value, the cold leg temperature will respond to reduce the error between T_{avg} and the T_{avg} set point.

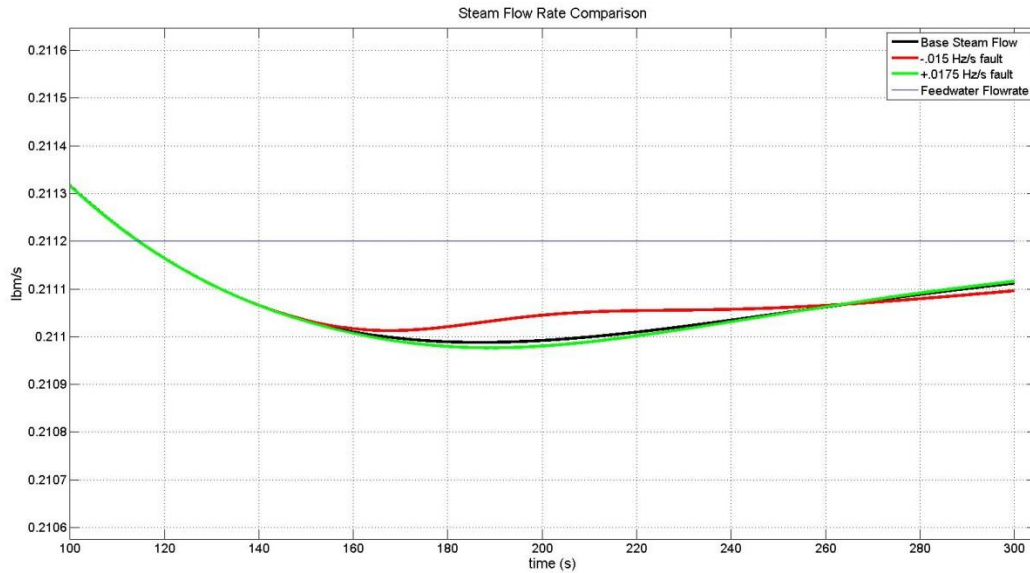


Figure 4.13: Steam flow response to current and voltage faults in the PMM

Although Figure 4.13 shows a change in the steam flow rate, the deviation from the baseline steam flow rate is trivial. Since the turbine power demand is not changing during this fault simulation, the steam flow rate will stay consistent since the steam flow rate is slaved to the turbine output. The dynamics concerning the turbine output and steam demand will be explained in greater detail in Chapter 5.

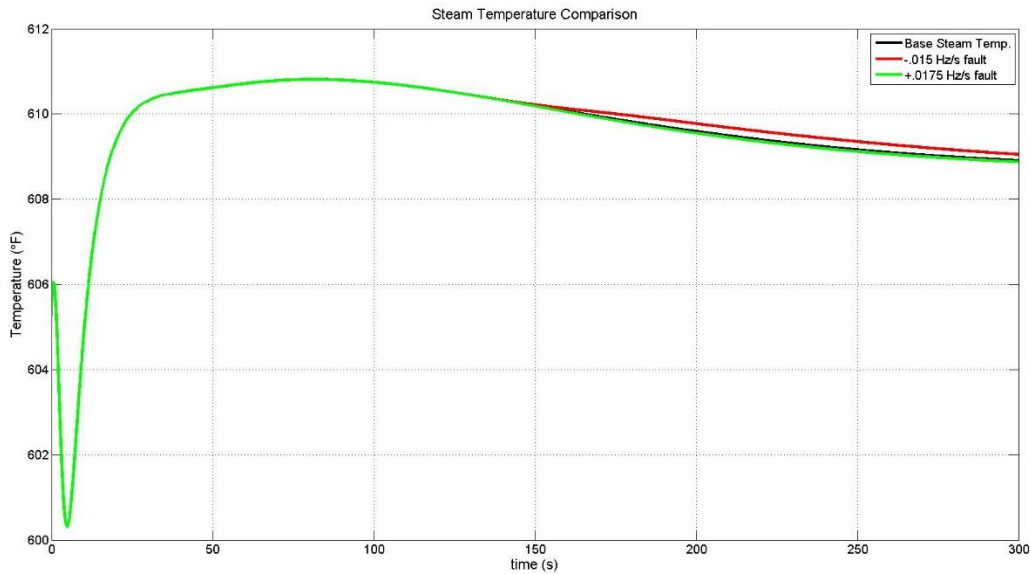


Figure 4.14: Steam temperature response to current and voltage faults in the PMM

The changes in the steam temperature during the faults are negligible. The small changes can be attributed to the changes in the hot leg temperature profile. This section has illustrated the difficulty detecting faults in the PMM can be. Identifying other parameters to monitor in the reactor can be difficult. This is especially true if changes in parameters resulting from the fault are comparable to the natural fluctuations they would experience during normal operation.

4.3.2 Perturbation of Operational Frequency

Comparing experimental data with computational data was one of the objectives during this set of simulations. This specific set of simulations involved comparing parameter response to a change in the operational frequency of the pump and motor. The normal operational frequency of the pump is rated at 60 Hz. Simulations were conducted from 55-60 Hz in .5 Hz increments. Data was then analyzed and modified to create a single data point for a simulation run. The data was modified by removing the initial startup transient data, then finding the mean value of the

signal. This was done in order to see what, if any, type of relationship could be found between frequency, power, and fluid flow.

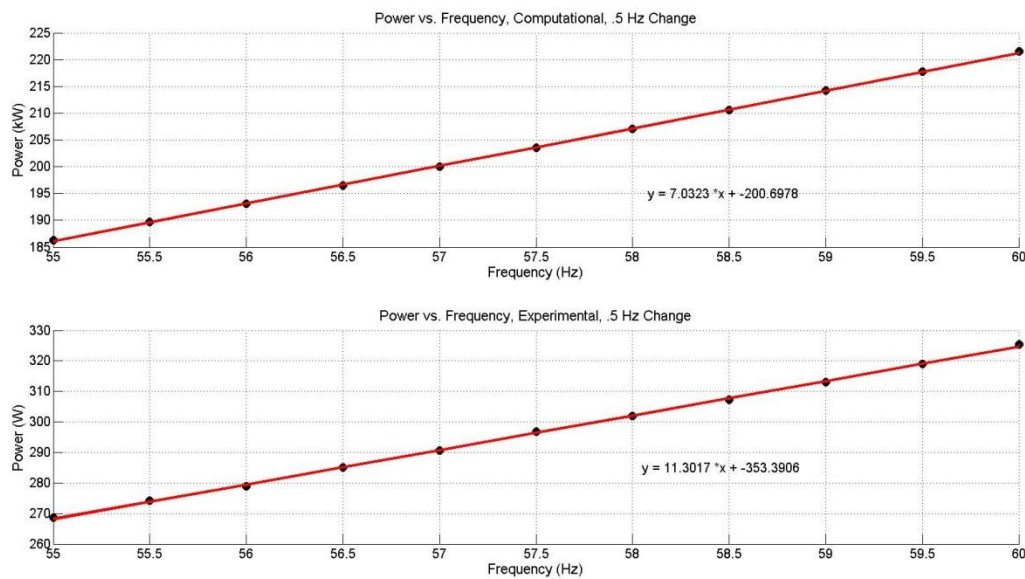


Figure 4.15: Power vs. Frequency plots for a 0.5 Hz change in frequency; simulation (top) and experiment (bottom)

The change in power from the frequency change can be seen in Figure 4.15. In both the experimental and the computational data sets, linear relationships exist between the power and frequency change. It should be noted while the linear trends are similar for both sets of data, the formulas generated through linear regression are remarkably different. Please note the scale used for the change in power. The experimental setup is in the watts range while kilowatts are used in the computational data set. The general relationship, however, appears to be accurate for the simulated faults based on the experimental data.

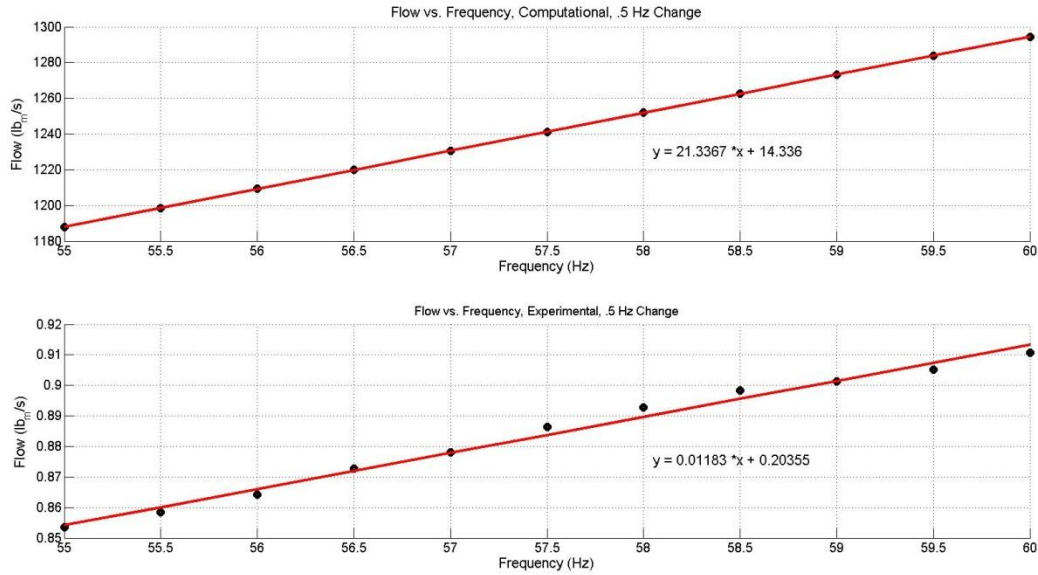


Figure 4.16: Flow vs. Frequency Plots for 0.5 Hz changes in the motor frequency; simulation (top) and experimental (bottom)

Similar to the results shown in Figure 4.15, Figure 4.16 displays the relationship obtained between a change in the motor frequency and the fluid flow through the pump. The linear fit for the simulation data is not subject to any noise or natural fluctuations during operation. This accounts for the seemingly perfect fit, in contrast to the experimental data which does experience real operational conditions. Even with the noise and natural fluctuations in the experimental data set, it still fits the linear regression trend line very well.

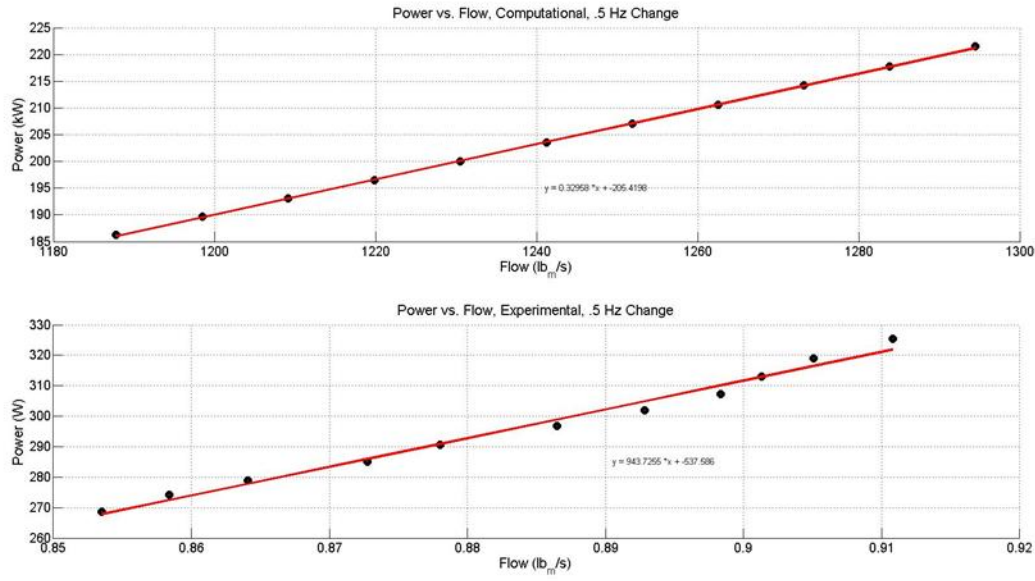


Figure 4.17: Power vs. Flow plots for a 0.5 Hz change in motor frequency; simulation (top) and experimental (bottom)

If Equation 4.4 is rearranged to solve for fluid flow instead of power, an increase in pump power is directly proportional to an increase in fluid flow. This indicates the power versus flow relationship, shown in Figure 4.17, is correct. These fault conditions illustrate the effects a seemingly small change in a motors nominal frequency can have on parameter operation. Flow drops in the PMM by approximately 9% during a 5 Hz change in motor frequency.

4.4. Remarks on the Pump and Motor Model

Changing the parameters in the PMM has an effect on IRIS operation. Faults stemming from the power signal or a fundamental change in the PMM can be detrimental to the health of machinery and safety of employees. In a real setting, it is likely this drastic change will not occur instantly or before operation, as it was performed here. Instead, it will likely be a more gradual change, similar to the faults demonstrated in Section 4.3.1. High or low flow rate though the pumps can lead to improper heat removal from the core, impacting plant performance. In addition, a high enough voltage or current in a motor would likely lead to a plant shutdown. These costly, unnecessary shutdowns affect plant performance and economics; the latter is one of the attractive features of SMR deployment.

5. LOAD-FOLLOWING SIMULATIONS AND SYSTEM RESPONSE

5.1. Importance of Load-Following Maneuvers (LFM) in SMRs

One of the marketable features of SMRs is their ability to perform LFMs. This is in contrast to traditional reactors operating at a base load condition. They provide power at close to 100% nominal power during a fuel cycle, except during times of maintenance. Due to the base load operating, plants may actually produce more power than necessary and as a result not be operating as profitable as they could be. LFMs allow utilities the opportunity to meet electrical demand, in a reasonable time, while producing the necessary amount of power. Power usage will normally fluctuate during the day and seasons. More power is typically needed during the summer and winter months to accommodate air conditioning and heating. In addition, more power is used at night when people return to their dwellings.

5.2. Dynamics of Reactor Systems during Load-Following

Load-following simulations were conducted for a variety of power increases and decreases as well as time scales. The following presents a general system dynamics overview for a change in turbine power output from 100% to 80%. The opposite scenario also holds true if power was increasing instead [9]:

- The reactor operator sets a load program (ex. 5% change per hour)
- An error signal is created between the desired load and the turbine output. The turbine inlet steam pressure is correlated to turbine output
- The difference created between reactor power and turbine output creates a signal to move the control rods
- The error created based on the difference in the actual average temperature (T_{avg}) and the reference average temperature is based on the real turbine output. The output is used to calculate the percent power in the T_{avg} vs. power program
- As the error in the T_{avg} signals change, the control rods move to decrease the reactor power
- The turbine control valves then actuate to maintain the programmed steam pressure value

- The load versus feed water flow program evaluates the necessary flow for these parameters. The feed water actuates to minimize the error in the flow
- The error in the desired load and actual turbine load corrects the feed water flow by decreasing the flow for this program
- Decreased feed flow translates to decreased steam production and subsequently, decreased steam pressure
- As the reactor power decreases, the measured T_{avg} decreases. Control rod motion stops once measure T_{avg} is equal to the reference T_{avg}

A typical example of an LFM profile can be shown in Figure 5.1. This specific maneuver is for two complete cycles; a decrease and increase in power. Specific maneuvers will be displayed for fault simulation in the next section.

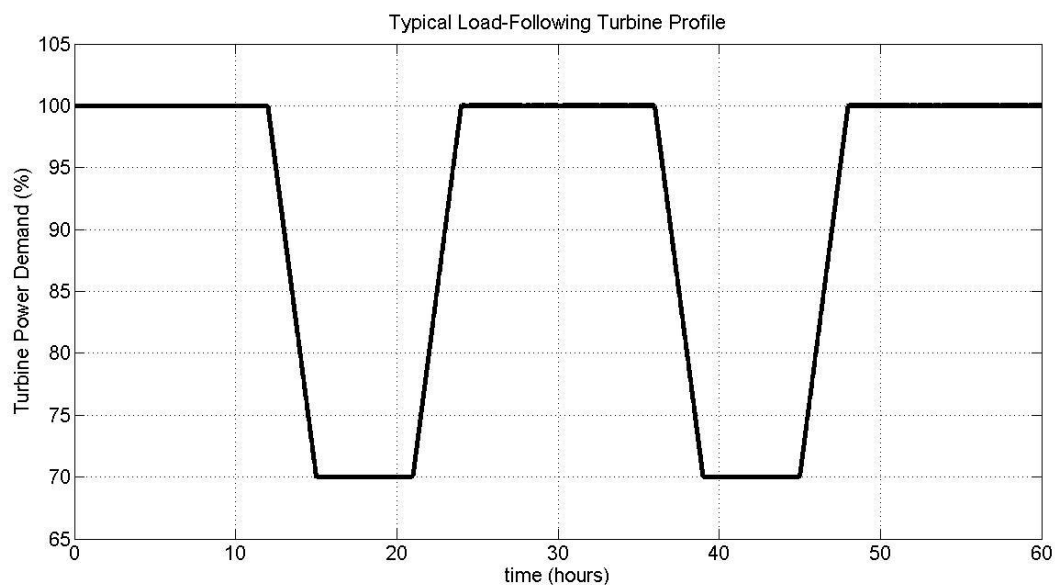


Figure 5.1: Turbine output for a typical LFM

5.3. Faults Introduced during LFM

The faults presented in this section are for a sensor fault and an actual fault in the system. The temperature sensor fault presented in Section 5.3.1 illustrates the effects bad data from a sensor can have on plant operation. Since sensor calibration can be costly and time consuming, the sensor fault effects directly show why cross checking system parameters and redundancy will be important for wide deployment of SMRs. In contrast to the temperature sensor faults, the

reactivity contributions from the CRDM were designed to be an actual fault i.e. not the result of a bad sensor. Since the LFM's are dependent of control rod movement, it is possible there could be improper movement of rods during operation. This is a critical system to be monitored since faulty movement from the CRDM could lead to unsafe or uneconomical conditions.

5.3.1 Temperature Sensor Faults

This set of simulations focus on the effects of a fault in the hot leg temperature sensor as well as noise added to the hot leg signal during an LFM. This was carried out in order to accomplish two goals; how will noise propagate in the system and see system response to a sensor fault in contrast to an actual change in the hot leg temperature.

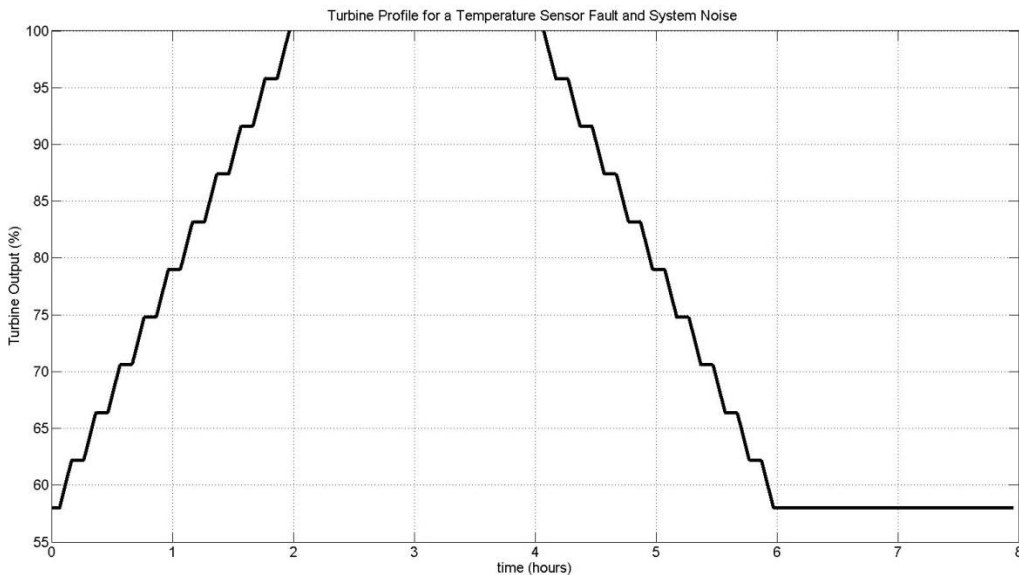


Figure 5.2: Turbine load profile for temperature sensor fault simulations

Figure 5.2 illustrates the turbine power profile used in this set of simulations. The LFM is based on a 5% ramp change in power from 57% to 100%, and back to 57% over a 6 hour time period; a relatively rapid change. The normalized reactor core profile can be seen in Figure 5.3. The fault was inserted into a full-power output during the steady state at 3 hours of simulation time. The range of faults conducted is for a positive and negative addition of 2, 5, or 7 °F. This section will display the results from the 7 °F fault exclusively. The other two faults had nearly identical effects on the system, but to a smaller degree.

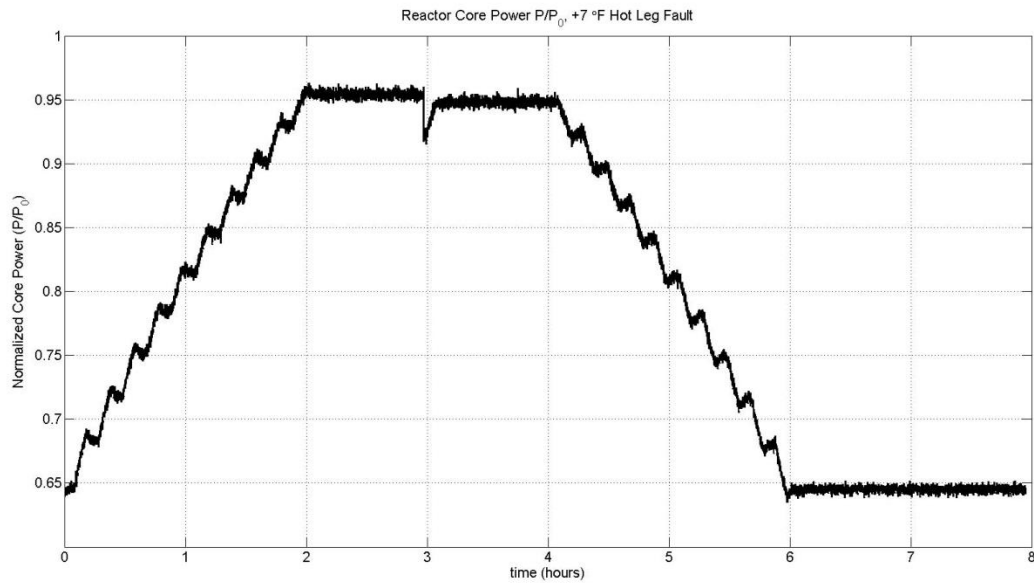


Figure 5.3: Reactor core power response with a +7 °F sensor fault

Noise was also added to this simulation set to determine if it could mask the temperature fault. The 7 °F had the greatest impact on plant parameters. The drop in the core power at the time of the fault in Figure 5.3 can be attributed to temperature related feedback effects from the fuel and coolant temperatures as well as from the T-avg controller. As temperature increases in the system due to the sensor fault, the controller works to return the average temperature back to its nominal set point by inserting control rods and dropping reactivity.

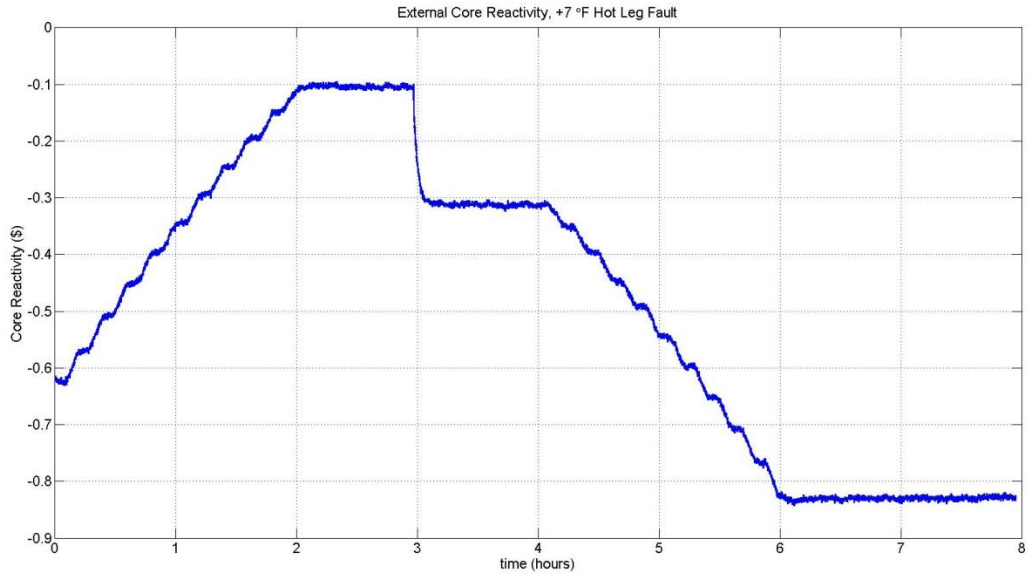


Figure 5.4: External core reactivity response with a + 7 °F sensor fault

The external core reactivity, shown in Figure 5.4, shows how LFMs affect the parameter yet the temperature fault is the single greatest effect on the reactivity. Reactivity in the system is calculated by a relatively simple relationship; the difference between T_{avg} and $T_{avg,set}$, then converted to dollars. Note the new steady state value achieved after the sensor fault occurs. The baseline value is 0.2 dollar less than before the fault. After the power is decreased back to 57%, the baseline is still lower than before the simulation started.

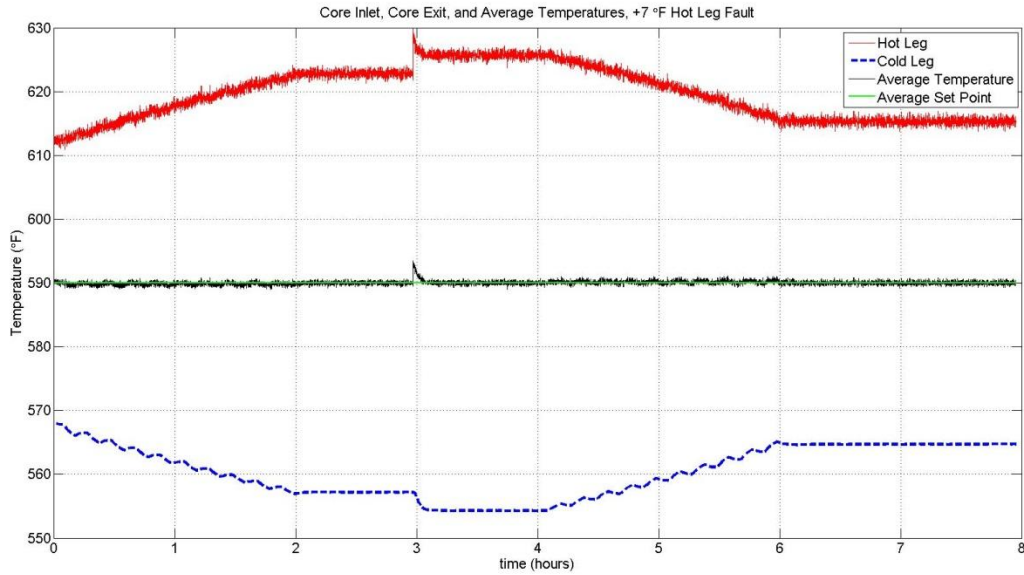


Figure 5.5: Primary coolant temperature profile with a + 7 °F sensor fault

Withdrawing control rods from the core will lead to an increase in fissions, power, and the hot leg temperature. This can be seen between 0 and 2 hours in Figure 5.5. Once the sensor fault was introduced into the hot leg signal at 3 hours, the increase occurs without control rod movement. Since the T_{avg} controller works to maintain the value as close to the set point and the hot leg permanently increased, the cold leg will respond in an equal but opposite manner. The +2 and 5 °F faults had similar effects. The 7 °F is shown here since it has the best figures for display.

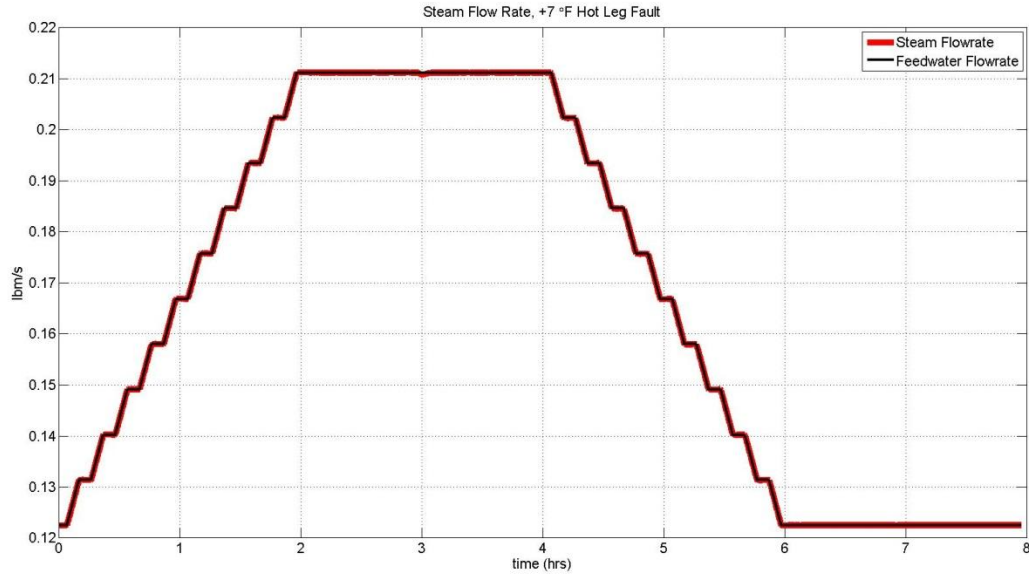


Figure 5.6: Steam flow rate with a + 7 °F sensor fault

Steam flow is directly correlated to turbine output at the time of the sensor fault insertion, a change in the steam flow is difficult to see as evident by Figure 5.6. If it is desired to perform cross checks on instrumentation, looking at data from the feed or steam flow would not help with fault identification.

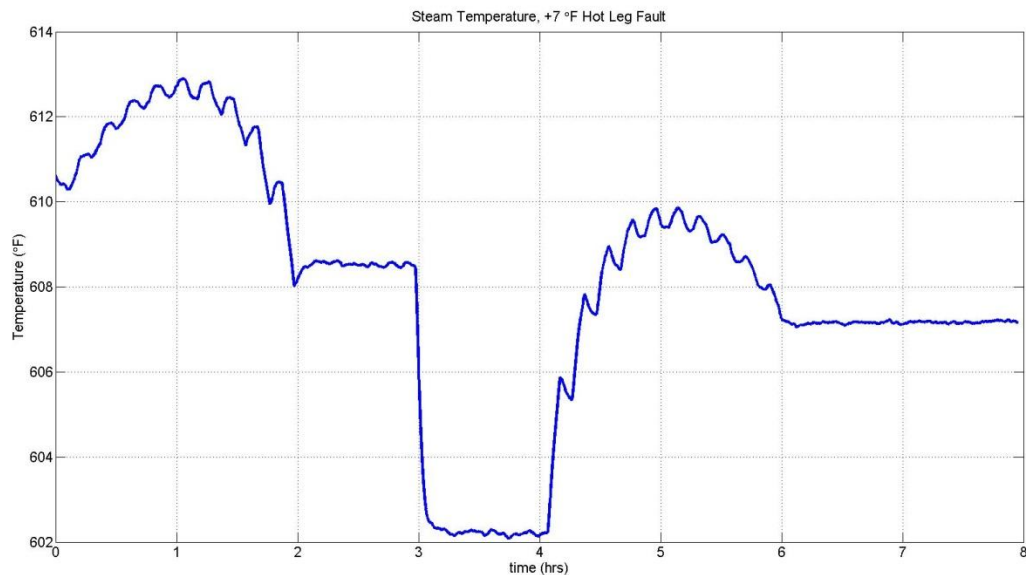


Figure 5.7: Steam temperature profile with a + 7 °F sensor fault

Figure 5.7 shows the steam temperature response during the LFM. Temperature change in the steam is likely attributed to the change in reactivity and power. During the LFM, it can be seen

that the steam temperature increases in response to the hot leg temperature change. The hot leg signal only appears to increase during the sensor fault, however, while the core power drops and therefore affects steam temperature.

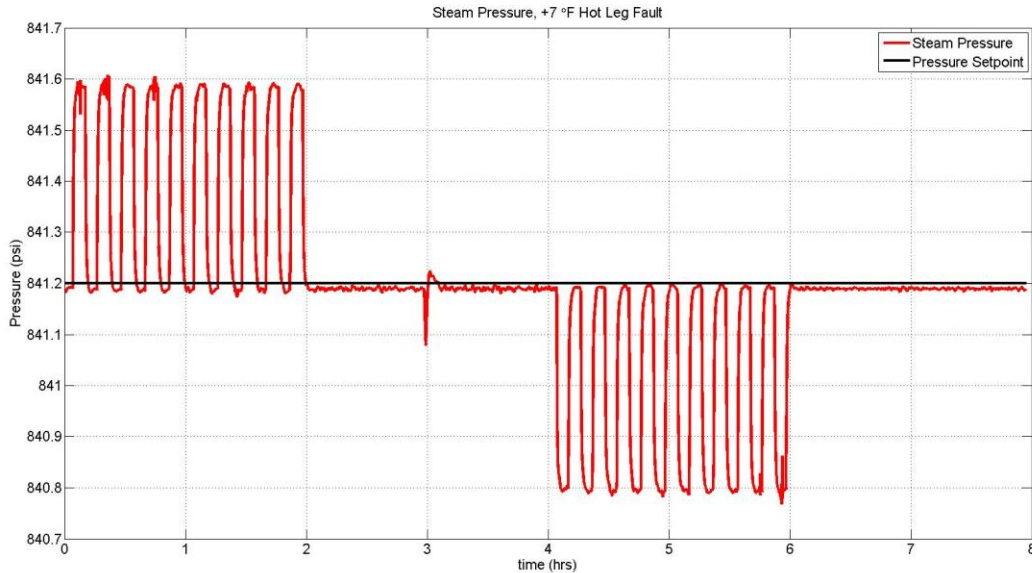


Figure 5.8: Steam pressure response with a + 7 °F sensor fault

The steam pressure responds rapidly due to changes primarily in the turbine load, as described by the maneuver synopsis. Figure 5.8 is slightly misleading in with the degree of change from the baseline condition. The set point value is set at 841.2 psi, and the maximum change is +/- .4 psi; a small change. This illustrates how well the steam pressure controller works during transients to return pressure to a baseline value. Monitoring the pressure signal may be useful for determining if a fault has occurred, especially if the power is held at 100% for a long time. Then it would be much easier to analyze data and make a decision. It should be noted the fault could be masked depending on the natural fluctuations in the steam pressure signal. While it is clear the fault provides a much greater spike than the noise, the largest value of the fault is still only approximately 0.12 psi.

5.3.2 Faulty Control Rod Movement

The general strategy of this fault is to simulate an improper movement of control rods in the CRDM. In addition to the problems mentioned with this type of fault detailed in Section 5.3, improper movement of the CRDM can also lead to unequal fuel irradiation and different temperatures or “hot spots” forming. It is necessary to simulate this type of condition since

power and LFMs are directly governed by movement of the CRDM [9]. IRIS was not designed with use of a dissolved neutron poisons in the coolant such as Boron. In the absence of other control actions, a stuck rod in or out of the reactor core will have a much more noticeable impact on plant parameters. This could also hold true if instrumentation for the CRDM is operating outside allowable margins, and faulty information is presented to operators. This will, again, facilitate the need for cross checks to be made with other parameters to confirm measurements. Simulations were made for positive and negative LFMs. The faults were inserted in the external reactivity block of the Simulink model.

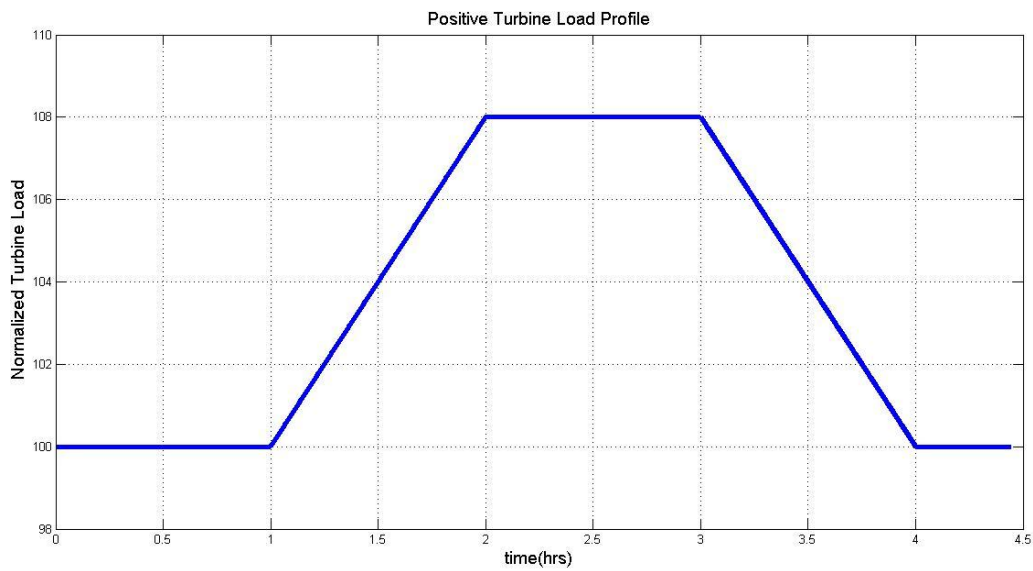


Figure 5.9: Turbine load demand profile for a positive load change

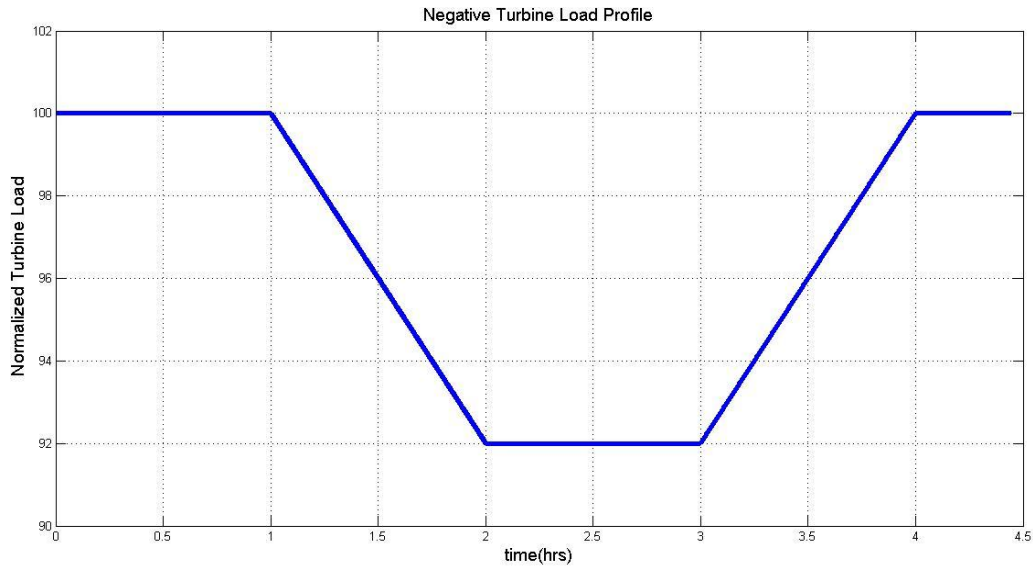


Figure 5.10: Turbine load profile for a negative load change

Figures 5.9 and 5.10 show the profiles used for Sections 5.3.3-5.3.6. Figure 5.9 shows power increasing to 108% and back down to 100%. In actual operation, this would not occur since a plant would likely not be rated for this high power increase over 100% base power. It was simply done for simulation purposes and avoided the necessity of dropping power to 92% then increasing back to 100%.

5.3.3 Negative Load Profile, Negative Reactivity

All simulations in the next 4 subsections are for fault insertions at 1.25 hours and ending at 4 hours. The simulations display the effects a 5, 7, or a 10% change in the nominal external reactivity value. This value was chosen to perturb since the T-avg controller reactivity is a direct result of this parameter. Figure 5.11 displays the effect of a negative reactivity contribution during a negative LFM. It is evident the main reactivity contribution results from the LFM and movement of the CRDM in contrast to the faulty reactivity contributions. The larger the negative reactivity insertion into the core, the less power will be produced. The change in power from the fault is only 0.001- 0.002 of 1000 MWth; this 1-2 MWth is a significant value.

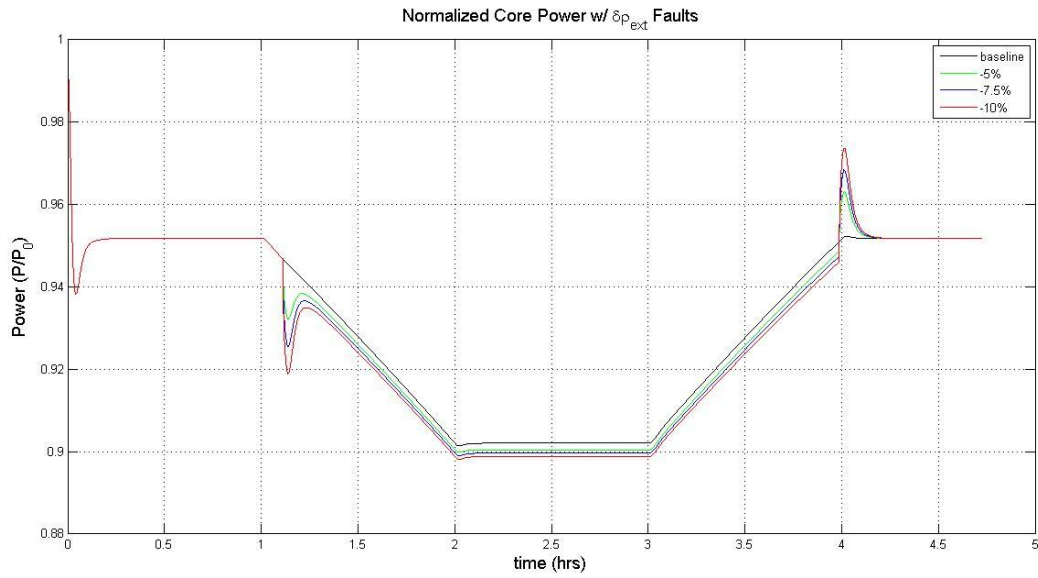


Figure 5.11: Reactor core profile for negative reactivity and a negative LFM

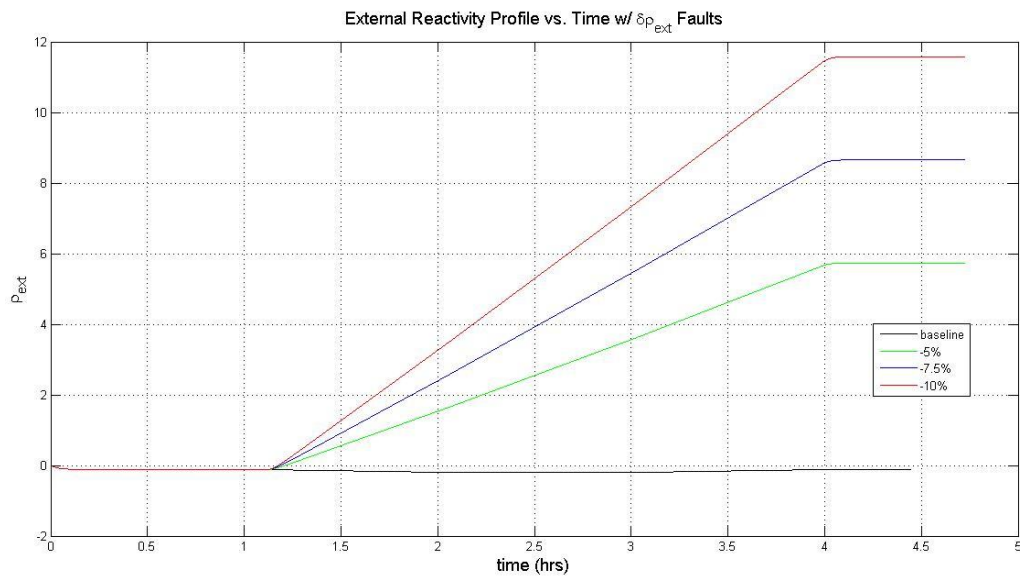


Figure 5.12: Negative external reactivity insertion profile

The fault profile for the negative reactivity insertions can be seen in Figure 5.12. The profile for the positive insertion is an equal but opposite set. Figure 5.12 can be misleading. The fault was added to the simulation after the Tav_g controller. This is why the value is increasing, the total reactivity decreases and thus decreases core power.

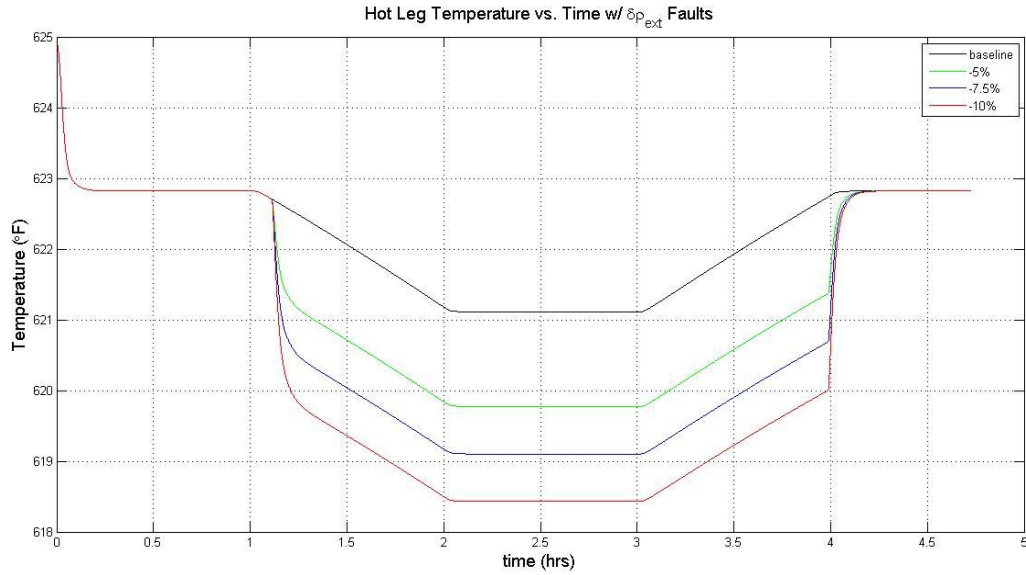


Figure 5.13: Hot leg temperature response for negative reactivity and a negative LFM

In order for the average temperature to remain relatively constant, the hot leg temperature will decrease when cold leg temperature increases. For an increase in core power, the opposite effect will hold true. The hot leg response, shown in Figure 5.13, has its largest change of -2.5 °F occurring during the -10% reactivity change.

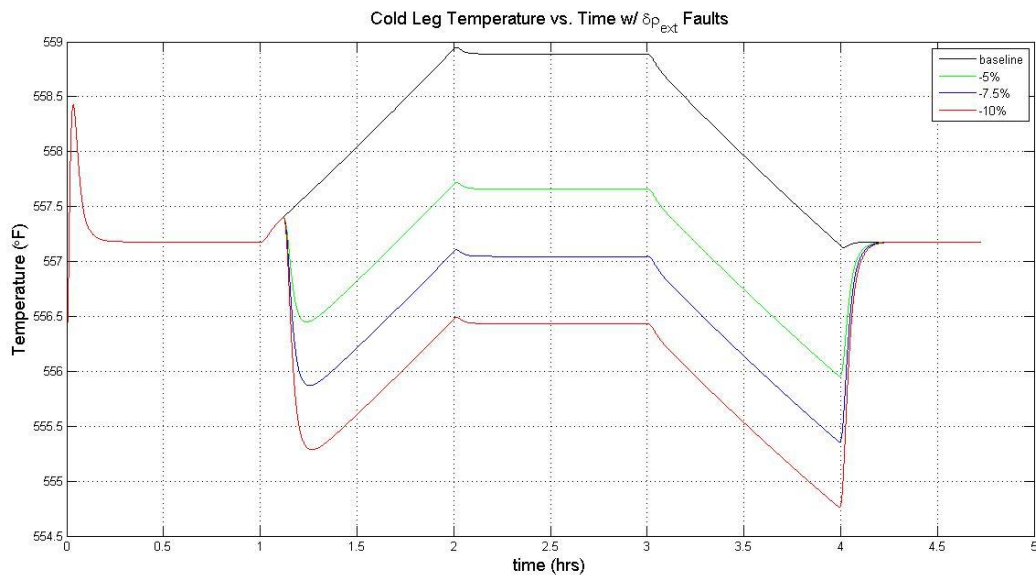


Figure 5.14: Cold leg temperature response for negative reactivity and a negative LFM

The cold leg temperature profile shown in Figure 5.14 responds in accordance with the hot leg change, shown in Figure 5.13. As warmer water reenters the core, density is increased

slightly due to the temperature change. Decreasing the density of the moderator leads to less effective moderation of neutrons, less fissions, and subsequently less power produced.

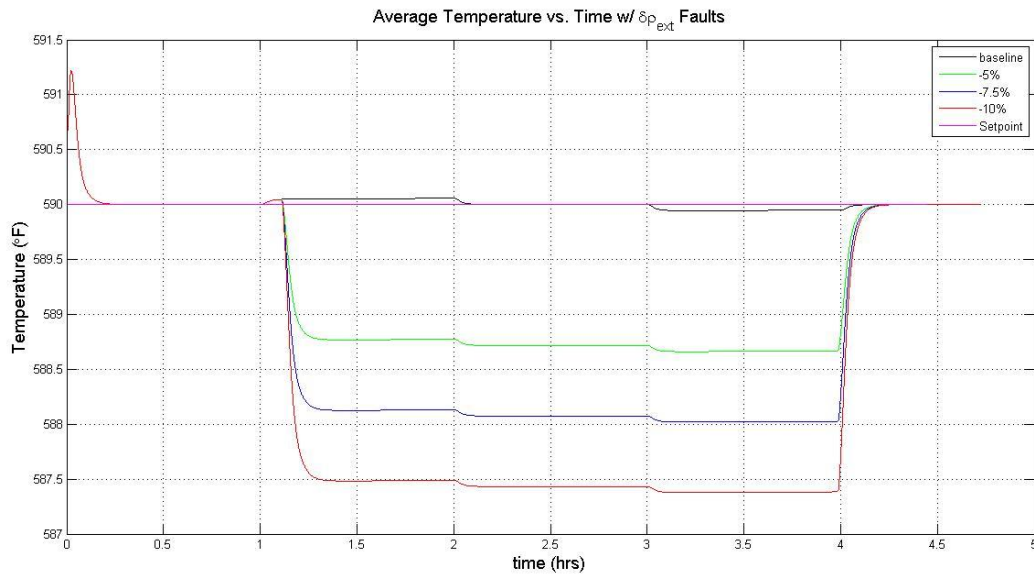


Figure 5.15: Average temperature changes for negative reactivity and a negative LFM

Figure 5.15 displays the results of the T-avg value during the LFM and reactivity insertion. The greatest change in the value is approximately 2.5 °F. This parameter may actually prove useful for use in cross checking the CRDM position or monitors. It is evident in Figure 5.15 the LFM does not result in a large change in the T-avg value, but the improper reactivity does. In contrast to the change of the T-avg value, the steam pressure signal changes, shown in Figure 5.16, have an almost trivial response to the reactivity insertion during the LFM. It can be seen at the beginning and end of the fault addition the deviation from the baseline is quickly changed by the steam pressure controller.

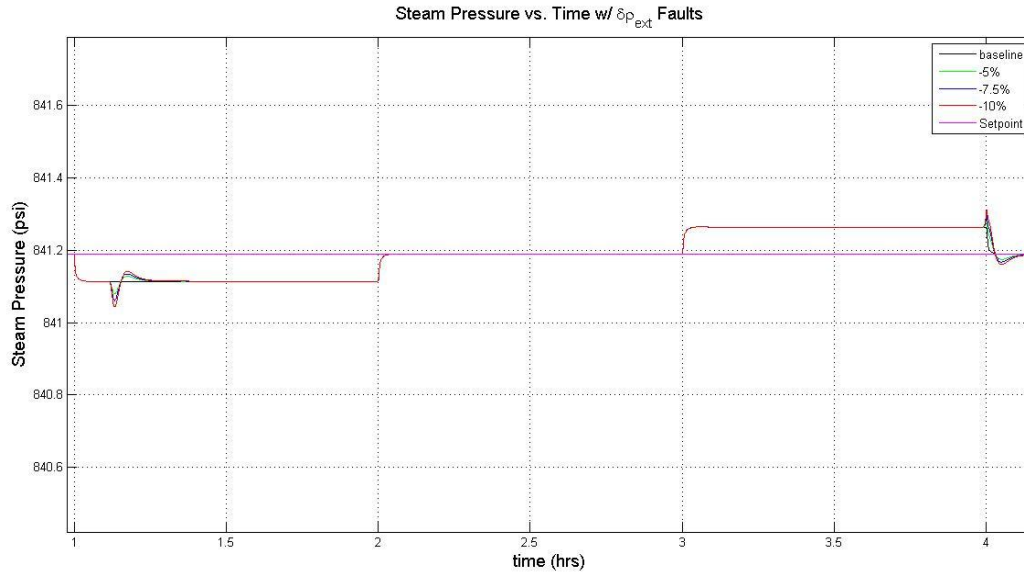


Figure 5.16: Steam pressure changes for negative reactivity and a negative LFM

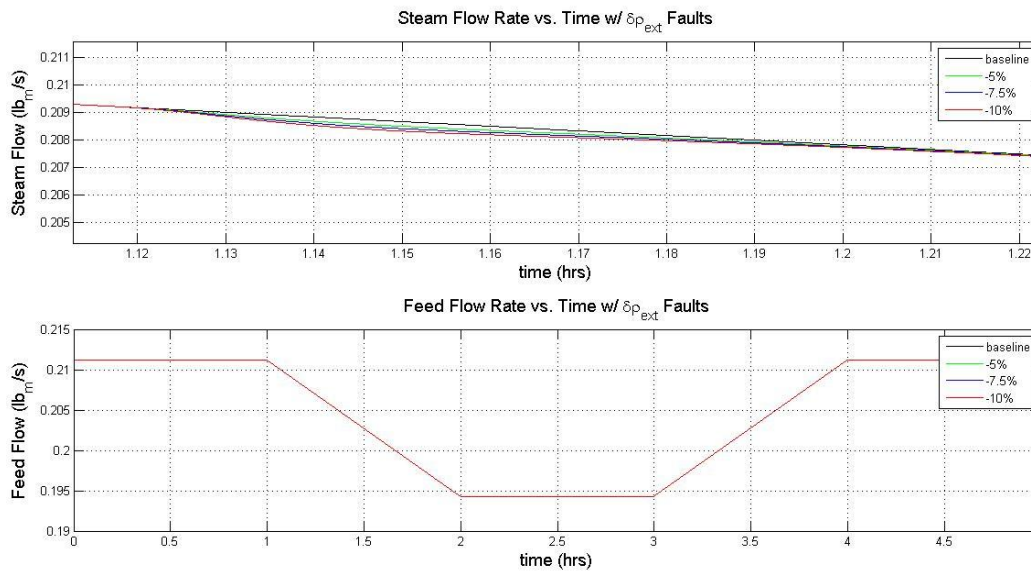


Figure 5.17: Steam and feed flow changes for negative reactivity and a negative LFM

Feed flow and steam flow experience a trivial change when the negative reactivity is added to the simulation. The time scale is scaled in for the steam flow rate in Figure 5.17 to show how little the values deviate. It is likely natural noise in the system would be greater than this change.

5.3.4 Negative Load Profile, Positive Reactivity

This set of simulations also uses a negative LFM, but instead has positive reactivity added to the system.

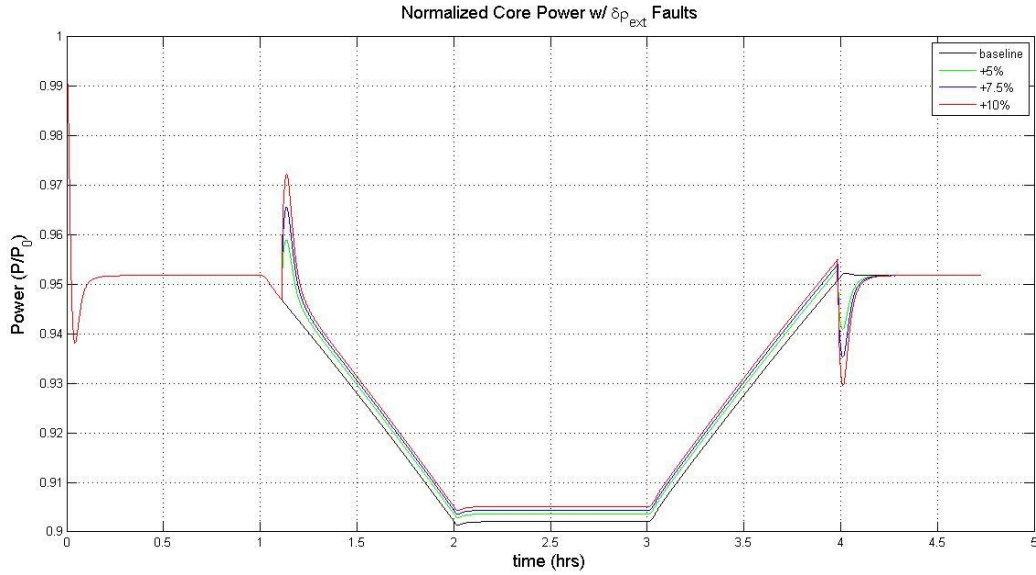


Figure 5.18: Reactor core profile for positive reactivity and a negative LFM

Compared to Figure 5.11, Figure 5.18 shows how a positive reactivity insertion affects the core power profile. The large peaks at the beginning and the end are the initial transients. The T_{avg} controller is effective in limiting the effects of the improper reactivity insertion or faulty sensor.

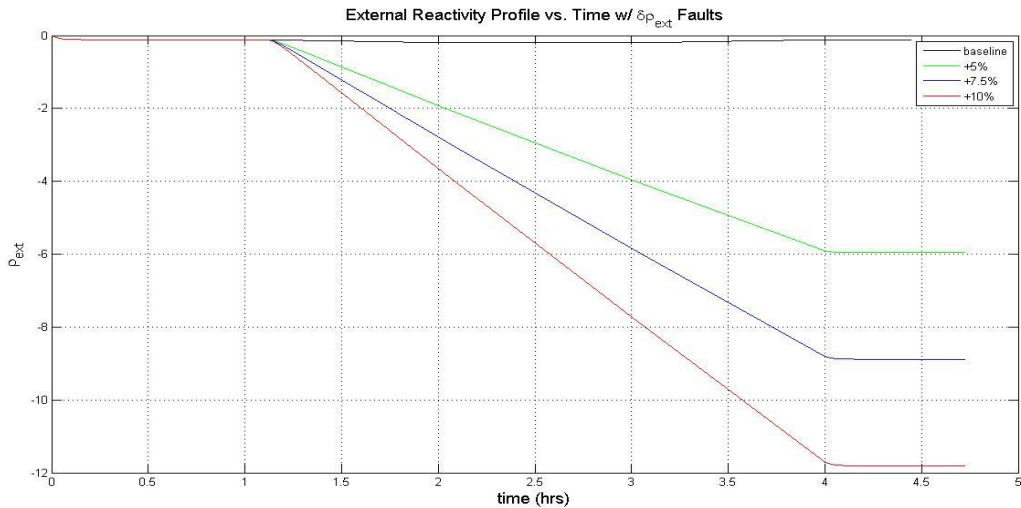


Figure 5.19: External reactivity positive insertion profile

Figure 5.19 is the reactivity profile used for this section. While the change in the external reactivity appears to be quite large, it is simply the result of the output data sent to the Matlab workspace. As described previously, the reactivity fault is added after the temperature block feeds data into the controller.

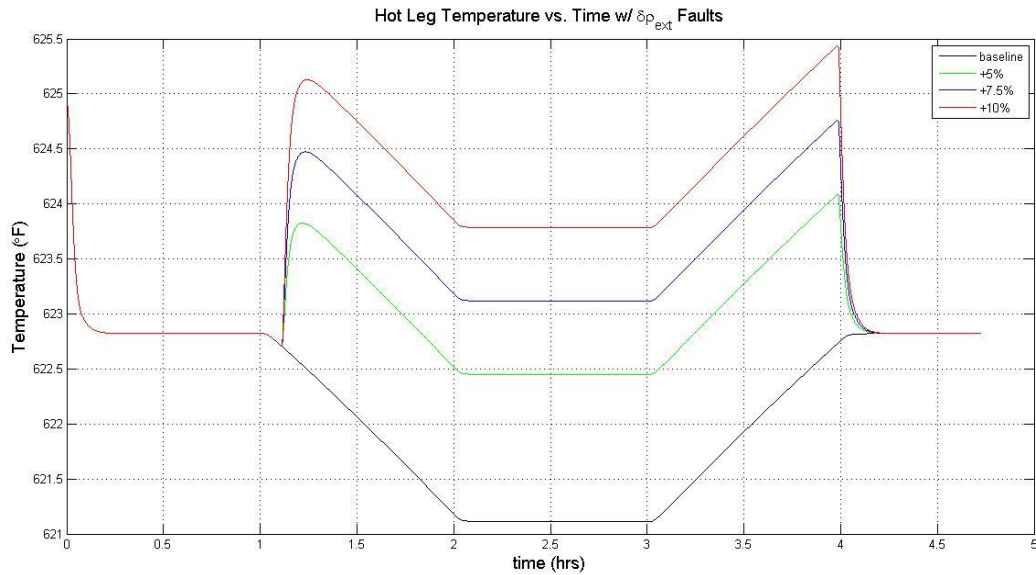


Figure 5.20: Hot leg temperature response for positive reactivity and a negative LFM

Compared to Figure 5.13, the reactivity insertion raises the hot leg temperature profile shown in Figure 5.20. This is the correct result since an increase in power will result in more heat transferred to the coolant. The change in the cold leg temperature, shown in Figure 5.21, responds in a similar fashion to the hot leg response. The average temperature response in Figure 5.22 shows the T-avg value changing by approximately 2.5 °F during the largest reactivity change. This value is an increase, however, compared to the negative LFM response for T-avg in Figure 5.15.

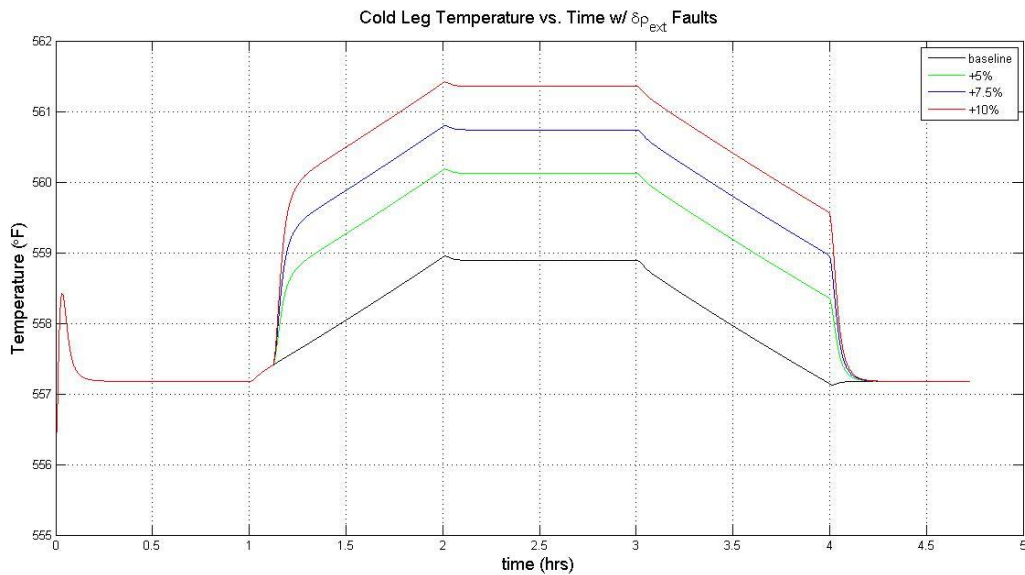


Figure 5.21: Cold leg temperature response for positive reactivity and a negative LFM

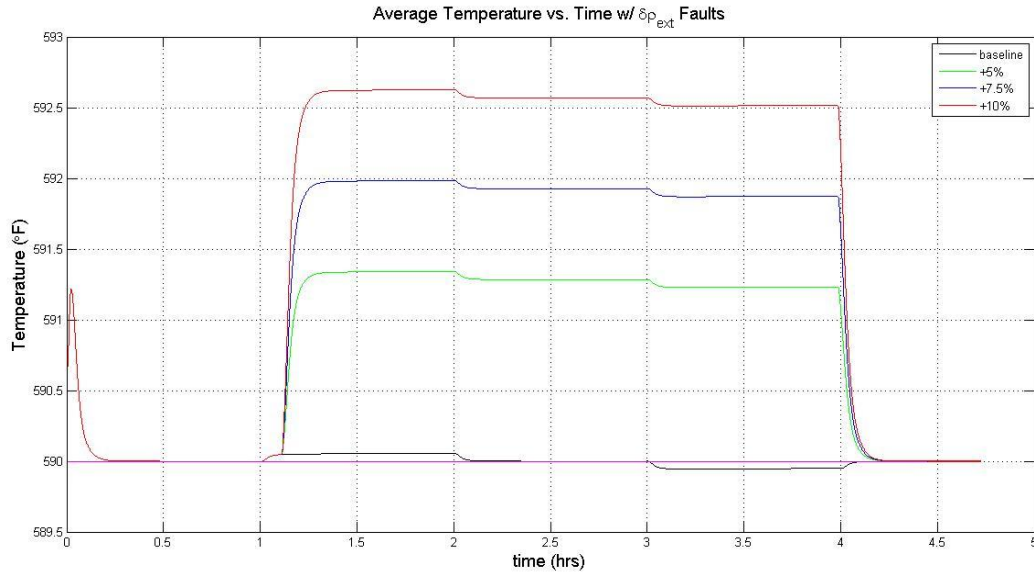


Figure 5.22: Average temperature changes for positive reactivity and a negative LFM

The steam pressure and flow rates on the secondary side of the system displayed similar results for response. These parameters changed in an opposite manner compared to Figures 5.16 and 5.17.

5.3.5 Positive Load Profile, Negative Reactivity

The simulations in Sections 5.3.5 and 5.3.6 refer to Figure 5.9 for the turbine load profile. This section will focus on negative reactivity inserted into the core.

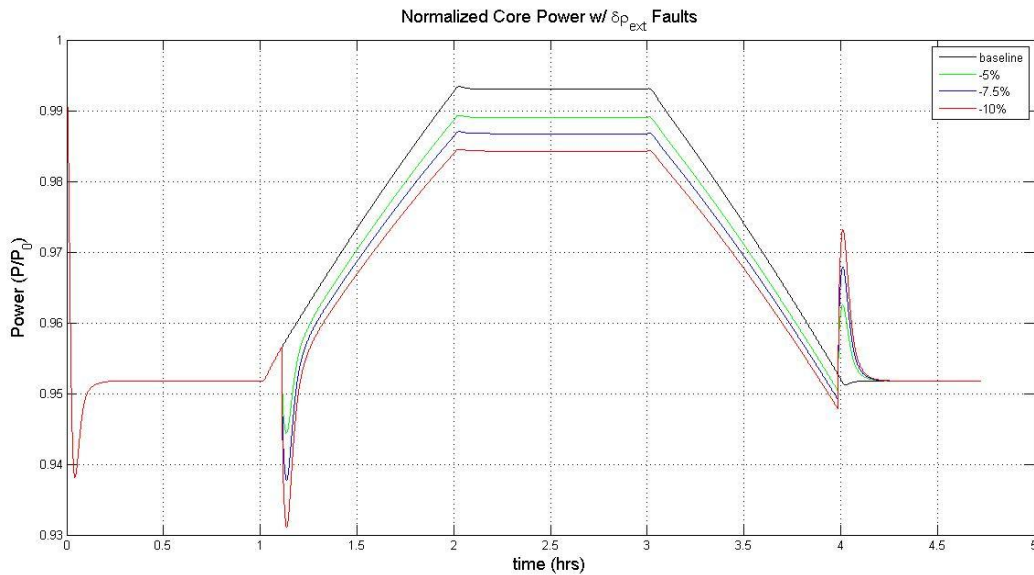


Figure 5.23: Reactor core power profile for negative reactivity and a positive LFM

A negative reactivity insertion coupled with a positive LFM result in a much more separation in the power profile difference. The 10% decrease in reactivity led to a drop of a full percentage point of the core power, about 10 MWth. This significant value would almost certainly be detected by operators. Figure 5.24 represents the reactivity profile; almost identical to the profile in Figure 5.12.

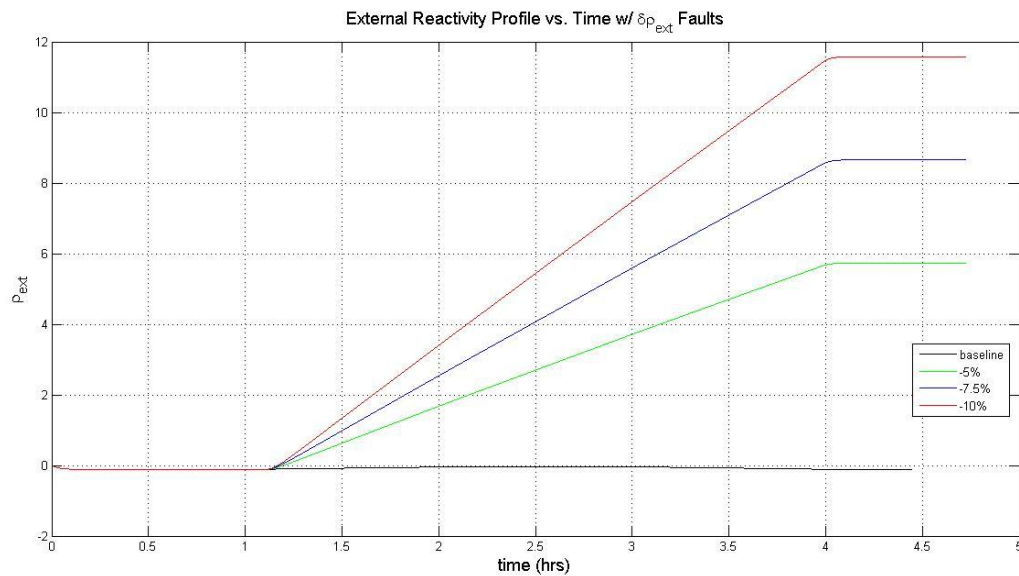


Figure 5.24: External reactivity insertion profile



Figure 5.25: Hot leg temperature response for negative reactivity and a positive LFM

As expected for a negative reactivity, Figure 5.25 shows how the decreased power level leads to a lower hot leg temperature. Even though the temperature is dropped, it ends up increasing as a

result of the LFM; the two operations counteract each other. This significant change in the power level, assuming the sensor is calibrated properly, should be identifiable.

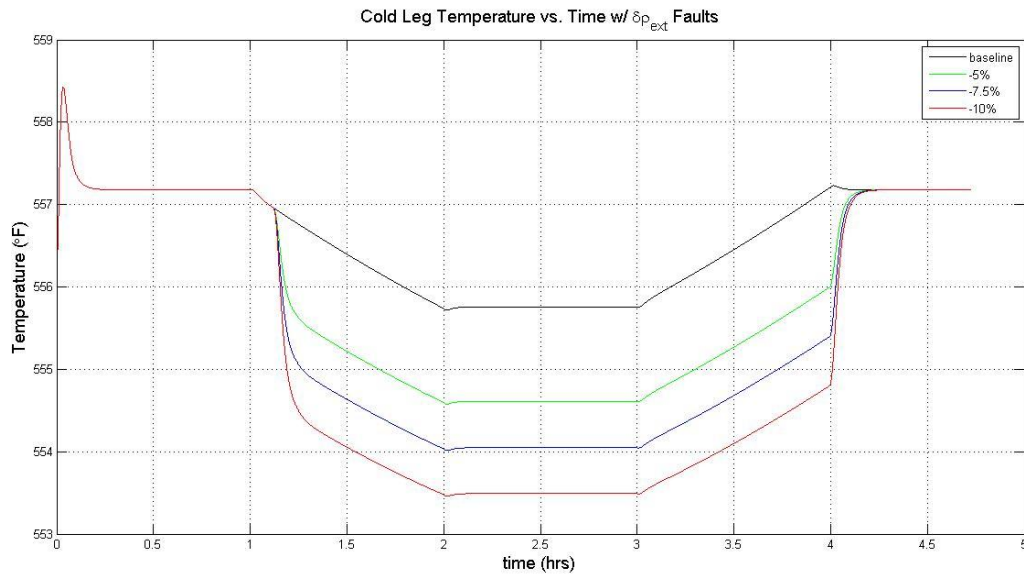


Figure 5.26: Cold leg temperature response for negative reactivity and a positive LFM

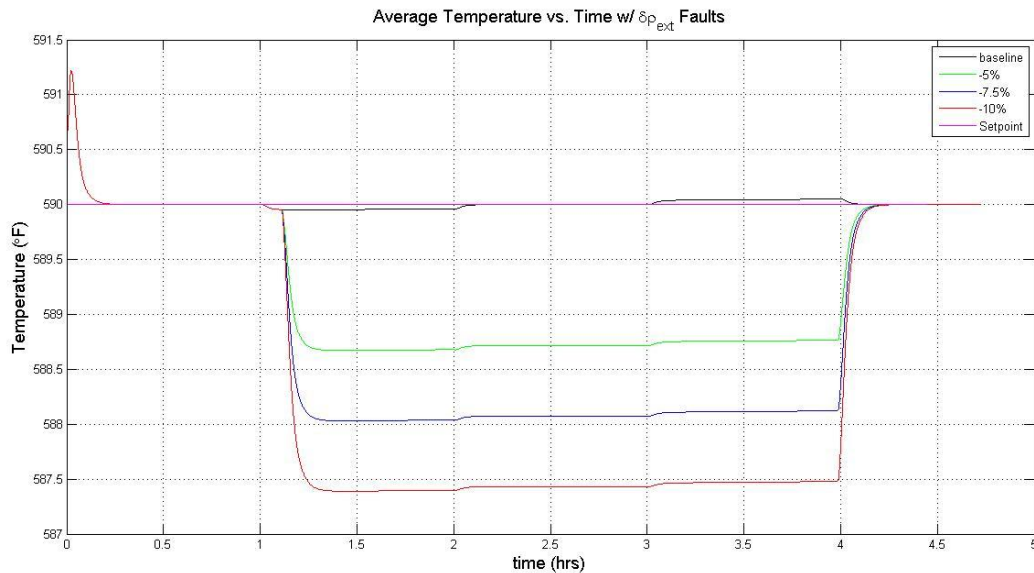


Figure 5.27: Average temperature changes for negative reactivity and a positive LFM

For the 10% decrease in reactivity in Figure 5.27, the average temperature drops by a value of approximately 2.5 °F. Since the LFM's effect on the Tav_g value is so small, using the Tav_g value to cross check the CRDM data output should be beneficial.

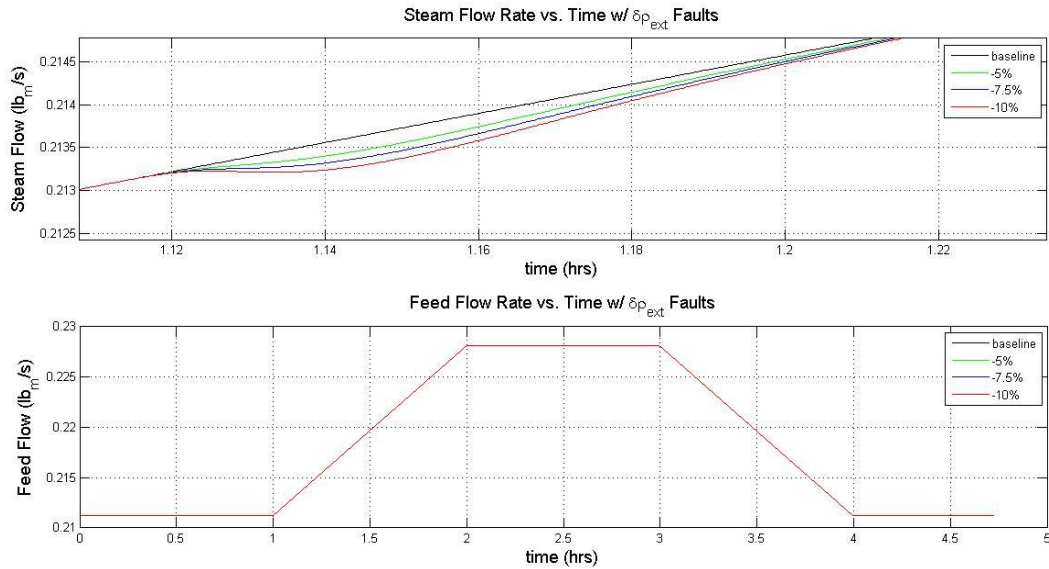


Figure 5.28: Steam and feed flow changes for negative reactivity and a positive LFM

Figure 5.28 illustrates the minimal effects the reactivity decrease has on the flow rate parameters. The changes are so small they likely would not be distinguishable on instrumentation from system noise.

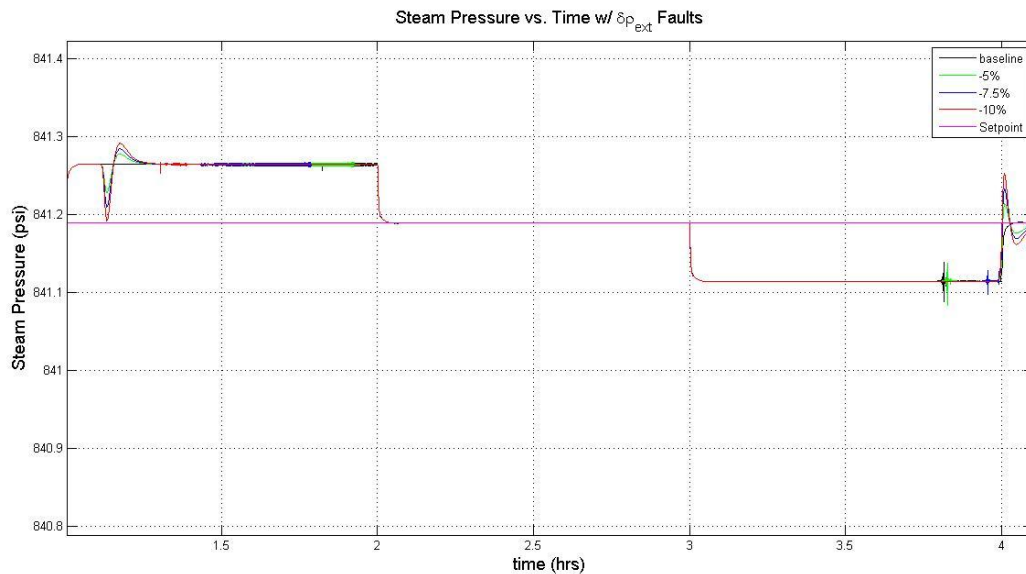


Figure 5.29: Steam pressure changes for negative reactivity and a positive LFM

Compared to the steam pressure changes in Figure 5.16, Figure 5.29 shows the inverse of the change in values. The deviation from the baseline during the LFM, however, indicates the changes in the steam pressure value will be difficult to distinguish since the pressure controller responds rapidly.

5.3.6 Positive Load Profile, Positive Reactivity

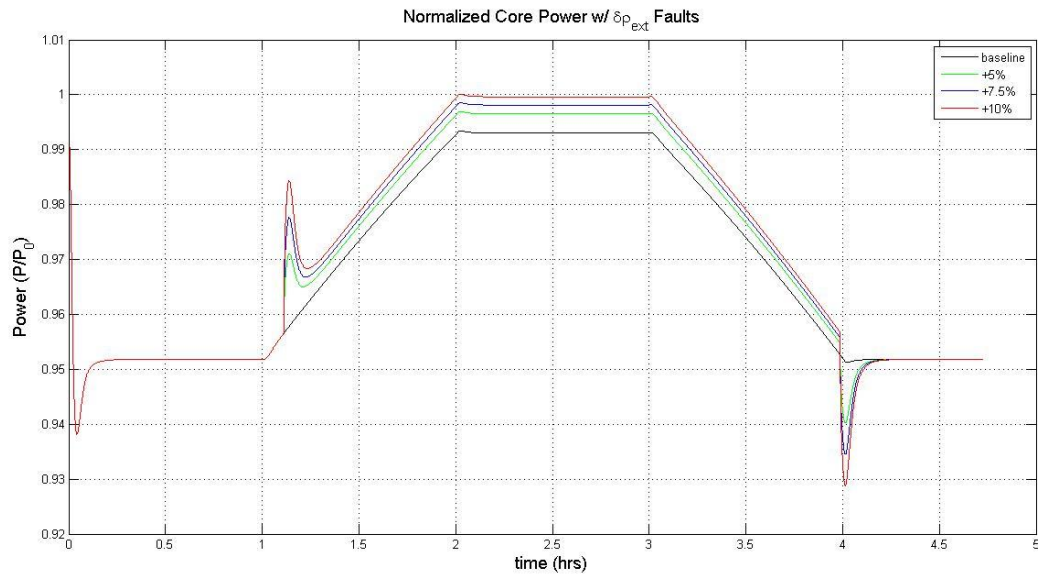


Figure 5.30: Reactor core power profile for positive reactivity and a positive LFM

The largest change in reactor power for Figure 5.23 is approximately 0.75%; approximately 7.5 MWth. This translates to a decrease of almost 2.5 MWe, which can significantly affect plant economics. The external reactivity profile, shown in Figure 5.31, is nearly identical to the profile used in Section 5.3.4.

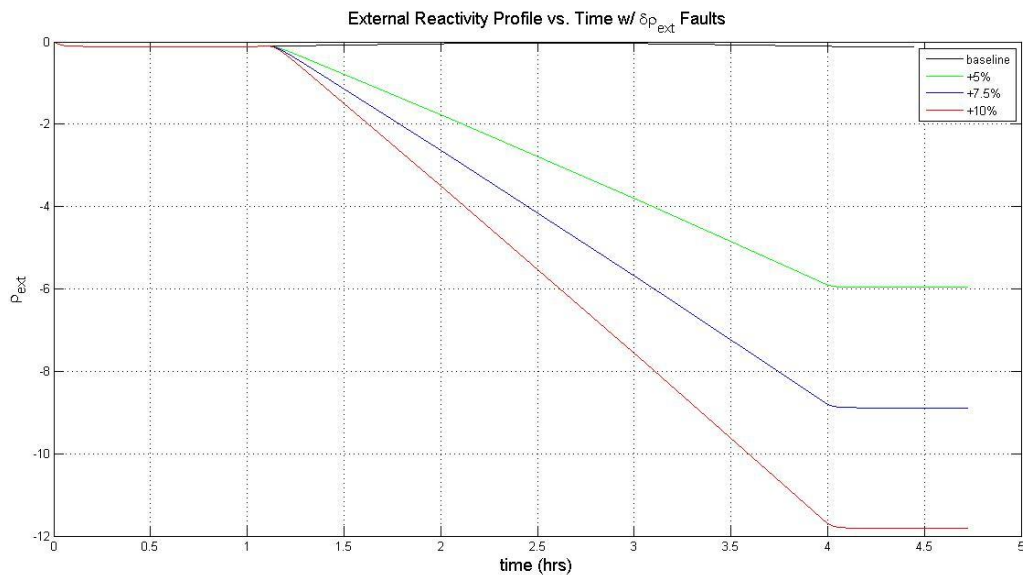


Figure 5.31: External reactivity positive insertion profile



Figure 5.32: Hot leg temperature response for positive reactivity and a positive LFM

The addition of reactivity has identical effects regardless of the type of LFM occurring. Figure 5.32 displays the linear relationship between reactivity change and the hot leg temperature increase. By this, the 10% change in reactivity increases the temperature twice as much as the 5% increase.

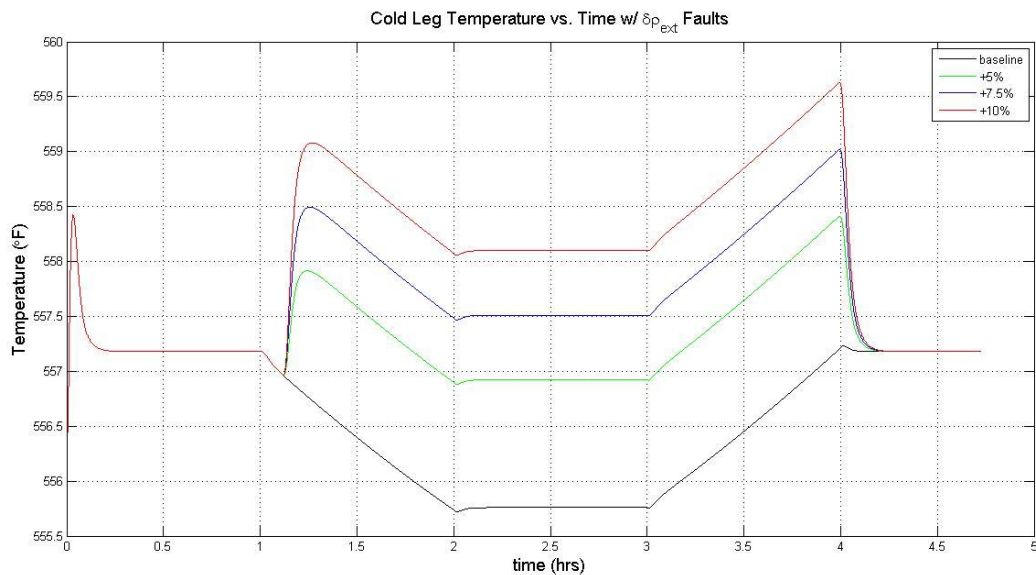


Figure 5.33: Cold leg temperature response for positive reactivity and a positive LFM

Due to the positive LFM occurring for this simulation section, the cold leg temperature response in Figure 5.33 increases at the end of the fault but returns to the baseline value at the end.

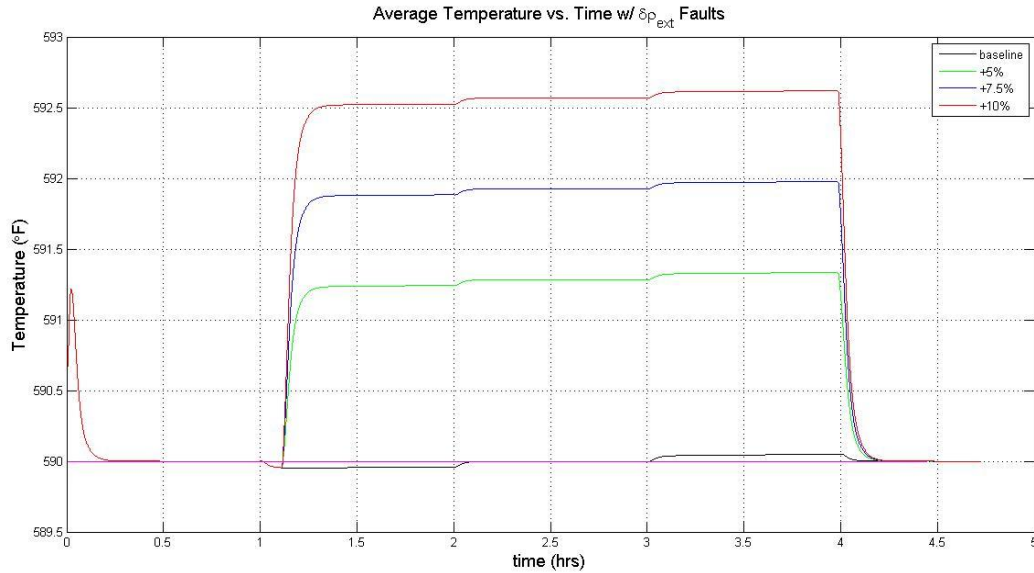


Figure 5.34: Average temperature changes for positive reactivity and a positive LFM

The T-avg value in all simulations for sections 5.3.3-5.3.6 are result in an increase or decrease of the parameter by 2.5 °F for the 10% change of external reactivity. These simulations have indicated the type of effects a change in reactivity, or sensor fault, can have during an LFM. Since the changes in temperature are only a few degrees, it will be necessary to have sensors with small deviations in their displays.

5.4 Remarks on System Response during LFM

A range of temperature faults were applied for load-following simulations. Although they are not displayed in this section, smaller temperature faults had similar effects to the +7 °F sensor fault. Other load-following profiles are present in this report for other types of fault simulation. Faults conducted during a general maneuver can have profound effects on system parameters, while some process variables have little to no response. This indicates which variables should be more closely monitored during a potential fault simulation.

With the exceptions of steam pressure and flow rates, the reactivity faults shown have noticeable effects on reactor power and plant parameters. A stuck or slow moving control rod, whether inside or outside of the core, can be a major problem at a power plant. Outside the obvious safety concerns, revenue will be affected by improper action by the CRDM. If the downtime at a plant can cost as much as \$250,000 per day for an 850 MWe plant [8] and the largest change in power was 2.5 MWe, the reactivity fault could cost approximately \$750 per

day in lost revenue. While this value may not seem significant, this cost could be substantial over an extended period of time.

6. FISSION PRODUCT POISONING EFFECTS IN SMRs

6.1. Motivation for Fission Product Subsystem

The effects on reactor operation by fission products of typical PWRs are already well understood. Simulating the effects these neutron poisons have on SMRs help with the goal of making the IRIS model more complex. Only two fission product isotopes were considered for simulation due to their large thermal neutron absorption cross sections and relatively large concentrations present during normal and transient reactor operations. Due to the long half-lives of the precursor isotopes of the poisons investigated, it was found the addition of the new subsystem did not greatly affect IRIS operation. Simulation results indicate approximately 100 hours of simulation time is needed for neutron poisons to achieve a steady-state value. Previous simulations conducted were not run for longer than 54 hours; sufficient to accomplish simulation goals. In order to see appreciable effects on the IRIS system from neutron poisons, it would be necessary to run at low power or a shutdown condition for an extended period of time and let the poison concentration increase.

6.2. Theory of Reactivity Poisoning in Thermal Reactors

Several isotopes produced during irradiation of fuel assemblies affect reactor operation. The most prevalent isotopes, Xenon-135 (Xe-135) and Samarium-149 (Sm-149), are focused on for this piece of the project. Two scenarios were investigated for this chapter; steady-state and transient reactor operation. It was necessary to investigate the effects for a change in turbine demand and subsequent reactor power change.

6.2.1 Fission Product Poisoning

Fuel irradiation of low-enriched uranium (LEU) introduces neutron poisons into the fuel pin structure. The isotopes considered, Xe-135 and Sm-149, have thermal neutron cross sections of 2.6×10^6 barns and 4.2×10^4 barns [27]. Compared to the neutron absorption cross section of Uranium-235, 681 barns, the probability for absorption in the neutron poisons is greatly increased. Neutron poison buildup poses challenges to reactivity control in the core due to the creation of additional negative reactivity. Neutron poisons also buildup during reactor shutdowns and other lower power conditions since lower flux is not burning up the poisons and also due to

the half-lives of the precursor isotopes Iodine-135 (6.58 hours) and Promethium-149 (54.0 hours) [28].

6.2.2 Xenon and Samarium Poisoning Models

Duderstadt and Hamilton [28] provide a good model for how these so called burnable absorbers are created in the reactor environment. Figures 6.1 and 6.2 illustrate the basic process for the creation of the poisons.

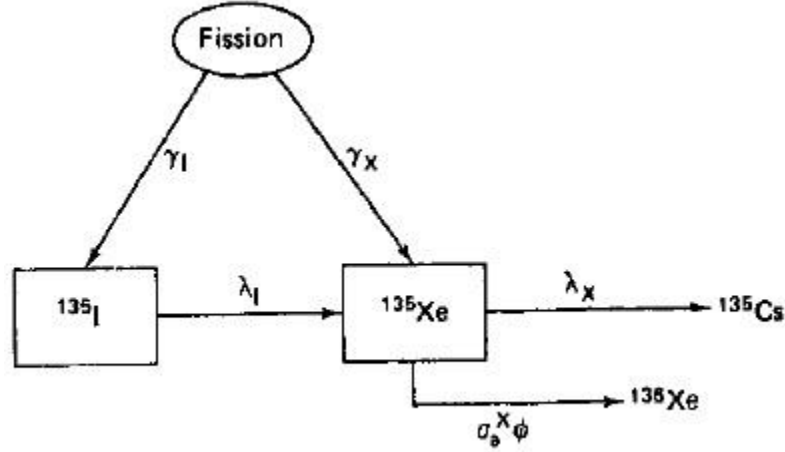


Figure 6.1: Basic Xenon-135 production pathways [28]

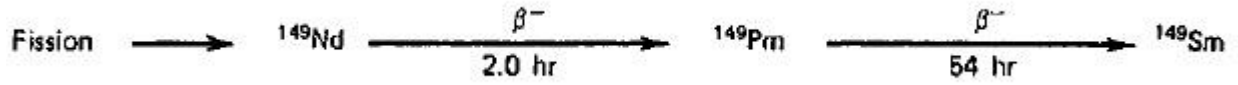


Figure 6.2: Basic Samarium-149 production method [28]

The creation of the two isotopes of interest can be explained using four differential equations.

$$\frac{\partial I}{\partial t} = \gamma_I \Sigma_f \phi(t) - \lambda_I I(t) \quad (6.1)$$

$$\frac{\partial X}{\partial t} = \gamma_X \Sigma_f \phi(t) + \lambda_I I(t) - \lambda_X X(t) - \sigma_a^X \phi(t) X(t) \quad (6.2)$$

$$\frac{\partial P}{\partial t} = \gamma_P \Sigma_f \phi(t) - \lambda_P P(t) \quad (6.3)$$

$$\frac{\partial S}{\partial t} = \lambda_P P(t) - \sigma_a^S \phi(t) S(t) \quad (6.4)$$

Where:

$I(t)$ = I-135 concentration (# atoms/cm³)

$X(t)$ = Xe-135 concentration (# atoms/cm³)

$P(t)$ = Pm-149 concentration (# atoms/cm³)

$S(t)$ = Sm-149 concentration (# atoms/cm³)

γ_I = I-135 fission product yield (fraction)

γ_X = Xe-135 fission product yield (fraction)

γ_P = Pm-149 fission product yield (fraction)

Σ_f = Macroscopic fission cross section of U-235 (cm⁻¹)

$\phi(t)$ = neutron flux (# neutrons/cm²-s)

λ_I = I-135 decay constant (hr⁻¹)

λ_X = Xe-135 decay constant (hr⁻¹)

λ_P = Pm-135 decay constant (hr⁻¹)

σ_a^X = microscopic neutron absorption cross section of Xe-135 (2.6E6 barns)

σ_a^S = microscopic neutron absorption cross section of Sm-135 (4.2E4 barns)

Solving these equations simultaneously allows for the creation of two general equations for the concentrations of Xe-135 and Sm-149. The two equations are general and can be applied for a dynamic or steady-state change in the reactor core power. The dynamic change in power was simplified to be a function of one variable, the reactor core neutron flux. The model also assumes that cross sections are based on a mono-energetic flux in the core with a neutron energy of 0.0254 eV. Equations 6.1-6.4 may be simplified into the following general equations:

$$I(t) = \frac{\gamma_I \Sigma_f \phi_1}{\lambda_I} \left[1 - \left(\frac{\phi_1 - \phi_0}{\phi_1} \right) e^{-\lambda_I t} \right] \quad (6.5)$$

$$X(t) = \frac{(\gamma_I + \gamma_X) \Sigma_f \phi_1}{\lambda_X + \sigma_a^X \phi_1} \left\{ 1 - \left(\frac{\phi_1 - \phi_0}{\phi_1} \right) \left[\frac{\lambda_X}{\lambda_X + \sigma_a^X \phi_0} e^{-(\lambda_X + \sigma_a^X \phi_1)t} + \left(\frac{\gamma_I}{\gamma_X + \gamma_I} \right) \left(\frac{\lambda_X + \sigma_a^X \phi_1}{\lambda_X + \sigma_a^X \phi_1 - \lambda_I} \right) [e^{-(\lambda_I t)} - e^{-(\lambda_X + \sigma_a^X \phi_1)t}] \right] \right\}$$

(6.6)

Where:

ϕ_1 = New neutron flux (# neutrons/cm²-s)

ϕ_0 = Old neutron flux (# neutrons/cm²-s)

When the change in the neutron flux is constant, that is reactor power is constant, the two equations can be further reduced to the following:

$$I(t) = I_{\infty} = \frac{\gamma_I \Sigma_f \phi_0}{\lambda_I} \quad (6.7)$$

$$X(t) = X_{\infty} = \frac{(\gamma_I + \gamma_X) \Sigma_f \phi_0}{\lambda_X + \sigma_a^X \phi_0} \quad (6.8)$$

The equations are only a part of the reactivity component in the reactor. Calculation of the neutron flux must also be determined to calculate the concentration of neutron poisons.

6.2.3 Determination of Neutron Flux in the IRIS Core

Neutron flux in the IRIS core can be calculated using a formula provided by Todreas and Kazimi [20]. The formula is relatively simple, but makes a few key assumptions. These assumptions included a uniform flux and mono-energetic thermal neutrons. The flux equation is given by:

$$\phi(t) = \frac{\langle q''' \rangle}{\chi_f \sigma_f^U N^{25}} \quad (6.9a)$$

Where:

$\langle q''' \rangle$ = Volumetric heat generation rate (W/m³)

χ_f = Average energy released per fission (3.04E-11 J/fission)

σ_f^U = Fission cross section of U-235

N^{25} = uranium atomic density

Multiplying the numerator of equation 6.9a by the volume of the fuel, V_{UO_2} , changes the equation to the following form:

$$\phi(t) = \frac{\dot{Q}}{\chi_f \sigma_f^U N^{25} V_{UO_2}} \quad (6.9b)$$

Where:

\dot{Q} = Reactor Power (MWth)

Parameters from the IRIS system are used to find the core flux (enrichment, mass of fuel, etc.) [9]. Once the value of the flux was determined, a function subsystem block was placed into the IRIS model to calculate a flux based on the core power. All other parameters are assumed to stay constant during simulations. This model does not include parameters for an end of cycle simulation.

6.2.4 Reactivity Change from a Neutron Poison

The relationship required for a reactivity change in a reactor can be approximated by the ratio of the macroscopic absorption cross section of the neutron poison to the fuel. This ratio is assumed to be constant for the IRIS parameters to facilitate easy computation. The basic relationship for the reactivity change is as follows [28]:

$$\Delta\rho \cong -\frac{\Sigma_a^p}{\Sigma_a} = -\frac{\sigma_a^p p(t)}{\Sigma_a} \quad (6.10)$$

Where:

$\Delta\rho$ = change in reactivity from the neutron poisons

Σ_a^p = Macroscopic absorption cross section of the poison of interest (cm^{-1})

Σ_a = Macroscopic absorption cross section of U-235 (cm^{-1})

σ_a^p = microscopic absorption cross section of the poison of interest (cm^2)

$p(t)$ = Concentration of the neutron poison of interest (# atoms/ cm^3)

In order for the reactivity change to be computed, Equations (6.5) and (6.6) are substituted into Equation (6.10) along with the associated microscopic absorption cross sections. It should also be noted the reactivity contribution from the Sm-149 poison remains constant during simulation. Since this concentration is assumed to be constant, the reactivity change contribution from Sm-149 can also be held constant.

6.3. Simulation of Fission Product Poisoning Effects

Figure 6.3 shows the response of the normalized Xe-135 concentration due to a 5% increase in the core flux and subsequent change in reactivity contribution. This simulation was conducted to illustrate the time required for the neutron poison to achieve a steady-state level from a change in neutron flux and hence the power in the reactor. A set of simulations was also conducted to see the poison effects during an LFM.

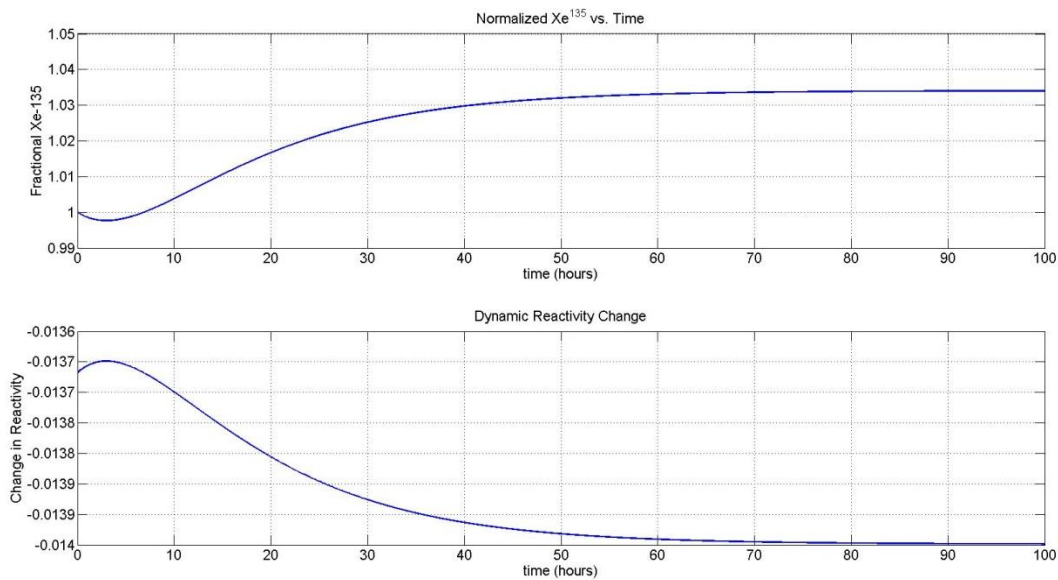


Figure 6.3: Xe-135 buildup due to a 5% increase in neutron flux

As seen in Figure 6.3, the time necessary for a new steady-state value approaches almost 100 hours. This time becomes especially important for long term simulations. When the neutron poisons were added to the IRIS model, the only noticeable effect in system parameters was observed during initial simulation startup.

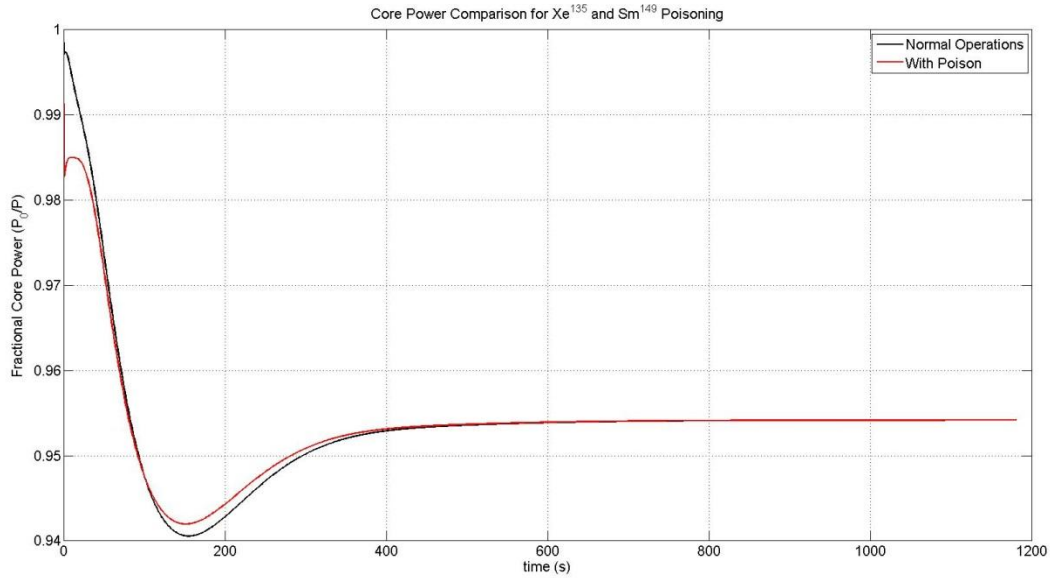


Figure 6.4: Addition of neutron poisons to the IRIS core power

Figure 6.4 shows how the core power changes when the model is first run. The T_{avg} controller in the model works during the addition of the negative reactivity contribution from the poisons. Due to the controller, a new steady state condition is achieved at the same fractional value as if the poison had not been introduced. This simulation was run for a steady state contribution of the poisons i.e. no change in the neutron flux or power other than the initial startup. Since the system achieves the same power value at approximately 600 seconds as the baseline conditions, the other system parameters are not displayed due to the trivial nature of change.

Two power conditions were run for load following conditions; positive and negative power changes. The simulations were carried out for 10 hours. This included letting the system achieve a steady state value before and after the maneuver. The simulations were carried out for two cycles.

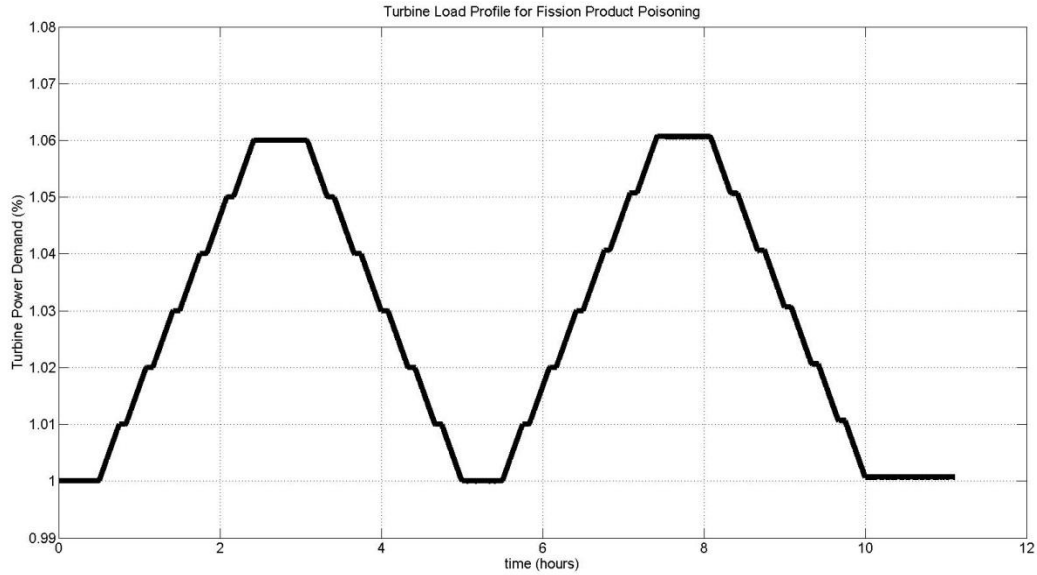


Figure 6.5: LFM profile for investigation of fission product effects

Figure 6.5 represents the base profile for this section. Turbine power was increased or decreased by 1% over an approximately 10 minute time period. It was necessary to run the load profile for two cycles to determine how the neutron poison contributions and associated reactivity changes would respond to the relatively quick transients. Compared to the 100 hours of time necessary for Xe-135 to reach a steady state concentration, the 11 hours of simulation time should not have a noticeable impact.

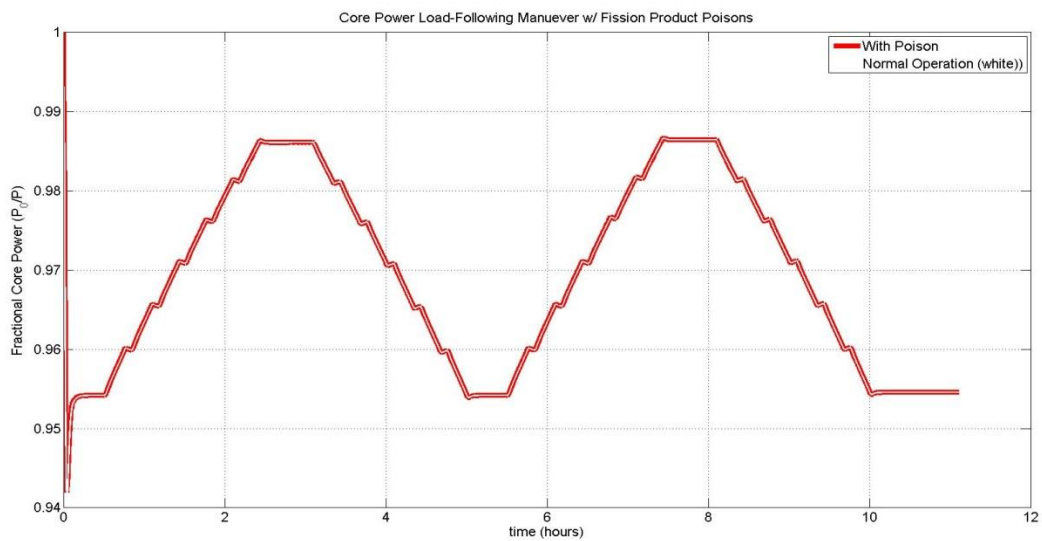


Figure 6.6: Addition of neutron poisons to the IRIS core power

Figure 6.6 illustrates the reactor core profile during the LFM with and without the addition of the neutron poisons. As evident, the effects of the poisons have a trivial effect on power. Since the simulation time was only 11 hours, the poisons do not have enough time to greatly affect operation due to the long half-lives. Figure 6.7 shows the startup response in the core profile.

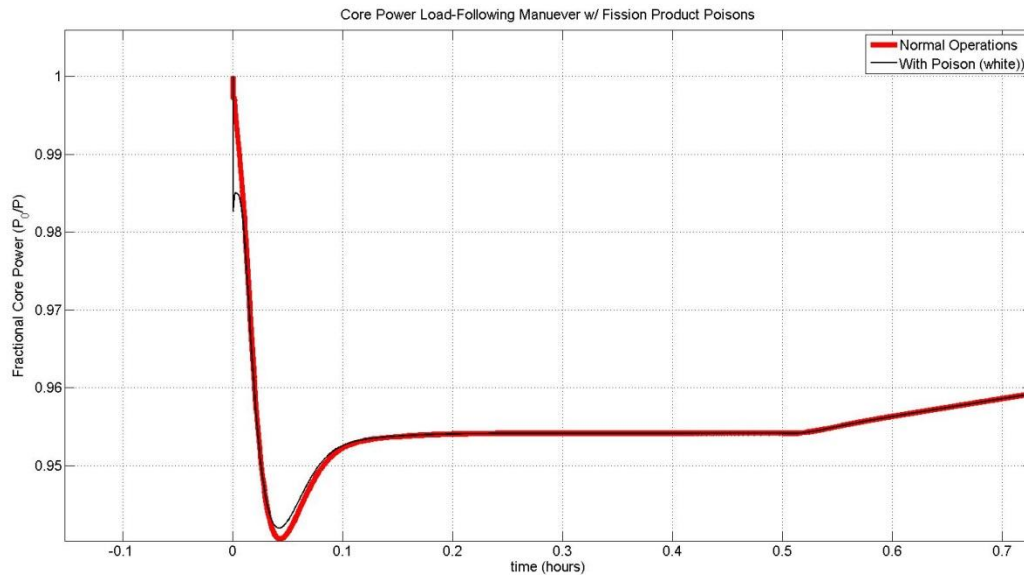


Figure 6.7: Start-up section of core power with neutron poison addition

It appears as if the neutron poisons have the most appreciable effect during the initial time period. This can be attributed to the time response required for the controller to respond and stabilize the core power. The dynamic response of the Xe-135 concentration can be seen in Figure 6.8. The concentration of the poison does not have a great change during the simulation. This was expected due to the time period required to achieve a steady state after a change in flux/power; evident in Figure 6.3.

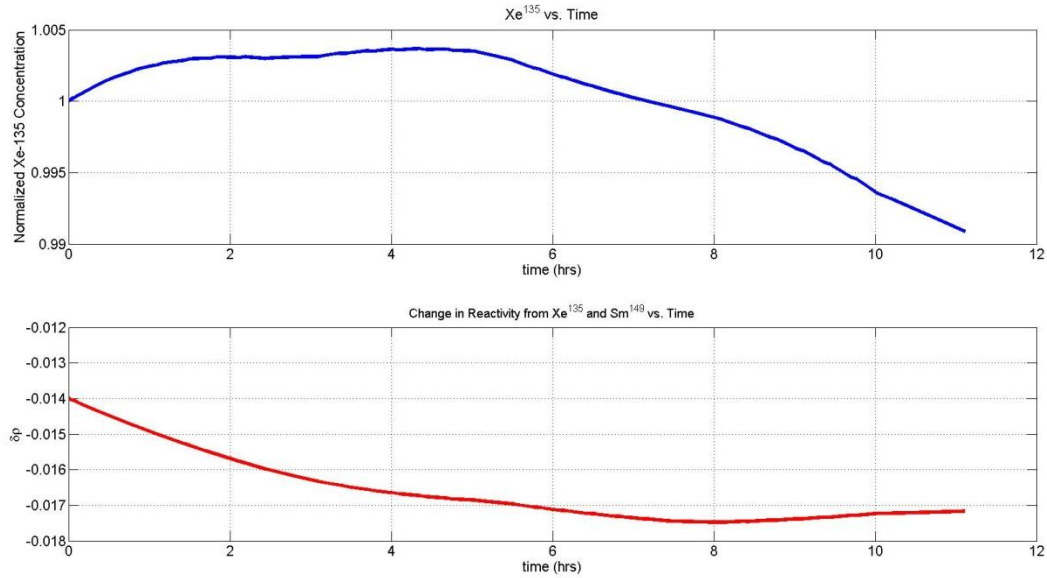


Figure 6.8: Neutron poison concentration buildup for a positive LFM

6.4. Remarks on Fission Product Poisoning Effects

The addition of the neutron poison reactivity contributions to the IRIS has helped increase the simulation complexity to the model. While there were several key assumptions made during the subsystem development, the formulas still hold consistent with how Duderstadt represents them [29]. For the length of the simulations conducted, the reactivity effects do not greatly affect system parameters. If simulations were run in the range of 100-200 hours, it may be easier to see how the buildup or deletion of neutron poisons in the core truly affects IRIS parameters. Reactors can certainly be affected by buildup of these poisons during a shutdown; utilities have to overcome this problem. Since Xe-135 decays, operators often let a non-refueling shutdown occur for a minimum amount of time. This ensures that the operators do not move the control rods prematurely, and thus risk introducing too much positive reactivity into the core once the poisons are burned out.

7. EFFECTS OF DEVICE AND PROCESS FAULTS ON SMR PERFORMANCE

7.1. Overview of Sensor Faults

Conditions analyzed in this chapter further involve faulty sensors, similar to the temperature faults. The steam pressure signal in the BOP section involved the use of a faulty signal; the pressure was assumed to be not changing. Turbine output is directly correlated to the steam pressure. If turbine output is not optimized for power production, there is the potential for a change in saturation conditions to occur which could lead to damage of the turbine blades. In addition to the steam pressure signal faults, values of the P-I controller were changed to simulate the sort of response the system would experience if these critical parameters were changed. The P-I constants were changed and also experienced a +4 °F step fault in the hot leg temperature. This affects the measured T_{avg} value as well as affecting the controller error.

7.2. Steam Pressure Signal Faults

Simulating faults in the steam pressure signal allows for determination of system response to different fault conditions. Since the actual pressure value is assumed to be constant and just a sensor fault, incorrect data feed to controllers and operators will result in improper action performed. There was also a goal in this particular fault to see if a relationship existed between a change in the steam pressure signal and reactor parameter response. These relationships, when created, could be used for fault detection and sensor signal confirmation. For example, based on the system parameter value, it could be determined whether an error or bias in the pressure signal and if controllers, sensors, or other elements need to be calibrated/replaced in order to minimize any detrimental effects on system performance.

7.2.1 Range of the Signal Faults

In order to establish the fault tolerance of the system, a range of simulations must be conducted. For this set of simulations, a bias error was added to the steam pressure signal. The fault is based on the value of the pressure signal set point used in the controller. Bias errors of positive and negative 2, 5, 7, and 10% were added based on the set point value of 841.2 psi. While a bias error of 10% (84.1 psi) may seem large, it was necessary to evaluate the sensitivity

of these errors on the reactor response. The plots in this section contain eight examples of bias error as well as the baseline value for comparison. The values of the faults are shown in the upper right-hand corner of each plot for clear identification. The results of the affected system parameters versus pressure bias errors are similar to a turbine LFM. The system changes are explained by the following procedure. The procedure described is for a positive bias in the steam pressure; a negative bias results in the opposite procedure:

- The pressure bias is added from the start of simulation; the steam pressure value returns to its set point value within a minute.
- The perceived change in steam pressure, positive or negative, causes the steam throttle valve to actuate and bring the pressure back to its set point value. Opening the valve increases steam flow and thus, reduce the pressure.
- The steam temperature is proportional to a perceived change in the steam pressure signal; steam temperature increases due to a positive bias in the steam pressure.
- When the steam temperature increases, more energy is removed from the core outlet (hot leg) coolant flow; this causes a subsequent drop in the core inlet (cold leg) coolant temperature.
- Colder coolant enters the core is denser than the at the baseline value of coolant temperature; this increased density increases neutron moderation and thus, increases the core power.
- Since the cold leg temperature is decreasing, the hot leg temperature would increase in order to maintain a constant average temperature. This is due to the change in the control rod reactivity that responds to the T_{avg} controller.
- Since power is increasing for a positive bias, the external reactivity will increase; it should be noted that the value is still negative; this indicates that the system still maintains a negative feedback effect.

7.2.2 System Response to Pressure Sensor Faults

Figure 7.1 illustrates the effects a steam pressure bias has on the core power for the full range of signal faults. The results of the change in the steam pressure are certainly significant and detectable. A $\pm 2\%$ stream pressure bias changes the power level by approximately 0.5% (+5 MWth). The +10% change affects power by as much as +2% (20 MWth).

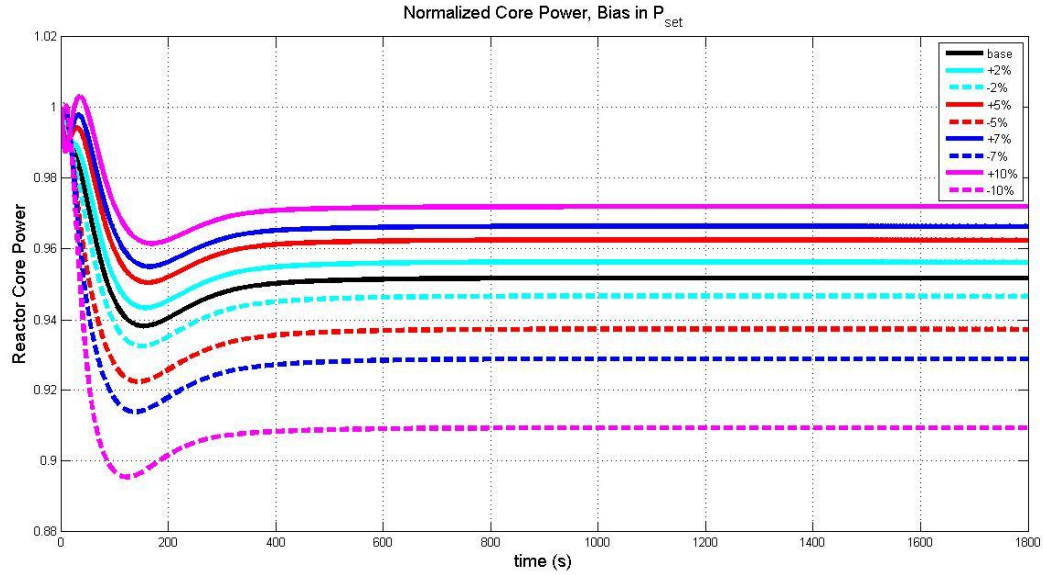


Figure 7.1: Core power profile for the pressure signal fault range

The -10% change in the steam pressure signal decreases power by nearly 4.5% (45 MWth). The numerical values of the changes for these faults are displayed in Table 7.1.

Table 7.1 Percent deviation of IRIS parameters based on a steam pressure bias

Variable	Units	Baseline	Bias							
			2%	-2%	5%	-5%	7%	-7%	10%	-10%
Core Power	P/P ₀	0.9475	0.528%	-0.253%	1.245%	-1.615%	1.699%	-2.522%	2.343%	-4.549%
Reactivity	Dollars (\$)	-0.0946	-7.400%	7.928%	-17.125%	22.410%	-23.362%	34.884%	-32.241%	62.685%
Hot Leg	°F	623.5078	-0.031%	-0.079%	-0.011%	-0.124%	0.020%	-0.164%	0.048%	-0.251%
Cold Leg	°F	557.6383	-0.033%	0.037%	-0.079%	0.103%	-0.108%	0.161%	-0.150%	0.290%
Steam Flow	lb _m	0.2112	0.000%	0.000%	0.000%	-0.047%	0.000%	-0.047%	0.000%	-0.095%
Steam Temp	°F	609.3017	0.235%	-0.315%	0.491%	-1.045%	0.620%	-1.838%	0.770%	-3.972%

These values illustrate the large changes the primary reactor parameters experience during the steam pressure signal faults. Figure 7.2 displays the same set of plots as Figure 7.1. The difference in the two plots is to show the effects of different steam pressure bias signals at the start of the simulation. At the 50 second mark, the power level for the positive and negative 10% bias differs by as much as 7.5% (75 MWth). The higher or lower power level feed to plant systems during this startup could lead to an improper insertion or withdrawal of the control rods, or even a reactor trip.

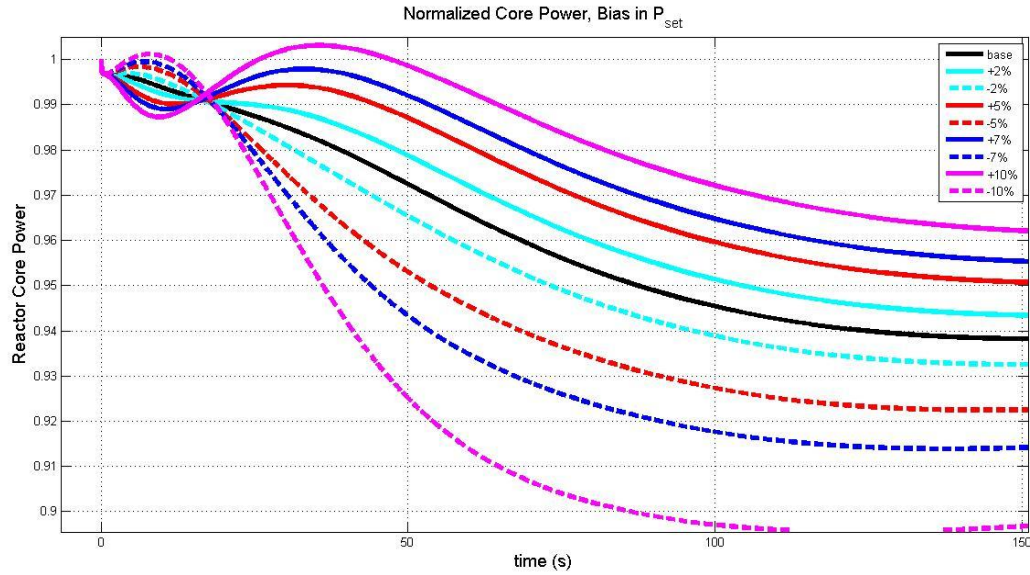


Figure 7.2: Initial power response during the pressure signal fault

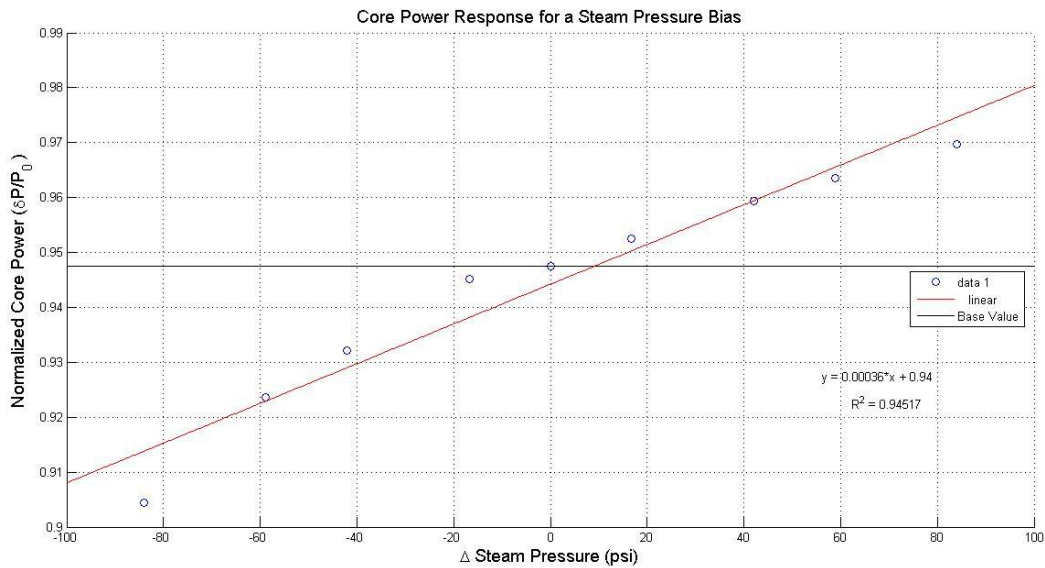


Figure 7.3: Relationship derived for the core power from the change in steam pressure

The graph in Figure 7.3 displays the relationship between the steam pressure bias and the resulting normalized core power level. The black line intersecting the data point a 0 psi steam pressure change represents the baseline value. The correlation value (R^2) for this relationship is calculated at 0.945, indicating a linear fit accurately models the power versus bias response. Operators could use this relationship to determine whether a fault is occurring in a system based on this relationship. Comparisons could be made based on the power level, back tracked to the pressure signal, and compared to the steam pressure signal on the instrumentation display. Based

on all information available, it could be determined if pressure sensors are at fault and require maintenance.

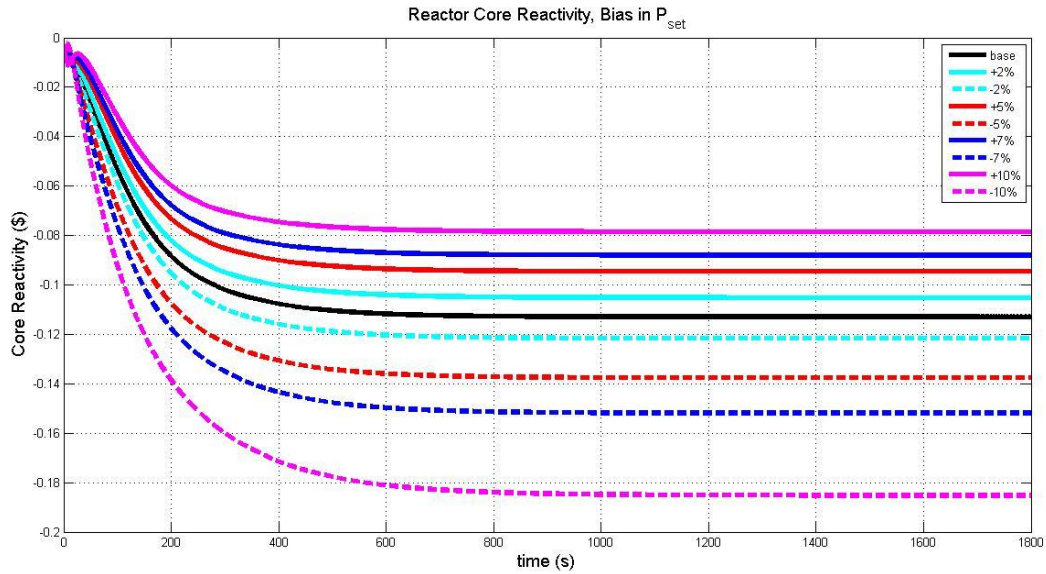


Figure 7.4: External core reactivity profile for the pressure signal fault range

The external core reactivity response for the IRIS core based on the steam pressure signal bias is shown in Figure 7.4. It should be noted the changes in the reactivity are not equal and opposite for different bias values. This effect can be seen in Table 7.1. The 10% pressure change results in either a -32% or +62% change in the reactivity value from the baseline. While these percent changes seem large, it should be compared to the reactor core power and temperature changes. These changes are within reasonable values. The linear relationship for this parameter is displayed in Figure 7.5. Since the reactor core power change is directly related to reactivity, it is expected the reactivity change in response to the steam pressure bias would also have a high correlation value (0.955).

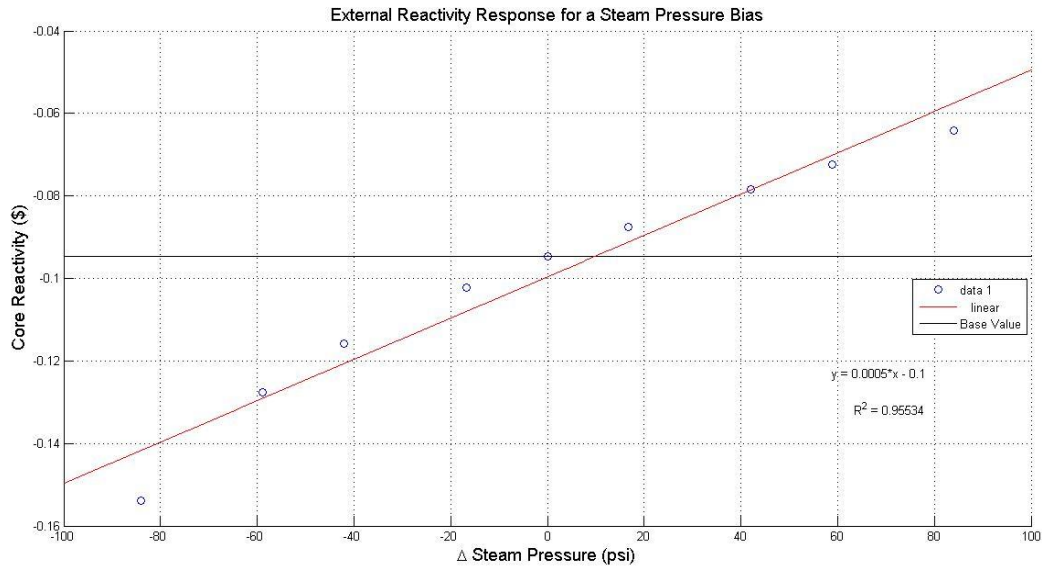


Figure 7.5: Relationship derived for the reactivity from the change in steam pressure

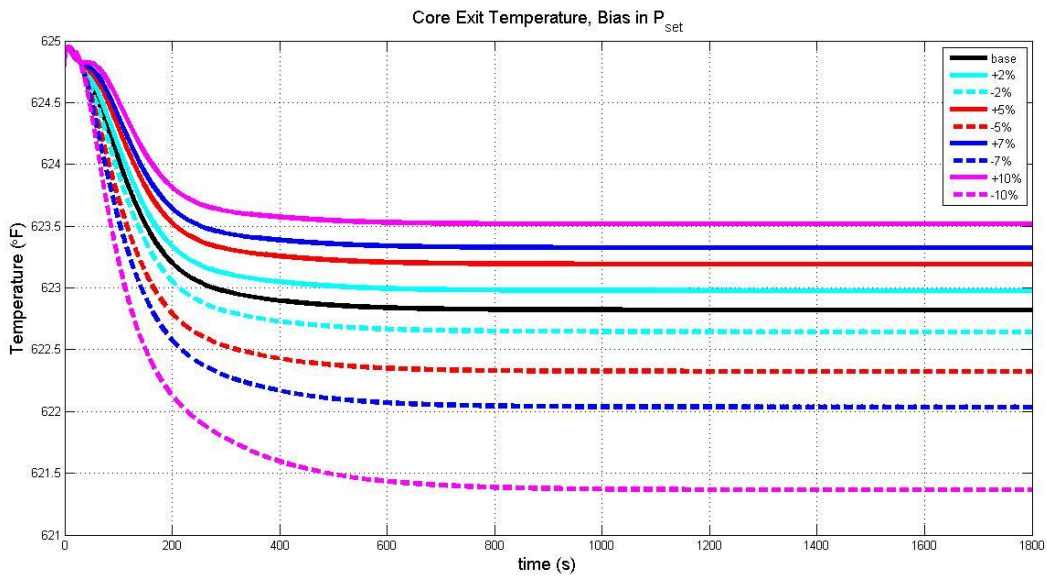


Figure 7.6: Hot leg temperature response for the pressure signal fault range

The variations in the hot leg temperature can be seen in Figure 7.6. It should be noted for all of the parameters monitored and displayed, the -10% pressure signal bias resulted in the largest deviation from baseline conditions; more so than the +10% signal bias. The changes in the temperature for the hot leg were also very small; approximately 1.5 °F for the largest pressure decrease. This indicates the hot leg temperature may not be a good choice for fault monitoring for the steam pressure value unless a sensor has a very small margin of display error.

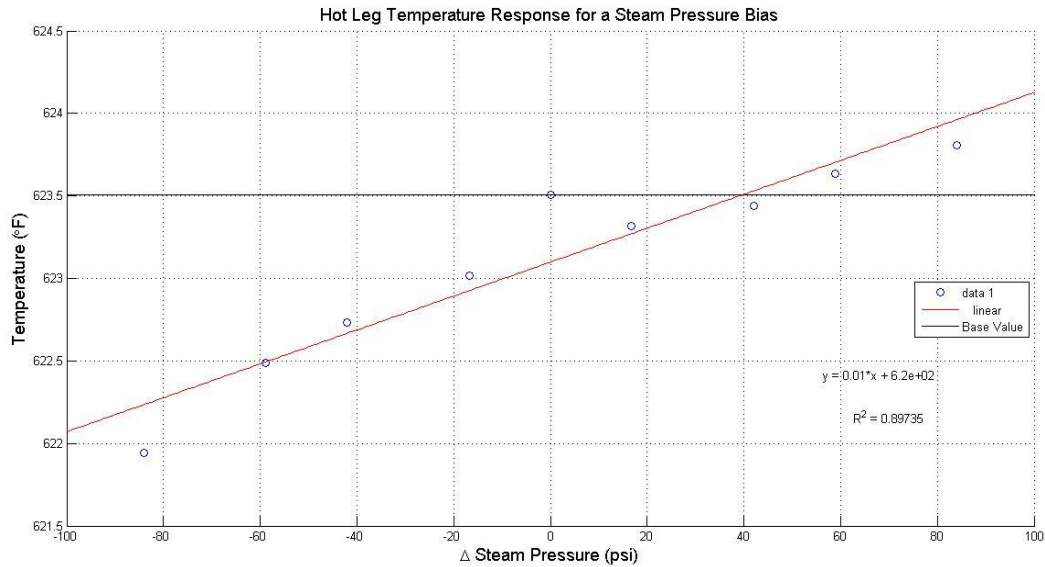


Figure 7.7: Relationship derived for the hot leg from the change in steam pressure

The linear temperature response to the hot leg temperature change in Figure 7.7 gives a better display of the small degree of change in the parameter.

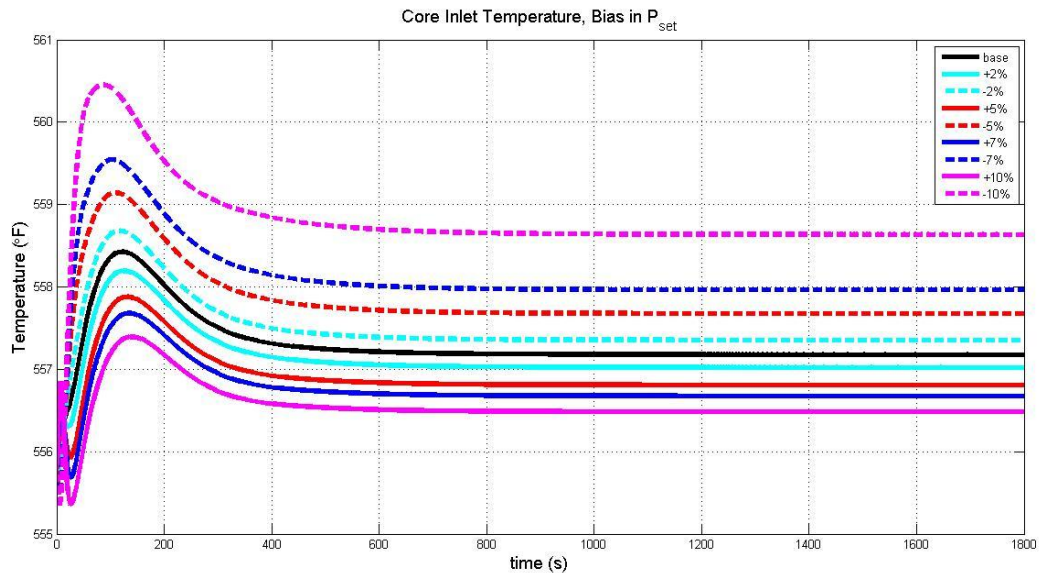


Figure 7.8: Cold leg temperature response for the pressure signal fault range

The changes in the cold leg temperature are not an equal and opposite value compared to the hot leg temperature change. A +1 °F change in the hot leg did not correspond to a -1 °F change in the cold leg temperature. While the error between the measured T_{avg} signal and the set point eventually returns to zero due to the P-I controller, the measurement error is what

creates the difference in the reactivity and subsequent power change. The linear trend for this parameter is shown in Figure 7.9.

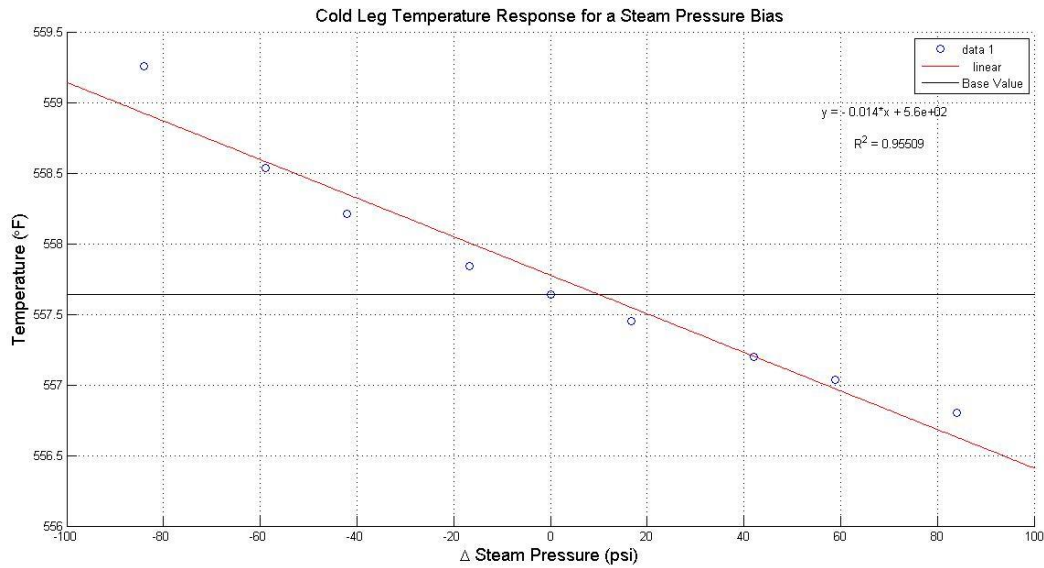


Figure 7.9: Relationship derived for the cold leg from the change in steam pressure

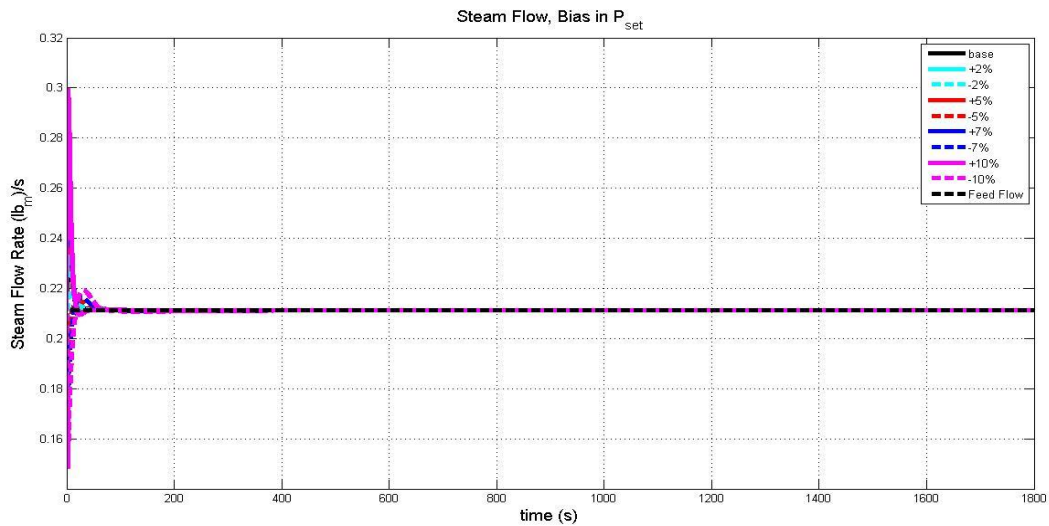


Figure 7.10: Steam flow response for the pressure signal fault range

Since an LFM is not occurring for this set of fault simulations, it is expected the steam flow and feed flow rates would not change in a vast manner for the entire simulation. The steam pressure value is regulated by the steam pressure controller in the BOP portion of the model [9].

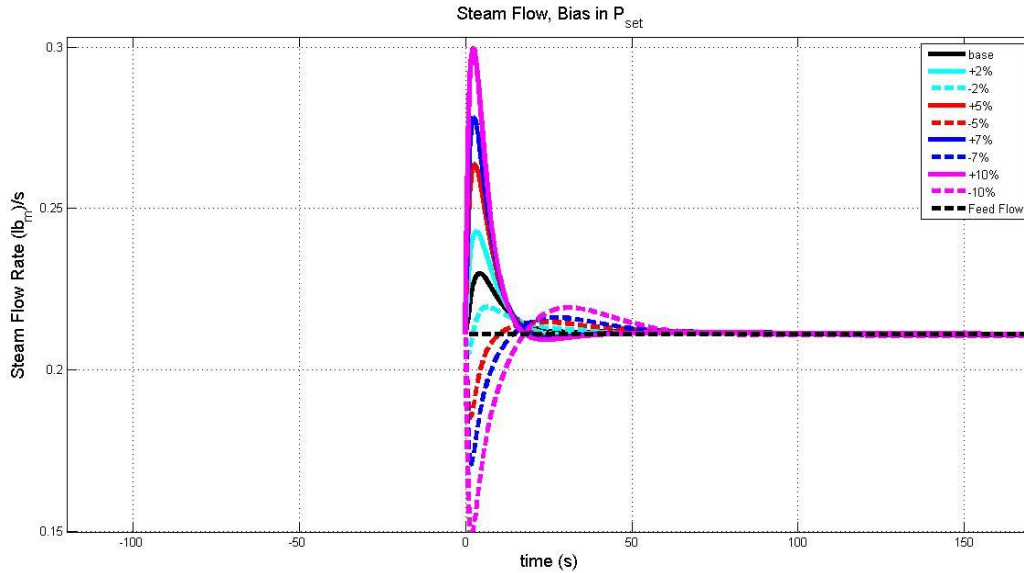


Figure 7.11: Initial steam flow response during the pressure signal fault

The start-up conditions of Figure 7.10 are shown in Figure 7.11. At the initial start of the simulation, there is a maximum increase of 0.3 lbm/s from the baseline 0.211 lbm/s; a 42% increase. This value, although large, returns to its baseline value within 100 seconds.

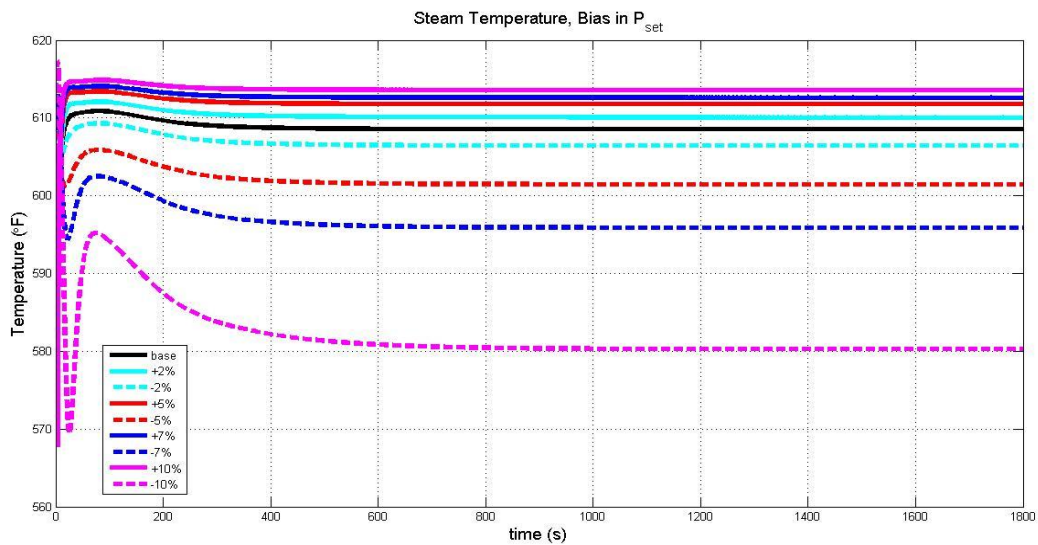


Figure 7.12: Steam temperature response for the pressure signal fault range

The steam temperature parameter experiences the greatest change during the steam pressure bias error. The nominal temperature of 609 °F experiences a maximum increase of 4.7 °F while the maximum temperature decrease is approximately 24.2 °F. This large decrease, however, is not the largest change, partly due to the startup transients as shown in Figure 7.13.

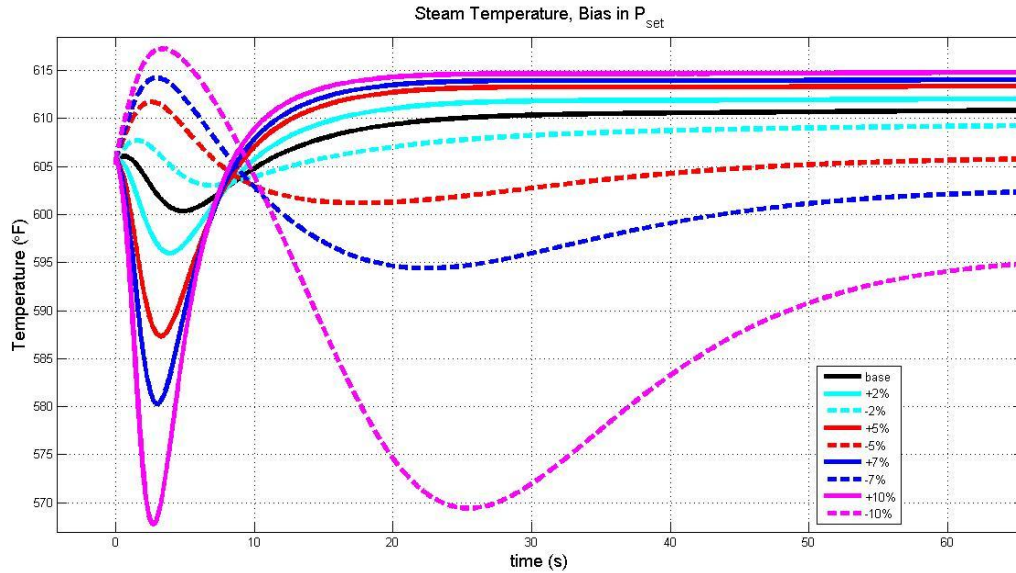


Figure 7.13: Initial steam temperature during the pressure signal fault

It is interesting to note the transient decrease in steam temperature for the +/-10% change in bias lead to a drop to approximately 570 °F; 40 °F less than the baseline temperature. It can be seen the baseline temperature does not experience nearly as a large a change in its value compared to the data experiencing faults. A 40 °F transient deviation from baseline could cause an alarm and possible turbine trip.

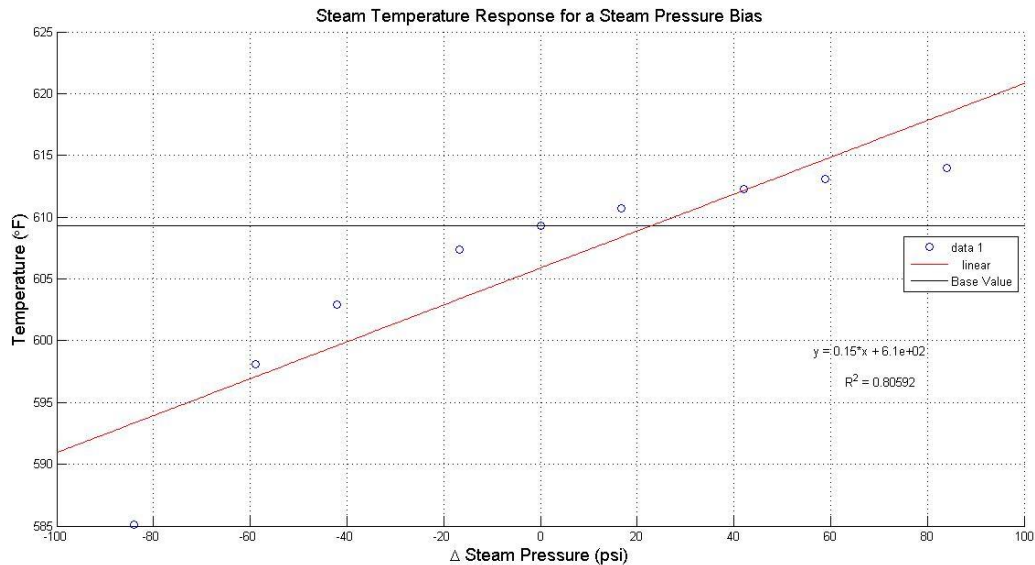


Figure 7.14: Relationship derived for the steam temperature from the change in steam pressure

The linear fit for the steam temperature change has an R^2 value of less than 0.9. Visual inspection of Figure 7.14 shows many of the data points fall within a short range of the linear trend with the exception of the -10% bias error.

7.3. Faults in the P-I Controller

In order to evaluate how changing the P-I controller would affect the system response, it was necessary to introduce a perturbation in the system. For this set of simulations, a +4 °F step fault was added to the hot leg temperature. This affects the measured average temperature and the controller error. The goal was to investigate the influence of varying the controller parameters, k_p and k_i , on the response times of the IRIS model to transients or sensor faults. The perturbations of the parameters were $\pm 10\%$ and $\pm 15\%$ of their nominal values.

7.3.1 Response to a change in the Proportional Constant

For the range of changes in the proportional constant shown in Figure 7.15, there is no noticeable change in the response time of the system. The response times of the controller for the temperature fault are within milliseconds of the baseline values. This indicates a reasonable change in the proportional constant of the system will not greatly affect the power if the temperatures are not also changing.

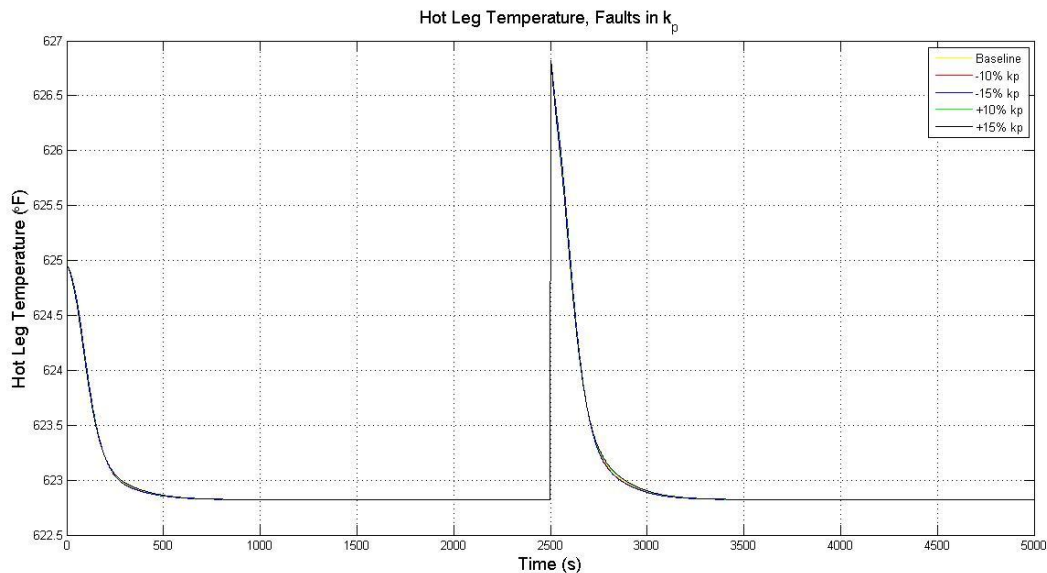


Figure 7.15: Hot leg temperature for a +4 °F Fault for a change in the proportional constant k_p

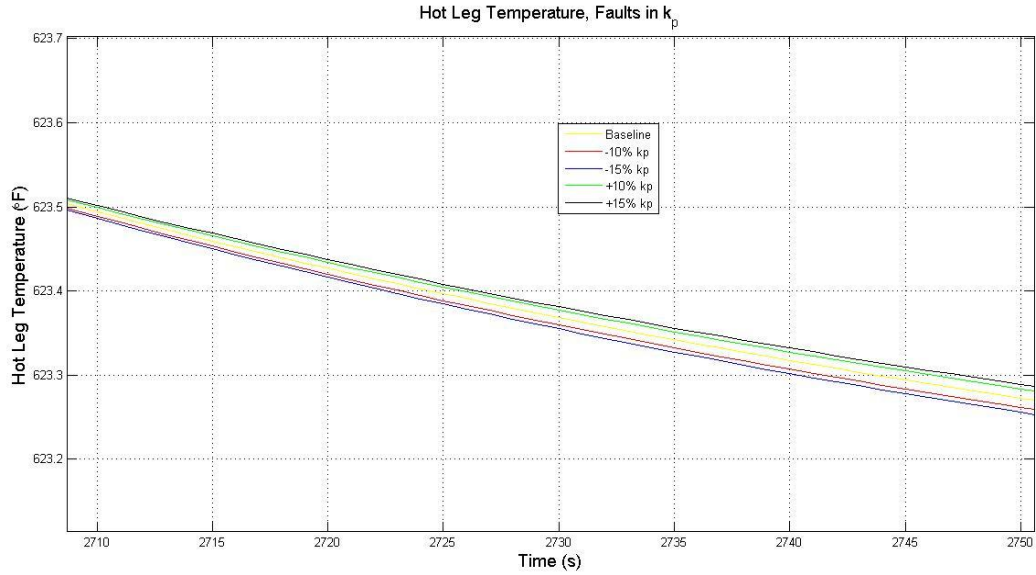


Figure 7.16: Close-up for the hot leg temperature response

Figure 7.15 illustrates the negligible effect of changing the proportional constant in the average temperature controller error. Figure 7.16 is a close-up of these variations.

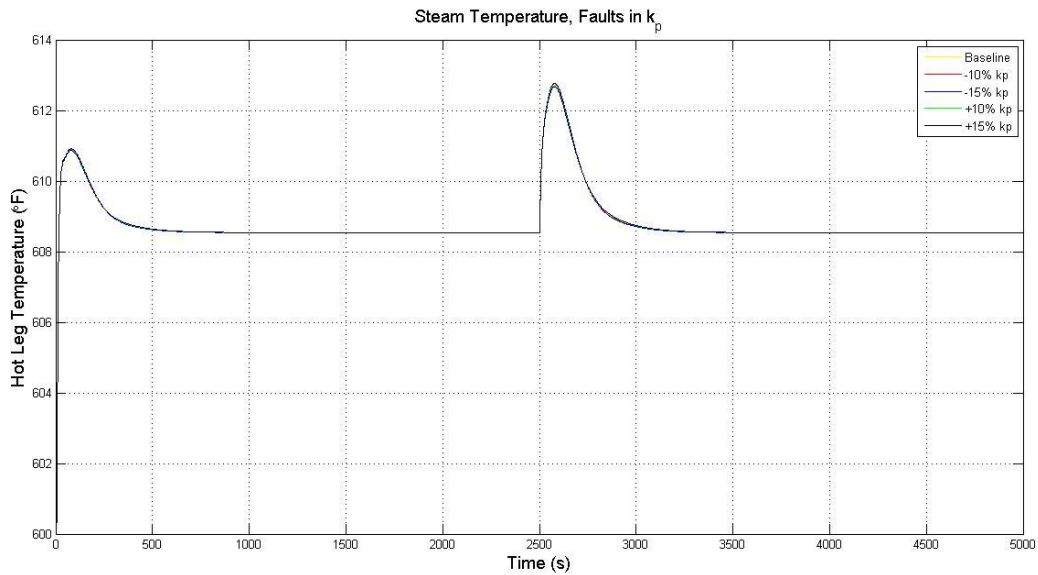


Figure 7.17: Steam temperature for a +4 °F Fault for a change in the proportional constant k_p

Figure 7.17 shows how the steam temperature in the BOP side of the model responds with the changes in the proportional constant. Figure 7.18 shows a close-up of the pressure variations.

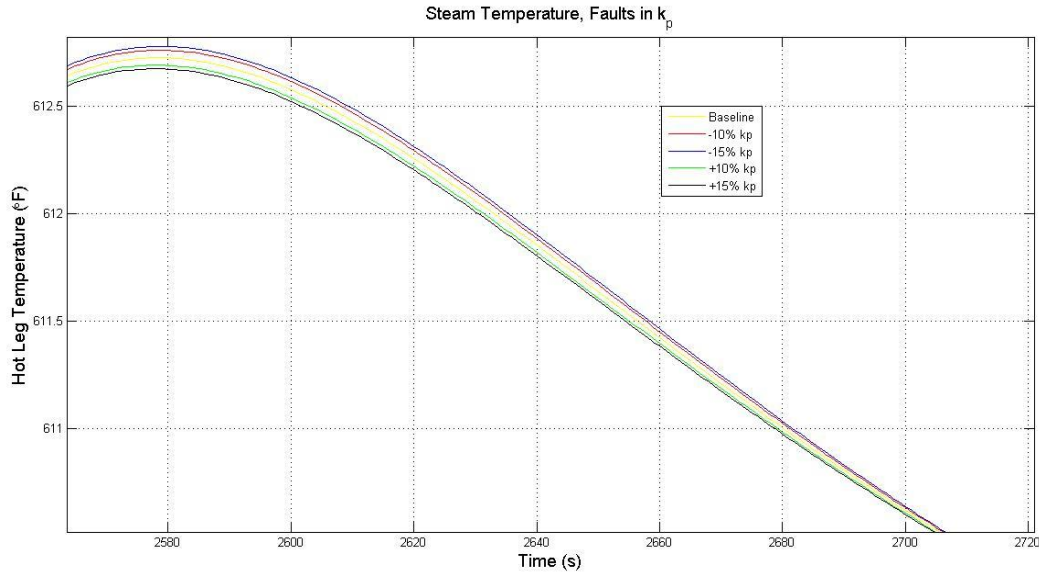


Figure 7.18: Zoomed in steam temperature response

Again, the effects of changing the proportional constant and simulating a transient condition in the model do not differ significantly. The initial change in the pressure is due to the perturbation in the T_{avg} measurement. Response to transients in a reactor must be fast enough to keep a system safe, but also stable. Since the selected parameters did not have an appreciable deviation in their response times to the temperature fault, figures displayed in Chapter 5 for the sensor fault hold consistent for the rest of the general IRIS parameters.

7.3.2 Response to a change in the Integral Constant

This section describes how changing the integral constant in the P-I controller affects the response of the IRIS model to the same hot leg measurement transient. In contrast to changing the values of the proportional constant, Figure 7.19 shows how the response time to a transient changes due to a change in the integral constant. Based on the results shown in Figures 7.19 and 7.20, changing the integral constant can have a significant effect on the response time of the system to a measurement error. A 15% decrease in the integral constant shows a decrease in the system response time by approximately 200 seconds. This is a significant amount of time. It should be noted, however, the actual change in the hot leg temperature is on the order of a fraction of a degree, not a significant change.

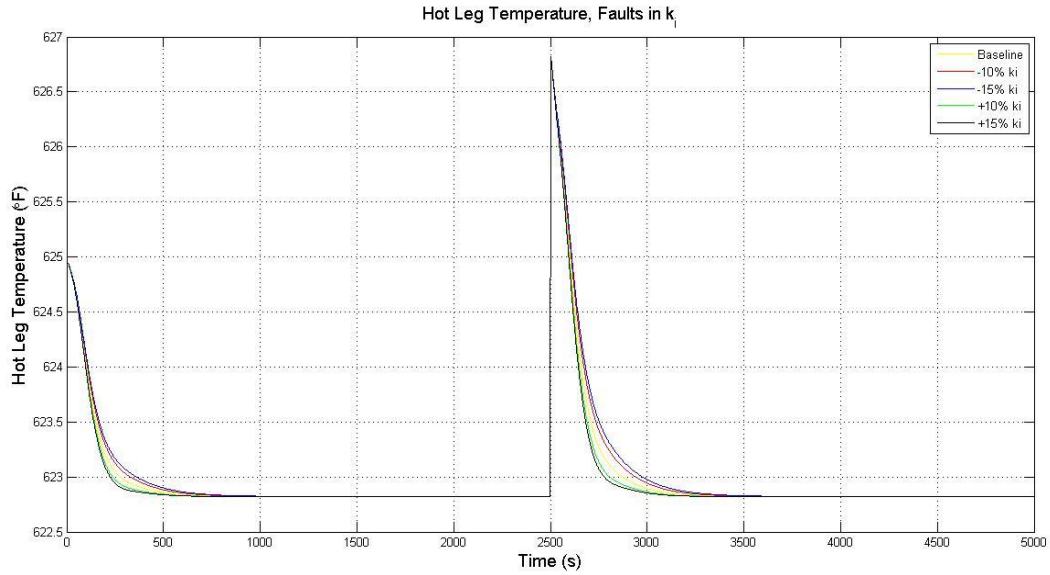


Figure 7.19: Hot leg temperature for a +4 °F Fault change in the proportional constant k_i

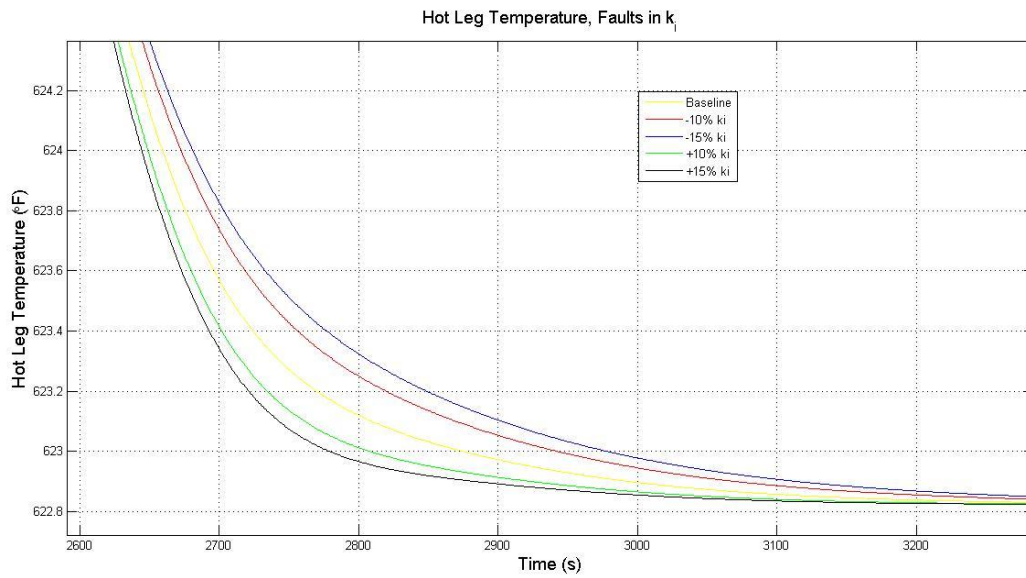


Figure 7.20: Close-up for the hot leg temperature

The deviation in the response for a change in k_i , at its largest value, is likely undetectable since it is such a small change. This change would probably be overshadowed by natural noise in the system.

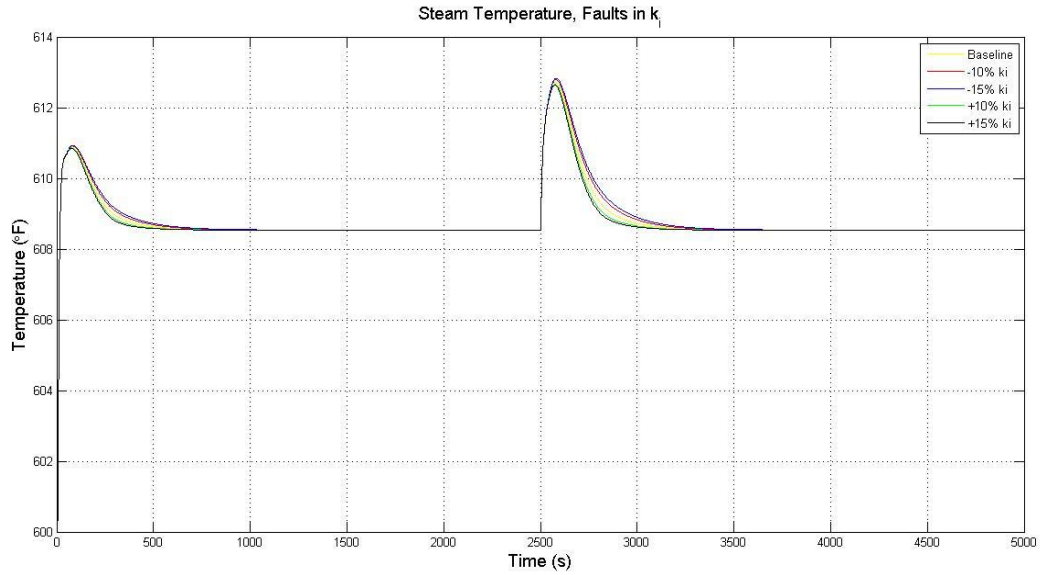


Figure 7.21: Variation in steam temperature for a +4 °F Fault change in the proportional constant k_i

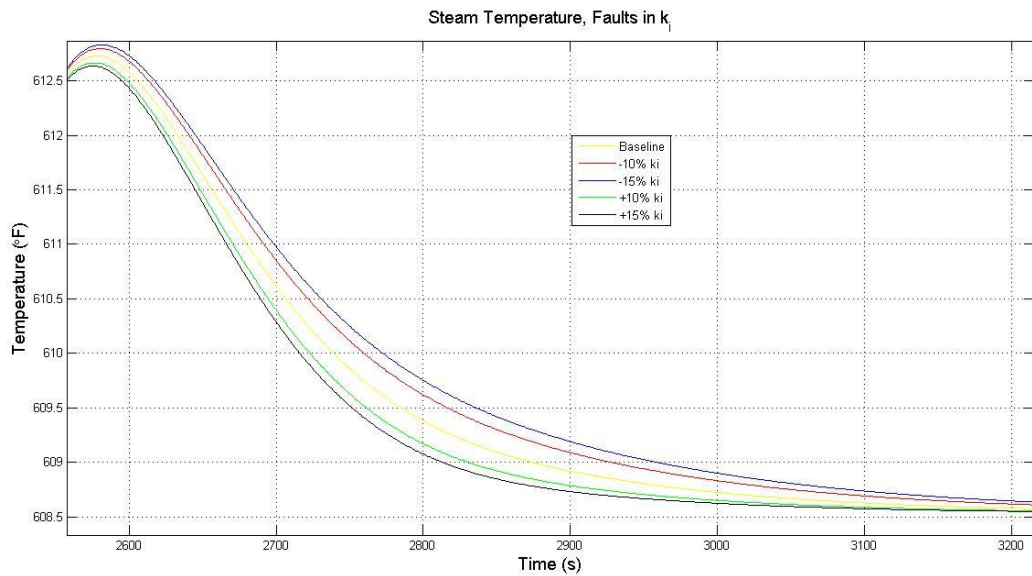


Figure 7.22: Close-up of the steam temperature response

The simulations show that changing the value of the integral constant can increase the response time of the average temperature controller in the IRIS model by approximately 200 seconds. The actual change in the steam temperature is not significant.

7.4. Remarks on General Process Faults

Changing the values of the P-I controller parameters in the T_{avg} controller can have a noticeable effect on response time during a temperature transient. The greatest effect was the response time for a change in the integral constant. Yet, the degree to which the state variables changed was not significant. A similar behavior was observed in the steam temperature response. In addition to faults in the P-I controller, the steam pressure sensor faults produced interesting results as well. The relationships obtained for the set of faults conducted may prove beneficial for fault identification and diagnosis of problems SMRs could experience. These relationships are especially useful for cross checking system information and sensors as a low-cost solution for data confirmation.

8. CONCLUDING REMARKS, SUMMARY AND RECOMMENDATIONS FOR FUTURE R&D

All the research and development tasks under this project (11/2011 – 10/2014) were completed. A summary of significant contributions of the project tasks presented in Volume 2 of the report is given in Section 8.2. Suggestions for future R&D work are outlined in Section 8.3.

8.1. Concluding Remarks

The primary goal of this NEUP funded research and development project was to develop and demonstrate in-situ equipment monitoring methods for small modular reactors (SMRs) with applications to reactor internals such as coolant pumps, valve-actuators, and control rod drive mechanisms. The objective of the project tasks presented in this volume was to develop simulation models of the components of a typical pressurized water reactor SMR and use the model for evaluating plant normal operation and operation under specified faults. These faults included sensor, device, and equipment anomalies and process anomalies.

Recent activities by light water reactor SMR vendors and developers (NuScale Power, Generation mPower, Westinghouse SMR, CAREM in Argentina, SMART design by KAERI, and others) have indicated an increased interest in the development of integral pressurized water reactors for deployment by 2025. SMRs in the 25-200 MWe range are useful for power supply in remote areas, especially in locations with limited infrastructure. SMRs can also be used for co-generation, combining electricity production and process heat for industrial applications, including water desalination. Because of the modular nature of SMRs and limited vessel penetrations, safety and security of such installations are greatly enhanced.

The research and development under this project was focused on the following three major objectives:

Objective 1: Identification of critical in-vessel SMR components for remote monitoring and development of their low-order dynamic models, along with a simulation model of an integral pressurized water reactor (iPWR).

Objective 2: Development of an experimental flow control loop with motor-driven valves and pumps, incorporating data acquisition and on-line monitoring interface.

Objective 3: Development of stationary and transient signal processing methods for electrical signatures, machinery vibration, and for characterizing process variables for equipment monitoring. This objective includes the development of a data analysis toolbox.

The following sub-tasks were accomplished under this Objective 1 and described in Volume 2 of the report.:

- A Pump-Motor Model was developed for simulation of new faults
- The IRIS model was upgraded with new subsystems for more complete simulations
- Process faults were generated and relationships were established for use in fault isolation and diagnosis.

The modeling of new components in the previously developed IRIS model had helped to establish a more complete SMR model. The faults simulated are based on real faults in nuclear plants that would likely be encountered during SMR operation. These faults must be quickly identified and remedied in order to minimize system downtime, maximize safety, and keep the plant economically competitive [7].

8.2. Summary of Significant Contributions Reported in Volume 2

The following is a list of significant contributions of the project tasks described in Volume 1 of the Final Report:

- A detailed literature review of various SMR types, including integral pressurized water reactors (iPWR), and electrical signature analysis of motor-driven systems was completed. A bibliography of literature is provided at the end of this report.
- The iPWR physics model was used to simulate normal operation data and operation with faulty sensors, primary coolant flow rate anomaly, and variations in process parameters such as heat transfer coefficients and reactivity feedback coefficients.
- The iPWR dynamic model was interfaced with the pump-motor model, and this feature was used to introduce variations in the electrical supply frequency and other anomalies in the equipment to simulate their degradation. The relationship between pump flow rate and motor power was verified using experimental data reported in Volume 1.
- The iPWR model was extended to include the dynamics of fission product poisoning and its long-term effect on reactor operation.

Other contributions include the participation by both graduate and undergraduate research assistants and information dissemination in the form of journal papers, conference proceedings, and presentations at national and international meetings.

8.3. Recommendations for Future Research and Development

While simulations conducted through this project have been beneficial for the necessary project goals, more can be done to further increase simulation accuracy. The model is still relatively simple; it can be run on a standard laptop or desktop. The core dynamics, governed by Mann's model [21], only have two nodes used for producing the necessary reactor dynamic equations. Adding nodes to the simulation or using a more complex core model would better model the PWR dynamics.

The primary coolant pressure was always held constant during the simulations. An actual reactor system will have variations in this pressure value during transient operation. The creation of a subsystem to accurately model pressurizer dynamics, like the fission product subsystem, would add another layer of complexity to the model. The greatest challenge faced during this project was the limited simulation time used for the pump-motor model (PMM) that was coupled to the IRIS system. It is unlikely the computational efficiency can be improved since many of the parameters require a small step time to accurately produce data. Another issue to consider in model development is the effect of perturbations in the primary coolant system that adversely influences the pump performance. This feedback coupling to the pump system would be beneficial in understanding the safety implications or the general system performance.

Topics of interest relating to plant control include R&D in the area of fault tolerant control and the incorporation of resiliency under system/equipment/device anomalies and accident conditions. In some applications model-based control strategies may be used as a back-up or parallel control action that have the characteristics of anticipating control actions over a finite future horizon [29].

REFERENCES FOR VOLUME 2

1. R. Pavey, "Price of Vogtle Expansion Could Increase \$900 Million." *The Augusta Chronicle* 11 May 2012: Web. <http://chronicle.augusta.com/news/business/local-business/2012-05-11/price-vogtle-expansion-could-increase-900-million>
2. The White House. Office of the Press Secretary. *Obama Administration Announces Loan Guarantees to Construct New Nuclear Power Reactors in Georgia*. Whitehouse.gov, 16 Feb. 2010. Web. <<http://www.whitehouse.gov/the-press-office/obama-administration-announces-loan-guarantees-construct-new-nuclear-power-reactors>>
3. *Plant Vogtle Units 3 & 4 Fact Sheet*. Southern Company, 2014. Web. <http://www.southerncompany.com/what-doing/energy-innovation/nuclear-energy/pdfs/Vogtle-Fact-Sheet.pdf>
4. H.D. Haynes, "Electrical Signature Analysis (ESA) Developments at the Oak Ridge Diagnostics Applied Research Center," Proceedings of COMADEM '95, the 8th International Congress on Condition Monitoring and Diagnostic Engineering Management, Kingston, Ontario, Canada, June 1995.
5. H.D. Haynes, D.E. Welch, D.F. Cox, and R.J. Moses, "Electrical Signature Analysis (ESA) as a Diagnostic Maintenance Technique for Detecting High Consequence Fuel Pump Failure Modes," Proceedings of the 6th Joint FAA/DOD/NASA Conference on Aging Aircraft, San Francisco, CA, September 19, 2002.
6. J.B. Coble, R. M. Meyer, P. Ramuhalli, L. J. Bond, H. M. Hashemian, B. D. Shumaker, and D. S. Cummins. *A Review of Sensor Calibration Monitoring for Calibration Interval Extension in Nuclear Power Plants*. Rep. no. PNNL-21687. Richland: Pacific Northwest National Laboratory, 2012.
7. H.M. Hashemian, "On-Line Monitoring Applications in Nuclear Power Plants." *Progress in Nuclear Energy* 53.2 (2011): 167-81. Science Direct, Web. <<http://www.sciencedirect.com/science/article/pii/S0149197010001307>>.
8. "Oconee Upgrades to Digital Turbine Controls." *Nuclear News*. American Nuclear Society, September 2005, Web. <<http://www2.ans.org/pubs/magazines/nn/docs/2005-9-2.pdf>>.
9. B.R. Upadhyaya and S.R.P. Perillo, *Advanced Instrumentation and Control Methods for Small and Medium Reactors with IRIS Demonstration, Vol. 5: Multi-modular Integral Pressurized Water Reactor Control and Operational Reconfiguration for a Flow Control Loop*,. Final Report

prepared for the U.S. Department of Energy, University of Tennessee. Report No. DE-FG07-07ID14895/UTNE/2011-7, May 2011.

10. "Small Modular Nuclear Reactors." *Energy.gov*. Office of Nuclear Energy, Web. Mar. 2014. <<http://www.energy.gov/ne/nuclear-reactor-technologies/small-modular-nuclear-reactors>>.

11. F. Franceschini, and B. Petrovic, "Advanced Operation Strategy for the IRIS Reactor: Load Follow through Mechanical Shim (MSHIM)." *Nuclear Engineering and Design* 238 (2007): 3240-252. Science Direct, Web: <<http://www.sciencedirect.com/science/article/pii/S002954930800294X>>.

12. M.D. Carelli, "IRIS: A Global Approach to Nuclear Power Renaissance," *Nuclear News*, pp. 32-42 pp. 32-42, September 2003.

13. "B&W Awarded Second Installment of Its DOE Funding for mPower SMR Development." *Nuclear Power Industry Ews* (28 Aug. 2013): Nuclear Street. Web. <http://nuclearstreet.com/nuclear_power_industry_news/b/nuclear_power_news/archive/2013/08/28/b_2600_w-awarded-second-installment-of-its-doe-funding-for-mpower-smr-development-082801.aspx#.VCxhw_ldVz9>.

14. J.M. Hylko, "Small Is the New Big: The B&W Small Modular Reactor," *Power Mag*. Electric Power, 01 Aug. 2012. Web. <<http://www.powermag.com/small-is-the-new-big-the-bw-small-modular-reactor/>>.

15. *NuScale Plant Design Overview*. Rep. no. NP-ER-0000-1198. Corvallis: NuScale Power, LLC, 2012.

16. "Construction of CAREM Underway." *World Nuclear News*. World Nuclear Association, 10 Feb. 2014. Web. <<http://www.world-nuclear-news.org/NN-Construction-of-CAREM-underway-1002144.html>>.

17. *NuScale Plant Design Overview – Revision 2*. Rep. no. NP-ER-0000-1198-NP. Corvallis: NuScale Power, LLC, Sept. 2013. Print.

18. M.D. Haggerty, M.T. Childerson, and J.A. Halinger. *B&W mPower Reactor Design Overview Technical Report*. Rep. no. 08-00000341-OOO(NP), May 2010, Web. <<http://pbadupws.nrc.gov/docs/ML1015/ML101550512.pdf>>.

19. "Generation mPower: Reactor Module Overview (Redacted)," Presentation to the NRC. 22 Mar. 2012. Web. <<http://pbadupws.nrc.gov/docs/ML1208/ML12087A071.pdf>>.

20. N.E. Todreas and M. Kazimi, "Chapter 3: Reactor Heat Generation." *Nuclear Systems Volume I: Thermal Hydraulic Fundamentals*. Vol. I. Boca Raton: CRC, 1989. Print.
21. S.J. Ball, "Approximate Models for Distributed-Parameter Heat-Transfer Systems," *ISA Transactions*, Vol. 3, No. 1, pp. 38-47, 1964.
22. J.M. Kujawski, D.M. Kitch, and L.E. Conway, "The IRIS Spool Type Reactor Coolant Pump," *Proceedings of ICONE-10, 10th International Conference on Nuclear Engineering*, Arlington, VA, April 2002.
23. J.M. Doster, IRIS Pump Characteristics, Private Communication, 2012.
24. Grundfos Management, Pump Handbook, Grundfos Management A/S, 2004.
25. S.T. Shiels, "Centrifugal Pump Application: Key Hydraulic and Performance Criteria," Imperial Oil Ltd., Dartmouth, Nova Scotia, Canada, 1995.
26. Isotope Cross sections: E.M. Baum, *Nuclides and Isotopes: Chart of the Nuclides*. Chart. 16th ed. Lockheed Martin, pp. 56-58.
27. "Chart of Nuclides." National Nuclear Data Center, BNL. <http://www.nndc.bnl.gov/chart/>
28. J.L. Duderstadt and L.J. Hamilton, *Fission Product Burnup: Analysis of Core Composition Changes*. In *Nuclear Reactor Analysis*, John Wiley, pp. 566-600, 1976.
29. J. Richalet, "Industrial Applications of Model-Based Predictive Control," *Automatica*, Vol. 29, No. 5, pp. 1251-1274, 1993.

REFERENCES AND BIBLIOGRAPHY

1. D.E. Holcomb, B.R. Upadhyaya, et al., Instrumentation, Controls, and Human-Machine Interface Technology Development Roadmap for Grid-Appropriate Reactors, ORNL-GNEP-LTR-2008-041, Oak Ridge National Laboratory, June 2008.
2. C.N. Obiozor, "Selection of motor operated Valves (MOV) for Nuclear Power Plant applications," IEEE Explore, 0-7803-2642, 1995.
3. S. Mukhopadhyay and S. Chaudhuri, "A Feature-Based Approach to Monitor Motor-Operated Valves Used in Nuclear Power Plants," IEEE Transactions on Nuclear Science, Vol. 42, No. 6, December 1995.
4. IEEE Standards Board, IEEE Guide for Motor-Operated Valve (MOV) Motor Application, Protection, Control, and Testing in Nuclear Power Generating Stations, IEEE Standard 1290™, 1996 (R2005).
5. B. Lu, B.R. Upadhyaya, and R.B. Perez, "Structural Integrity Monitoring of Steam Generator Tubing Using Transient Acoustic Signal Analysis," IEEE Transactions on Nuclear Science, Vol. 52, No. 1, pp. 484-493, February 2005.
6. J.W. Hines *et al.*, Technical Review of On-line Monitoring for Performance Assessment, Volumes 1, 2, 3, NUREG/CR-6895, 2008.
7. U.S. Department of Energy, Nuclear Energy Research and Development Roadmap, Report to Congress, April 2010.
8. IAEA Nuclear Energy Series: *On-line Monitoring for Improving Performance of Nuclear Power Plants*, Parts 1 & 2, IAEA Technical Report No. NP-T-1.1 & NP-T-1.2, 2008.
9. J. Coble and J.W. Hines, "Applying the General Path Model to Estimation of Remaining Useful Life," International Journal of Prognostics and Health Management, 2010.
10. D.T. Ingersoll, "Deliberately Small Reactors and the Second Nuclear Era," Progress in Nuclear Energy, Vol. 51, pp. 589-603, 2009.
11. W. Gunther and K. Sullivan, "Detecting and Mitigating Rod Drive Control System Degradation in Westinghouse PWRs," IEEE Transactions on Nuclear Science, Vol. 38, No. 6, December 1991.

12. W. Gunther and K. Sullivan, Aging assessment on PWR Control Rod Drive Systems, BNL-NUREG-52232, Brookhaven National Laboratory. November 1990.
13. R.C. Kryter, Aging and Service Wear of Solenoid-Operated Valves Used in Safety Systems of Nuclear Power Plants –Volume II, Evaluation of Monitoring Methods, NUREG/CR-4819, ORNL/TM-12038, Vol. 2, July 1992.
14. D. Casada and S. Bunch, “The Use of the Motor as a Transducer to Monitor Pump Conditions,” Proceedings of the P/PM Technology Conference, Indianapolis, December 1995.
15. H.D. Haynes, D.E. Welch, D.F. Cox, and R.J. Moses, "Electrical Signature Analysis (ESA) as a Diagnostic Maintenance Technique for Detecting High Consequence Fuel Pump Failure Modes," Proceedings of the 6th Joint FAA/DOD/NASA Conference on Aging Aircraft, San Francisco, CA, September 19, 2002.
16. C. Maxey and H.D. Haynes, "Distributed Capacitance Motion Sensor Employing Electrical Signature Analysis," Proceedings of the Institute of Nuclear Materials Management (INMM), 46th Annual Meeting, Phoenix, Arizona, 2005.
17. H.D. Haynes, "Application of Signature Analysis for Determining the Operational Readiness of Motor-Operated Valves Under Blow-down Test Conditions," Proceedings of the 16th Water Reactor Safety Information Meeting, National Bureau of Standards (NBS), Gaithersburg, MD, October 1988.
18. D.M. Eissenberg, “Status of motor-operated valve aging assessment,” Conf-890373 presentation, 1989.
19. H.D. Haynes, "Evaluation of Check Valve Monitoring Methods," Proceedings of the 17th Water Reactor Safety Information Meeting, Rockville, MD, October 1989.
20. H.D. Haynes, "Recent Improvements in Check Valve Monitoring Methods," NUREG/CP-0114, Vol. 3, pp 403-430, Proceedings of the 18th Water Reactor Safety Information Meeting, Rockville, MD, October, 1990.
21. H.D. Haynes, Aging and Service Wear of Check Valves Used in Engineered Safety-feature Systems of Nuclear Power Plants - Volume II, Aging Assessments and Monitoring Method Evaluations, NUREG/CR-4302, ORNL-6193/V2, April 1991.
22. H.D. Haynes, “Check valve aging assessment,” Conf-9103142 presentation, 1991.
23. H.D. Haynes, "Electrical Signature Analysis (ESA) Developments at the Oak Ridge Diagnostics Applied Research Center," Proceedings of COMADEM '95, the 8th International

Congress on Condition Monitoring and Diagnostic Engineering Management, Kingston, Ontario, Canada, June 1995.

24. K.L. McElhaney, H.D. Haynes, D.F. Cox, P.J. Otaduy, R.H. Staunton, and W.E. Vesely, A Methodology for Evaluation of In-Service Test Intervals for Pumps and Motor-Operated Valves, NUREG/CR-6578, January 1999.

25. H.D. Haynes, D.E. Welch, D.F. Cox, and R.J. Moses, "Electrical Signature Analysis (ESA) as a Diagnostic Maintenance Technique for Detecting High Consequence Fuel Pump Failure Modes," Proceedings of the 6th Joint FAA/DOD/NASA Conference on Aging Aircraft, San Francisco, CA, September 2002.

26. H.D. Haynes, Aging and Service Wear of Electric Motor-operated Valves used in Engineered Safety-feature Systems of Nuclear Power Plants – Vol. 2, Aging Assessments and Monitoring Method Evaluation, NUREG/CR-4234, August 1989.

27. N.E. Huang, et al., "The empirical mode decomposition and the Hilbert transformation for nonlinear and non-stationary time series analysis," Proc. Roy. S. London, Vol. 454, pp. 903-995, 1998.

28. G. Damm, W. Krauthausen, and J. Wolters, Improvements to the Primary Circuit of the FRJ-2, Research Center Jülich, Germany, D-52425.

29. J.S. Park, J.I. Kim, C.W. Lee, J.H. Seo, and L. Wang, "A Rotor dynamic Analysis: Model for Rotor Shaft of SMART MCP," Transactions of the 15th International Conference on Structural Mechanics in Reactor Technology(SMiRT-15) Seoul, Korea, August,1999.

30. H. Huh, J.S. Park, and J.I. Kim, "Thermal Analysis of Canned Induction Motor for Main Coolant Pump in System-Integrated Modular Advanced Reactor," KIEE International Transactions on EMECS, Vol. 3-B, No. 2, pp. 1-6, 2003.

31. Instrumentation Needs for Integral Primary System Reactors (IPSRs), Westinghouse Electric Company LLC, Cooperative Agreement DE-FC07-05ID14690.

32. A.C.O. Barroso *et al.*, "IRIS Pressurizer Design," Proceedings of ICAPP '03, Córdoba, Spain, May 2003.

33. J.M. Kujawski, D.M. Kitch, and L.E. Conway, "The IRIS Spool Type Reactor Coolant Pump," Proceedings of ICONE-10, 10th International Conference on Nuclear Engineering, Arlington, VA, April 2002.

34. Westinghouse Electric Company LLC, AP 1000 design control document, Chapter 5 Reactor Coolant System and Connected Systems.
35. M.D. Carelli, Westinghouse Electric Company LLC, IRIS International Reactor Innovative and Secure, Final technical progress report, November 2003.
36. E. Grove, W. Gunther, and K. Sullivan, Effect of Component Aging on PWR Control Rod Drive Systems, BNL-NUREG-47470, June 1992.
37. D.E. Welch et al., "Electrical Signature Analysis (ESA) as a Diagnostic Maintenance Technique for Detecting the High Consequence Fuel Pump Failure Modes," Proceedings of the 6th Joint FAA/DOD/NASA Conference on Aging Aircraft, San Francisco, CA, September 2002.
38. H.D. Haynes and R.C. Kryter, "Motor Current Signature Analysis for Determining Operational Readiness of Motor-Operated Valves," Proceedings of the 4th Conference on Utility Experience in Reactor Noise Analysis, Hartford, CT, May 1987.
39. R.C. Kryter and H.D. Haynes, "Condition Monitoring of Machinery Using Motor Current Signature Analysis," Proceedings of the Seventh Power Plant Dynamics, Control, and Testing Symposium, Knoxville, TN, May 1989.
40. D. Casada, "Using the Motor to Monitor Pump Conditions," Proceedings of the Fourth NRC/ASME Symposium on Valve and Pump Testing, NUREG/CP-0152, July 1996.
41. E.M. Blake, "The year ahead: This time for sure?" Nuclear News, Vol. 55, No. 1, pp.44-47, January 2012.
42. R.J. Fetterman, A.W. Harkness, M.C. Smith, and C. Taylor, "An Overview of the Westinghouse Small Modular Reactor," Proceedings of the ASME 2011 Small Modular Reactors Symposium, SMR 2011, Washington, D.C., September 2011.
43. Westinghouse Nuclear, www.westinghousenuclear.com/smr
44. B.R. Upadhyaya and S.R.P. Perillo, Advanced Instrumentation and Control Methods for Small and Medium Reactors with IRIS Demonstration, Vol. 5: Multi-modular Integral Pressurized Water Reactor Control and Operational Reconfiguration for a Flow Control Loop. Final Report prepared for the U.S. Department of Energy, University of Tennessee. Report No. DE-FG07-07ID14895/UTNE/2011-7, May 2011.
45. Final Safety Evaluation Report for AP1000, 2004.
46. F. Pollak, Pump Users Handbook, Gulf Publishing Company, 1984.

47. B. Ozpineci and L.M. Tolbert, "Simulink Implementation of Induction Machine Model – A Modular Approach," IEEE Transactions on Power Systems, 2003.

48. National Instruments, "NI 9201." 8-Ch, $\hat{A}\pm 10$ V, 500 KS/s, 12-Bit Analog Input Module, C Series. National Instruments. Web. 30 Mar. 2012.

<http://sine.ni.com/nips/cds/view/p/lang/en/nid/208798> .

49. National Instruments, "NI 9227." 4-Channel Current Input C Series Module. National Instruments. Web. 30 Mar. 2012. <http://sine.ni.com/nips/cds/view/p/lang/en/nid/208794> .

50. National Instruments, "NI 9211." 4-Channel, 14 S/s, 24-Bit, $\hat{A}\pm 80$ MV Thermocouple Input Module. National Instruments. Web. 30 Mar. 2012.

<http://sine.ni.com/nips/cds/view/p/lang/en/nid/208787> .

51. National Instruments, "NI 9234." - 4-Channel, $\hat{A}\pm 5$ V, 51.2 KS/s per Channel, 24-Bit IEPE. National Instruments. Web. 30 Mar. 2012. <http://sine.ni.com/nips/cds/view/p/lang/en/nid/208802>

52. Gould Submersible Pump. Advertisement. KG Power Systems, March 2006. Web. <http://store.kgpowersystems.com/1dw51clea-goulds-pump-submersible-dewatering-1-2-hp-1-phase-3450-rpm-230-volts.aspx> .

53. Fluke, "I200s AC Current Clamp." I200s. Fluke. Web. 30 March 2012.

<http://www.fluke.com/Fluke/usen/Accessories/Current-Clamps/i200s.htm?PID=56289> .

54. G.P. Schultz, Transformers and motors: a single-source reference for electricians. Woburn, MA: Newnes, 1989.

55. HVAC Heating Ventilation & Air Conditioning, Department of Natural Resources, State of Louisiana. N.p., n.d. Web. 27 March 2012.

<http://dnr.louisiana.gov/assets/TAD/education/ECEP/hvac/d/d.htm> .

56. "Model of the dynamics of single phase asynchronous machine with squirrel-cage rotor – Simulink," MathWorks - MATLAB and Simulink for Technical Computing, March 2012.

<http://www.mathworks.com/help/toolbox/phymod/powersys/ref/singlephaseasynchronousmachine.html?nocookie=true> .

57. "Model the dynamics of three-phase asynchronous machine, also known as induction machine - Simulink." MathWorks - MATLAB and Simulink for Technical Computing. N.p., n.d. Web. 27 March 2012.

<http://www.mathworks.com/help/toolbox/phymod/powersys/ref/asynchronousmachine.html> .

58. J.W. Hines, B.R. Upadhyaya et al., Advanced Instrumentation and Control Methods for Small and Medium Reactors with IRIS Demonstration, Vol. 1: Executive Summary. Final Report prepared for the U.S. Department of Energy, University of Tennessee. Report No. DE-FG07-07ID14895/UTNE/2011-3, May 2011.

59. J.S. Bendat and A.G. Piersol, Random Data: Analysis and Measurement Procedures, Third Edition, Wiley Interscience, New York, 2000.

60. B.P. Lathi, *Signal Processing and Linear Systems*, Oxford University Press, New York, 1998.

61. S.M. Kay, Modern Spectral Estimation, Prentice-Hall, Englewood Cliffs, NJ, 1988.

62. R.B. Randall, Frequency Analysis, Bruel & Kjaer, Denmark, 1984.

63. S.L. Marple, Jr., Digital Spectral Analysis with Applications, Prentice-Hall, Englewood Cliffs, NJ, 1987.

64. O. Rioul and M. Vetterli, "Wavelets and Signal Processing," IEEE Signal Processing Magazine, Vol. 8, No. 4, pp. 14-38, October 1991.

65. D.E. Newland, An Introduction to Random Vibrations, Spectral & Wavelet Analysis, (Third Edition) Longman Group Limited, Essex, England, 1993.

66. B. Lu, B.R. Upadhyaya, and R.B. Perez, "Structural Integrity Monitoring of Steam Generator Tubing Using Transient Acoustic Signal Analysis," IEEE transactions on Nuclear Science, Vol. 52, No. 1, pp. 484-493, February 2005.

67. N.E. Huang et al., "The Empirical Mode Decomposition and the Hilbert Transformation for Nonlinear and Non-stationary time series analysis," Proc. Royal Society of London, A 454, pp. 903-995, 1998.

68. IMI Sensors Product Catalog, IMI, 2003, www.vitek.com.br. 2003. Web. 05 June 2012.

http://www.vitek.com.br/imi/catalogo_imi.pdf .

69. "Pressure Transducers." Pressure Transducers. Omega, n.d. Web. 12 June 2012.
<http://www.omega.com/prodinfo/pressuretransducers.html> .
70. "Accelerometer Concepts." PCB Piezotronics, Inc. - Tech Support. PCB, 2012. Web. 18 June 2012. http://www.pcb.com/techsupport/tech_accel.php .
71. "ILK Dresden - Durchfluss Berechnung Nach ISO 5167." ILK Dresden - Durchfluss Berechnung Nach ISO 5167. 8 Oct. 2009. Web. 25 May 2012.
<http://www.ilkdresden.de/iso5167/index.html> .
72. M. Naghedolfeizi and B.R. Upadhyaya, *Dynamic Modeling of a Pressurized Water Reactor Plant for Diagnostics and Control*, Research Report prepared for the U.S. Department of Energy, University of Tennessee, DOE/NE/88ER12824-02, June 1991.
73. I. Karassik and R. Carter, *Centrifugal Pumps*, McGraw-Hill, New York, 1976.
74. F. Pollak, *Pump Users Handbook*, Gulf Publishing Company, 1981.
75. Final Safety Evaluation Report for the Westinghouse AP1000 Reactor, 2004.
76. Technical Review No. 3, Bruel & Kjaer, Hilbert Transform, Denmark, 1984.
77. B. R. Upadhyaya and T. W. Kerlin, "Estimation of Response Time Characteristics of Platinum Resistance Thermometers by the Noise Analysis Technique," *ISA Transactions*, Vol. 17, pp. 21-38, 1978.
78. B. R. Upadhyaya and M. Kitamura, "Stability Monitoring of Boiling Water Reactors by Time Series Analysis of Neutron Noise," *Nuclear Science and Engr.*, Vol. 77, No. 4, pp. 480-492, 1981.
79. B.R. Upadhyaya, O. Glockler, and J. Eklund, "Multivariate Statistical Signal Processing Technique for Fault Detection and Diagnostics," *ISA Transactions*, Vol. 29, No. 4, pp. 79-95, 1990.
80. K.M. Kim, B.I. Lee, D. Lee, H.H. Cho, and K.H. Jeong, "Experimental and numerical study on local pressure distributions in a system-integrated modular reactor," *Annals of Nuclear Energy*, Vol. 47, pp. 216-224, 2012.
81. J.N. Reyes, Jr., "NuScale Plant Safety in Response to Extreme Events," *Nuclear Technology*, Vol. 178, pp. 153-163, May 2012.

82. J. Eklund and B.R. Upadhyaya, "An Automated System for Motor-Operated Valve Diagnostics," *Power Engineering*, pp. 38-41, December 1991.
83. M. Sharp, *Prognostic Approaches Using Transient Monitoring Methods*, Doctoral Dissertation, University of Tennessee, Knoxville, 2012.
84. J.J. Jelovich and G. Werber, "Application of the Digital Rod Drop Indication for Establishment of Control Rod Drive-Line Dynamic Characteristics of a PWR," *IEEE Transactions on Nuclear Science*, Vol. NS-25, No. 1, February 1978.
85. W. L. Dufek, J.J. Jelovich, and J.A. Neuner, "A Fault Tolerant, Multiplexed Control Rod Position Detection and Indication System for Nuclear Power Plants," *IEEE Transactions on Nuclear Science*, Vol. NS-24, No. 1, February 1977.
86. Grundfos Management, *Pump Handbook*, Grundfos Management A/S, 2004.
87. S.T. Shiels, "Centrifugal Pump Application: Key Hydraulic and Performance Criteria," Imperial Oil Ltd., Dartmouth, Nova Scotia, Canada, 1995.
88. H.M. Hashemian, E. Riggsbee, and R. O'Hagan, *Wireless Sensors for Predictive Maintenance of Rotating Machinery in DOE's Research Reactors*, Final Project Report prepared for DOE by Analysis and Measurement Services Corp., December 2012.
89. H.M. Hashemian, "Wireless Sensors for Predictive Maintenance of Rotating Equipment in Research Reactors," *Annals of Nuclear Energy*, Vol. 38, pp. 665-680, 2011.
90. H.M. Hashemian, C.J. Kiger, G.W. Morton, and B.D. Shumaker, "Wireless Sensor Applications in Nuclear Power Plants," *Nuclear Technology*, Vol. 173, No. 1, pp. 8-16, 2011. 91. H.M. Hashemian, *Wireless Sensors for Predictive Maintenance of Rotating Equipment in DOE's Research Reactors*, DOE Phase I Final Report, AMS Corp., DE-FG02-08ER85004, May 2009.
92. *Guidelines for Wireless Technology in Power Plants, Volume 1: Benefits and Considerations*, 1003584, Electric Power Research Institute, 2002.
93. *Guidelines for Wireless Technology in Power Plants, Volume 2: Implementation and Regulatory Issues*, 1007448, Electric Power Research Institute, 2002.
94. B.J. Kaldenbach et al., *Assessment of Wireless Technologies and their Application at Nuclear Facilities*, NUREG/CR-6882, July 2006.
95. *Revised Guidelines for Wireless Technology in Power Plants, Volume 1: Benefits and Considerations*, EPRI Report 1013485. Project Manager: A Hussey, December 2006.

96. D. Shull and J. Cordaro, "Careful, hot wireless," InTech Magazine, January 2008.
97. E.F. Policastro, "Driving Data Node to Node," ISA InTech Magazine, pp. 32-35, June 2005.
98. Wireless Sensor Networks, National Instruments, <http://www.ni.com/wsn/>
99. C.B. Jacobsen, The Centrifugal Pump, Grundfos Research and Technology, 2004.
100. J.M. Doster, IRIS Pump Characteristics, Private Communication, 2012.
101. U.S. Nuclear Regulatory Commission, Cyber Security Programs for Nuclear Facilities, Regulatory Guide 5.71, January 2010.
102. I. Daubechies, Ten Lectures in Wavelets, Society for Industrial and Applied Mathematics, Philadelphia, PA, 1992.
103. G. Strang and T. Nguyen, Wavelets and Filter Banks, Wellesley-Cambridge Press, Wellesley, Massachusetts, 1996.
104. C.S. Burrus, R.A. Gopinath, and H. Guo, Introduction to Wavelets and Wavelet Transforms, Prentice-Hall, Upper Saddle River, NJ, 1998.
105. O. Rioul and M. Vetterli, "Wavelets and Signal Processing," IEEE Signal Processing Magazine, Vol. 8, No. 4, pp. 14-38, October 1991.
106. R.M. Rao, *Wavelet Transforms: Introduction to Theory and Application*, Addison-Wesley, Canada, 1998.
107. A.M. Gaouda *et al.*, "Monitoring HVDC systems using wavelet multi-resolution analysis," IEEE Transactions on Power Systems, Vol. 16, pp. 662-670, 2001.
108. M. Young, The Technical Writer's Handbook. Mill Valley, CA: University Science, 1989.
109. International Atomic Energy Agency (IAEA), *Advanced Surveillance, Diagnostic and Prognostic Techniques in Monitoring Structures, Systems and Components in Nuclear Power Plants*, IAEA Nuclear Energy Series No NP-T-3.14, Vienna, Austria, September, 2013.
110. Isotope Cross sections: E.M. Baum, *Nuclides and Isotopes: Chart of the Nuclides*. Chart. 16th ed. Lockheed Martin, pp. 56-58.

111. S.F. Mughab, M. Divadeenam, and N.E. Holden, "Neutron Cross Sections from Neutron Resonance Parameters and Thermal Cross Sections," *The Isotopes Project*. LBNL, 1981. Web. <http://ie.lbl.gov/ngdata/sig.htm#A=231>
112. "Chart of Nuclides." *National Nuclear Data Center*, BNL. <http://www.nndc.bnl.gov/chart/>
113. J.L. Duderstadt and L.J. Hamilton, Fission Product Burnup: Analysis of Core Composition Changes. In *Nuclear Reactor Analysis*, John Wiley, pp. 566-600, 1976.
114. N.E. Todreas, "Chapter 3: Reactor Heat Generation." *Nuclear Systems I: Thermal Hydraulic Fundamentals*, New York: Taylor & Francis, 1990.
115. J.W. Hines *et al.*, *Technical Review of On-line Monitoring for Performance Assessment*, Volumes 1, 2, 3, NUREG/CR-6895, 2008.
116. J. Henkel, *Development of a Safeguards Monitoring System for Special Nuclear Facilities*, Doctoral Dissertation, University of Tennessee, August 2011.
117. B.R. Upadhyaya, C. Mehta, V.B. Lollar, J.W. Hines, and D. de Wet, "Approaches to Process Monitoring in Small Modular Reactors," Proceedings of the ASME 2014 Small Modular Reactors Symposium, Washington, D.C., April 2014.
118. J.W. Hines and D. Garvey, "Development of a Process and Equipment Monitoring (PEM) Toolbox and its Application to Sensor Calibration Monitoring," *Fourth International Conference on Quality and Reliability (ICQR4)*, Beijing, PRC, 2005.
119. B.R. Upadhyaya, C. Mehta, and D. Bayram, "Integration of Time Series Modeling and Wavelet Transform for Monitoring Nuclear Plant Sensors," IEEE transactions on Nuclear Science, Vol. 61, No. 5, pp. 2628-2635, October 2014.
120. J. Richalet, "Industrial Applications of Model-Based Predictive Control," *Automatica*, Vol. 29, No. 5, pp. 1251-1274, 1993.

